The Synthesis, Characterisation and Properties of Self-Assembled Hollow and Low Density Microspheres

By

Stephen J. Mee

A thesis submitted to the
University of Birmingham
For the degree of
DOCTOR OF ENGINEERING

School of Chemical Engineering
College of Engineering and Physical Sciences
University of Birmingham
May 2011

49808 words

UNIVERSITY^{OF}BIRMINGHAM

*Anybody who has been seriously engaged in scientific work of
any kind realizes that over the entrance to the gates of the temple of science
are written the words: Ye must have faith.*

Max K. E. L. Planck, 1932
b. 1858 – d. 1947

Dedicated to my beloved,

beyond measure.

Abstract

Hollow low density microspheres were prepared by adsorbing kaolin nanoparticles onto a polystyrene (PS) template. A cationic polyelectrolyte, poly(diallydimethylammonium chloride), was initially adsorbed on the PS to render the surface cationic enabling the kaolin nanoparticles to form a shell structure due to electrostatic attraction forces. An increase in ionic strength by the addition of 0.1 M NaCl increased the amount of polyelectrolyte adsorbed at the PS surface. Solvent relaxation NMR experiments indicated that solvent molecules were bound at the PS surface suggesting attached polymer chains. Zeta potential experiments indicated a change in the surface potential at the PS interface due to the addition of a polyelectrolyte, as little as 0.1 g m^{-2} of polyelectrolyte was required to change the PS surface potential. Surface saturation of the PS resulted in a zeta potential of 63.5 ±2.6 mV, at pH 6.6 ±0.2.

Kaolin adsorption was determined by reduced sediment volume experiments and observed by the use of scanning electron microscopy (SEM). The influence of an increase in the kaolin ratio and the calcination process on the microsphere structure was investigated. When calcined at 1000 ºC for 60 min the microsphere properties exhibited a particle size (d_{50}) of 11.2 ±0.4 μm and a bulk density of 0.13 ±0.01 g/cm^3. The internal structure of the calcined microspheres were characterised by the use of SEM and focused ion beam (FIB) instruments. The characteristic properties of the calcined kaolin microspheres were determined by thermogravimetric analysis (TGA), X-ray diffraction (XRD), X-ray fluorescence (XRF), and X-ray photoelectron spectroscopy (XPS).

Acknowledgment

Table of Contents

Prologue

1. Chapter One: Hollow Microspheres

4. Chapter Four: Materials Characterisation

5. Chapter Five: Adsorption Studies of Polyelectrolyte and Kaolin Fine Particles on Polystyrene

6. Chapter Six: Removal of Sacrificial Core Material by Calcination

7. Chapter Seven: Conclusions and Extension of Research

Appendices

List of Figures

List of Tables

Chapter One: Hollow Microspheres

1.1.   Introduction

Hollow microsphere structures are of great interest in many current and emerging areas of technology. Their sales are continuously increasing because of a large number of well-known and new applications [Bertling, et al. 2004]. While most of the current needs for hollow microspheres are met by inorganic by-products of combustion processes, the fabrication of tailor-made hollow microsphere structures by processes like emulsion and suspension techniques is gaining more interest. Understanding the surface phenomena has also become an important role as far as the formation, properties and stability of hollow microspheres are concerned.

Hollow microspheres have a promising potential because of their advantageous properties such as low effective density and high specific surface area. The shell structure may be made from glass, oxide ceramics, mixed oxides, silicates and alumo-silicates, polymers or metals. Hollow microspheres are widely used in numerous industrial applications for the reduction of material weight, the encapsulation of bioactive and catalytically active substances, the modification of strength of compounds, improvements in thermal and acoustical insulation etc. The use of hollow microspheres in the mass market as fillers for construction materials, thermoplastics, resins, or sintered materials or for the manufacture of syntactic foams requires the availability of large quantities at low prices. On an industrial scale, hollow microspheres have been manufactured by using single-process methods suitable for controlling the structure on the macro- and micro scale these include: high temperature smelting processes [Veatch, et al. 1962; Beck, et al. 1968] and by spray drying technologies [Netting, 1974; Sands, 1983]. The size distribution of these fabricated microspheres mainly

1

depends on the process parameters [Wilcox, et al. 1995; Bertling, et al. 2004]. At present, the manufacturing of hollow microspheres on a commercial scale requires narrow size distribution and non-porous shell structures to avoid costly secondary treatment processes.

The properties of hollow microspheres are promising; the most prospective applications will probably be the modification of materials and the manufacturing of composites for pharmaceutical and medical applications. At present, the correlation between process parameters, structures formed, and application properties is far from being fully understood. It is possible, that the most promising way to obtain tailor-made hollow structures is provided by various template techniques, whereby inorganic, organic and even hybrid structures are possible.

The opportunities for the applications of spherically shaped materials are extensive. The ability to synthesise and fabricate materials into spherical geometries, either hollow or solid, provides components with some important performance capabilities for a wide variety of products. Some of the applications for solid and hollow microspheres are as follows (i) free flowing delivery, (ii) catalyst support, (iii) fillers, (iv) coatings and paint additives, (v) refractory thermal insulation, and (vi) light weight composites, (vii) encapsulation of drug and agricultural products, (viii) gas and chemical storage devices, and (ix) lightweight concrete and cement. When hollow microspheres are added to materials as fillers they usually impart a variety of useful properties, not only can they reduce density, they also can contribute to dimensional stability, impart insulating properties and add rigidity and stress resistance. Although microspheres are sometimes specified to reduce the initial cost of the material to which they are added, performance improvements are the principle reason for their use. Perhaps the best known use of microspheres has been as fillers for such plastics as

polyesters and vinyls, as hollow glass microspheres have approximately one-fifth density of most resins. The design of a hollow microsphere for a particular application depends upon the demand that the processing makes on the physical strength of the microsphere. Hollow microspheres with high aspect ratios are generally suitable for applications involving mild agitation and low pressure.

1.2.   *Properties of Hollow Microspheres*

Functions being performed by solid and hollow microspheres of organic and inorganic materials include (i) the containment of solids, liquids or gases, (ii) creation of composites with desirable electrical, mechanical, optical, thermal and density properties, and (iii) free flowing material characteristics. Microspheres are usually white or grey in colour, and several manufacturers offer various inorganic hollow microspheres. The wall thickness of the particles are generally 10% of their diameter [Sands, et. al. 1982], the latter mainly exhibiting dimensions which range between 20 to 100 μm (d_{50}), however, the narrow size distributions of the individual product types differ widely. The bulk densities of hollow microspheres generally vary between 0.1 and 0.7 g/cm^3 and thus are clearly below those of the conventional fillers. Hollow microspheres are characterised by a number of parameters including geometric properties (size distribution and shell thickness), physical properties (effective density, specific surface area, thermal and electrical resistance and mechanical strength), the spherical shape has a uniform curvature so that any applied force causes the least stress concentration and so provides for maximum strength, optical properties (refractive index and colour), and chemical properties (pH in suspension, surface chemistry and chemical resistance against hydrolysis and oxidation).
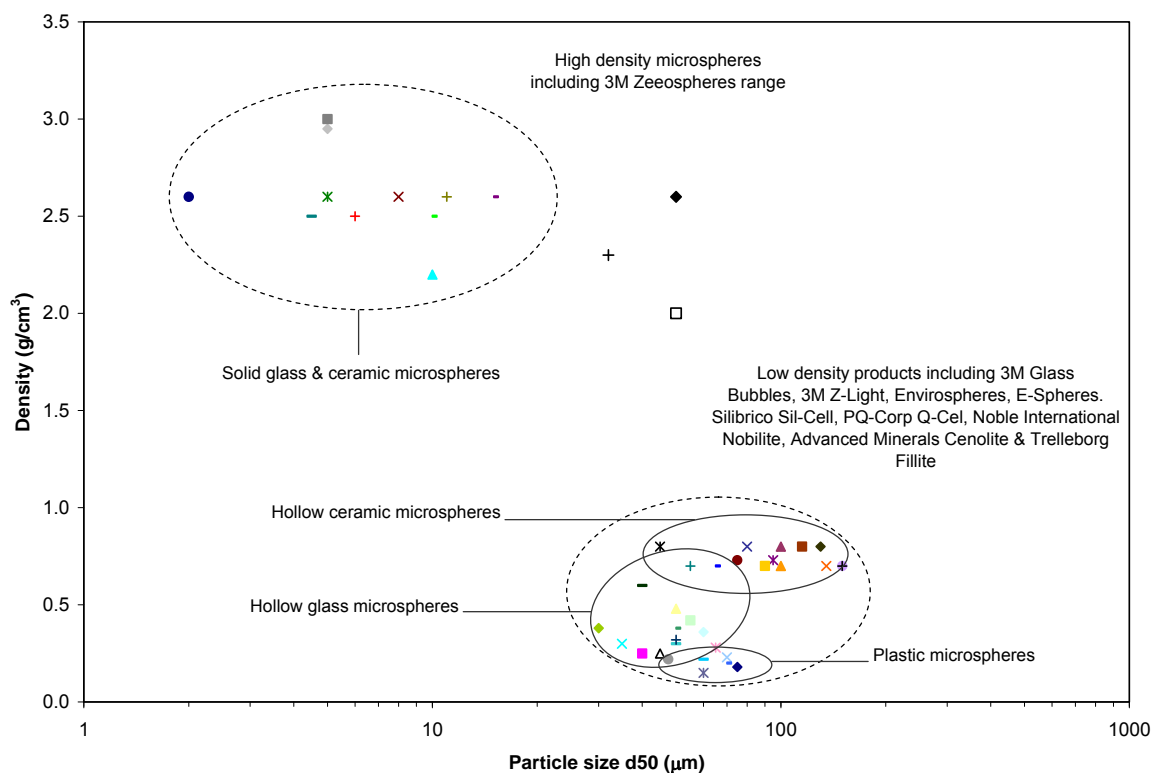
Figure 1.1 *Minimum values for density as a function of average size for a range of commercial microsphere products and patent claims.*
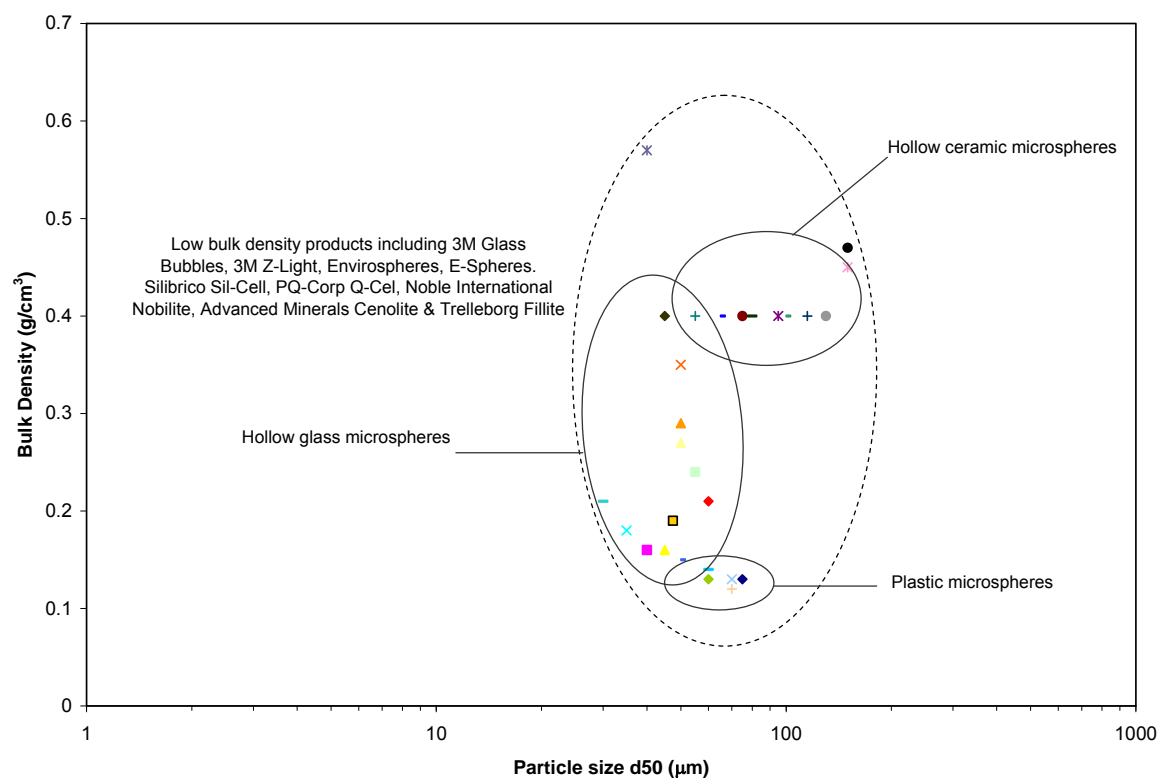
Figure 1.2 *Minimum values for bulk density as a function of average size for a range of commercial microsphere products and patent claims.*

Figures 1.1 and 1.2 indicate the relationship between the particle size for commercial microspheres, density and bulk density, respectively. Figure 1.1 indicates that as the microsphere particle size is reduced the density is increased. With regards to low bulk density, most commercial microspheres are in the particle size range of 30 to 90 μm

As an example of their capacity to reduce weight, the addition of 8% hollow microspheres (weight) to a 20 wt% glass reinforced polyester laminate reduces the bulk density value from 1.31 to 1.03 g/cm^3 [Bledzki, et. al. 1985]. The disadvantage of adding hollow microspheres to a composite is that they can cut flexural strength and modulus. In a phenolic (thermosetting resin) the addition of 25 wt% hollow microspheres reduced the mechanical properties, but improved the electrical and thermal properties. Hollow microspheres when used in the core of syntactic foam composites not only serves to make the sandwich structure lightweight, but also increases stiffness and improves crack resistance of the thermoformed parts [Houston, 1975]. Figure 1.3 describes the properties that can be attributed to an ideal microsphere structure when added to a material as a filler component [Sargeant, 1991].
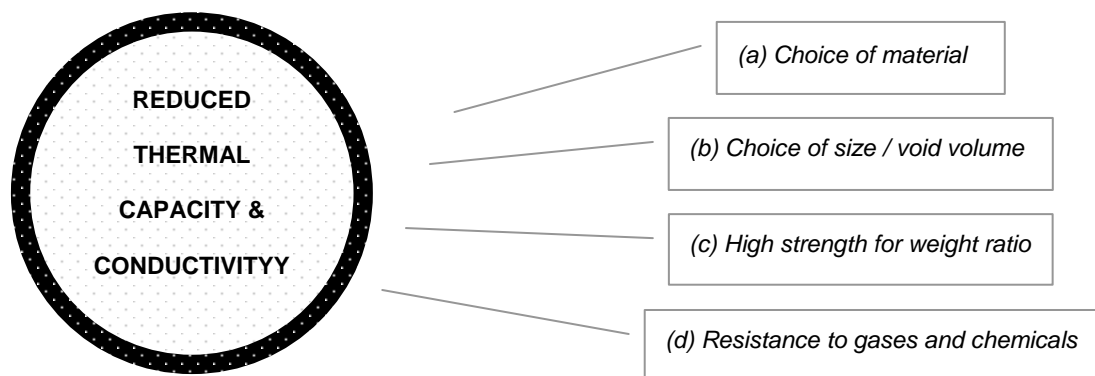
Figure 1.3 *Section of an ideal hollow microsphere.*

Numerous applications desire fine particle size microspheres, as low as 10 μm and below. Generally, the manufacturing and supplying of microspheres less than 10 μm have not been achieved often due to limitations of the manufacturing process. Bulk density and specific gravity values for microspheres reported in Table 1.1 vary depending on whether they are solid and hollow, glass, ceramic or plastic. Typical loading levels for microspheres are in the 10% by weight range for most applications, but can go as high as 50% for selected end uses such as electromagnetic interference shielding.

Table 1.1 *Typical specific gravity values by product type.*

Microsphere Material	Structure	Specific Gravity (g/cm³)
Glass	Solid	2.5
Glass	Hollow	0.15 – 0.6
Ceramic	Solid	2.4
Ceramic	Hollow	0.7
Plastic	Unexpanded	0.1
Plastic	Expanded	0.01

Glass microspheres are the dominant type of microsphere consumed. There are two main methods for producing solid glass microspheres including; (i) fire polishing of crushed particles and (ii) atomisation of molten materials. Hollow glass microspheres are often produced by using a spray nozzle technique, while ceramic microspheres are a by-product of an incineration process. Hollow ceramic microspheres can be produced by mixing a sol-gel precursor and a volatile liquid. Hollow thermoplastic microspheres are generally manufactured by an emulsion polymerisation process.

1.3.   Commercial Microsphere Properties

Microspheres provide a variety of functional benefits to the compounds in which they are employed. These benefits range from lighter weight, thermal stability to unique electrical properties as listed in Table 1.2. Their spherical shape offers the lowest surface-area-to-volume ratio of any geometry for high volume loading. Identical spherical shapes facilitate good handling and flow properties.

Table 1.2 *Performance benefits required from microspheres by application.*

Application	Weight Reduction	Thermal Reduction	Sound Insulation	Strength
Adhesives	X	X	-	X
Auto coatings	X	-	X	X
Coatings	X	X	-	X
EMI shielding	X	-	-	-
Reinforced plastics	X	-	-	X
Offshore products	X	X	-	X
Paper	X	-	-	-
Sealants	X	-	X	X

A specific number of performance improvements that could expand the market use of microspheres have been identified, these include; pre-packed emulsions of microspheres to improve processing in coatings; increased R-value[1] of hollow microspheres to increase the thermal insulating properties in coatings, sealants, and offshore products; an opaque microsphere to improve opacity in coatings and replace the need for expensive titanium white and; an increased crush strength of hollow microspheres to reduce damage during the mixing process in numerous applications.

---

[1] The R-value is a measure of thermal resistance, under uniform conditions the R-value is the ratio of the temperature difference across an insulator and heat flow per unit area.

1.4. **Alternative products**

Microspheres only accounted for a small fraction of the 14 billion tonne market for filler materials consumed in North America in 2004. These products are used in numerous end uses, initially they were used to reduce raw material costs and provide only nominal performance benefit to the final product. However, over the last few decades, a great deal of research has been conducted on fillers that also add functional benefits to the material in which they are incorporated. In 2004, the major markets that incorporated filler materials included: paper, plastics, coatings, rubber, adhesives and sealants. Of these, the plastics market has experienced the most dramatic growth over the past decade increasing its use of fillers far in excess of the growth of plastics demand. The major driving force for this growth in the use of fillers has been; rising costs of polymers; increasing need for lighter weight materials in automotive and aerospace industries; need for higher temperature plastics for electronics and automotive components and; the emergence of the building products market as a major user of plastics. Microspheres represent only a small portion of this growing filler market, refer to Table 1.3 for a classification of filler materials and their major applications. However, microspheres are considered to be a special filler material and have no direct competition that can provide the unique blend of performance properties.

Table 1.3 *Key advantages and limitations of alternative filler types.*

Filler Material	Major Application	Primary Benefit	Major Disadvantage
Calcium carbonate	Coatings	Extender	High density
Fibreglass	Thermoplastics	Reinforcement	High density
Kaolin	Sealants	Thickener	Surface acidity
Metal powders	EMI shielding	Conductivity	Cost
Silica	Adhesives	Thermal	High density

1.5. **Microsphere Products**

1.5.1. Glass microspheres

As fillers, solid glass microspheres provide several unique properties including high compressive strength, low coefficient of thermal expansion, and excellent chemical resistance. They are available in a variety of particle sizes, but for the applications considered in this report, typical mean particle sizes ranged from 1 µm for some electronic applications to 60 µm for fillers in thermoplastics. When used in plastics, solid glass microspheres impart improved heat deflection temperature, tensile strength, flexural modulus, dimensional stability, and decreased water adsorption.

Hollow glass microspheres provide the benefit of high heat and chemical resistance, but with the added property of lighter weight. Products are available in a broad range of bulk densities from as low as 0.12 to 0.50 g/cm^3. The crush strength of hollow glass microspheres is directly related to its density. The major applications for hollow glass microspheres include sealants, reinforced plastics, offshore products, and coatings.

In automotive and construction sealants, hollow glass microspheres reduce weight and improve the insulation of the sealant. They also reduce moisture penetration and improve flow of application. In offshore foams they provide buoyancy and thermal insulation, while in a variety of coatings, hollow glass microspheres provide low resin demand, good flow, and reduce drying time.

1.5.2. Plastic microspheres

Plastic microspheres are available in both thermoplastic and thermoset forms, but thermoplastic products dominate the speciality applications market. Plastic microspheres come in two forms, expanded and unexpanded. Unexpanded microspheres have particle sizes between 6 and 40 μm. When expanded they can be 20 to 150 μm. Plastic microspheres are the highest priced microspheres.

1.5.3. Ceramic microspheres

Ceramic microspheres are available in both solid and hollow forms. Solid microspheres range in mean particle size from 5 to 40 μm and have a bulk density of over 1.0 g/cm^3. Hollow microspheres range in the mean particle size from 100 to 130 μm having a bulk density of approximately 0.4 g/cm^3. Ceramic microspheres are generally supplied to lightweight spackle producers, minor amounts are also supplied for use in automotive and offshore applications.

1.6.   Applications

1.6.1. Adhesives

Microspheres are typically used in several different adhesive applications, the major markets include aerospace adhesives and marine adhesives. In these hollow glass microspheres with median particle size of 60 to 70 μm and density of 0.1 to 0.25 g/cm^3 are loaded at fairly high levels, anywhere from 10 to 40% by weight. In addition to reducing weight, microspheres have excellent dielectric properties and low thermal conductivity, which improves dimensional stability. In marine adhesives, both hollow and plastic microspheres are utilised

in polyester adhesives to lower the weight. Particle size is generally below 10 μm and the density is as low as possible. Loading is usually at a level of less than 5%.

1.6.2. Speciality coatings

Microspheres are used as additives in a variety of industrial coatings. They have minimal impact on viscosity, provide good flow characteristics and allow high solids content, thus reducing drying time. Speciality coatings applications for microspheres include marine coatings, metal coatings, concrete coatings, thick film architectural coatings, and scrubbable coatings. In marine coatings, hollow glass microspheres with particle size of 15 to 80 μm and bulk density of 0.2 g/cm^3 are preferred. All of these coatings are generally epoxy-based and the microspheres when loaded at less than 10% by weight, lower the oil absorption and reduce the volatile organic compounds in the formulation. Ceramic microspheres are used in metal primer coatings, with a particle size generally lower than 10 to 15 μm. Concrete coatings are a significant application for hollow glass microspheres. These coatings use hollow glass microspheres at high loadings at levels up to 50% by weight to reduce shrinkage. The microspheres, typically less than 50 to 100 μm and 0.2 g/cm^3 are very effective fillers that do not affect the key properties of chemical resistance and permeability of the concrete at high filler loadings. Hollow glass microspheres provide lightweight to architectural coatings, lower density coatings give less spatter and less sag once applied. Therefore, they are sometimes utilised in thick film coatings at loading levels roughly 10% by weight. Generally 50 to 100 μm grades of hollow glass microspheres with densities in the 0.1 to 0.3 g/cm^3 range are employed.

1.6.3. Electromagnetic interference shielding

Hollow glass microspheres with a density of 0.15 g/cm^3 and mean particle size of 60 μm are the most common grade used. For EMI coatings and laminates, finer particle size microspheres are used, generally in the 1 to 10 μm range. Microspheres are cost effective conductive fillers because only the surface of the particle is coated with silver, copper, or nickel. Silver is frequently specified for military applications. Typical coating levels from 15 to 30% by weight for hollow microspheres and 4 to 12% for solid microspheres. Coating only the surface is very cost effective compared with the use of pure metal fillers.

1.6.4. Engineering thermoplastics

Microspheres are used as additives in selected types of thermoplastics in order to enhance mechanical thermal, and chemical resistance properties. In nylon, solid glass microspheres impart improved heat deflection temperature, increased tensile strength, improved flexural modulus, and good dimensional stability. Typical loading levels of both hollow and solid microspheres in thermoplastics typically range from less than 10 to 20% by weight. Particle size for the microspheres used is usually in the 10 to 50 μm size range.

1.6.5. Paper

Polystyrene or styrene acrylic microspheres have been used for many years in paper and paperboard coatings to enhance the gloss of the coating and to improve opacity and brightness. Typical particle size for plastic pigment is in the 0.5 to 1 μm range with a 45% void volume.

1.6.6. Reinforced thermoset plastics

Microspheres are utilised in automotive moulded compounds to reduce the weight of the fabricated part. The majority of these parts are fabricated from polyester resin and are frequently loaded at less than 5 to 10% with hollow glass microspheres to reduce weight. In some cases a 30% weight reduction in the finished part is achieved by employing microspheres. The hollow and solid microspheres used in reinforced plastics are in the particle size range of 15 to 40 μm.

1.6.7. Sealants

In automotive sealants, microspheres are primarily used to reduce weight and improve sound insulation. In addition they reduce moisture penetration and improve adhesion of the sealant. Applications include polyurethane and acrylic sealants, usually loaded 10% or less with 50 to 60 μm hollow glass microspheres with bulk densities in the range of 0.15 to 0.20 g/cm^3. In electronic sealants, solid glass microspheres are used as spacers and to maintain bond line thickness. Microspheres added to the sealant also act as stress absorbers reducing the potential of cracking and delamination. Generally fine particle size microspheres are consumed with size of 10 μm or less. Construction sealants often use hollow glass microspheres or ceramic microspheres, often loading is high, at 50 to 60% by weight. The microspheres utilised improve whiteness and sandability. Generally microspheres with a mean particle size of 60 μm and bulk density of 0.15 g/cm^3 are preferred.

1.6.8. Other applications

Hollow glass microspheres are used in two offshore products, buoyancy foams and pipe insulation coatings. Syntactic foams for buoyancy typically use 10 to 100 μm hollow glass

microspheres. Pipe insulation coatings use 50 to 60 µm hollow glass microspheres to provide thermal insulation. Automotive under body coatings use hollow glass microspheres and plastic microspheres, typically in the 10 to 40 µm range to reduce weight, provide sound insulation, and moisture protection.

1.7.   Thesis Aims

The thesis aims are to fabricate kaolin hollow and low density microspheres using a commercially viable route.

1.8.   Thesis Structure

Chapter 2 reviews the published literature referring to the fabrication of hollow microspheres and describes numerous methods that have been applied in the fabrication of spherical structures. **Chapter 3** focuses attention on the 'proof of concept' experiments to fabricate hollow microspheres and on the reliable determination of initial parameters, which can be used for the quantitative characterisation of the interactions between the template material, polyelectrolyte in solution, and the shell coating material. **Chapter 4** focuses on the characterisation of the materials used in the fabrication of low density, hollow microspheres.

The main body of results in this thesis are discussed in Chapter 5 and 6. In **Chapter 5**, an attempt is made to find a correlation between the PS microspheres, the polyelectrolyte adsorbed on the surface of the template material, and the mineral coating material. In the first part of **Chapter 6** an overview of the removal of the sacrificial core material by calcination is reviewed. Subsequently, a case study is presented in the second part of this chapter, which considers the ideal calcination programme and details the effects of calcination on the final

structure. As is customary, the thesis finishes with a general conclusion and suggestions for further work.

1.9. *References*

Beck, W.R., O'Brien, D.L. (Minnesota Mining & MFG.) **1968**. Glass bubbles prepared by reheating solid glass particles. United States patent application 3365315.

Bertling, J., Blömer, J., Kümmel, R. *Chem. Eng. Technol.* 27 (**2004**) 829.

Houston, A.M. *Mater. Eng.* 81 (**1975**) 58.

Netting, D.I. (Philadelphia Quartz Co.) **1974**. Hollow spheres consisting of alkali metal silicate and a polysalt. United States patent application 3794503.

Sands, B.W. (PQ Corporation) **1983**. Manufacturing process for hollow microspheres. United States patent application 4421562.

Sands, B.W., Howes, W.C., Smiley, L.H. *Plast. Eng.* 38 (**1982**) 31.

Sargeant, G.K. *Br. Ceram. Trans.* 90 (**1991**) 132.

Vetch, F. Alford, H.E., Croft, R.D. (Standard Oil Co.) **1962**. Hollow glass particles and method of producing the same. United States patent application 3030215.

Wilcox, D., Berg, M. *Mat. Res. Soc. Symp. Proc.* 372 (**1995**) 3.

Chapter Two: Literature Review

2.1.   Introduction

The diversity of applications for hollow microspheres span a wide range of technologies and attracts the expertise of individuals from a broad set of disciplines, consequently, this knowledge and capability is widely dispersed. Academically and industrially many terms are used to describe the spherical component, hollow microspheres are often referred to as shells, microballons, shirasuballons, vesicles and microcapsules. A microcapsule refers to a microsphere that is composed of an excipient matrix and a core substances, whereas, in the field of biomaterials the term vesicle is commonly used as a colloidal term for spheres formed from surfactants in aqueous systems [Arshady, 1989; 1990; Wilcox, et. al. 1995].

The synthesis of uniformed sized hollow microspheres in liquid or solid form has gained increasing attention in recent years. Hollow microspheres represent a special class of materials which are of interest in the fields of medicine and material science. Several kinds of composites have been fabricated by mixing hollow ceramic microspheres with matrices such as metals and plastics [Cochran, 1998].

The objective of this chapter is to review the numerous fabrication methods that are capable of producing a broad range of hollow microspheres. Various hollow polymer, oxide, metal, and glass composite microspheres have been produced using nozzle reactor technology [Gutsol, 1999; Yano, et. al. 1999; Iskandar, 2003]. But the microsphere size is limited to usually greater than 20μm. Emulsion and phase separation procedures, however, offer the opportunity to create hollow microspheres in the nano size range [Caruso, 1999; Sarikaya, 2001; Romero-Cano, 2002; Hentze, 2003].

In the sacrificial template technique a coating is deposited on the core as a result of controlled surface precipitation of inorganic molecular precursors from solution or direct surface reactions, and the core can be subsequently removed by heating or by chemical dissolution.

The techniques available for fabrication which are relevant within this research can be classified and reviewed in four specific categories: (1) conventional hard templating synthesis, (2) sacrificial templating synthesis, (3) soft templating synthesis, and (4) template-free methods. An overview of these approaches is shown in Figure 2.1.
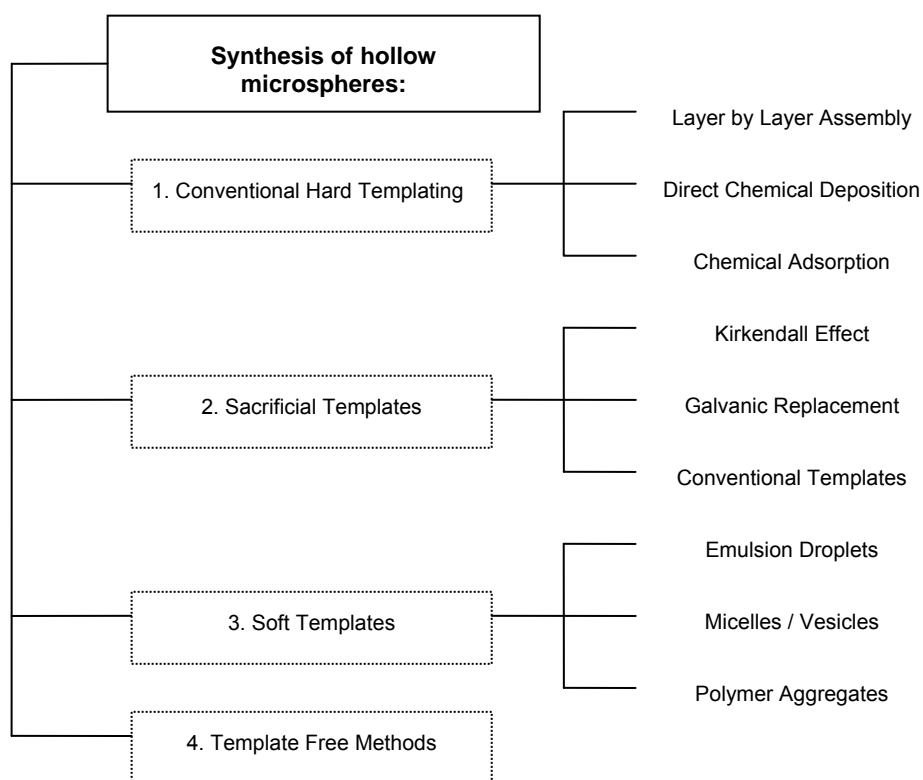
Figure 2.1 *General synthesis methods for fabricating hollow microspheres.*

2.2. Synthetic Approaches to Hollow Microspheres

2.2.1. Conventional hard templating

Preparation of hollow structures by templating against hard particles is conceptually straightforward. In general, it involves four steps; (1) preparation of the hard templates; (2) modification of template surface to achieve favourable surface properties; (3) coating the templates with designed materials; and (4) selective removal of the templates to obtain hollow structures [Lou, et al. 2008]. The most commonly employed hard templates include silica particles and polymer latex colloids. These templates are advantageous for several reasons including their narrow size distribution, availability in relatively large amounts, and availability in a wide range of sizes from commercial sources. Carbon, metals, and metal oxides, have also been used as templates.

In principle the removal of the template material is the simplest process. It typically entails the selective removal of the template in appropriate solvents or calcination. By using either approach, special care is required to prevent collapse of the shells during template removal. When using solvents swelling of the polymer can cause rupture of the hollow structure, causing the shell to manifest uncontrolled shape change. The coating and the shell formation process is generally regarded as the most challenging because it requires vigorous methods for efficiently precipitating shell materials on substrate with sizes in the nano/micro range. Incompatibility between the template surface and shell material can be overcome by modifying the template with special functional groups or characteristics, for example electrostatic charges, before applying subsequent coating and deposition of shell materials. In some cases, functional groups are introduced during the synthesis of the template particles.

2.2.1.1.   Layer by layer (LbL) assembly

LbL assembly refers to sequential deposition of oppositely charged polymer species on substrates mediated by electrostatic interactions. Combining this approach with colloidal templating has resulted in the preparation of hollow inorganic silica capsules through the electrostatic assembly of negatively charged silica nanoparticles and positively charged polymer [Caruso, et al. 1998]. The assembly cycle can be repeated to form multilayer structures with well defined wall thickness. The versatility of the LbL method is one of its main strengths. It also facilitates excellent structure size control and uniformity of the shell. Polymer capsules derived from this route enable the encapsulation of diverse components and are of special interest in biological applications [Zelikin, et al. 2006; Liu, et al. 2005].

The LbL technique has been extensively applied to prepare hollow structures of a wide range of inorganic or composite materials including zeolite/SiO_2 [Rhodes, et al. 2000], TiO_2 [Chen, et al. 2005; Caruso, et al. 2001], SnO_2 [Martinez, et al. 2005], Au [Liang, et al. 2003], magnetic Fe_3O_4 [Caruso, et al. 2001]. While most research involves LbL assembly of preformed nanoparticles, the polyelectrolyte multilayers on templating colloids can be exploited as nanoreactors for the in situ formation of inorganic shells by sol-gel processes. Metal oxide, $LiNbO_3$, hollow structures have also been prepared by infiltration and subsequent hydrolysis and condensation of the precursor ($LiNb(OC_2H_5)_6$) in the polyelectrolyte shell, followed by calcination [Wang, et al. 2002]. Despite its versatility and growing popularity, the LbL method suffers from three distinctive problems. First, the method is difficult to use for preparation of smaller hollow structures with sizes <200 nm. Second, the LbL assembly procedure becomes quite tedious when many layers are required. Finally, inorganic and hybrid hollow structures prepared from the method generally lack the mechanical robustness of particles prepared using other approaches.

2.2.1.2. Direct chemical deposition

Chemical deposition involves the precipitation of the shell materials or precursors on the template particles through various chemical or physical interactions with the template. The deposition process is typically followed by a calcination step to obtain compact shells. Metal oxides (SiO_2, TiO_2, ZrO_2) hollow spheres have been prepared and controlled hydrolysis of their metal alkoxide precursors in the presence of template particles, followed by removal of the templates. Control of the hydrolysis rate and hetercoagulation is crucial for the success of the process. This synthesis demands strict control of the reaction conditions to obtain smooth shell coatings. The requirements are especially stringent in the case of TiO_2.

Smooth and uniform TiO_2 shells on polystyrene templates have been reported by several groups [Imhof, 2001; Eiden, et al. 2002; Kim, et al. 2006]. The slight negative charge on the hydrolysed titania species ensures their rapid deposition on the positively charged polystyrene spheres. Synthesised titania is amorphous, and post calcination at high temperature is usually employed to simultaneously crystallise the particles and burn off the polymer templates. Shrinkage during the crystallisation process and, possibly, escape of gases produced by pyrolysis of the polymer templates, often lead to defects such as holes on the surface of the final particles [Imhof, 2001]. As a result, hollow structures derived from this route are generally quite fragile. Uniform coatings of titania on anionic polystyrene spheres have also been reported using ammonia-catalysed hydrolysis of titanium tetrabutoxide in mixed solvents [Wang, et al. 2006; Cheng, et al. 2006]. A particularly successful application of this approach is found in the synthesis of hollow SiO_2 structures.

Uniform deposition of SiO_2 from ammonia-catalysed hydrolysis of tetraethoxysilane (TEOS) is known to be relatively easy, particularly on inorganic templates [Graf, et al. 2003]. As a

result, smooth SiO_2 coating on particles of numerous materials has been reported. Silica hollow spheres have been prepared using surface functionalised polystyrene latex templates [Lu, et al. 2004; Chen, et al. 2006]. Clay-silica hybrid hollow microspheres with ultrathin walls have been prepared through deposition of negatively charged clay particles on cationic latex templates followed by sealing with silica [Putlitz, et al. 2001].

Hollow microspheres of many materials have been synthesised by chemical deposition. ZnS can be deposited on both silica and polystyrene templates under acidic conditions with zinc nitrate and thioacetamide as precursors [Velikov, et al. 2001; Hosein, et al. 2007]. Au/Pt hollow spheres have been prepared by chemical precipitation of Pt on Au seeded silica templates followed by removal of the silica in HF solution [Lu, et al. 2003]. $Ni_{1-x}Pt_x$ alloy hollow spheres have also been prepared by chemical reduction of Ni^{2+} adsorbed on the surface of poly(styrene-*co*-methacrylic acid) templates and subsequent alloying with Pt via replacement reaction [Cheng, et al. 2007]. Mesoporous Fe_3O_4 hollow spheres have been prepared by chemical adsorption of Fe^{2+} on carboxyl-functionalised polystyrene templates at 80 °C in the presence of ethylene glycol [Huang, et al. 2005].

2.2.1.3. *Chemical adsorption on surface layer*

Hollow spheres have been prepared by a number of groups using a direct adsorption-calcination route. In this method, pre-treatment of the template particles is usually required. Pd hollow spheres have been synthesised via three major steps: functionalisation of silica templates with –SH groups, adsorption of Pd precursor into functionalised template surface, and Pd shell formation by CO reduction generated during calcination [Kim, et al. 2002]. This approach is typical for hard-templating fabrication of hollow spheres. However, formation of a complete shell after template removal is quite difficult because the adsorbed precursor

amount is rather limited on the monolayer functionalised surface. The resulting hollow spheres usually exhibit very thin walls and rough surfaces and appear to be aggregated [Kim, et al. 2002]. Hollow spheres of Ga_2O_3 have also been prepared [Sun, et al. 2004] by adsorption of metal cations into the surface layer of hydrophilic carbon spheres with copious –OH groups, followed by calcination in air. Despite significant shrinkage during the calcination process, Ga_2O_3 hollow sphere with smooth surfaces and a uniform shell thickness can be obtained. This simple method has been extended by other groups to prepare hollow spheres of a wide range of metal oxides [Li, et al. 2004; Titirici, et al. 2006] and Pt hollow capsules [Yang, et al. 2006].

An interesting approach to prepare inorganic hollow spheres via preferential adsorption of inorganic precursors into sulphonated shell layers of polystyrene templates has been reported [Yang, et al. 2005; Yang, et al. 2003]. The core-shell polystyrene templates are obtained by an inward sulphonation of polystyrene particles with concentrated sulphuric acid. The sulphonation process produces hydrophilic shells with sulphonic acid $\left(SO_3^-H^+\right)$ groups randomly attached to polystyrene chains. Because these groups are capable of adsorption of or complexation with a large variety of species, such as metal cations, TiO_2 sols from alkoxides, and even organic monomers, the method is quite versatile [Yang, et al. 2005]. During the process, the sulphonation time determines the thickness of the sulphonated shell, which in turn sets the thickness of the organic hollow sphere. The same approach has been applied to prepare hollow spheres of numerous inorganic materials (SnO_2, In_2O_3, $BaTiO_3$, $SrTiO_3$) [Xu, F. et al. 2007; Xu, H.F. et al. 2007].

2.2.2. Sacrificial templates

The key feature of a sacrificial template is that the template itself is involved as a reactant in the synthetic process of the shell material. Analogous to conventional hard templates, sacrificial templates directly determine the shape and approximate cavity size of the resultant hollow structures, but the template simultaneously plays the role of structure-directing scaffold and precursor for the shell. As a result, the sacrificial template is consumed partially or completely during the shell-forming process. In this regard, sacrificial template synthesis is inherently advantageous because it requires no additional surface functionalisation and shell formation is guaranteed by chemical reaction [Lou, et al. 2008].

The process is therefore typically more efficient, especially when the sacrificial template is completely consumed during the shell-formation reaction. These characteristics have motivated synthesis of an increasingly broad array of hollow structures using an equally diverse range of sacrificial templates. A number of special formation mechanisms such as the Kirkendall effect and Galvanic replacement have been identified that can be used to understand the fundamentals of hollow particle synthesis by sacrificial templates.

2.2.2.1. The Kirkendall effect

The Kirkendall effect provides a mechanism for void formation near interfaces due to different interdiffusion rates in a bulk diffusion couple [Smigelskas, et al. 1947]. The net flow of mass in one direction is balanced by a flux of vacancies, which may condense into voids preferably around the interface. It was first applied to explain the formation of hollow compound nanocrystals of cobalt oxides in the nano scale by reacting presynthesised Co nanocrystals with sulphur, oxygen, and selenium [Yin, et al. 2004]. During the process the Co nanocrystals are first covered with a thin layer of cobalt sulphide, further reaction

between Co and S (growth of the cobalt sulphide shell) requires diffusion of S or Co through the previously formed compound shell. In the Co-S system, the dominant outward diffusion of Co generates a single void in each nanoparticle. However, these studies are based on highly idealised models, the observation that the shell is multicrystalline and microporous might suggest that there is an outward flow of Co through the shell by surface diffusion, instead of bulk diffusion.

Similar evolution of structure was also observed when amorphous Fe-Fe_3O_4 core/shell particles are transformed to crystalline Fe_3O_4 hollow particles upon heating and controlled oxidation in the presence of the oxygen-transfer agent trimethylamine *N*-oxide [Peng, et al. 2007]. The formation of oxide hollow particles through oxidation of metal nanoparticles (Zn, Al, Fe, Cu) has also been reported [Nakamura, et al. 2007a; 2007b], where the outward diffusion of metal was explained based on the Caberra-Mott theory, that the metal cations diffuse through a thin oxide layer at the initial oxidation stage driven by electrostatic fields.

Based on the Kirkendall process, many other hollow particles have been synthesised. Crystalline bi-phase TiO_2 hollow microspheres with mesoporous shells have been fabricated by hydrothermal treatment of acidic $(NH_4)_2TiF_6$ aqueous solution in the presence of glucose at 180 °C for 24 hr, and then calcined [Yu, et al. 2007]. Mesoporous spinel $Li_4Ti_5O_{12}$ microspheres have also been prepared based on a hydrothermal conversion of amorphous hydro titanium oxide spheres to mesoporous $Li_4Ti_5O_{12}$ in a mixed solvent of ethanol-water and following heat treatment [Tang, et al. 2009].

The Kirkendall effect has been embraced as a general method for synthesising hollow structures, however, attributing the formation of hollow structures to the Kirkendall effect is

in many cases speculative. In situations where the hollow structures are synthesised in aqueous solution, it is likely that the shell is porous, and the interior void is filled with solution. Under these conditions, normal solution transport would appear to be the predominant shell-growth process.

2.2.2.2. Galvanic replacement

As another special class of sacrificial template synthesis, Galvanic replacement reactions have been widely employed for general preparation of metal hollow structures. In a typical reaction, the salt of a more noble metal (B) is reduced with preformed nanocrystals of a less noble metal (A), resulting in deposition of B on the surface of A. Upon complete consumption of metal A, hollow structures of metal B can be obtained under controlled conditions. The shape and void size of the derived hollow structure are largely determined by the sacrificial nanocrystals of A [Lou, et al. 2008].

Various metal (Au, Pt, Pd) hollow structures have been prepared in both aqueous and organic solutions through Galvanic replacement reactions with Ag nanocrystals [Selvakannan, et al. 2005; Yin, et al. 2006; Gao, et al. 2007]. The Ag nanocrystals in a wide range of sizes and shapes are synthesised by the versatile polyol process in the presence of a capping agent (PVP). For the preparation of Au hollow structures in aqueous solution the Galvanic replacement reaction can be described by the following equation:

$$3\text{Ag}(s) + \text{AuCl}_4^-(aq) \rightarrow \text{Au}(s) + 3\text{Ag}^+(aq) + 4\text{Cl}^-(aq) \qquad [2.1]$$
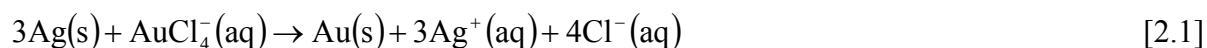
The formulation mechanism of Au hollow structures can be extremely complicated, depending upon the reaction system [Sun, et al. 2004]. The formation of the hollow void is

generally attributed to the 3:1 stoichiometric relationship between Ag and Au in the reaction. After initial deposition of Au on the surface of Ag nanostructures forming a thin shell, further growth of the Au shell is outward. Electrons flow from the Ag template to the exterior surface of the Au shell where further growth of Au takes place, accompanied by the dissolution of the Ag template inside the shell.

Cobalt nanocrystals have also been extensively used as sacrificial templates for preparation of noble-metal hollow particles through Galvanic replacement reactions [Guo, et al. 2007]. Hollow structures of Pt, bimetallic AuPt [Liang, et al. 2004], and Au [Liang, et al. 2005] have been prepared using Co nanoparticles as sacrificial templates. The formation of the structure can be attributed to the magnetic dipole interaction of the templating Co nanocrystals.

2.2.2.3.   *Conventional sacrificial templates*

Amorphous Se colloids have been employed as sacrificial templates for preparation of hollow spheres of Ag_2Se [Jeong, et al. 2005; Zhu, et al. 2006; Camargo, et al. 2007]. The conversion, carried out in ethylene glycol, takes advantage of the high reactivity of Se towards Ag to form Se-Ag core/shell particles, with the shell thickness controlled by the relative amounts of reactants. The unreacted Se core can be selectively dissolved in hydrazine solution. Se-Ag_2Se core/shell particles can be converted to Se-MSe (M=Zn, Cd, Pb) by performing cations exchange with respective metal cations. After removal of the Se core, hollow structures of ZnSe, CdSe, and PbSe can be obtained. Hollow nanospheres of CdX (X=Te, Se, S) have been prepared utilising Cd(OH)Cl nanoparticles as sacrificial templates [Miao, et al. 2007], and ZnX (X=S, Se) hollow spheres based on sonochemical anionic exchange of ZnO nanospheres [Geng, et al. 2007]. Synthesis of Cu_2O hollow

nanospheres from Cu nanospheres through halide-induced corrosion oxidation with the aid of surfactants have been produced [Huang, et al. 2006] and ZnO hollow microspheres with a dandelion-like morphology have been fabricated [Liu, et al. 2004]. The synthesis is based on oxidation dissolution of Zn micropowders, which serve as the template for nucleation and growth of the ZnO shell.

High temperature gas-solid reactions have also been devised to prepare ceramic hollow particles where the solid particles serve as the sacrificial templates. Silicon carbide (SiC) hollow spheres have been synthesised by reacting carbon nanospheres with thermally generated Si or SiO vapour at approximately 1300 °C [Zhang, et al. 2006; Liu, et al. 2007]. The shell thickness can be controlled by varying the reaction time, and the unreacted inner carbon cores can easily be removed by combustion in air. Synthesis of polycrystalline aluminium nitride (AlN) hollow spheres through the reaction of Al nanopowder with a CH_4-NH_3 gas mixture at approximately 1000 °C have also been fabricated [Ma, et al. 2006].

Sacrificial templates are not restricted to solid particles; they can sometimes be liquid droplets. Metal carbide (TiC, VC, ZrC) hollow spheres have been fabricated by co-reduction and then reaction of metal source ($TiCl_4$, VCl_4, $ZrCl_4$), and carbon source (C_4Cl_6, C_6Cl_6) on the surface of metallic Na droplets at 500-600 °C [Li, et al. 2003; Shen, et al. 2004]. Also reported, GaN hollow spheres have been produced through interfacial chemical reaction between liquid Ga droplets and NH_3 gas in a carefully controlled temperature gradient zone [Yin, et al. 2005]. Li_2NH hollow spheres have been prepared through a reaction between Li droplets and NH_3 gas [Xie, et al. 2008]. While the above synthesis involve liquid droplet-gas reactions, the formation mechanism of the hollow particles have been ascribed to the Kirkendall effect by the authors.

2.2.3. Soft templates

Templating against solid templates is arguably the most effective, and certainly the most common, method for synthesising hollow micro and nano structures. However, hard templates have several disadvantages, which range from the inherent difficultly of achieving high product yields from the multi-step synthetic process to the lack of structural integrity of the shells upon template removal. Additionally, key applications of hollow structures, such as drug and therapeutic delivery, require facile access to the hollow interior void. With the hard templates, refilling the hollow interior with functional species or in situ encapsulation of guest molecules during the formation of the shells, though possible is challenging. These difficulties have prompted interest in simpler synthetic approaches for producing hollow microspheres that permit easy encapsulation and release of guest species. Among these approaches, templating against soft (liquid or gaseous) templates has attracted the greatest attention and significant progress has been made in the last decade.

2.2.3.1. *Emulsion droplets*

When two immiscible liquids are mixed together through mechanical agitation, liquid droplets of one phase can be dispersed in the other continuous phase, forming an emulsion. In general, emulsions are thermodynamically unstable, thus surfactants which self-assemble at the interface between the droplets and continuous phase, are required to increase kinetic stability [Ni, et al. 2006; Zimmermann, et al. 2007; Buchold, et al. 2007]. The concept is to deposit the shell materials exclusively around the interface between the emulsion droplets and the continuous phase. The precursor of shell materials can initially exist in either the continuous phase of the droplets or both phases, depending on the chemistry chosen. Sol-gel processes for metal alkoxides are commonly employed in emulsion templating to synthesise hollow spheres of metal oxides such as silica and TiO_2 [Collins, et al. 2003; Miyao, et al.

2005; Jovanovic, et al. 2005; Joncheray, et al. 2006]. However, such derived hollow spheres typically have sizes in the micrometer range and possess broad size distributions [Fowler, at el. 2001a; 2001b]. TiO$_2$ hollow microspheres (3-20 μm) have been prepared by templating against toluene microdroplets in an ionic solution: 1-butyl-3-methylimidasolium hexaflurophosphate ([C$_4$min]PF$_6$) [Nakashima, et al. 2003]. The precursor, Ti(OBu)$_4$, is dissolved in the toluene phase. Upon emulsification with [C$_4$min]PF$_6$ by vigorous stirring, Ti(OBu)$_4$ hydrolyses selectively at the interface with the trace amount of water adsorbed in the [C$_4$min]PF$_6$ phase. This method also allows incorporation of functional particles and organic molecules. Synthesised hollow spheres of aluminosilicate with mesoporous shells by combining emulsion droplet templating and surfactant templating has been reported [Li, et al. 2003]. The O/W emulsion is formed by adding TEOS into aqueous Al$_2$(SO$_4$)$_3$ solution. The surfactant: hexadecylcetyltrimethylammonium bromide (CTAB) molecules are responsible for stabilisation of the droplets and templating the mesoporous shell formation. Despite the general difficulty in preparing monodisperse hollow spheres by emulsion templating, several reports describe how the method can be used for preparation of monodisperse silica hollow spheres [Hah, et al. 2003; Wang, et al. 2007; Zoldesi, et al. 2005].

In addition to sol-gel processes, many other synthetic approaches, such as hydrothermal methods [Ni, et al. 2006] and γ-irradiation [Hu, et al. 2005; Wu, et al. 2004; Yang, et al. 2006] have been employed in combination with emulsion templating to synthesis hollow particles of various materials, including metals [Bao, et al. 2003; Wang, et al. 2006], oxides [Chen, et al. 2007] and inorganic/polymer composites [Wu, et al. 2004; Yang, et al. 2006].

The liquid character and deformability of emulsion droplets provide important advantages for hollow particle synthesis [Imhof, et al. 1997]. Compared to solid templates, the liquid

cores can be easily removed by low-stress-generating processes such as evaporation or dissolution in solvents such as ethanol after the shell formation. The high deformability of the droplets should allow them to accommodate larger levels of shrinkage, which reduces fracturing during post-treatments such as drying and calcination. More importantly, templating against liquid droplets allows facile and efficient introduction of functional liquid cores or species inside the structure which is particularly attractive in biological and pharmaceutical applications. In practice, controlling the size, uniformity, and interfacial reactions in emulsion droplets remains a serious challenge.

2.2.3.2.   *Micelles & vesicle structures*

Amphiphilic molecules such as surfactants can be made to self-assemble into micelles or vesicles with different structures when their concentration in solution exceeds some critical value. For example, at concentrations above ca. 8.2 mM at 25 °C, (the critical micelle concentration (CMC)) in an aqueous solution, sodium dedecly sulphate (SDS) will spontaneously form spherical micelles, each containing about 50 molecules arranged in a regular radial pattern [Fendler, 1980; 1984; Bunton, et al. 1991]. At concentrations well above the CMC the spherical micelle phase transforms into vesicles comprised of a closed bilayer structure. In general, the structure and stability of micelles or vesicles are affected by many factors such as solvent polarity, pH value, and ionic strength of the solution. This sensitivity of micelle and vesicle structure to easily controlled synthesis conditions can in principle provide exquisite control over template morphology and structure. However, the exact geometric and structural characteristics of micelles and vesicles in particular synthesis are rarely known. Thus, unless independent information about the phase morphology or surfactant templates in the reaction media are provided, it is safe to conclude that any vesicular templating mechanisms are best regarded as proposals based on structures

produced. To fully understand the diversity of hollow structures and geometrics possible with micelle and vesicle templating, fundamental studies of the phase behaviour of surfactants in typical particle synthesis media are required.

In the absence of detailed understanding of micelle and vesicle templating processes, hollow particles based on a wide range of inorganic material chemistries have been prepared using both types of templates. Silica is nonetheless by far the most popular inorganic material used in the synthesis of hollow particles via soft templating [Kim, et al. 1998; Hentze, et al. 2003; Djojoputro, et al. 2006; Zhang, et al. 2007]. Silica vesicles with the shells constructed of lamellar sheets have been prepared [Kim, et al. 1998]. The method is based on supramolecular assembly through hydrogen bonding between neutral surfactants of the type $C_nH_{2n+1}NH(CH_2)_2NH_2$ and silica precursors derived from TEOS. A method to produce hollow silica particles by direct growth of silica on equilibrium icosaheadrally facetted cationic vesicles has also been reported [Lootens, et al. 2003]. The wall of these micelles is constructed of surfactant bilayers, made from cetyltrimethylammonium hydroxide (CTAH) and myristic acid. Micelles or vesicles have also been utilised as soft templates to synthesis hollow spheres of other materials, such as carbon [Sun, et al. 2005], metal oxides [He, et al. 2004; Cong, et al. 2007], as well as some metals [Zhang, et al. 2006; Chen, et al. 2007; Liu, et al. 2007].

2.2.3.3.   *Polymer aggregates*

The interaction between polyelectrolytes and surfactants has received great attention because of the variety of applications in which the systems can be used [Abuin, et al 1984]. It has been found that the systems of polyelectrolytes and surfactants of opposite charge generally show strong interactions, whereas the systems of uncharged polymers and ionic surfactants

or polyelectrolytes and surfactants of the same charge show relatively weak or no interaction. When the concentration reaches some critical value known as the critical aggregation concentration (CAC), which is analogous to CMC, the surfactant-polymer or surfactant-free polymer systems tend to aggregate to form micelles or vesicles.

It has been reported [Zhang, et al. 2002; Qi et al. 2002] that complex poly(ethylene oxide)-*block*-poly(methacrylic acid)-sodium dodecylsulphate (PEO-*b*-PMAA-SDS) micelles have been used as soft templates to prepare $CaCO_3$ and Ag hollow microspheres. It is known that PEO can interact with anionic SDS to form PEO-SDS complex micelles with EO groups intermingling in the head region of the SDS micelles. Therefore, core/shell micelles are formed in the PEO-*b*-PMMA-SDS system with a core of PEO segment solubilised in the head region of the SDS micelles, and a corona of PMMA segments. The anionic PMMA corona is beneficial for arresting cationic metal ions. Hollow silica spheres with mesostructured shells have been prepared using a vesicle template of CTAB-SDS-P123 (P123~$EO_{20}PO_{70}EO_{20}$) [Yeh, et al. 2006].

Surfactant-free polymer aggregates have also been widely used to direct the formation of hollow spheres. Poly(ethylene glycol) (PEG) micelles have been used as soft templates for synthesis of Cu_2O/PEG composite hollow spheres [Xu, et al. 2007], and Co and CoPd hollow spheres [Zhou, et al. 2007; Li, et al. 2006]. Formation of hollow structures from self-assembly of preformed nanoparticles is challenging. However, if one can take advantage of the unique self-assembly or aggregation characteristics of specially designed polymers, multiple nanoparticles can be spontaneously assembled into hollow structures. Silica and gold particles can be cooperatively assembled with poly(lysine)-poly(cysteine) diblock copolypeptide into robust hollow microspheres [Wong, et al. 200]. The cysteine and lysine

blocks interact with gold through Au-S bonding and silica nanoparticles through electrostatic interaction, such that the walls of these formed hollow spheres consist of a distinct layer of gold surrounded by an outer layer of silica. Beside the ease of synthesis under mild conditions, the other advantage is that water-soluble compounds, such as enzyme and dye molecules, can be easily encapsulated by adding a solution of the compound to the polymer aggregates prior to addition of nanoparticle sols [Rana, et al. 2005; Yu, et al. 2007].

2.2.3.4.   *Gas bubbles*

Gas bubbles dispersed in a liquid suspension can be used to create stable emulsions and foams, which have recently emerged as promising soft templates for synthesis of an increasing number of hollow particles. The process can be conceptualised in three steps: formation of fine nanoparticles and gas bubbles, attachment of fine nanoparticles on the gas/liquid interface, and further aggregation of nanoparticles forming compact shells around the gas bubbles [Peng, et al. 2003; Han, et al. 2005]. It is known that the attachment of solid particles to gas bubbles is a complex process, which is affected by many factors, such as particle surface properties, particle size, electrostatic interactions, and hydrodynamic conditions [Fan, et al. 2004].

$CaCO_3$ hollow spheres have been prepared by blowing a mixed gas (CO_2 and N_2) into a solution of $CaCl_2$ and ammonia [Han, et al. 2005], while the majority of such works involve use of in situ generated gas bubbles. ZnSe hollow spheres have been synthesised under hydrothermal conditions with hydrazine as the reducing agent, in which the resultant N_2 gas bubbles are proposed to play the role of soft templates [Jiang, et al 2005]. ZnS hollow spheres have been prepared via aggregation of nanoparticles around the evolved H_2S bubbles produced from decomposition of thioacetamide [Gu, et al. 2006]. Synthesised hollow spheres

of TiO_2 and Co_2P have been reported by templating against gas bubbles of O_2 [Li, et al. 2006], PH_3 and CH_4 [Hou, et al. 20056], and N_2 [Wu, et al. 2006]. Gas bubble templating has also been suggested as a means for preparing hollow spheres of CuS, Fe_3O_4 [Chen, et al. 2004; 2006], and SnO_2 [Wang, et al. 2008].

Another special type of gas bubble templating is utilised in sonochemical synthesis of hollow particles, where the gas bubbles generated from the collapse of the acoustic cavitation serve as the soft template for shell formation [Suslick, 1990; Shchukin, et al. 2006]. It has been suggested that cavitation microbubbles created by sonication of a surfactant-containing medium are particularly advantageous because they can be stabilised in a similar manner to normal liquid-liquid emulsion [Shchukin, et al. 2006]. Electrostatic LbL assembly of polyelectrolyte multilayers (polyallylamine, poly(styrene sulfonate)) was successfully accomplished on the surface of air-containing microbubbles made by ultrasonic agitation of a mixture of co-polymers [Shchukin, et al. 2005]. This ultrasound-assisted method has been applied for synthesising hollow silica spheres with mesoporous walls by the application of ultrasound to an aqueous solution containing surfactant and silica precursor (TEOS) [Prouzet, et al. 2002]. Ultrasonic synthesis appears very effective for production of hollow particles such as CdSe [Zhu, et al. 2003] by ultrasonically induced reactions between initial precursors at the gas/liquid interface of the microbubble.

2.2.4. Template free methods

Templating methods have proven very effective and versatile for synthesising a wide array of hollow nano and micro-structures. Disadvantages related to high cost and tedious multiple procedures have impeded industrial scale-up of many of the template methods for large scale applications. For instance, the template removal process is indispensable when hard

templates are used, which not only significantly complicates the process but also detrimentally affects the quality of the hollow particles. Ideally, one would prefer a one-step method for controlled preparation of hollow structures in a range of sizes. Recently, one-step methods based on novel mechanisms, such as inside-out Ostwald ripening, a spontaneous process that refers to the growth of large precipitates at the expense of smaller precipitates caused by energetic factors [Ostwald, 1900], have been successfully applied to synthesise hollow structures. Template-free synthesis of polycrystalline SnO_2 hollow nanostructures has been reported [Lou, et al., 2006].The synthesis is performed in an ethanol-water mixed solvent using potassium stannate ($K_2SnO_3 \cdot 3H_2O$) as the precursor. Discrete spherical hollow and interconnected hollow core/shell SnO_2 structures can be prepared by adjusting the synthetic conditions (e.g. ethanol fraction in the mixed solvent). At the initial stage of reaction, amorphous solid spheres are formed by hydrolysation of stannate. With time, the surface layer of the nanosphere crystallises first due to contact with the surrounding solution. As a result, the materials inside the solid sphere have a strong tendency to dissolve, which provides the driving force for the spontaneous inside-out Oswald ripening. The dissolution process initiates at regions either near the surface or around the centre of the solid spheres, depending on the packing of the primary nanoparticles and ripening characteristics, to produce hollow core/shell particles or hollow spheres. A similar inside-out evacuation process has been reported to produce CdS, ZnS [Xie, et al., 2000] and titania [Guo, et al., 2003] core/shell structures.

A single step process has also been capable of producing TiO_2 hollow spheres with diameters of 0.2 to 1.0 μm by hydrothermally heating a TiF_4 solution in which Oswald ripening was employed to account for the hollowing effect [Yang, et al., 2004]. Reducing the overall surface energies provides the driving force for Oswald ripening within an ensemble of

particles. But with respect to hollow formation of a particle, no apparent driving force can easily be identified. It is argued that for solid spheres composed of numerous small particles, the small particles in the inner cores have high surface energies compared to those in the outer surfaces [Lou, et al. 2008]. Although fundamental evidence in support of this mechanism is lacking, it has been shown to be applicable in many systems, including Cu_2O [Teo, et al., 2006], ZnS and Co_3O_4 [Liu, et al., 2005], Sb_2S_3 [Cao, et al., 2006], $Ti_{1-x}Sn_xO_2$ [Li, et al., 2007], Fe_3O_4 [Zhu, et al., 2008], and ZnO [Zhu, et al., 2007].

The mechanism for this self-template formation of hollow structures has recently been further elaborated in several publications [Yu, et al., 2006; 2007; 2008]. The term 'localized Oswald ripening' is used to describe the dissolution of the particle interior. In essence, the chemically induced self-transformation is characterised by the initial kinetically favoured deposition of amorphous solid spheres. With increasing reaction time, the surface layer first transforms to a thermodynamically more stable form, as the supernatant falls in the surrounding solution. Thus an ultrathin shell of less-soluble crystalline phase is formed on the amorphous solid spheres. As a result, the amorphous core will have a strong tendency to dissolve and diffuse out of through the shell because it remains out of equilibrium with the surrounding solution.

The process of dissolution of the particle interiors can be further rationalised by considering the stabilisation effect on the surface layer by surfactants or inorganic ions in the solution. As a result, the interior materials will have relatively high surface energy and dissolve preferentially. This selective dissolution of interior core material is demonstrated in syntheses of iron oxide hollow structures [Lu, et al. 2006, Mao, et al. 2007, Jia, et al. 2008]. Inorganic anions such as phosphate and sulphate are known to adsorb strongly on surface of

iron oxides and since the exterior surface of the particles are protected by the adsorbed species, the dissolution will occur in the interior.

There are many other template-free methods that appear to involve non-conventional mechanisms. As an example, amorphous iron oxide spheres are transferred into hollow structures upon exposure to high energy electron beam [Latham, et al. 2006]. An aerosol pyrolysis method has been reported for direct synthesis of silica coated γ-Fe$_2$O$_3$ hollow spheres from a methanol solution containing iron ammonium citrate and TEOS. The low solubility of the iron ammonia citrate in methanol, compared to that of TEOS, promotes the initial precipitation of the iron solid shell. With the continuous shrinkage of the aerosol particles, iron salt and TEOS enrich at the surface, which eventually decomposes to produce silica coated γ-Fe$_2$O$_3$ hollow spheres [Tartaj, et al. 2001]. Although with low versatility, once developed, such novel methods might be able to produce high quality hollow particles of important materials in a surprisingly efficient way.

2.3.   *Closing Comments*

A variety of chemical and physiochemical procedures have been employed for the manufacture of hollow polymer, glass, metal, and ceramic microspheres. These main routes include, nozzle reactor processes, emulsion and phase separation techniques, and sacrificial core methods.

The most promising way to obtain tailor made hollow microspheres is provided by various template techniques however, template-based synthetic approaches suffer from several intrinsic disadvantages, which range from difficultly of achieving high product yields from

the multi-step process to the lack of structural robustness of the shell structures upon template removal.

The next chapter reviews initial experiments which were conducted to fabricate spherical structures based on a self assembly and templating method. The chapter describes the experimental process and the resulting structures. The most important parameters that influence the structure formation are also discussed.

2.4. **References**

Abuin, E.B., Scaiano, J.C. *J. Am. Chem. Soc.* 106 (**1984**) 6274.

Arshady, R. *Polym. Eng. Sci.* 29 (**1989**) 1746.

Arshady, R. *J. Bioact. Compat. Polym.* 5 (**1990**) 315.

Bao, J.C., Liang, Y.Y., Xu, Z., Si, L. *Adv. Mater.* 15 (**2003**) 1832.

Bertling, J., Blömer, J., Kümmel, R. *Chem. Eng. Technol.* 27 (**2004**) 829.

Bledzki, A., Kwasek, A. *Kunststoffe* 75 (**1985**) 421.

Buchold, D.H.M., Feldmann, C. *Nano Lett.* 7 (**2007**) 3489.

Bunton, C.A., Nome, F., Quina, F.H., Romsted, L.S. *Acc. Chem. Res.* 24 (**1991**) 357.

Cao, X.B., Gu, L., Zhuge, L., Gao, W.J., Wang, W.C., Wu, S.F. *Adv. Funct. Mater.* 16 (**2006**) 896.

Caruso, F. *Chem. Mater* 11 (**1999**) 3309.

Caruso, F. *Chem. Eur. J.* 6 (**2000**) 413.

Caruso, F., Caruso, R.A., Mohwald, H. *Science* 282 (**1998**) 1111.

Caruso, F., Shi, X.Y., Caruso, R.A., Susha, A. *Adv. Mater.* 13 (**2001**) 740.

Caruso, F., Spasova, M., Susha, A., Giersig, M., Caruso, R.A. *Chem. Mater.* 13 (**2001**) 109.

Chen, H.M., He, J.H., Zhang, C.B., He, H. *J. Phys. Chem. C* 111 (**2007**) 18033.

Chen, G.C., Kuo, C.Y., Lu, S.Y. *J. Am. Ceram. Soc.* 88 (**2005**) 277.

Chen, X.Y., Wang, Z.H., Wang, X., Zhang, R., Liu, X.Y., Lin, W.J., Qian, Y.T. *J. Cryst. Growth* 263 (**2004**) 570.

Chen, M., Wu, L.M., Zhou, S.X., You, B. *Adv. Mater.* 18 (**2006**) 801.

Chen, G., Xia, D.G., Nie, Z.R., Wang, Z.Y., Wang, L., Zhang, L., Zhang, J.J. *Chem. Mater.* 19 (**2007**) 1840.

Chen, X.Y., Zhang, Z.J., Li, X.X., Shi, C.W. *Chem. Phys. Lett.* 422 (**2006**) 294.

Cheng, X.J., Chen, M., Wu, L.M., Gu, G.X. *Langmuir* 22 (**2006**) 3858.

Cheng, F.Y., Ma, H., Li, Y.M., Chen, J. *Inorg. Chem.* 46 (**2007**) 788.

Cochran, J.K. *Curr. Opin. Solid State Mater. Sci.* 3 (**1998**) 474.

Collins, A.M., Spickermann, C., Mann, S. *J. Mater. Chem.* 13 (**2003**) 1112.

Cong, H.P., Yu, S.H. *Adv. Funct. Mater.* 17 (**2007**) 1814.

Djojoputro, H., Zhou, X.F., Qiao, S.Z., Wang, L.Z., Yu, C.Z., Lu, H.Q. *J. Am. Chem. Soc.* 128 (**2006**) 6320.

Eiden, S., Maret, G. *J. Colloid Interface Sci.* 250 (**2002**) 281.

Fan, X., Zhang, Z., Li, G. Rowson, N.A. *Chem. Eng. Sci.* 59 (**2004**) 2639.

Fendler, J.H. *Acc. Chem. Res.* 13 (**1980**) 7.

Fendler, J.H. *Science* 223 (**1984**) 888.

Fowler, C.E., Khushalani, D., Mann, S. *Chem. Commun.* (**2001**) 2028.

Fowler, C.E., Khushalani, D., Mann, S. *J. Mater. Chem.* 11 (**2001**) 1968.

Gao, J.N., Ren, X.L., Chen, D., Tang, F.Q., Ren, J. *Scr. Mater.* 57 (**2007**) 687.

Graf, C., Vossen, D.L.J., Imhof, A., van Blaaderen, A. *Langmuir* 19 (**2003**) 6693.

Gu, F., Li, C.Z., Wnag, S.F., Lu, M.K. *Langmuir* 22 (**2006**) 1329.

Guo, C.W., Cao, Y., Xie, H., Dai, W.L., Fan, K.N. *Chem. Commum.* (**2003**) 700.

Guo, S.J., Fang, Y.X., Dong, S.J., Wang, E.K. *J. Phys. Chem. C* 111 (**2007**) 17104.

Gutsol, A. *Progress in Plasma Processing of Materials, 5th International Thermal Processing Conference* (**1999**) 625.

Hah, H.J., Kim, J.S., Jeon, B.J., Koo, SM., Lee, Y.E. *Chem. Commun.* (**2003**) 1712.

Han, Y.S., Hadiko, G., Fuji, M., Takahashi, M. *Chem. Lett.* (**2005**) 152.

He, T., Chen, D.R., Jiao, X.L., Xu, Y.Y., Gu, Y.X. *Langmuir* 20 (**2004**) 8404.

Hentze, H.P., Kaler, E.W. *Curr. Opin. Colloid Interface Sci.* 8 (**2003**) 164.

Hentze, H.P., Raghavan, S.R., McKelvey, C.A., Kaler, E.W. *Langmuir* 19 (**2003**) 1069.

Hosein, I.D., Liddell, C.M. *Langmuir* 23 (**2007**) 2892.

Hou, H.W., Peng, Q., Zhang, S.Y., Guo, Q.X., Xie, Y. *Eur. J. Inorg. Chem.* (**2005**) 2625.

Houston, A.M. *Mater. Eng.* 81 (**1975**) 58.

Hu, Y., Chen, J., Chen, W., Lin, X., Li, X. *Adv. Mater.* 15 (**2003**) 726.

Hu, Y., Chen, J.F., Jin, X.Z., Chen, W.M. *Mater. Lett.* 59 (**2005**) 234.

Imhof, A. *Langmuir* 17 (**2001**) 3579.

Imhof, A., Pine, D.J. *Nature* 389 (**1997**) 948.

Iskandar, F., Gradon, L., Okuyama, K. *J. Colloid Interface Sci.* 265 (**2003**) 296.

Jia, B.P., Gao, L. *J. Phys. Chem. C.* 112 (**2008**) 666.

Jiang, C.L., Zhang, W.Q., Zou, G.F., Yu, W.C., Qian, Y.T. *Nanotechnology* 16 (**2005**) 551.

Joncheray, T.J., Audebert, P., Schwartz, E., Jovanovic, A.V., Ishaq, O., Chavez, J.L., Pansu, R., Duran, R.S. *Langmuir* 22 (**2006**) 8684.

Jovanovic, A.V., Underhill, R.S., Bucholz, T.L., Duran, R.S. *Chem. Mater.* 17 (**2006**) 3375.

Kawashita, M., Shineha, R., Kim, H.M., Kokubo, Y., Araki, N., Hiraoka, M., Sawada, Y. *Biomaterials* 24 (**2003**) 2955.

Kim, S.W., Kim, M., Lee, W.Y., Hyeon, T., *J. Am. Chem. Soc.* 124 (**2002**) 7642.

Kim, T.H., Lee, K.H., Kwon, Y.K. *J. Colloid Interface Sci.* 304 (**2006**) 370.

Kim, S.S., Zhang, W.Z., Pinnavaia, T.J. *Science* 282 (**1998**) 1302.

Latham, A.H., Wilson, M.J., Schiffer, P., Williams, M.E. *J. Am. Chem. Soc.* 128 (**2006**) 12676.

Lee, J.S., Park, J.K. *Ceram. Int.* 29 (**2003**) 271.

Li, X.L., Lou, T.J., Sun, X.M., Li, Y.D. *Inorg. Chem.* 43 (**2004**) 5442.

Li, Y.S., Shi, J.L., Hua, Z.L., Chen, H.R., Ruan, M.L., Yan, D.S. *Nano Lett.* 3 (**2003**) 609.

Li, J., Zeng, H.C. *J. Am. Chem. Soc.* 129 (**2007**) 15839.

Li, X.X., Xiong, Y.J., Li, Z.Q., Xie, Y. *Inorg. Chem.* 45 (**2006**) 3493.

Li, Y.G., Zhou, P., Dai, Z.H., Hu, Z.X., Sun, P.P., Bao, J.C. *New J. Chem.* 30 (**2006**) 832.

Liang, H.P., Guo, Y.G., Zhang, H.M., Hu, J.S., Wan, L.J., Bai, C.L. *Chem. Commun.* (**2004**) 1496.

Liang, Z.J., Susha, A., Caruso, F. *Chem. Mater.* 15 (**2003**) 3176.

Liang, H.P., Wan, L.J., Bai, C.L., Jiang, L. *J. Phys. Chem. B* 109 (**2005**) 7795.

Liang, H.P., Zhang, H.M., Hu, J.S., Guo, Y.G., Wan, L.J., Bai, C.L. *Angew. Chem. Int. Ed.* 43 (**2004**) 1540.

Liu, Y., Chu, Y., Zhuo, Y.J., Dong, L.H., Li, L.L., Li, M.Y. *Adv. Funct. Mater.* 17 (**2007**) 933.

Liu, B., Zeng, H.C. *Small.* 1 (**2005**) 566.

Liu, X.Y., Gao, C.Y., Shen, J.C., Mohwald, H. *Macromol. Biosci.* 5 (**2005**) 1209.

Lootens, D., Vautrin, C., van Damme, H., Zemb, T. *J. Mater. Chem.* 13 (**2003**) 2072.

Lou, X.W., Wang, Y., Yuan, C., Lee, J.Y., Archer, L.A. *Adv. Mater.* 18 (**2006**) 2325.

Lou, X.W., Archer, L.A., Yang, Z. *Adv. Mater.* 20 (**2008**) 3987.

Lu, J., Chen, D.R., Jiao, X.L. *J. Colloid Interface Sci.* 303 (**2006**) 437.

Lu, Y., McLellan, J., Xia, Y.N. *Langmuir* 20 (**2004**) 3464.

Lu, L.H., Sun, G.Y., Xi, S.Q., Wang, H.S., Zhang, H.J., Wang, T.D., Zhou, X.H. *Langmuir* 19 (**2003**) 3074.

McDonald, C.J., Bouck, K.J., Chaput, A.B., Stevens, C.J. *Macromolecules* 33 (**2000**) 1593.

Mao, B.D., Kang, Z.H., Wang, E.B., Tian, C.G., Zhang, Z.M., Wang, C.L., Song, Y.L., Li, M.Y. *J. Solid State Chem.* 180 (**2007**) 489.

Martinez, C.J., Hockey, B., Montgomery, C.B., Semancik, S. *Langmuir* 21 (**2005**) 7937.

Miyao, T., Minoshima, K., Naito, S. *J. Mater. Chem.* 15 (**2005**) 2268.

Moh, K.H. *Materials Research Society Symposium Proceedings* 372 (**1995**) 15.

Nakamura, R., Tokozakura, D., Nakajima, H., Lee, J.G., Mori, H. *J. Appl. Phys.* 101 (**2007**) 074303.

Nakamura, R., Lee, J.G., Tokozakura, D., Mori, H., Nakajima, H. *Mater. Lett.* 61 (**2007**) 1060.

Nakashima, T., Kimizuka, N., *J. Am. Chem. Soc.* 125 (**2003**) 6386.

Ni, Y.H., Tao, A., Hu, G.Z., Cao, X.F., Wei,X.W., Yang, Z.S. *Nanotechnology* 17 (**2006**) 5013.

Oswald, W. *Z. Phys. Chem.* 34 (**1900**) 495.

Park, J.H., Oh, C., Shin, S.I., Moon, S.K., Oh, S.G. *J. Colloid Interface Sci.* 266 (**2003**) 107.

Peng, Q., Dong, Y.J., Li, Y.D. *Angew. Chem. Int. Ed.* 42 (**2003**) 3027.

Ping, S., Sun, S.H. *Angew. Chem. Int. Ed.* 46 (**2007**) 4155.

Prouzet, E., Cot, F., Boissiere, C., Kooyman, P.J., Larbot, A. *J. Mater. Chem.* 12 (**2002**) 1553.

Putlitz, B.Z., Landfester, K., Fischer, H., Antonietti, M. *Adv. Mater.* 13 (**2001**) 500.

Qi, L.M., Li, J., Ma, J.M. *Adv. Mater.* 14 (**2002**) 300.

Rana, R.K., Mastai, Y., Gedanken, A. *Adv. Mater.* 14 (**2002**) 1414.

Rana, R.K., Murthy, V.S., Yu, J., Wong, M.S. *Adv. Mater.* 17 (**2005**) 1145.

Rhodes, K.H., Davis, S.A., Caruso, F. Zhang, B.J., Mann, S. *Chem. Mater.* 12 (**2000**) 400.

Romero-Cano, M.S., Vincent, B. *J. Controlled Release* 82 (**2002**) 127.

Sands, B.W., Howes, W.C., Smiley, L.H. *Plast. Eng.* 38 (**1982**) 31.

Sargeant, G.K. *Br. Ceram. Trans.* 90 (**1991**) 132.

Sarikaya, Y., Sevinç, İ., Akinç, M. *Powder Technol.* 116 (**2001**) 109.

Selvakannan, P.R., Sastry, M. *Chem. Commun.* (**2005**) 1684.

Shchukin, D.G., Kohler, K., Mohwald, H., Sukhorukov, G.B. *Angew. Chem. Int. Ed.* 44 (**2005**) 3310.

Shchukin, D.G., Mohwald, H. *Phys. Chem. Chem. Phys.* 8 (**2006**) 3496.

Smigelskas, A.D., Kirkendall, E.O. *Trans. Am. Min. Metall. Pet. Eng.* 171 (**1947**) 130.

Sun, X.M., Li, Y.D. *Angew. Chem. Int. Ed.* 43 (**2004**) 3827.

Sun, X.M., Li, Y.D. *J. Colloid Interface Sci.* 291 (**2005**) 7.

Sun, Y.G., Xia, Y.N. *J. Am. Chem. Soc.* 126 (**2004**) 3892.

Suslick, K.S. *Science* 247 (**1990**) 1439.

Tang, Y., Yang, L., Qiu, Z., Huang, J. *J. Mater. Chem.* 19 (**2009**) 5980.

Tartaj, P., Gonzalez-Carreno, T., Serna, C.J. *Adv. Mater.* 13 (**2001**) 1620.

Teo, J.J., Chang, Y., Zeng, H.C., *Langmuir* 22 (**2006**) 7369.

Titirici, M.M., Antonietti, M., Thomas, A. *Chem. Mater.* 18 (**2006**) 3808.

Velikov, K.P., van Blaaderen, A. *Langmuir* 17 (**2001**) 4779.

Wan, Y., Yu, S.H. *J. Phys. Chem. C* 11 (**2008**) 3641.

Wang, D.Y., Caruso, F. *Chem. Mater.* 14 (**2002**) 1909.

Wang, P., Chen, D., Tang, F.Q. *Langmuir* 22 (**2006**) 4832.

Wang, H.Z., Liang, J.B., Fan, H., Xi, B.J., Zhang, M.F., Xiong, S.L., Zhu, Y.C., Qian, Y.T. *J. Solid State Chem.* 181 (**2008**) 122.

Wang, H.R., Song, Y.L., Medforth, C.J., Shelnutt, J.A. *J. Am. Chem. Soc.* 128 (**2006**) 9284.

Wang, Q.B., Yan, L., Yan, H. *Chem. Commun.* (**2007**) 2339.

Wilcox, D., Berg, M. *Mat. Res. Soc. Symp. Proc.* 372 (**1995**) 3.

Wu, D.Z., Ge, X.W., Zhang, Z.C., Wang, M.Z., Zhang, S.L. *Langmuir* 20 (**2004**) 5192.

Wu, C.Z., Xie, Y., Lei, L.Y., Hu, S.Q., Yang, C.Z. *Adv. Mater.* 18 (**2006**) 1727.

Xie, Y., Huang, J.X., Li, B., Liu, Y., Qian, Y.T. *Adv Mater.* 12 (**2000**) 1523.

Xu, Y.Y., Chen, D.R., Jiao, X.L., Xue, K.Y. *Phys. Chem. C* 111 (**2007**) 16284.

Xu, F., Wei, W., Zhang, C.L., Ding, S.J., Qu, X.Z., Liu, J.G., Lu, Y.F., Yang, Z.Z. *Chem. Asian J.* 2 (**2007**) 828.

Xu, H.F., Ding, S.J., Wei, W., Zhang, C.L., Qu, X.Z., Liu, J.G., Yang, Z.Z. *Colloid Polym. Sci.* 285 (**2007**) 1101.

Yang, R.Z., Li, H., Qui, X.P., Chen, L.Q. *Chem. Eur. J.* 12 (**2006**) 4083.

Yang, S., Liu, H.R. *J. Mater. Chem.* 16 (**2006**) 4480.

Yang, M., Ma, J., Zhang, C.L., Yang, Z.Z., Lu, Y.F. *Angew. Chem. Int. Ed.* 44 (**2005**) 6727.

Yang, Z.Z., Niu, Z., Lu, Y.F., Hu, Z.B., Han, C.C. *Angew. Chem. Int. Ed.* 42 (**2003**) 1943.

Yang, H.G., Zeng, H.C. *J. Phys. Chem. B* 108 (**2004**) 3492.

Yano, T., Imai, M., Kaida, T., Hashimoto, K., Toda, Y. *Key Eng. Mater.* 161 (**1999**) 407.

Yeh, Y.Q., Chen, B.C., Lin, H.P., Tang, C.Y. *Langmuir* 22 (**2006**) 6.

Yin, Y.D., Erdonmez, C., Aloni, S., Alivisatos, A.P. *J. Am. Chem. Soc.* 128 (**2006**) 12671.

Yin, Y.D., Rioux, R.M., Erdonmez, C.K., Hughes, S., Somorjai, A.P., Alivisatos, A.P. *Science* 304 (**2004**) 711.

Yu, J.G., Guo, H.T., Davis, S.A., Mann, S. *Adv. Funct. Mater.* 16 (**2006**) 2035.

Yu, J., Wang, G. *J. Phys. Chem. Solids* 69 (**2008**) 1147.

Yu, J., Yaseen, M.A., Anvari, B., Wong, M.S. *Chem. Mater.* 19 (**2007**) 1277.

Yu, H.G., Yu, J.G., Liu, S.W., Mann, S. *Chem. Mater.* 19 (**2007**) 4327.

Yu, J.G., Yu, H.G., Guo, H.T., Li, M., Mann, S. *Small*. 4 (**2008**) 87.

Zelikin, A.N., Li, Q., Caruso, F. *Angew. Chem. Int. Ed.* 45 (**2006**) 7743.

Zhang, X.J., Li, D. *Angew. Chem. Int. Ed.* 45 (**2006**) 5971.

Zhang, L.X., Li, P.C., Liu, X.H., Du, L.W., Wang, E. *Adv. Mater.* 19 (**2007**) 4279.

Zhang, D.B., Qi, L.M., Ma, J.M., Cheng, H.M. *Adv. Mater.* 14 (**2002**) 1499.

Zhu, Y.F., Fan, D.H., Shen, W.Z. *J. Phys. Chem. C* 111 (**2007**) 18629.

Zhu, L.P., Xiao, H.M., Zhang, W.D., Yang, G., Fu, S.Y. *Cryst. Growth Des.* 8 (**2008**) 957.

Zhu, J.J., Xu, S., Wang, H., Zhu, J.M., Chen, H.Y. *Adv. Mater.* 15 (**2003**) 156.

Zhuo, P., Li, Y.G., Sun, P.P., Zhou, J.H., Bao, J.C. *Chem. Commun.* (**2007**) 1418.

Zimmermann, C., Feldmann, C., Wanner, M., Gerthsen, D. *Small* 3 (**2007**) 1347.

Zoldesi, C.I., Imhof, A. *Adv. Mater.* 17 (**2005**) 924.

Chapter Three: Initial Scoping Experiments

3.1.   Introduction

The origins of LbL electrostatic assembly of charged species onto solid surfaces date back to the work published during the mid-1960s, where it was shown that particles could be sequentially deposited onto solid substrates [Iler, 1966]. Also pioneering work of Decher and colleagues showed that polycations and polyanions (charged polyelectrolytes) could also be LbL assembled onto solid surfaces [Decher, et al. 1992; Decher, et al. 1994; Decher, 1997]. Following this, the LbL technique was widely expanded to a broad range of other charged species, including inorganic nanoparticles, biomolecules, and dyes, resulting in polyelectrolyte composite multilayer films [Caruso, et al. 1998; Donath, et al. 1998; Caruso, 2000; 2003; Schneider, et al. 2004; 2008]. The LbL method has also been applied to particles, substituting planar substrates with colloids of interest.

3.2.   Background

Several groups have utilised the LbL approach to prepare coated colloids. For example, the construction of alternating composite multilayers of exfoliated zirconium phosphate sheets and charged redox polymers on silane modified silica particles [Keller, et al. 1995]. The depositing of nanosized alumina particles in alternation with poly(acrylic acid), which acts as the bridging polymer, on submicrometer sized alumina core particles [Chen, et al. 1998]. Alternatively assembled metal nanosized particles (Au, Pd, and Pt) and oppositely charged polyelectrolyte onto polystyrene microspheres [Dokoutchaev, et al. 1999]. Caruso and colleagues have shown that the LbL method allows the deposition of multiple layers of various polyelectrolytes on colloids in a controlled fashion. By substituting one of the

charged polyelectrolyte components with a preferred inorganic nanoparticle, it was demonstrated that a wide range of nanoparticle based coatings could be prepared on submicron and micron sized particles. For example, these include silica [Caruso, et al. 1998; Lvov, et al. 2002; Yuan, et al. 2005], zeolite [Zhang, et al. 2003], calcium carbonate [Lu, et al. 2005], iron oxide [Shiho, et al. 2000; Dai, et al. 2005; Wang, et al. 2005], manganese oxide [Yang, et al. 2006], titania [Caruso, et al. 2001; Collins, et al. 2003; Strohm, et al. 2004], cadmium [Zhang, et al. 2005], gold [Gittins, et al. 2000; 2001; 2002;], magnetite [Caruso, et al. 1999] nanoparticles.

In the general LbL colloid coating method, a polyelectrolyte solution is added to a colloidal suspension [Decher, 1997; Caruso, et al. 1998]. The key point is that the added polyelectrolyte has an opposite charge to that on the colloids, thereby adsorbing through electrostatic interactions. The LbL assembly of polyelectrolytes onto colloid particles can be performed in two main ways: (i) the concentration of polyelectrolyte added is just enough to form a saturated layer or (ii) the concentration is in excess to cause saturation adsorption [Donath, et al. 1998; Sukhorukov, et al. 1998]. The first method requires accurate determination of the exact amount of polyelectrolyte needed to saturate the particle surface, which involves separate adsorption experiments to determine the relative concentrations of polyelectrolyte and particles. In the second method, which is generally favoured, the excess polyelectrolyte is removed prior to the addition of the next oppositely charged component to prevent the formation of polyelectrolyte complexes in bulk solution. The excess polyelectrolyte can be removed by several centrifugation, wash, and dispersion cycles in water or by filtration [Voigt, et al. 1999].

In the coating process, particle aggregation should be suppressed at all stages of the preparation, when the centrifugation, wash and dispersion approach is used, care needs to be taken not to use too high centrifugation speeds, as strongly aggregated particles in the form of a sediment are difficult to redisperse. Regardless of the method used, coating particle concentrations of up to a few weight percent are used in order to avoid particle aggregation upon addition of the coating species. After adsorption of a polyelectrolyte layer, the charge on the surface of the particle is reversed, which aids in the deposition of possible subsequent layers of a wide range of charged components as already discussed. Hollow inorganic microspheres are obtained from coated colloids following calcination. The elevated temperature treatment removes the organic matter (i.e. the sacrificial core and polyelectrolyte) and sinters the preformed particles, hence providing structural integrity for the hollow microsphere.

The scope of this research has been divided into four specific stages; (i) to initially prove a concept and fabricate hollow microspheres through colloid template self assembly of kaolin nanoparticles, (ii) to characterise the raw materials and process used to fabricate hollow microspheres, (iii) to optimise a calcination program to produce hollow microspheres, and (iv) to consider the economics and industrial commercialisation of the microsphere project.

3.3. *Experimental Process*

3.3.1. Materials

Anionic hollow polystyrene (PS) microspheres with an approximate 0.9 μm diameter in suspension were supplied by Rohm & Haas Co., (Philadelphia, US). A hollow PS structure would be less detrimental to the formation of a kaolin microsphere shell during the

calcination process. Solid PS microspheres may cause excessive amounts of volatile material to build up within the shell formation and result in critically fracturing the shell as the material escapes the void as the calcination temperature increases.

A fine kaolin mineral, classified as FK-8489, with an approximate particle size (d_{50}) of 0.13 μm was selected as a coating material to form a shell structure on the PS microsphere surface. The particle size ratio of the fine kaolin mineral to the PS microsphere particle size indicated that the kaolin particles would sufficiently cover the PS microsphere surface in a smooth layer formation and compensate for the surface curvature of the PS microsphere. Due to the anionic state of both the PS microsphere surface and the kaolin mineral, a commercial cationic polyelectrolyte was selected to render the PS microsphere surface cationic and therefore favourable for kaolin mineral adsorption. A low molecular weight cationic polyelectrolyte, poly(diallydimethylammonium chloride), (polyDADMAC), was supplied by Sigma Aldrich Chemicals (Dorset, UK).

3.3.2. Analytical methods

3.3.2.1.   *Scanning electron microscopy*

A JEOL JSM 6700-F (JEOL Ltd., JP) scanning electron microscopy (SEM) instrument was used, incorporating a cold cathode field emission gun, ultra high vacuum and sophisticated digital technologies for high resolution high quality imaging of structures. The microscope operates at accelerated voltages ranging from 0.5 to 30 kV and has a resolution of 1.0 nm at 15 kV and 2.2 nm at 1.0 kV. It has secondary electron detectors and backscattered electron imaging with both compositional and topographical imaging contrast. Substrates used

included: aluminium, mica, quartz glass and adhesive carbon templates. Best results were achieved when using a flat surface.

3.3.2.2. *Environmental scanning electron microscopy*

A Philips XL30 FEG (FEI Co. NL) environmental scanning electron microscopy (ESEM) instrument was used to provide information detailing the changes in structure while being heat treated. The Phillips XL30 offers high resolution secondary electron imaging at pressures as high as 10 torr and sample temperatures as high as 1500 ºC. The instrument employs a Schottky field emission source enabling outstanding observation of potentially problematic samples for conventional high vacuum SEM.

3.3.2.3. *Focused ion beam analyser*

A Strata FIB201 (FEI Co., NL) gallium focused ion beam (FIB) instrument was used for sectioning and high-resolution imaging of particles. The instrument was capable of producing a gallium ion beam of between 7 nm and 300 nm diameter at 30 keV energy with a beam current of 1 pA to 12 nA respectively [Mee, et al. 2008]. A platinum organometallic gas injector allows ion beam assisted deposition of platinum over selected areas of the sample. This facility can be used prior to sectioning in order to protect the top surface of the sample during ion milling.

For sample sectioning, an ion current of 350 pA or 1nA was used to remove material by scanning the beam in a line to make a lateral cut and then moving the beam progressively upwards into the sample to remove any further material. A good quality cut can be produced in this way, while minimising the possibility of redeposition of material onto the cut face.

The sample was then tilted at 45° and the polished face imagined using the same ion beam, generally at a much lower beam current between 4 and 11 pA, to achieve higher resolution.

3.3.3. Initial adsorption experiments

Initially, an experimental process was developed for preparing hollow microspheres by coating colloidal particles with a layer of oppositely charged polyelectrolyte (PE) and nanoparticles, followed by a calcination process to remove the colloidal sacrificial core material as shown in Figure 3.1.
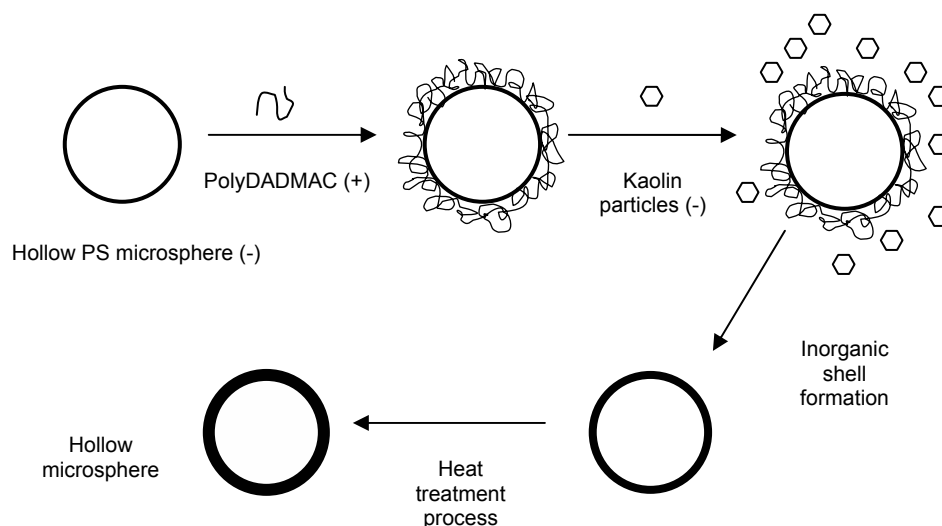
Figure 3.1 *Schematic illustration of the sacrificial core template process.*

The initial step in the fabrication of the hollow microspheres was to prepare the colloidal dispersion of the hollow PS microparticles: the PS microsphere suspensions were diluted from 27 to 0.5 wt% solids using laboratory grade distilled water. This was done to reduce any particle aggregation or PE bridging during the addition of a cationic polyelectrolyte.

The PS suspensions were then washed, filtered and resuspended using distilled water to remove any excess monomer or surfactants. The 100 ml PS colloidal suspensions at 0.5 wt% were then treated for 2 min with ultrasound in an ultrasonic bath (Bandelin Sonorex Digital, UK) to improve dispersity.

Prior to the deposition of the inorganic kaolin nano particles, a precursor cationic polyelectrolyte layer film was assembled at the anionic PS surface. The precursor PE layer was consecutively deposited onto the negatively charged PS lattice from a 2 g L^{-1} PE solution. The 100 ml polyelectrolyte solution was added drop wise using a burette. The concentration of polyelectrolyte was considered to be sufficient to saturate the PS surface. The suspension was gently stirred for 60 min to enable the adsorption mechanism to initiate, resulting in cationic polymer chains anchoring to the surface of the anionic PS surface. Ideally, the majority of the PS surface should be rendered cationic. To remove any excess PE from the PS suspension, the suspensions were filtered, washed and resuspended using distilled water.

The mineral samples were washed, filtered and dried prior to use. This procedure was to ensure that any contaminants or excess dispersion agents were removed. Fine kaolin particles at (i) 0.125 g and (ii) 0.750 g were subsequently deposited by exposing the cationic PS microspheres to a 100 ml kaolin suspension in 0.1 M NaCl. The ionic strength of the kaolin suspension was adjusted to ensure the moderate shielding of the kaolin surface charge. Adsorption time was 20 min under gently stirring at room temperature. The build up of the multilayers, cationic PE and anionic kaolin particles, was facilitated by the electrostatic interactions between the negatively charged inorganic particles and the positively charged groups of the polyDADMAC.

3.3.4. Initial calcination experiments

Samples were dried in a Carbolite fanned convection laboratory oven at 60 ℃ overnight and the removal of the PS template material was achieved by soak calcination at an elevated temperature. Initial calcination temperatures allowed removal of the core material and to study the effect of the heating rate. Experiments were conducted by heating the samples at various temperatures between 350 and 1250 ℃ using a Carbolite muffle chamber furnace (Carbolite Ltd., UK) in an oxygen environment.

3.4.   *Initial Results*

3.4.1. Coating process

It was important to ask oneself how much kaolin would be required to achieve full surface coverage of the PS microspheres. An excess amount of kaolin would likely result in a more dense microsphere particle. The coverage, expressed as a ratio of effective area covered by the clay, A_{part}^{cov}, and the total area of the template material, A_{PS} has been previously expressed by using the following equation [Cauvin, et al. 2005]:

$$Coverage = \frac{A_{part}^{cov}}{A_{PS}} = \frac{4}{3\pi}\left(\frac{w_{clay}}{w_{poly}}\right)\left(\frac{\rho_{PS}}{\rho_{clay}}\right)\left(\frac{R_{PS}}{h}\right) \tag{3.1}$$

where w_{clay} and w_{poly} being the mass of clay and template material used in g, ρ_{PS} and ρ_{clay} being the densities of the template material and clay in g/cm^3, R_{PS} being the radius of the template in nm, and h being the rim height of the clay pellet in nm. However, this equation was considered crude and was based on various assumptions that were not made clear.

Therefore, kaolin nanoparticles in suspension were added to a PS microsphere solution based on the predetermined specific surface area properties of the PS and kaolin materials, where the specific surface area of the PS was reported to be 7.0 m^2/g, and the kaolin specific surface area was measured, using a BET gas adsorption method, at 28.3 m^2/g (refer to Chapters 4.3.4. and 4.4.3.). These initial kaolin concentrations were chosen to achieve partial coverage and saturation of the PS microsphere surface.

3.4.1.1.   Initial scanning electron microscopy results

Analytical electron microscope characterisation techniques were used to determine a number of processes, these include; the adsorption of fine kaolin mineral particles on the surface of PS and the removal of the PS sacrificial core material due to calcination.
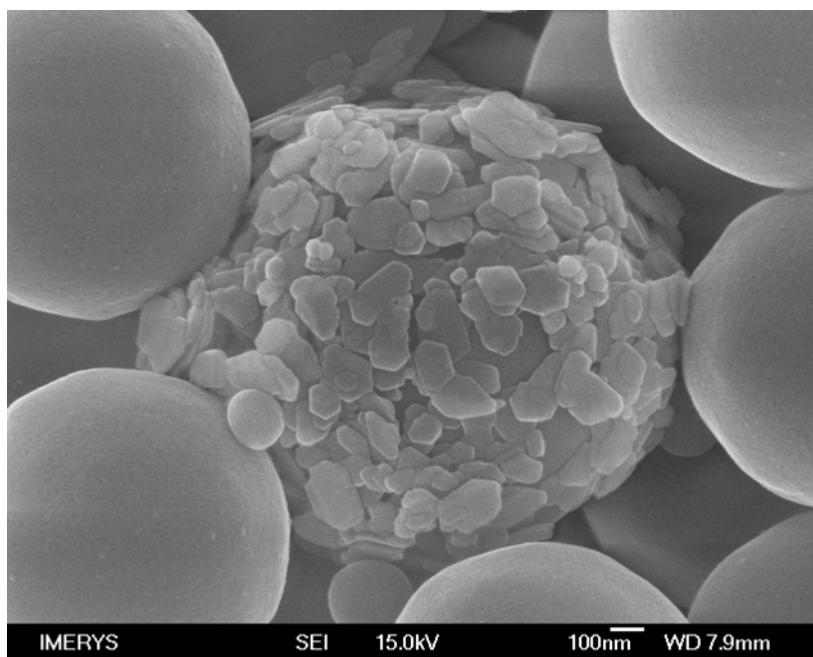
Figure 3.2 *SEM image showing the localised coating of a PS microsphere.*
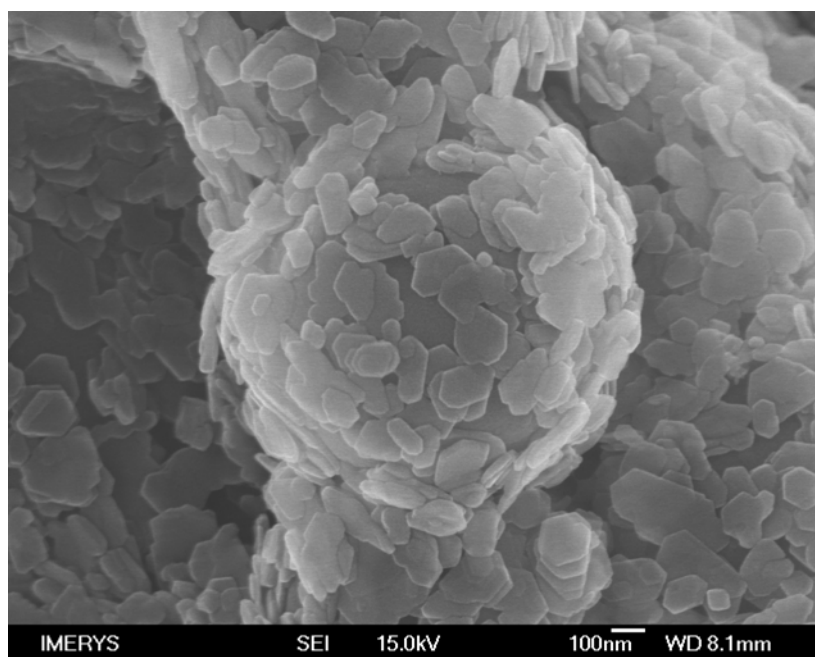
Figure 3.3 *Adsorption of kaolin particles at a concentration exceeding saturation and resulting in bridging.*

SEM images were used to observe whether or not kaolin particles would form a monolayer shell on the PS microspheres. Figure 3.2 indicated that cationic PS could be coated with anionic kaolin fine particles. The amount of kaolin added to the PS suspension was 0.125 g however, this initial value did not take into account the coverage of larger kaolin particle by smaller kaolin particles forming a shell structure. This mechanism of layered particles is evident in Figure 3.2. One significant point of interest worth noting, when 0.125 g of kaolin was added to a PS suspension a *localised* coating phenomena was observed [Gittins, 2006; Luckham, 2006; Vincent, 2006], as shown in Figure 3.2. This is understood to occur at low concentrations when individual template particles are favoured by the coating material and a near complete shell may be formed whereas neighbouring particles show very little if any surface attachment of the shell forming material. This *localised* phenomena has been observed but has not been reported in the published literature. One possible reason for this surface coating phenomena is that the surface properties of individual template material are simply more favourable for adsorption and the process may take place without any

55

competing forces. The mixing regime during the addition of the shell forming material may also influence the adsorption process at the template interface.

A second experiment at a higher kaolin concentration, 0.75 g, resulted in the surface area of the PS microspheres being sufficiently covered, however, aggregation was evident, due to the either the high concentration of kaolin added to the PS sample or the sample preparation technique. Upon consideration, the drying process was also expected to be detrimental to the sample integrity. Aggregation of particles due to bridging of kaolin particles is evident in Figure 3.3.

3.4.2. Calcination and removal of core material

The initial calcination program was predetermined at a heating step rate of 10 ℃ per min until a plateau temperature was reached. Initial plateau temperatures varied enabling the optimum temperature to be investigated. Temperatures included; 350, 550, 750, 1050 and 1250 ℃, the predetermined plateau temperature was kept constant for 60 min. A cooling rate of 10 ℃ per min was used until the furnace temperature reached room temperature.

3.4.2.1.   Initial scanning electron microscopy results

Figures 3.4 to 3.7 represent SEM images of structures that were formed after calcining PS microspheres coated with kaolin nanoparticles. The structure in Figure 3.4 was formed after a low weight concentration of kaolin was added to a PS suspension as described previously. The sample after drying was calcined at a plateau temperature of 350 ℃ for 60 min.
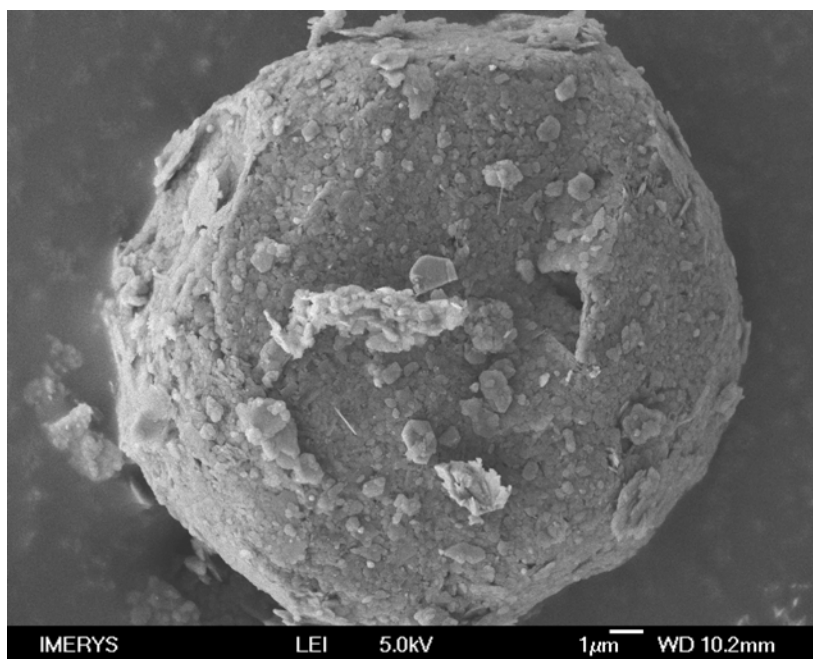
Figure 3.4 *SEM image of a discrete particle after calcination for 60 min. at 350 ℃.*

Figure 3.4 shows a spherical particle with a diameter of approximately 11 μm, the particle diameter is possibly due to aggregated PS microspheres covered in kaolin particles. Calcination at 350 ℃ has not resulted in sintering of the kaolin particles as individual kaolin plates are evident. SEM images also revealed structures with voids, either where the PS surface was not sufficiently covered with kaolin particles, or where the latex escaped from the internal structure during the calcination process by piercing through weak-bonded surface particles.

The preparation of the samples for SEM imaging also may be detrimental to the final structure. When higher concentrations of ultra fine kaolin were added to a PS suspension as described within the initial experimental procedure, once calcined the resulting structure showed no individual spherical structures as shown in Figure 3.4, aggregation became more evident.
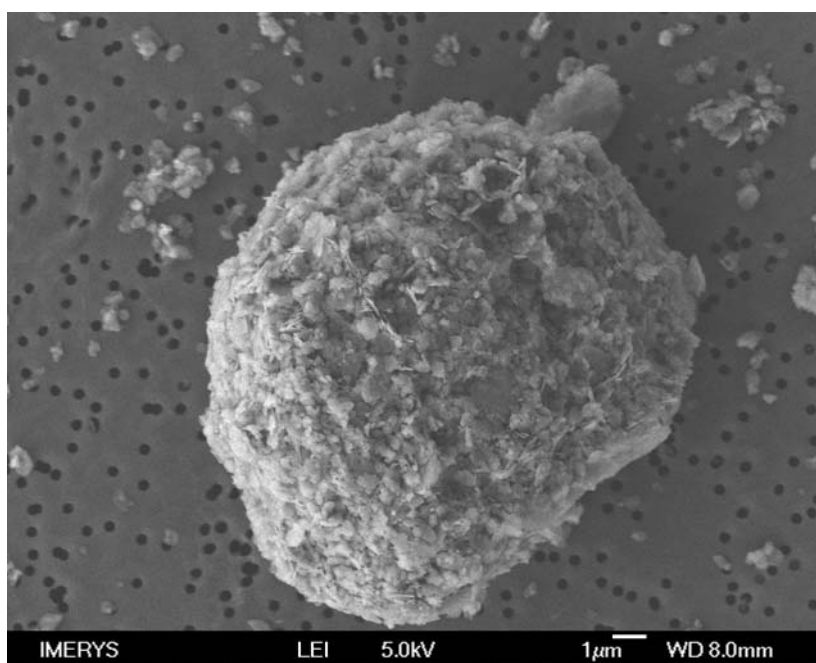
Figure 3.5 *SEM image of a discrete particle after calcination for 60 min. at 550 ℃.*
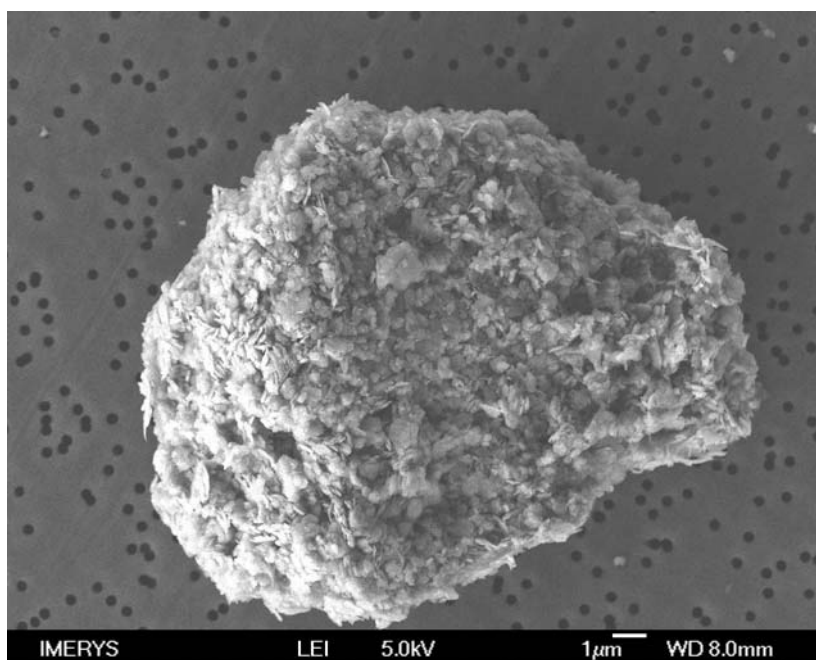
Figure 3.6 *SEM image of a discrete particle after calcination for 60 min. at 750 ℃.*
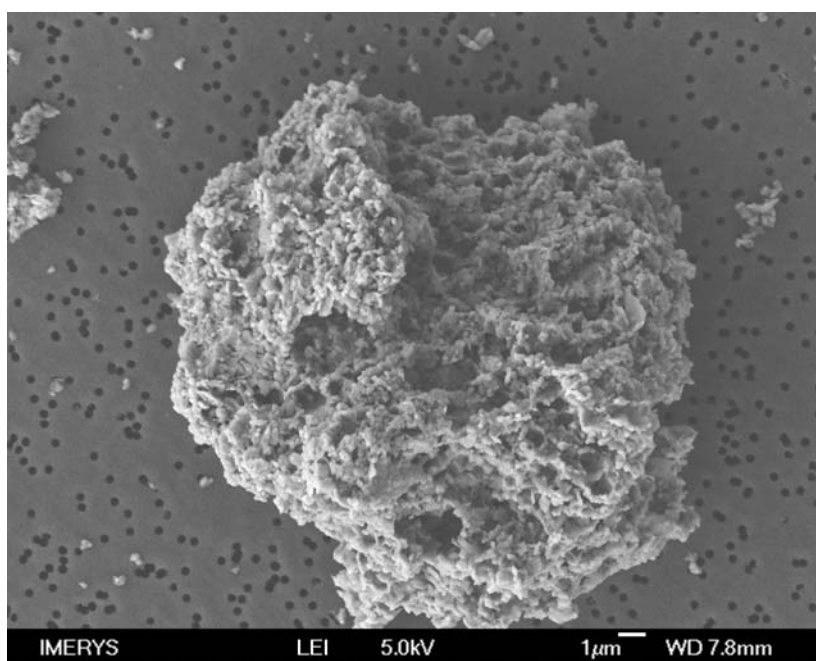
Figure 3.7 *SEM image of a discrete particle after calcination for 60 min. at 1050 ℃.*
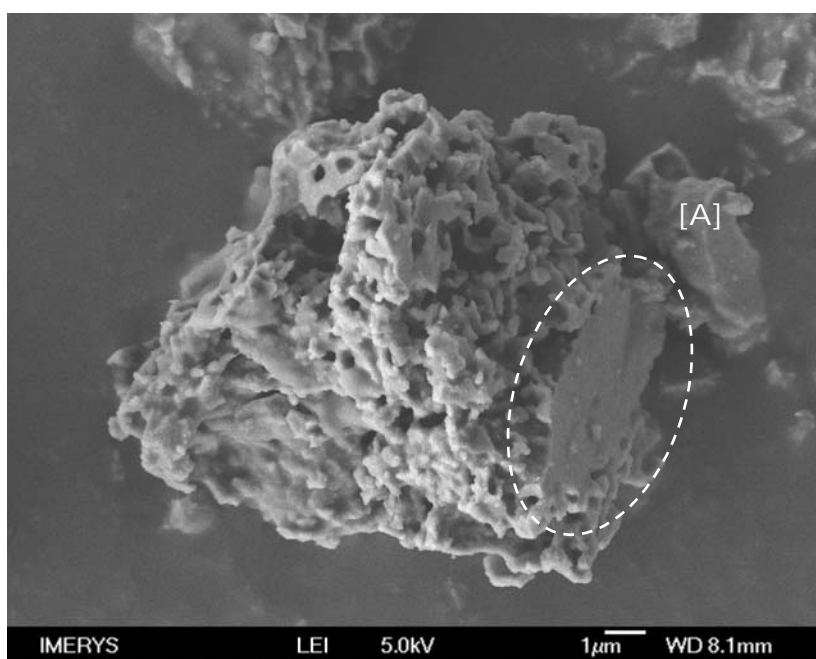
Figure 3.8 *SEM image of a discrete particle after calcination for 60 min. at 1250 ℃.*

Figures 3.5 and 3.6 show the resulting structures after calcination at 550 and 750 ºC, respectively. No discrete spherical particles being present within the samples; it is evident that the kaolin particles become aggregated.

Figures 3.7 and 3.8 show aggregated particles of ultra fine kaolin measuring approximately 10 μm in diameter. The surface of these structures show voids where the sacrificial core material has been extracted by heat treatment. What is interesting is whether these particles have internal voids and whether these voids decrease with an increase in temperature. Figure 3.7 again shows a structure of approximately 10 μm in diameter with less well-defined voids, the SEM image also shows the sintering and fusing of the kaolin particles due to the higher calcination temperature. Figure 3.8 shows a complete coalescence of the aggregated kaolin structure resulting in a solid particulate (exhibited by the letter A) due to the collapse of any internal voids. However, the surface of this aggregate still has numerous open pores visible.

3.4.2.2.   Initial environmental scanning electron microscopy results

A Phillips XL30 ESEM instrument (Centre for Electron Microscopy, University of Birmingham) was used to provide information detailing the changes in structure while being heat treated. The already dried sample was placed in the ESEM chamber and heated at 10 ºC per min until the plateau temperature of 1000 ºC was reached. The plateau temperature was kept constant for 60 min.

ESEM images were recorded as the temperature increased, at approximate 20 ºC increments. However, due to movement of the sample during heating and the release of volatile material from the PS, very few images showed detailed information regarding formed structures.
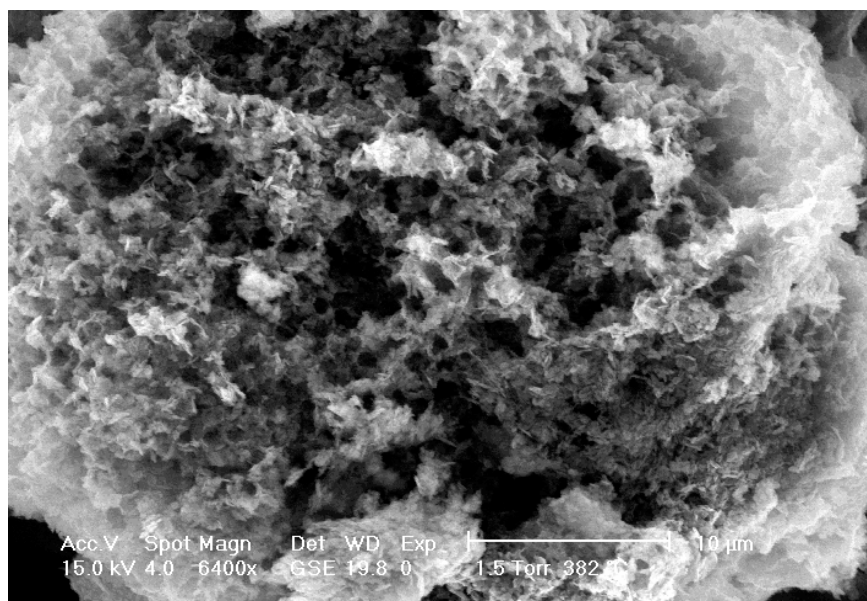
Figure 3.9 *ESEM image showing the formation of an aggregated structure during calcination, temp. 382 ºC.*
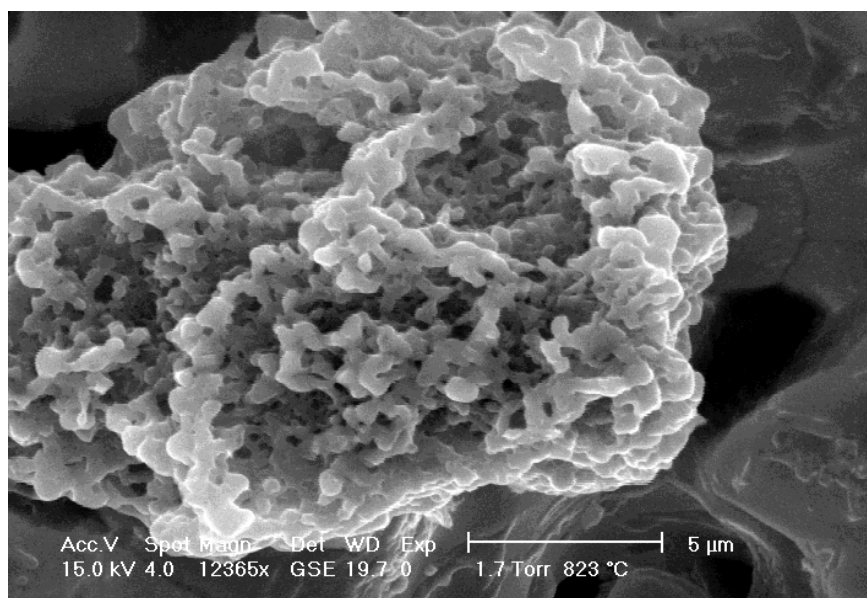
Figure 3.10 *ESEM image showing the fusing of kaolin particles forming an aggregate structure, temp. 823 ºC.*

Figure 3.9 shows a likely aggregate of PS microspheres and kaolin, it is not possible to determine whether the PS microspheres are actually coated with kaolin mineral particles. However, it is possible to determine that as the calcination temperature increases the aggregate structure decreases in size. Figure 3.10 shows an aggregated kaolin structure that has been formed due to the removal of the PS microspheres material. Most notably, the information obtained from this experiment detailed that between 370 and 450 ºC the majority of PS that had not been coated with the fine kaolin mineral had been removed and the fine kaolin particles became aggregated.

Once aggregated, the kaolin particles formed honeycomb structures with numerous visible open pores. Various structures, ranging from 10 to 15 μm in size were evident. Between the temperatures of 400 and 750 ºC the sacrificial core material was removed from the sample, and the ESEM images showed very little change to the sample during this process. The first notable change occurred at approximately 800 ºC when the kaolin particles first start to sinter. As the temperature reached 1000 ºC the kaolin particles had become completely fused.

With the use of an ESEM instrument, it has been possible to identify two important factors; (i) at approximately 750 ºC it is expected that the majority of the PS microspheres material was removed from the aggregated sample. PS microspheres that have not been coated with kaolin particles are expected to be removed at a lower temperature, and (ii) the first signs of sintering of the kaolin mineral particles occurs at approximately 800 ºC. From the ESEM experiment, it is evident that the drying process has significant importance upon the final particle structure. The final aggregated product may result in a low density material with a honeycomb internal structure that is also of commercial interest. This information will help to determine a more reliable calcination programme.

3.4.2.3.   Initial focused ion beam results

A Strata FIB201 gallium focused ion beam instrument (Interface Analysis Centre, University of Bristol) was used for sectioning and high-resolution imaging of calcined particles. The FIB offers a promising alternative to other characterisation techniques, such as transmission electron microscopy or microtoming [Koprinarov, et al. 2001; Han, et al. 2005; Zhang, et al. 2009]. The FIB allows in situ cross sectioning of specific particles. Figures 3.11 to 3.16 represent the internal structures of calcined particles.
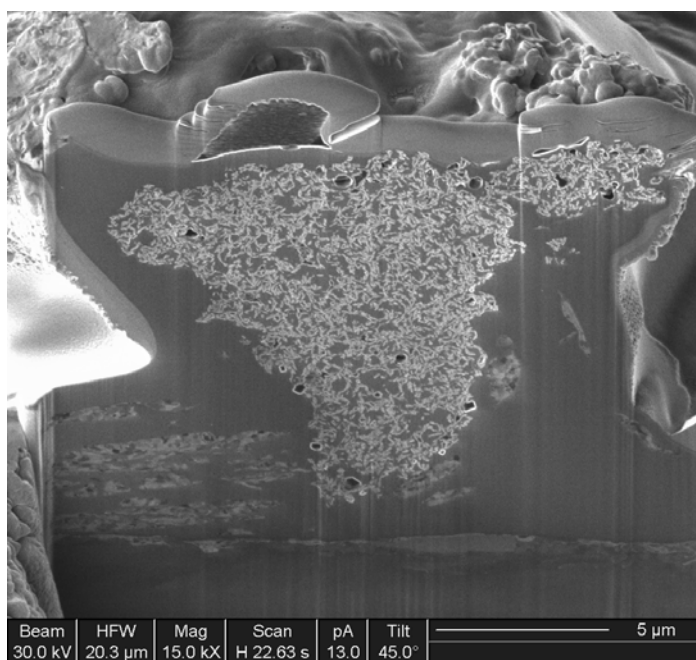
Figure 3.11 *FIB induced secondary electron image showing the cross section view of an aggregated structure after calcination at 350 ºC.*
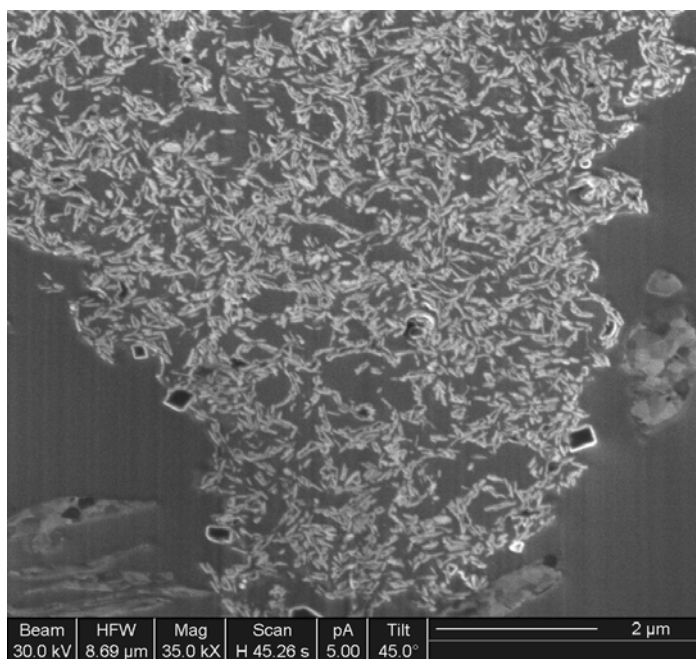
Figure 3.12 *Cross section view detailing the orientation of kaolin particles and PS within an aggregate structure, calcined at 350 ℃.*

Figure 3.13 *FIB induced secondary electron image showing the cross section view of an aggregated structure after calcination at 550 ℃.*
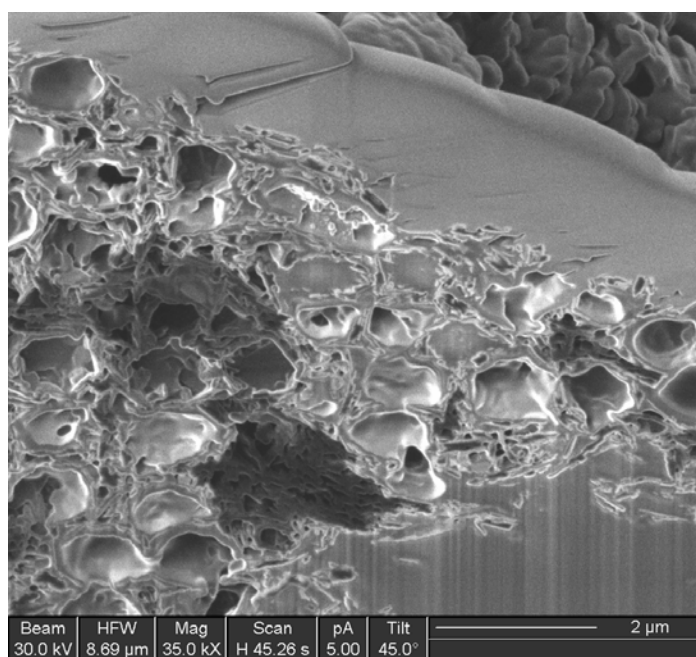
Figure 3.14 *Cross section view detailing the orientation of kaolin particles and PS within an aggregate structure, calcined at 550 ℃.*
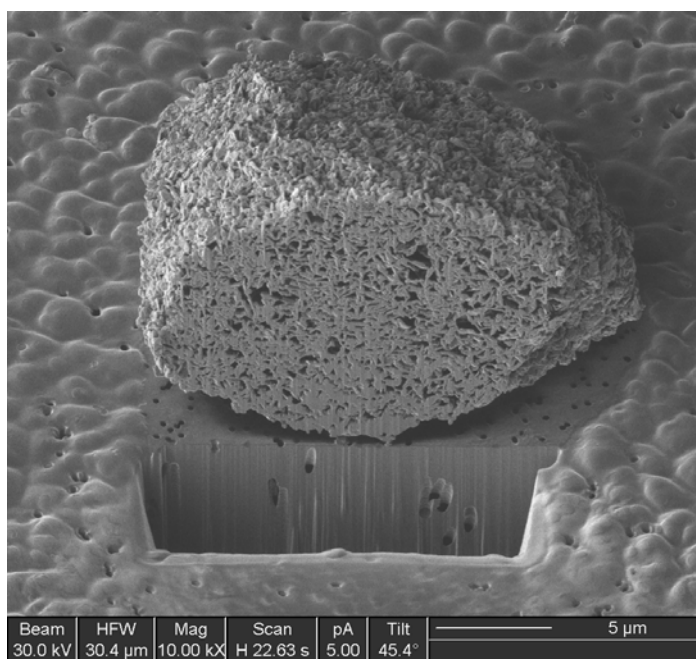
Figure 3.15 *FIB induced secondary electron image showing the cross section view of an aggregated structure after calcination at 750 ℃.*
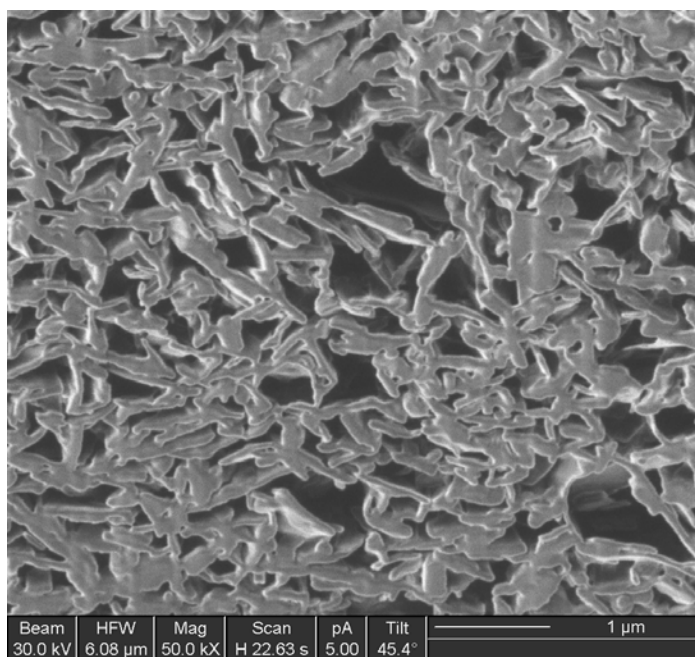
Figure 3.16 *Cross section view detailing the orientation of kaolin particles, with no PS evident within the aggregate, calcined at 750 ℃.*

The change of the internal structure of the particulate was dependent upon the temperature. Figures 3.11 and 3.12 show a structure resulting from calcination at 350 °C and the PS material was evident throughout the structure. Figures 3.13 and 3.14 also show PS evident within the structure, it was also evident that kaolin particles have coated the PS microspheres, however, aggregation was still problematic. At this high temperature it was expected that all the PS would have been removed. However, the colloid particles are armoured with fine kaolin particles. Figures 3.15 and 3.16 showed no sign of PS within the aggregated structure when the sample has been calcined at 750 °C for 60 min. However, it was evident that any spherical voids formed within the internal structure collapsed at high temperatures.

3.5.   Conclusions

Initial adsorption experiments of a cationic PE on hollow anionic PS microspheres proved that the LbL technique can be successfully used to adsorb fine kaolin particles onto the modified surface of anionic PS microspheres. It has been demonstrated that the solution adsorption conditions of precursor coatings on particles are of paramount importance for forming intact microspheres upon core removal and reduction of particle aggregation.

It was possible that the sacrificial template approach allows the fabrication of hollow microspheres, however, a number of variables are to be addressed these include: (i) The coating material, could other materials be used, for example alternative commercial grades of kaolin, zeolites or calcium carbonates? (ii) What would the required ratio of kaolin to PS be to form a shell structure around the template material? (iii) What would be the best process for preparing the samples for calcination? (iv) What calcination temperature would be required to remove the sacrificial core material and sinter the coating material to form a shell structure? These issues are to be addressed in the following chapters.

3.6.   References

Caruso, F., Caruso, R.A., Möhwald, H. *Science* 282 (**1998**) 1111.

Caruso, F., Lichtenfeld, H., Giersig, M., Möhwald, H. *J. Am. Chem. Soc.* 120 (**1998**) 8523.

Caruso, F., Susha, A.S., Giersig, M., Möhwald, H. *Adv. Mater.* 11 (**1999**) 950.

Caruso, F. *Chem. Eur. J.* 6 (**2000**) 413.

Caruso, F. *Adv. Mater.* 13 (**2001**) 11.

Caruso, F., Shi, X., Caruso, R.A., Susha, A. *Adv. Mater.* 13 (**2001**) 740.

Caruso, F. *Top Curr. Chem.* 227 (**2003**) 145.

Cauvin, S., Colver, P.J., Bon, S.A.F. *Macromolecules* 38 (**2005**) 7887.

Cochran, J.K. *Curr. Opin. Solid State Mater. Sci.* 3 (**1998**) 474.

Collins, A.M., Spickermann, C., Mann, S. *J. Mater. Chem.* 13 (**2003**) 1112.

Dai, Z., Meiser, F., Möhwald, H. *J. Colloid Interface Sci.* 288 (**2005**) 298.

Decher, G., Hong, J.D., Schmitt, J. *Thin Solid Films* 210 (**1992**) 831.

Decher, G. Lvov, Y., Schmitt, J. *Thin Solid Films* 244 (**1994**)772.

Decher, G. *Science* 277 (**1997**) 1232.

Donath, E., Sukhoroukov, G.B., Carusi, F., Davis, S.A., Möhwald, H. *Angew. Chem. Int. Ed.* 37 (**1998**) 2201.

Gittins, D.I., Caruso, F. *Adv. Mater.* 12 (**2000**) 1947.

Gittins, D.I. *Private communications*, Imerys Minerals Ltd., St. Austell, August (**2006**)

Gittins, D.I., Caruso, F. *J. Phys. Chem. B.* 105 (**2001**) 6846.

Gittins, D.I., Susha, A.S., Schoeler, B., Caruso, F. *Adv. Mater.* 14 (**2001**) 508.

Han, S., Jang, B., Kim, T., Oh, S.M., Hyeon, T. *Adv. Funct. Mater.* 15 (**2005**) 1845.

Hotz, J., Meier, W. *Langmuir* 14 (**1998**) 1031.

Iler, R.K. *J. Colloid Interface Sci.* 21 (**1966**) 569.

Kawahashi, N., Matijevic, E. *J. Colloid Interface Sci.* 138 (**1990**) 534.

Kawahashi, N., Matijevic,E. *J. Colloid Interface Sci.* 143 (**1991**) 103.

Koprinarov, I., Hitchcock, A.P., Heng, Y.M., Stöver, H.D.H. *Macromolecules* 34 (**2001**) 4424.

Lu, C., Xiaoyu, H., Wang, X., Yang, J., Yang, L., Zhang, D., Ma, J., Cao, W. *Chem. Mater.* 17 (**2005**) 5218.

Luckham, P. *Private communications*, Imperial College, London, August (**2006**)

Lvov, Y., Price, R., Gaber, B., Ichinose, I. *Colloids Surf., A* 198 (**2002**) 375.

Mee, S.J., Hart, J.R., Singh, M., Rowson, N.A., Greenwood, R.W., Allen, G.C., Heard, P.J., Skuse, D.R. *Appl. Clay Sci.*39 (**2008**) 72.

Schneider, G., Decher, G. *Nano Lett*. 4 (**2004**) 1833.

Schneider, G., Decher, G. *Langmuir* 24 (**2008**) 1778.

Shiho, H., Kawahashi, N. *J. Colloid Interface Sci.* 226 (**2000**) 91.

Strohm, H., Löbmann, P. *J. Mater. Chem.* 14 (**2004**) 138.

Sukhorukov, G.B., Donath, E., Lichtenfeld, H.,Knippel, E., Knippel, M., Möhwald, H. *Colloids Surf., A* 137 (**1998**) 253.

Texter, J. Tirrell, M. *AIChE J.* 47 (**2001**) 1706.

Thurmond, K.B, Kowalewski, T., Wooley, K.L. *J. Am. Chem. Soc.* 119 (**1997**) 6656.

Vincent, B. *Private communications*, University of Bristol, Bristol, June (**2006**)

Voigt, A., Lichtenfeld, H., Sukhorukov, G.B., Zastrow, H., Donath, E., Bäumler, H., Möhwald, H. *Ind. Eng. Che. Res.* 38 (**1999**) 4037.

Walsh, D., Mann, S. *Nature* 377 (**1995**) 320.

Wang, D., Song, C., Gu, G., Hu, Z. *Mater. Lett.* 59 (**2005**) 782.

Wendland, M.S., Zimmerman, S. *J. Am. Chem. Soc.* 121 (**1999**) 1389.

Wilcox, D.L., Berg, M., Bernat, T., Kellerman, D., Cochran, J.K. (eds). Hollow and solid spheres and microspheres. Materials Research Society Proceedings, Pittsburgh, **1998**, p. 372.

Yan, C., Xue, D. *J. Phys. Chem.* 110 (**2006**) 7102.

Yang, Z., Zhang, W., Wang, Q., Song, X., Qian, Y. *Chem. Phys. Lett.* 418 (**2006**) 46.

Yuan, J., Zhou, B., Wu, L. *Chem. Mater.* 17 (**2005**) 3587.

Zhang, S., Zhu, Y., Yang, X., Li, C. *Colloids Surf., A* 264 (**2005**) 215.

Zhang, Y., Chen, F., Shan, W., Zhuang, J., Dong, A., Cai, W., Tang, Y. *Microporous Mesoporous Mater*. 65 (**2003**) 277.

Zhang, H., Zhou, K., Li, Huang, S. *Biomed. Mater.* 4 (**2009**) 1.

Chapter Four: Materials Characterisation

4.1.   Introduction

A generic understanding of the interactions between the template core material, the cationic polyelectrolyte, the industrial minerals, and their behaviour during the adsorption and calcination process would enable a reproducible system to be developed. This chapter has been written to give the reader an understanding of the materials and why the materials have been selected. The materials of specific interest for characterisation include PS samples that may be suitable as core template material and fine mineral products that can be used as a shell forming material. Throughout the characterisation process certain materials that are considered inappropriate will be withdrawn from further characterisation processes, this was due to industrial constraints. At the end of this chapter alternative template components are listed, which may become a viable economic alternative in the future. A review of the synthesis of hollow polystyrene structures is found in Appendix A, whereas, a review of kaolin properties and the mineral surface characteristics is discussed in Appendix B.

Numerous techniques have been used to determine the characteristic properties of both the PS template material and the shell forming mineral. The important characteristics of the materials will determine their appropriate selection to fabricate hollow microspheres. Methods previously described to characterise resulting structures have not been included in this chapter. As the majority of the following techniques have been used to characterise both PS and mineral particles, sample preparation and specific instrument operating parameters are outlined in the relevant paragraphs.

4.2. *Analyses Methods*

4.2.1. Transmission electron microscopy

A Hitachi H-7000 (Hitachi Corp., JP) transmission electron microscope (TEM) operating at 120 kV was used to determine structural characteristics of the polystyrene samples. For analysis samples were mounted on a Cu grid holder and inserted into a vacuum column. Electrons are accelerated down the column and pass through the sample to form an image in the beam. Electromagnetic lenses control and magnify the image such that a resolution of 0.5 nm can be achieved. A tilting stage ±60º allows production of stereo images. The image is recorded digitally using a Megaview 2 CCD camera.

4.2.2. Electrokinetic measurements

The pH, stability and zeta potential of polystyrene and kaolin samples were measured by standard procedures using an AcoustoSizer II.v3 (Colloidal Dynamics, US) instrument. The technique is based on electroacoustics, the application of high frequency alternating electric fields to a suspension of particles [Hunter, 1998; Greenwood, et al. 2007]. Electrokinetic sonic amplitude measurements are carried out by passing an alternating high frequency electric field into the suspension as it passes through the electroacoustic cell. As the wave hits the particles near the surface of the cell, there is a resulting sound wave that returns through the cell and is recorded. From knowledge of the dielectric constant, particle density, and mass fraction in suspension, the dynamic mobility can be measured and hence the zeta potential can be determined.

4.2.3. Particle size and shape analysis

4.2.3.1.   *Laser particle size analysis*

A CILAS 1064 particle size analyser (Compagnie Industrielle de Lasers, FR) was used to determine the particle size and size distribution of the polystyrene microspheres within a suspension using the diffraction of a laser beam. CILAS integrates two sequenced laser sources positioned at 0º and 45º to produce a diffraction pattern analysed on a 64 channel silicon detector. Laser diffraction is based on the Mie and Fraunhofer scattering theories. During analysis the polystyrene samples were constantly mechanically stirred at 120 rpm to maintain dispersity. Data acquisition was complete in 30 seconds, the precision of the particle size measurements were in the range of ±1%.

4.2.3.2.   *Sedimentation measurements*

The Micromeritics Sedigraph 5100 (Micromeritics Instruments Corp., US) is an instrument that employs X-ray attenuation technology to determine the particle size distribution of a sample. A dilute mineral suspension settles in a cell in the path of collimated X-ray beam. The cell is calibrated with suspending liquid (100% transmission) and homogeneous suspension prior to settling (0% transmission). The attenuation of the beam is progressively reduced as the settling particles leave the beam path. Diameters obtained by the sedimentation method are expressed as equivalent spherical diameter (esd), the diameter of a sphere which settles at the same velocity as the particle.

4.2.3.3.   *New shape factor measurements*

Kaolin has a disc like morphology, which can be ascribed an 'aspect ratio' or 'shape factor' defined as the plate diameter divided by the plate thickness or height. More specifically, the

shape factor as used herein is the measure of an average value (weight averaged basis) of the ratio of mean particle diameter to particle thickness for a population of particles of varying size and shape as measured using the electrical conductivity method described in US patent application number 5128606 [Gate, et al. 1992]. Measurements of shape factor were made in the laboratory using a stop flow conductivity measurement instrument known as Particle Assessment by Natural Alignment and Conductivity Effect Analysis, (PANACE), developed by Imerys Minerals Ltd.

4.2.4. Thermal analysis

Thermogravimetric analysis (TGA) using a Netzsch STA-449EP (Netzsch-Gerätebau GmbH, DE) instrument was used to determine the physical change both in mass and structural transformation of polystyrene and kaolin samples. Representative samples of a similar weight were placed in an alumina crucible within the furnace system of the thermogravimetric instrument and heated at a predetermined rate, 10 ºC per minute. The reference material used was α-Al_2O_3 and the sensitivity was ± 50 μV. The precision of the measurements were in the range of $\pm 5\%$.

TGA measures change in mass as a function of temperature. Differential scanning calorimetry (DSC) measures change in energy flow. When a difference in temperature develops between the sample and the reference material, an automatic control loop heats the cooler of the two until the difference is eliminated. The electrical power required to accomplish an equilibrium state is plotted against temperature. An endothermic change signifies that an enthalpy increase has occurred in the sample.

4.2.5. Specific surface area measurements

Measurements were conducted using a Gemini VII 2390 (Micromeritics Instruments Corp., US) instrument determined by a standardised laboratory method. Data was collected using Gemini VII Windows software. Specific surface area measurements were based on the BET gas adsorption method, named after Brunauer, Emmett, and Teller [Brunauer, et al. 1938; 1940]. The specific surface area of the mineral samples was measured to help determine an effective coverage ratio. Samples were initially pre-treated to remove adsorbed contaminants acquired from atmospheric exposure. The mineral was then cooled under vacuum. An adsorptive (nitrogen) was admitted to the solid in controlled increments. After each dose of adsorptive, the pressure is allowed to equilibrate and the quantity of gas adsorbed is calculated. The gas volume adsorbed at each pressure defines an adsorption isotherm, from which the quantity of gas required to form a monolayer over the mineral external surface is determined.

4.2.6. Reflectance spectrometry

Measurements of the mineral brightness were done using an Elrepho 450X instrument (Datacolor, US). A pressed powder disc was placed in the diffuse reflectance spectrophotometer, the reflectance at a range of wavelengths is measured and used to express the colour of the kaolin. The powder brightness of a kaolin mineral is the reflectance at a wavelength of 457 nm (blue light absorbed). An estimate of the yellowness of a sample can be obtained by subtracting the reflectance at 457 from that at 570 nm (yellow light absorbed). The instrument is calibrated using standards supplied by the International Standards Organisation and the results are expressed as ISO Brightness.

4.2.7. X-ray photoelectron spectroscopy

XPS is a quantitative technique that measures the elemental composition of a sample. Each element produces a characteristic set of XPS peaks at characteristic binding energy values that directly identify each element that exists in the material being analysed. These characteristic peaks correspond to the element configuration of the electrons within the atoms. Surface analysis of the PS and kaolin samples was performed using a VG Escascope instrument (Fisons Instruments, UK) with a base pressure of 2×10^{-10} mbar. The dual anode X-ray source produced Al $K\alpha$ radiation, the maximum X-ray power used was 280 W. The binding energies are estimated to be accurate within ±0.2 eV, unless stated otherwise. Variance in XPS binding energies may be attributed to matrix effects, such as differences in crystal potential [Kim, et al. 1975].

4.2.8. X-ray diffraction analysis

X-ray diffraction (XRD) is a rapid analytical technique primarily used for phase identification of a crystalline material and can provide information on unit cell dimensions [Hanawalt, et. al. 1936]. X-ray diffraction is also used for the identification of unknown crystalline materials (e.g. minerals, inorganic compounds). XRD analyses were conducted using a PANalytical X'Pert Pro MRD powder diffractometer (PANalytical Ltd., UK), solid state detector and Cu radiation source (λCu $K\alpha$ = 1,54060 Å) at 40 kV and 40 mA were utilised. Back-filled kaolin pressed sample mounts were made to minimise transparency and sample displacement effects. The process works by a divergent beam of monochromatised radiation impinging on the flat surface of the powder sample and a Geiger counter scanning a range of 2θ values at a constant angular velocity, the intensity diffracted is recorded automatically. The data acquisition was performed using X'Pert Data Collector Software,

version 2.1a, the results were interpreted using an ICDD (International Centre for Diffraction Data) database.

4.2.9. X-ray fluorescence analysis

Quantification of elements was accomplished by analysing fused kaolin powder discs with a PANalytical Magix-Pro X-ray fluorescence spectrometer (PANalytical Ltd., UK) equipped with a Sc/Mo dual anode source. The XRF spectrometer was equipped with an Epsilon 5 X-ray tube, operated at 40 kV and with an emission current of 30 mA. Powder samples were flat pressed using a laboratory press prior to being placed in the spectrometer. The XRF spectrometer measures the individual component wavelengths of the fluorescent emission produced by a sample when irradiated by secondary X-rays.

4.3.   *Characterisation of Polystyrene Microspheres*

4.3.1. Material selection

Three PS samples were chosen as possible sacrificial core templates. Firstly, hollow PS Ropaque^{TM} AF1055 (research grade) from Rohm & Haas Co. (Philadelphia, US). Secondly, a solid PS product classified as DPP-722E supplied by Dow Chemicals (Illinois, US) and thirdly, a solid PS product supplied as PPs-1.0 by G. Kisker Laboratories GbR., (Frankfurt, DE). The microsphere samples supplied were purified by; filtration, ion exchange or centrifugation [Madaeni, et al. 2000]. In the present work, the PS microsphere samples were dialysed for at least 24 hr against distilled water using a polyethersulfone ultra-filtration membrane. This is for the removal of unreacted monomer, initiator and surfactant.

4.3.2. Scanning electron microscopy characterisation

PS microsphere samples were washed, filtered and redispersed using an ultra filtration system, Amicon 5200 stirred cells (Millipore Ltd., UK) at 1 wt% solids using distilled water. The samples were then further diluted using a water-methanol solution and were sonicated for 60 s. Small quantities of the dispersion were then sprayed onto a clean mica surface for observation. The scanning electron microscopy images represent the three different commercial PS products.
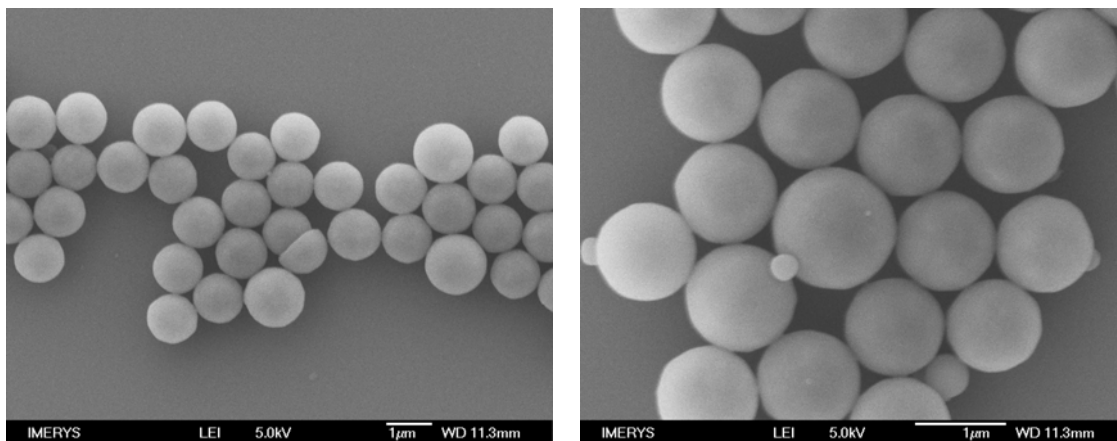
Figure 4.1 and **4.2** *SEM images of PS AF1055 microspheres.*
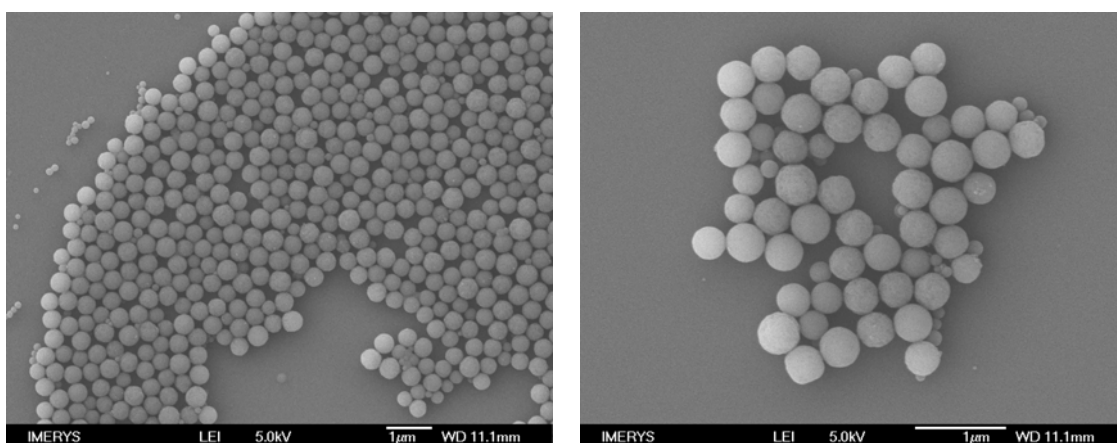
Figure 4.3 and **4.4** *SEM images of PS DPP-722E microspheres.*
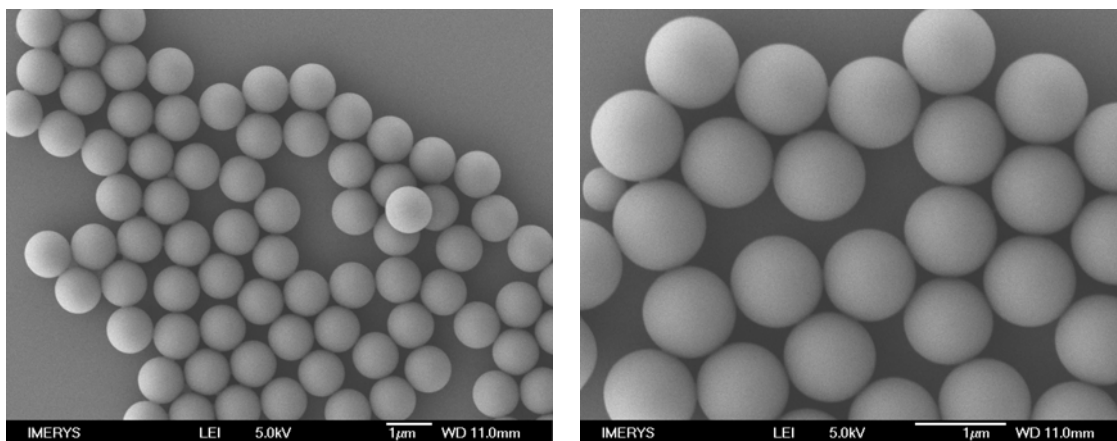
Figure 4.5 and **4.6** *SEM images of PS PPs-1.0 microspheres.*

Figures 4.1 to 4.6 show SEM micrographs of PS particles. Figures 4.1 and 4.2 show the spherical shape of AF1055 hollow PS microspheres. Figures 4.3 and 4.4 show a solid PS product with a wide-spread size distribution. Figures 4.5 and 4.6 represent SEM images indicating a monodispersed solid PS product with a narrow size distribution.

4.3.3. Transmission electron microscopy characterisation

PS microsphere samples were prepared by the following process; samples were washed, filtered and redispersed at 1 wt% solids using distilled water. Centrifugation was not possible due to the low density value of the hollow PS microspheres. Once dispersed, the PS samples were sonified for 90 sec to improve dispersity. The samples were further prepared by mounting a small quantity of the dispersion on a Cu grid Lacey Carbon and analysed. The structure and morphologies of PS particles were determined by TEM images.
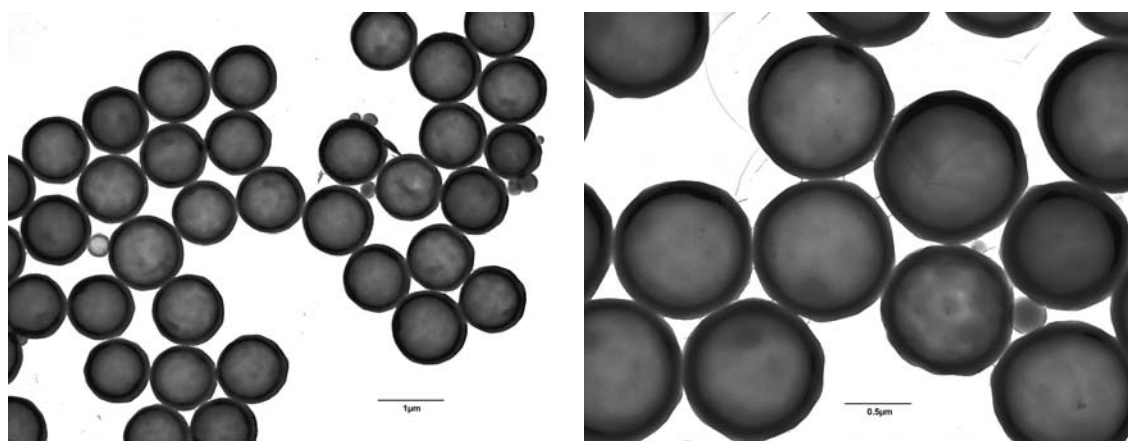
Figure 4.7 and **4.8** *TEM images of PS AF1055 microspheres.*
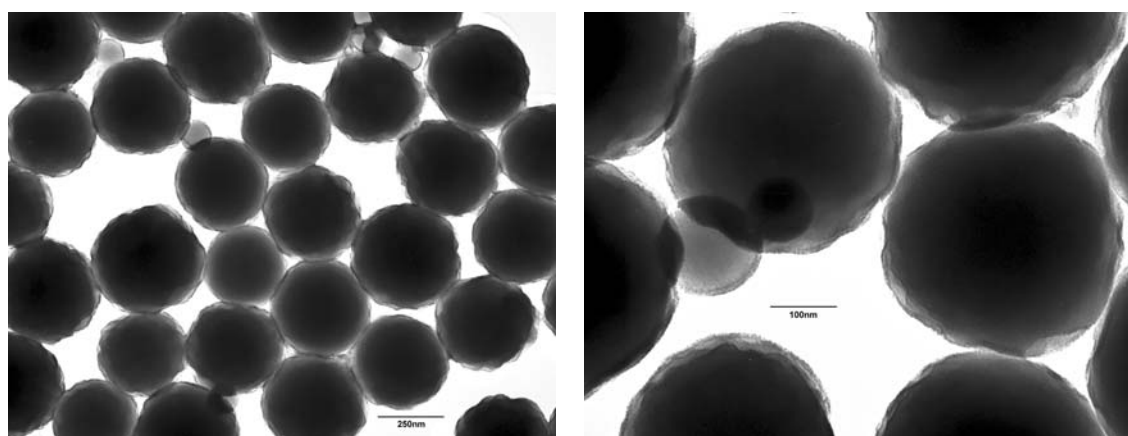
Figure 4.9 and **4.10** *TEM images of PS DPP-722E microspheres.*
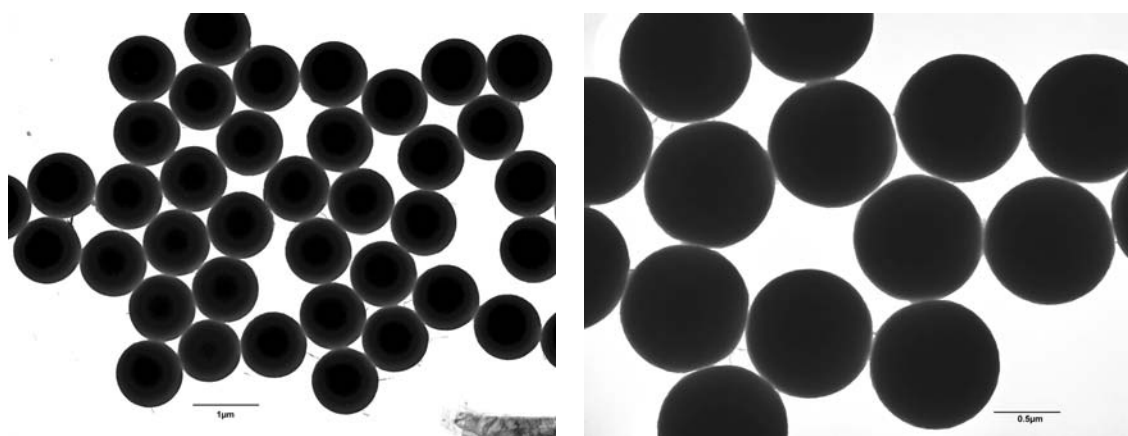
Figure 4.11 and **4.12** *TEM images of PS PPs-1.0 microspheres.*

Figures 4.7 and 4.8 show the structure of the AF1055 hollow PS microspheres, the actual shell structure is evident and measurement of the core diameter and shell thickness is possible. Figures 4.9 and 4.10 indicate a solid PS product with a soft surface structure possibly due to unreacted monomer. Figures 4.11 and 4.12 are of TEM images representing a monodispersed solid PS product with a narrow size distribution.

4.3.4. Properties of polystyrene microspheres

The pH, stability and zeta potential of each sample were measured by standard procedures using an AcoustoSizer II.v3. The 160 mL PS suspensions were agitated for 2 min in an ultrasound bath and transferred to the testing vessel, after which the zeta potential and pH measurements were recorded. The software requires specific data to calculate the zeta potential, including the mass fraction, particle density, and the dielectric constant of the particles [Greenwood, 2005]. The mass fraction of each PS microsphere sample was obtained after washing and filtering the PS, by drying the samples on a quartz dish in a Carbolite fanned convection laboratory oven at 60 ºC overnight and measuring the mass of dried samples. The density values of the PS particles were reported by the suppliers and the dielectric constant of 2.5 was considered appropriate [O'Brien, 2005]. Stability of the PS samples was assessed by measuring the zeta potential every 150 s for approximately 30 min.

Table 4.1 *Preliminary characteristics of PS microspheres.*

PS Product	Particle Structure	Concentration $(g\ L)^{-1}$	Density (g/cm^3)	pH	Zeta Potential Range (mV)
AF1055	Hollow	1.0 ± 0.1	1.02	6.6 ± 0.2	-51.1 ± 1.1
DPP-722E	Solid	1.0 ± 0.1	1.05	6.7 ± 0.2	-35.1 ± 3.2
PPs-1.0	Solid	1.0 ± 0.1	1.05	6.7 ± 0.2	-48.2 ± 3.4

Laser particle size analysis using a CILAS 1064 instrument was used to determine the particle size and the size distribution of the PS particles within a suspension using the diffraction of a laser beam based on the *Fraunhofer* theory. 150 mL PS suspensions at 1 wt% were agitated for 2 min and 10 ml samples were transferred to the testing vessel. The surface area of each PS product was reported by suppliers. The results and data are represented in Table 4.2.

Table 4.2 *Properties of PS microspheres.*

PS Product	d_{10} (μm)	d_{50} (μm)	d_{90} (μm)	d_{mean} (μm)	Surface Area (m^2/g)
AF1055	0.34	0.90	1.58	0.81 ± 0.03	7.0
DPP-722E	0.07	0.26	0.68	0.33 ± 0.02	17.0
PPs-1.0	0.53	0.64	1.27	0.90 ± 0.02	5.0
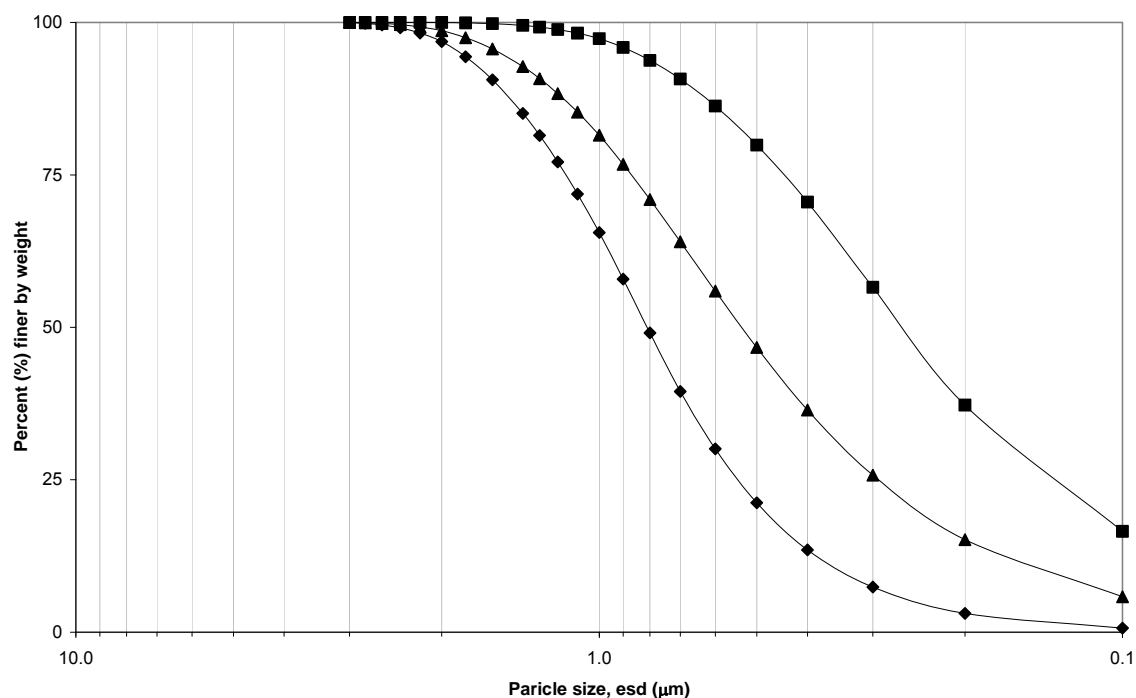
Figure 4.13 *Particle size distributions of PS microsphere samples; AF1055 (♦); PPs-1.0 (▲); and DPP-722E (■).*
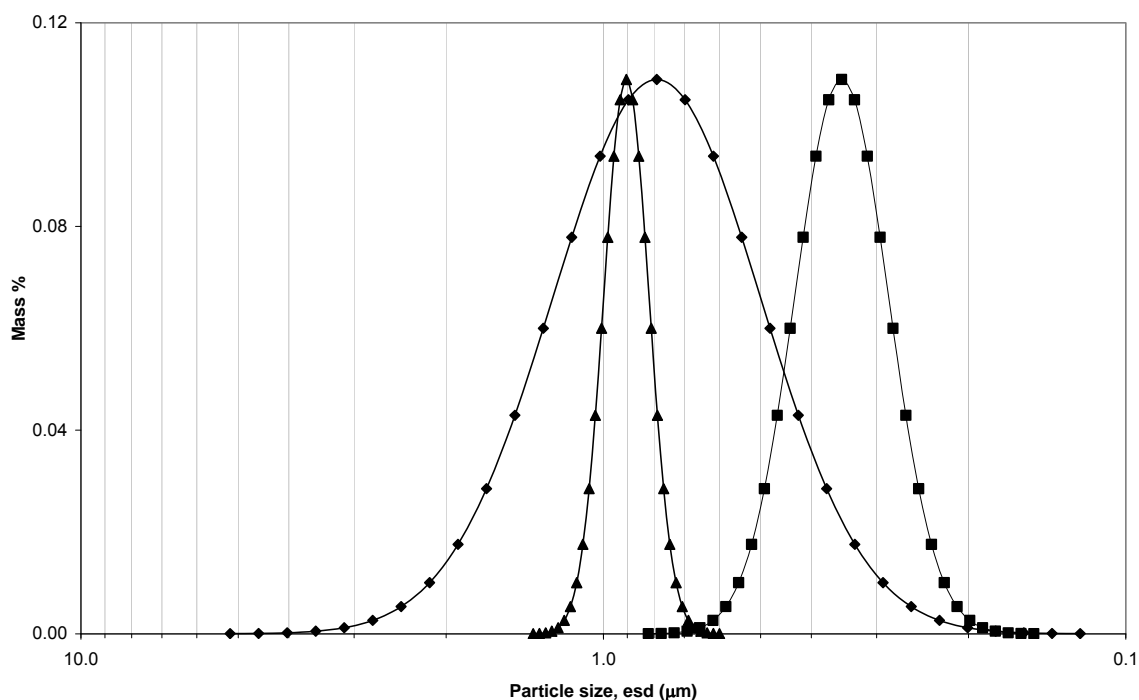
Figure 4.14 *Particle size distributions of PS microsphere samples; AF1055 (♦); PPs-1.0 (▲); and (■) DPP-722E.*

Figure 4.13 shows a cumulative size distribution with particle size expressed on a logarithm scale, measured using CILAS, whereas Figure 4.14 represents data plotted as a frequency distribution, with size expressed on a logarithmic scale measured using an AcoustoSizer, both methods show similar results. Figure 4.15 represents three distinctive particle size distributions; sample AF1055 indicates the broadest particle size distribution, while sample DPP-722E indicates a narrow size distribution.

4.3.5. Thermogravimetry analysis of polystyrene microspheres

Derivative thermogravimetry (DTG), differential scanning calorimetry (DSC), and thermogravimetry analysis (TG) are analytical techniques that explore and quantify details of thermally induced reactions in specific minerals, materials and chemicals.
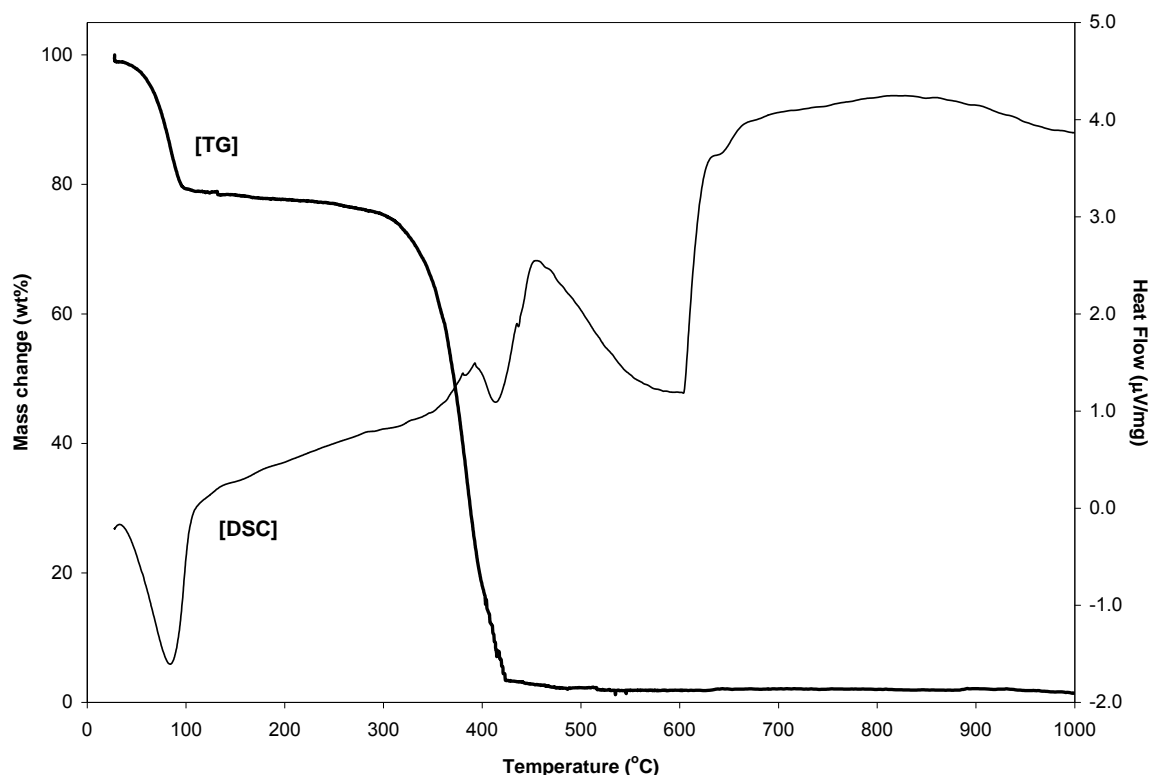
Figure 4.15 *TG/ DSC measurements of hollow PS microspheres.*

Figure 4.15 summarises TG and DSC analysis for specific reactions. The TG curve shows a 20 wt% loss at 98 °C due to the removal of residual moisture from the PS surface and within the hollow particle structure. The second significant weight loss takes place between 315 and 425 °C as the majority of the organic material is removed. The residual mass of PS remaining at 1000 °C is approximately 2 wt%. The DSC curve shows, there is a strong endothermic signal at 85 °C with removal of residual moisture from the sample. A second endothermic peak is evident at about 415 °C with the decomposition of the organic material.

A similar TG curve for the decomposition of solid PS was shown in Figure 4.16. Published data report similar results [Faridi-Majidi, et al. 2007; Huang, et al. 2004; Tang, et al. 2007; Xu, et al. 2005].
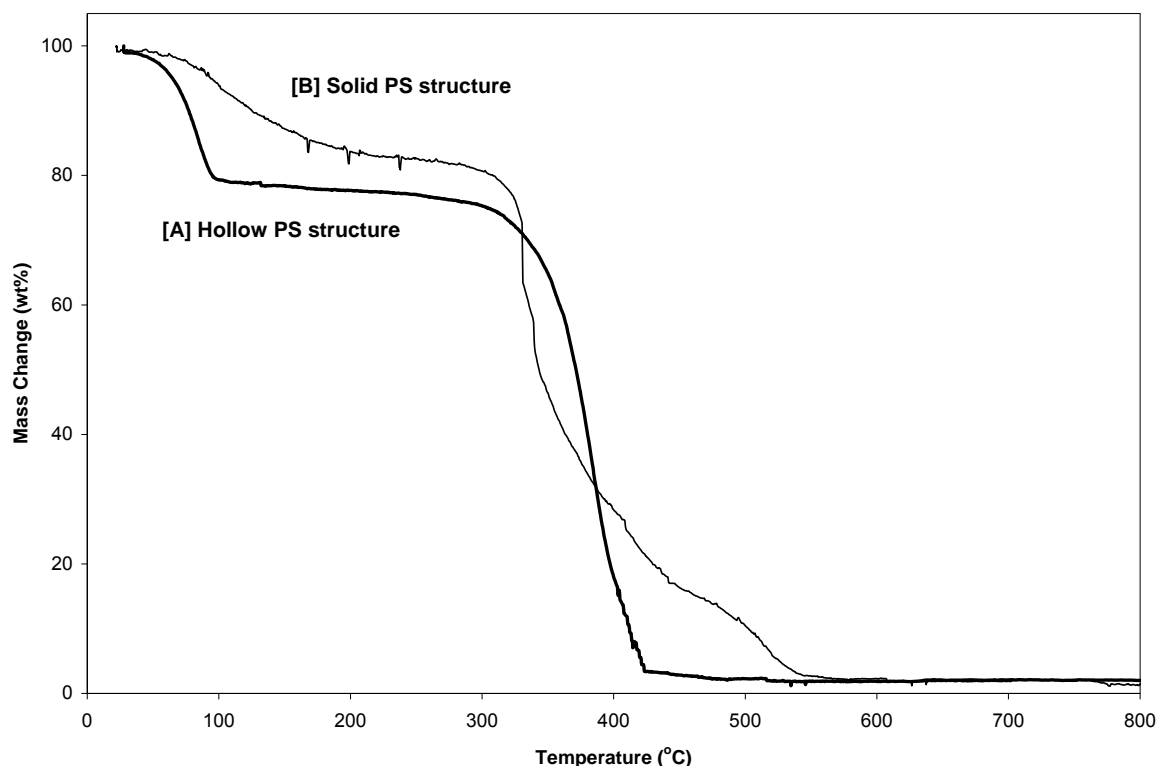
Figure 4.16 *TG measurements of hollow and solid PS microspheres.*

Up to 100 °C, a small mass loss of approximately 5% was observed during TG due to the evaporation of residual moisture in the solid PS sample [curve B]. It can be seen that solid PS has an increase in the end temperature of decomposition; the difference in rate decomposition of the PS samples was probably due to the difference in PS structures. Additionally, the decomposition for both PS products is similar. The thermal behaviour and fast rate of decomposition of the hollow PS composite provided a strong support for selection as a sacrificial core material.

4.3.6. Surface characterisation of the polystyrene surface

The X-ray photoelectron spectroscopy (XPS) spectra were obtained using a VG Escascope instrument manufactured by Fisons Instruments (UK). The instrument employed Al K_α X-

rays (energy 1486.6 eV) and atomic analyses were obtained from peak areas. All XPS experiments were conducted at the Interface Analysis Centre (University of Bristol).
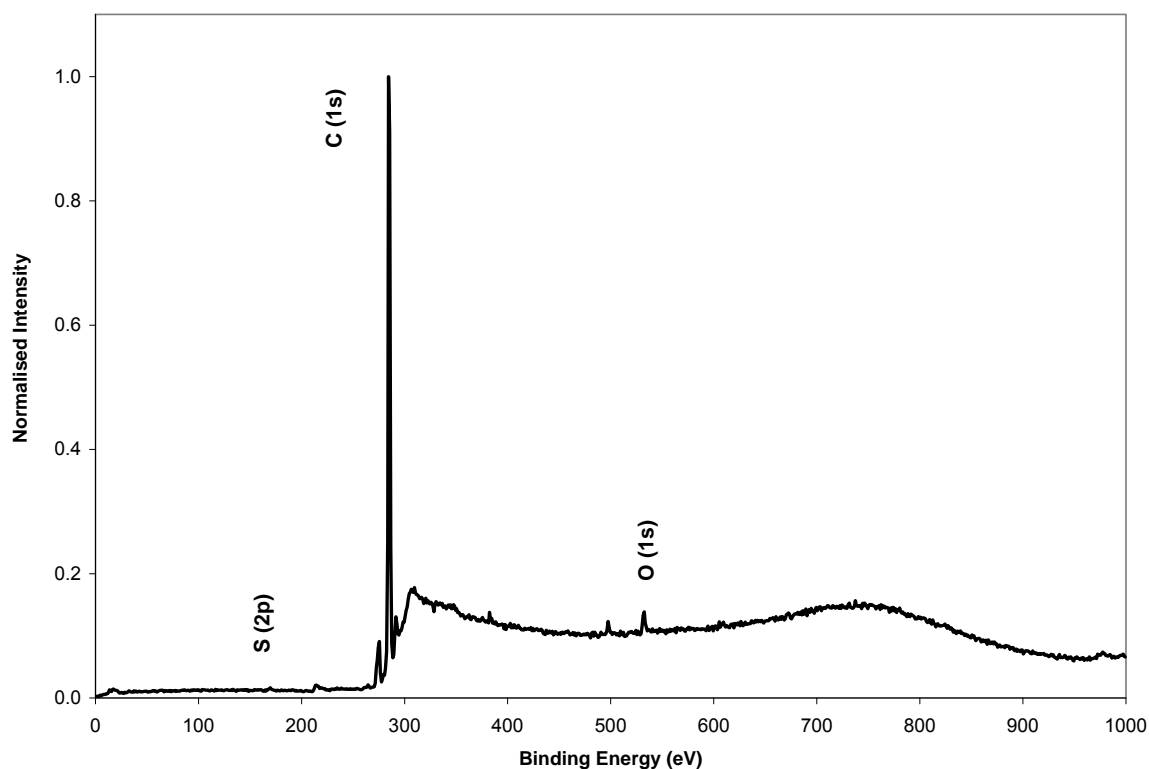
Figure 4.17 *XPS survey of the hollow PS microsphere surface.*

The XPS spectrum of PS is shown in Figure 4.17. Since, there are a large number of CH_2, COO^- and CH groups in the PS particles; the binding energy of the C_{1s} in the long alkyl chain is used as reference. The C_{1s} spectra consist of peaks at 284.8 eV (reference peak), corresponding to backbone carbon atoms ($-CH_2-$ and $-CH-$), ester methyls ($-CH_3$), ester ($-COO-$) and carboxylic ($-COO^-$) carbons. The O_{1s} spectra measured consist of peaks mainly at 532.0 eV corresponding to O_{1s} in PS. The weak peak of S_{2p} is at 168.6 eV corresponding to sulphur in polystyrene, which is in agreement with S_{2p} in S-O. The content of elements; C, O, S and Na at the surface layer of the PS were 98.2, 1.3, 0.3 and 0.2%, respectively.

4.4. *Characterisation of Kaolin Mineral*

4.4.1. Material selection

Numerous industrial minerals were characterised for potential use as a coating shell-forming material. These included various fine kaolin mineral grades -8489 (Cornwall, UK); a fine kaolin mineral classified as IK-3939 (Georgia, US); a fine kaolin mineral classified as HE471-HC (Amazon-Delta, BR); an industrial calcium carbonate mineral, grades CG-525-A and CG-526-B (Georgia, US), and a zeolite fine grade mineral (Georgia, US). All mineral samples were supplied by Imerys Minerals Ltd. Prior to characterisation all industrial minerals were washed using distilled water to remove any excess dispersant or surface contaminants, samples were pressure filtered with a Amicon 8200 stirred cell (63.5 mm grade) PBMK06210 filter membrane from Millipore (UK), dried at 60 ºC using a Carbolite laboratory bench oven.

4.4.2. Scanning electron microscopy characterisation

SEM can be used for the determination of the particle size distribution, particle shape and aggregation however, direct measurement of particle size using electron microscopy is not routinely used. SEM images in Figures 4.18 to 4.33 represent the numerous mineral samples that were available for this research thesis. Prior to SEM characterisation all industrial minerals were washed repeatedly with distilled water and centrifuged to remove electrolyte impurities and filtered. For characterisation, the mineral samples were dispersed in a methanol water solution, sonified for 90 seconds, sprayed onto clean mica sheet and gold coated using a SC-7640 Sputter Coater (Quorum Technologies Ltd., UK), plasma current operating at 5 to 10 mA, chamber pressure at $<6 \times 10^{-2}$ mbar, to help increase conductivity, reduce thermal damage and enhance secondary electron emission.
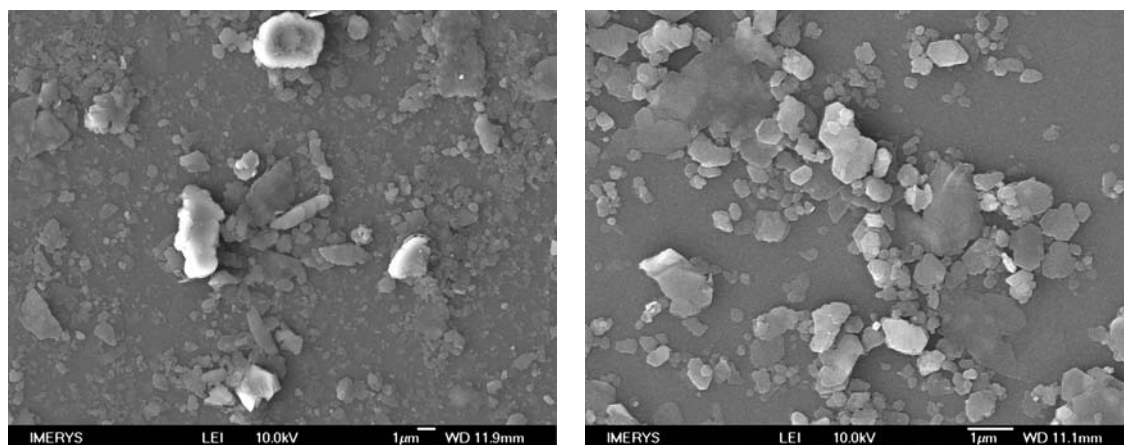
Figure 4.18 and **4.19** *SEM images of fine kaolin particles, sample K-8489.*
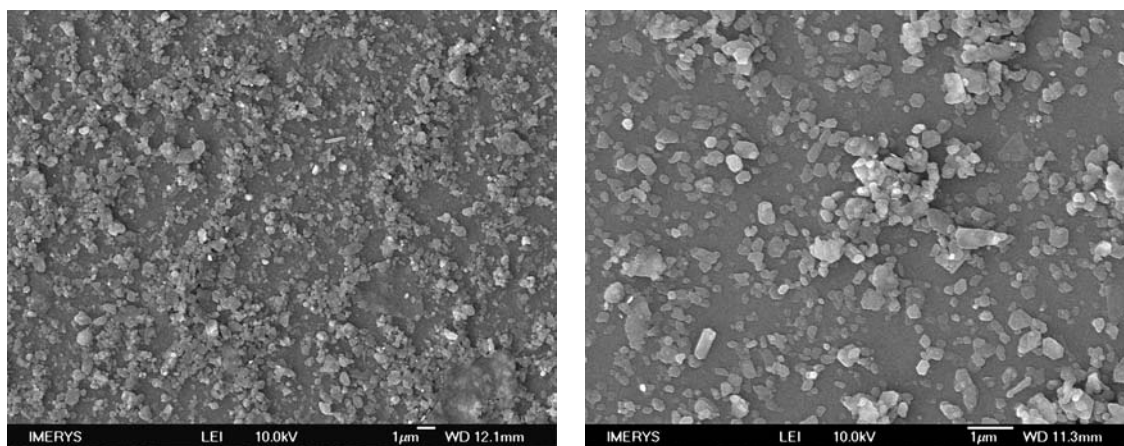
Figure 4.20 and **4.21** *SEM images of fine kaolin particles, sample FK-8489.*
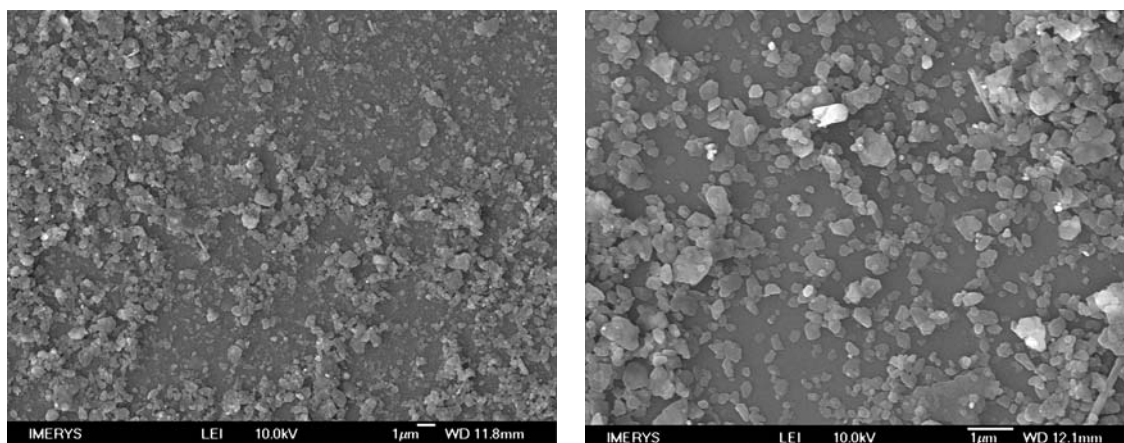
Figure 4.22 and **4.23** *SEM images of fine kaolin particles, sample UFK-8489.*
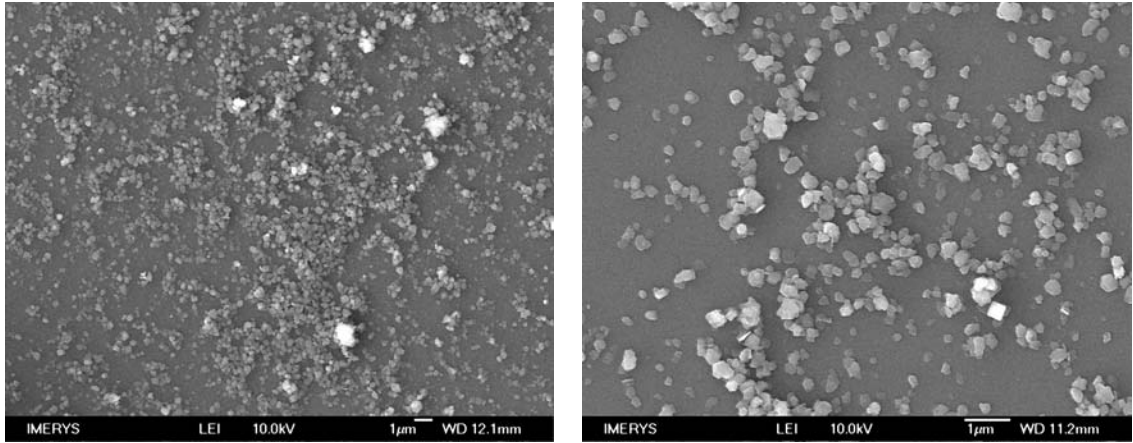
Figure 4.24 and **4.25** *SEM images of fine kaolin particles, sample PE471-HC.*
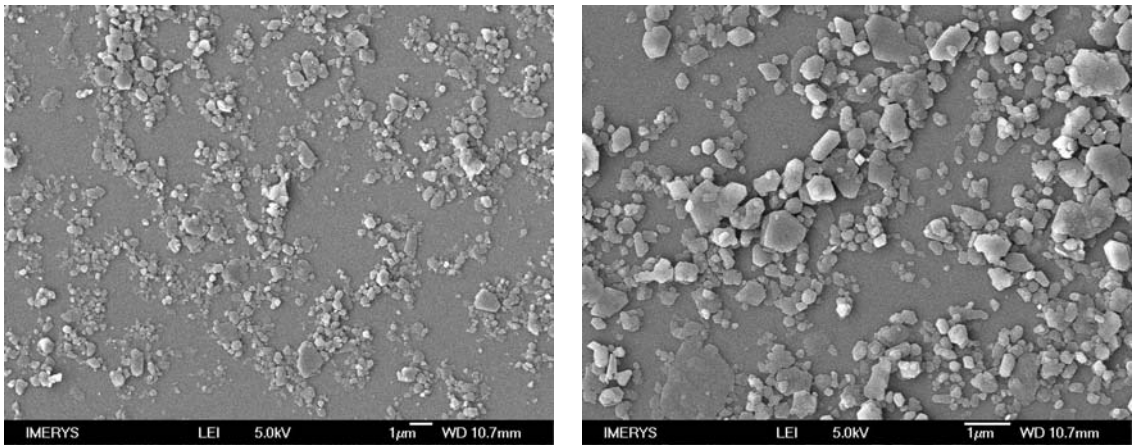
Figure 4.26 and **4.27** *SEM images of fine kaolin particles, sample IK-3939.*

The SEM investigation indicates that the majority of kaolin samples exhibit pseudohexagonal particle formation in face-to-face arrangement. The SEM images in Figures 4.18 to 4.33 represent a general distribution of the samples characterised. Figure 4.18 indicates that a number of aggregated particles in the range of 1 to 2 μm are present in the sample. Figure 4.19 represents the kaolin sample K-8489 and exhibits numerous individual large kaolin particles. Figures 4.20 to 4.23 represent two different fine grade kaolin samples from Cornwall, (FK-8489 and UFK-8489), both samples indicate a fine mean particle size and a narrow size distribution. Figures 4.24 and 4.25 represent a fine kaolin mineral sample from Brazil, classified as PE471-HC. The SEM images indicate a fine blocky kaolin particle

with a narrow size distribution. Figures 4.26 and 4.27 represent a fine kaolin mineral from Georgia, classified as IK-3939. The images indicate a wide particle size distribution, with particles ranging in general diameter size 0.1 to 0.5 μm. Caution should be taken when determining particle size using SEM images, the preparation technique results in face-to-face orientation of particles and over-lapping of particles can result in misleading particle size dimensions.
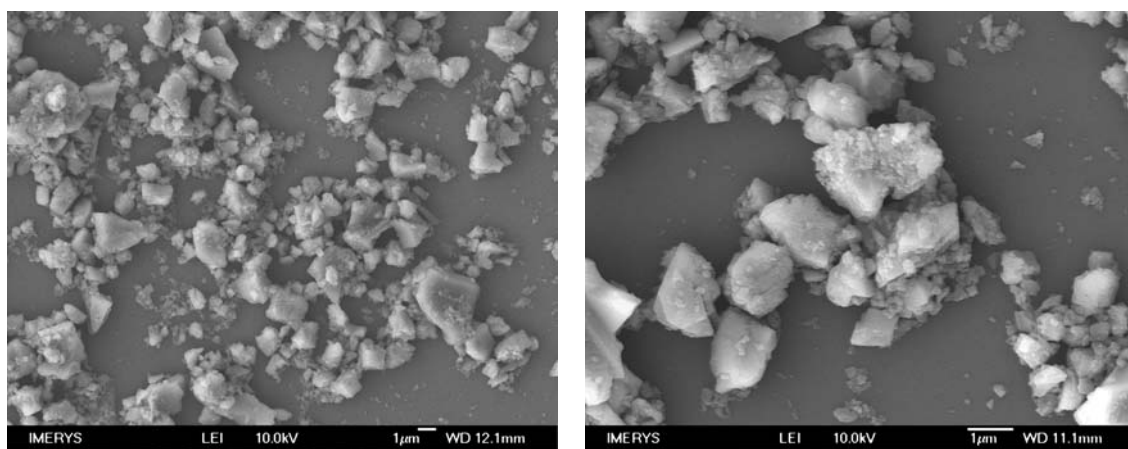
Figure 4.28 and **4.29** *SEM images of calcium carbonate particles, sample CG-525-A.*
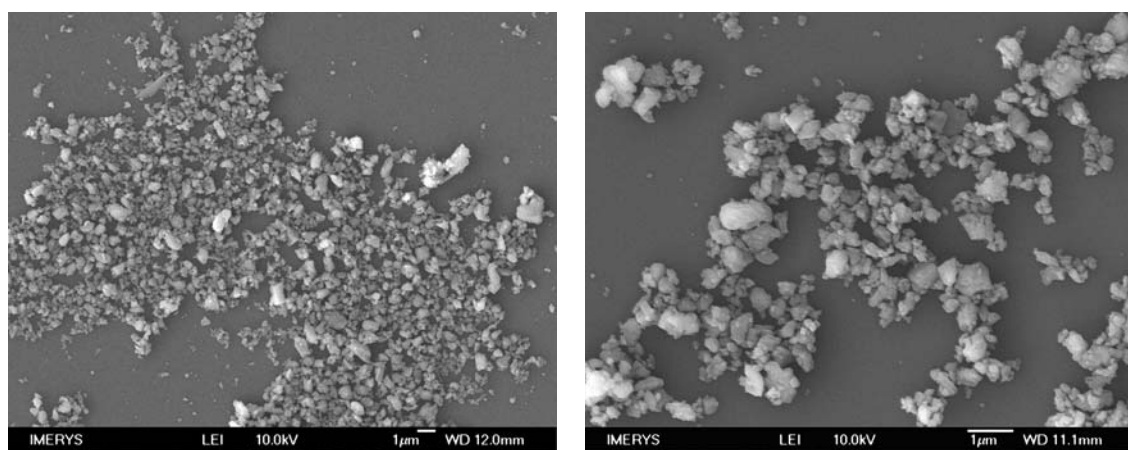
Figure 4.30 and **4.31** *SEM images of calcium carbonate particles, sample CG-526-B.*
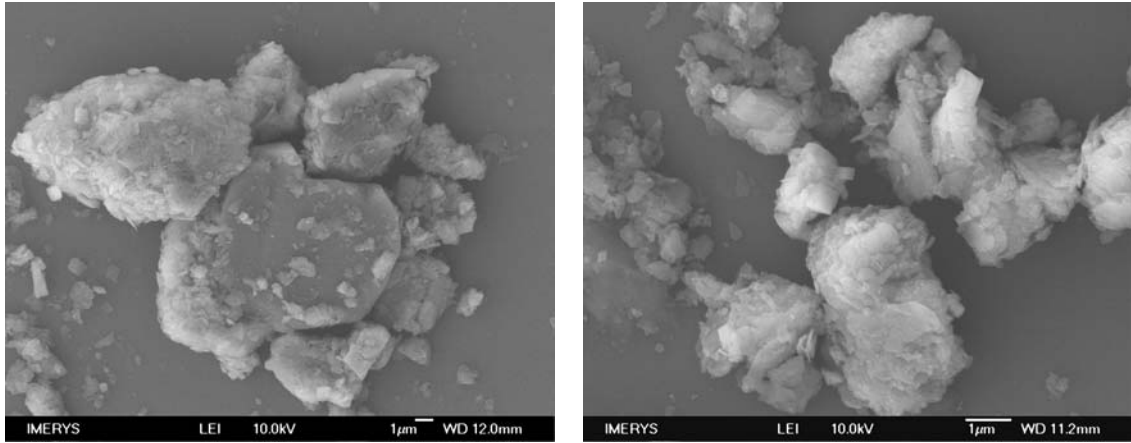
Figure 4.32 and **4.33** *SEM images of zeolite particles.*

Figures 4.28 to 4.31 represent SEM images of two calcium carbonate samples from Georgia. Figures 4.28 and 4.29 indicate a coarse calcium carbonate sample, while Figures 4.30 and 4.31 represent a calcium carbonate sample with a finer particle size. However, using sedimentation as a technique to determine particle size, the two calcium carbonate samples have a similar d_{50} as indicated in Table 4.3, the significant difference being in particle size distribution as represented in Figures 4.28 and 4.30. Figures 4.32 and 4.33 represent a zeolite sample from Georgia, fine individual zeolite particles are visible, however the SEM images indicate a coarse zeolite mineral due to particle aggregation and stacking of particle plates was evident.

4.4.3. Particle characterisation of minerals

4.4.3.1. Particle size distribution

All of the mostly widely used methods to determine particle size distribution of kaolin and other industrial minerals are based on sedimentation. Diameters obtained by sedimentation methods are expressed as equivalent spherical diameter (esd), the diameter of a sphere which settles at the same velocity as the particle (refer to Appendix B.3). Sedimentation methods

require that the mineral particle suspensions are fully deflocculated so that there are no aggregates present, and that the suspension is dilute enough to avoid hindered settling (less than 10 mass %).

The Micromeritics Sedigraph 5100 is an instrument that employs X-ray attenuation technology to determine the particle size distribution of a sample. This method has limitations, the small size and the sample used calls into question whether the precision and accuracy would hold for a truly representative sample of larger size. Also particles finer than 0.2 μm cannot be accurately determined, as Brownian motion hinders settling. However, the lower limit can be extended below 0.2 μm by increasing g, with a specially designed centrifuge. It should be recognised, that the analysis presented in Table 4.3 is based on an industrial standard technique used to determine particle size (d_{50}) and particle size distribution.

Table 4.3 *Particle size distributions of kaolin, calcium carbonate and zeolite samples.*

Mineral Sample	Classification	D_{25} (μm)	d_{30} (μm)	d_{50} (μm)	d_{70} (μm)	d_{75} (μm)
Kaolin	K-8489	0.09	0.13	0.29	0.79	0.87
Kaolin	FK-8489	0.06	0.07	0.13	0.21	0.25
Kaolin	UFK-8489	0.04	0.05	0.08	0.12	0.14
Kaolin	PE471-HC	0.04	0.09	0.15	0.24	0.27
Kaolin	IK-3939	0.05	0.09	0.18	0.26	0.29
Calcium carbonate	CG-525-A	0.18	0.22	0.43	0.86	1.04
Calcium carbonate	CG-526-B	0.32	0.35	0.44	0.57	0.61
Zeolite	Z-fine	0.81	1.09	2.97	8.12	10.82

Data represented in Table 4.3 can be used to identify a mineral that would be suitable as a shell forming material. The physical requirements of such a mineral include; (i) a mean

particle size (d_{50}) below 0.2 μm; (ii) a mineral sample with a narrow particle size distribution; and (iii) a non-contaminated or aggregated sample.

4.4.3.2. Surface area measurements

The surface area of a divided solid increases relative to volume as grain size decreases and also with increasing porosity. The area and volume of a mineral particle are related to some characteristic length (such as diameter *d*) through shape factors. The surface area and the volume of the mineral particle are related [Undabeytia, et al. 2002]. It is possible to state some specific areas [Pulobesova, et al. 1997], which can be defined per unit volume, or mass (*m*), or mole. The most convenient specific surface area is the surface area per unit mass, because it can be determined by some standardised experimental method. The surface area of the mineral samples listed in Table 4.4 were measured using a Gemini VII 2390 (Micromeritics Instruments Corp., US) instrument. Repeatability of measurements was in the range of ±3%.

Table 4.4 *Specific surface area measurements for mineral samples.*

Mineral	Classification	BET Specific Surface Area (m^2/g)
Kaolin	K-8489	26.4
Kaolin	FK-8489	28.3
Kaolin	UFK-8489	43.2
Kaolin	PE471-HC	19.1
Kaolin	IK-3939	22.0
Calcium carbonate	CG-525-A	10.3
Calcium carbonate	CG-526-B	27.4
Zeolite	Z-F	9.9

At this stage of the characterisation process a number of minerals including the calcium carbonate and zeolite samples can be excluded from further characterisation because of their large mean particle size (d_{50}) >0.3 μm and therefore are considered undesirable at the moment as a coating and shell-forming mineral.

4.4.3.3.   Shape factor measurements

Stoke's Law makes the assumption that particles are roughly spherical, this is clearly not true for kaolin as their particle shape is in form of a plate structure due to a result of cleavage planes between the silica and alumina sheets. Kaolin has a disc like morphology, which can be ascribed an 'aspect ratio' or 'new shape factor' defined as the plate diameter divided by the plate thickness or height. For kaolins, a new shape factor of <10 relates to a 'blocky' mineral, a new shape factor of 15 refers to a platy mineral; and a value >30 defines a 'very platy' kaolin mineral structure. With such high new shape factor values, the esd can give a misleading impression of the size of the particle. The important dimension is the plate dimension diameter, which can be as much as 5 times larger than the esd.

Measurements of shape factor were made using a stop flow conductivity measurement instrument, known as Particle Assessment by Natural Alignment and Conductivity Effect Analysis, (PANACE), developed by Imerys Minerals Ltd. In Table 4.5, the shape factors are reported for the kaolin samples, the highest factors are for the fine kaolin samples (K-8489, FK-8489) from Cornwall, while the lowest shape factor was for the Brazilian kaolin (PE471-HC) is from the Amazon-Delta.

Table 4.5 *Further characteristic properties of kaolin samples.*

Mineral	Deposit	Classification	New Shape Factor	
Kaolin	Cornwall (UK)	K-8489	47.4	*Very platy*
Kaolin	Cornwall (UK)	FK-8489	28.3	*Very platy*
Kaolin	Cornwall (UK)	UFK-8489	7.2	*Blocky*
Kaolin	Amazon-Delta (BR)	PE471-HC	4.0	*Blocky*
Kaolin	Georgia (US)	IK-3939	13.9	*Platy*

A fine kaolin mineral with a blocky characteristic feature and a narrow particle size distribution may form a shell with weak bonds between kaolin plates and the microsphere structure may collapse during calcination as volatile material is removed. An over-lap configuration of kaolin plates with a slightly larger d_{50} may result in a stronger shell arrangement and improve the integrity of the structure.

4.4.3.4.   *Mineral brightness measurements*

The brightness of a kaolin mineral is controlled by two factors, the proportion of incident light scattered (the scattering coefficient, *S*) and the amount absorbed by coloured impurities (the absorption coefficient, *K*). Coloured impurities which affect the absorption coefficient of kaolins are largely a result of Fe^{3+} containing phases. These occur in the lattice, where substitution of octahedral Al^{3+} by Fe^{3+} occurs and results in electron transfer effects which absorb strongly in the near UV-vis violet part of the spectrum (these give kaolin their yellow shade). On the particle surface, there are discrete areas of FeOOH and Fe_2O_3. These are removed by leaching the kaolin with a reducing agent, sodium dithionite (hydrosulphite) ($Na_2S_2O_3$). Iron containing impurities can be removed from kaolin using high intensity magnetic separation. Organic impurities can also affect the colour of kaolins. Measurements

of the mineral brightness were done using a diffuse reflectance spectrophotometer, Elrepho 450X instrument (Datacolor, US).

Table 4.6 *Brightness and Yellowness values (%) for kaolin samples.*

Mineral	Classification	ISO Brightness	Yellowness	Fe_2O_3 (wt%)	TiO_2 (wt%)
Kaolin (UK)	K-8489	87.8	4.3	0.62	0.79
Kaolin (UK)	FK-8489	87.2	5.9	1.09	1.42
Kaolin (UK)	UFK-8489	82.9	6.9	1.08	1.41
Kaolin (BRZ)	PE471-HC	86.5	5.8	0.31	1.04
Kaolin (US)	IK-3939	88.5	4.6	0.54	0.42

Typical ISO brightness ranges for common commercial kaolin minerals can be classified as: 80 to 90% for US kaolins; 85 to 90% for BRZ kaolins; and 77 to 89% for UK kaolins. From Table 4.6, the lowest brightness value was assigned to the kaolin mineral UFK-8489; the mineral has the highest value for yellowness and has the highest coloured impurities. The chemical compositions of the minerals in Table 4.6 are taken from X-ray fluorescence data represented in Table 4.10.

4.4.4. Electrokinetic potential measurements of kaolin

Kaolin with an ideal formula of $Al_4Si_4O_{10}(OH)_8$ exhibits very little substitution in the structural lattice resulting in a minimal layer charge and low base exchange capacity. The layered structure of kaolin suggests that the octahedral basal (face) surface of a particle should consist of closely-packed OH groups. The tetrahedral basal surface would be expected to resemble that of silica and consist of SiO (siloxane) groups. Hence, in theory, the two faces display different chemistries. However, it is believed that the surface of kaolin is

covered with an adsorbed layer of silicic acid $[SiO_x(OH)_{4-2}]_n$ from natural leaching of sand, and therefore both surfaces are likely to consist of silanol groups [Wypych, et al. 2004]. The faces therefore carry an overall negative charge as pH is raised due to ionisation of silanol groups:

$$\left(Si-OH\right)+OH^- \rightarrow SiO^- + H_2O \qquad [4.1]$$

At the crystal edges, bonds are broken and both aluminium oxide and silanol groups are exposed, which are pH sensitive. The net charge is believed to vary in both size and magnitude with pH. Under acidic conditions (<pH 4) aluminium species carry a positive charge:

$$\left(Al-OH\right)+H^+ \rightarrow Al-OH_2^+ \qquad [4.2]$$

Above approximately pH 8, the aluminium groups are expected to deprotonate:

$$\left(Al-OH\right)+OH^- \rightarrow Al-O^- + H_2O \qquad [4.3]$$

Hence, the edges of the kaolinite crystal are positively charged under acidic conditions. Since the faces carry a constant negative charge, at acid pH the particles are in a state of edge-to-face flocculation. The zero point of charge of the edges has been measured for a range of kaolinite and is typically found at pH 7.3 [Rand, et al. 1977; Herrington, et al. 1992]. At above pH 9, deflocculation is observed as the particles now carry a negative charge over all surfaces, resulting in mutual repulsion and therefore a state of natural deflocculation. The surface characteristics of kaolin is further discussed in Appendix B.

Information about the electrokinetic properties of kaolin dispersions were obtained by using an Acoustosizer instrument based on electroacoustics. All kaolin samples were washed, filtered and dried at 60 ºC to remove any contaminates or excess dispersant from the mineral surface. The 160 mL kaolin suspensions at 10 mass % were agitated for 2 min in an ultrasound bath. The mass fraction of each kaolin sample were obtained after washing and filtering, by drying the samples on a quartz dish in a Carbolite fanned convection laboratory oven at 60 ºC overnight and measuring the mass of dried samples. The density of the particles was taken to be 2.65 g cm^{-3} and the dielectric constant 11.8 [Greenwood, 2005]. Stability of the kaolin samples were also assessed by measuring the zeta potential and pH every approximately 5 min for 120 min. The mean zeta potential and pH of these samples are given in Table 4.7.

Table 4.7 *Stability of kaolin suspensions in distilled water.*

Mineral	Classification	Content (mass %)	Temp. (ºC)	pH	Zeta Potential (mV)
Kaolin (UK)	UF-8489	10.0 ± 0.1	26.3 ± 1.2	7.5 ± 0.4	-45.0 ± 1.0
Kaolin (BRZ)	PE471-HC	10.0 ± 0.1	24.5 ± 1.1	7.6 ± 0.1	-59.8 ± 0.7
Kaolin (US)	IK-3939	10.0 ± 0.1	24.9 ± 1.2	7.3 ± 0.1	-50.9 ± 0.3

Experiments were also conducted to determine the isoelectric point of the kaolin sample FK-8489 in distilled water, the pH of the suspension was adjusted to 9.5 with 1 M-NaOH and an automatic titration was performed of the suspension back to pH 2.5 in steps of 0.5 pH units using 1 M-HCl solution. The pH values represent an average value recorded by the Acoustosizer II. The zeta potential versus pH for the kaolin FK-8489 sample reflecting the ionisation of various surface groups is shown in Figure 4.34. Similar pH titration experiments were conducted using kaolin samples form Georgia and the Amazon-Delta, data is presented in Figure 4.35.
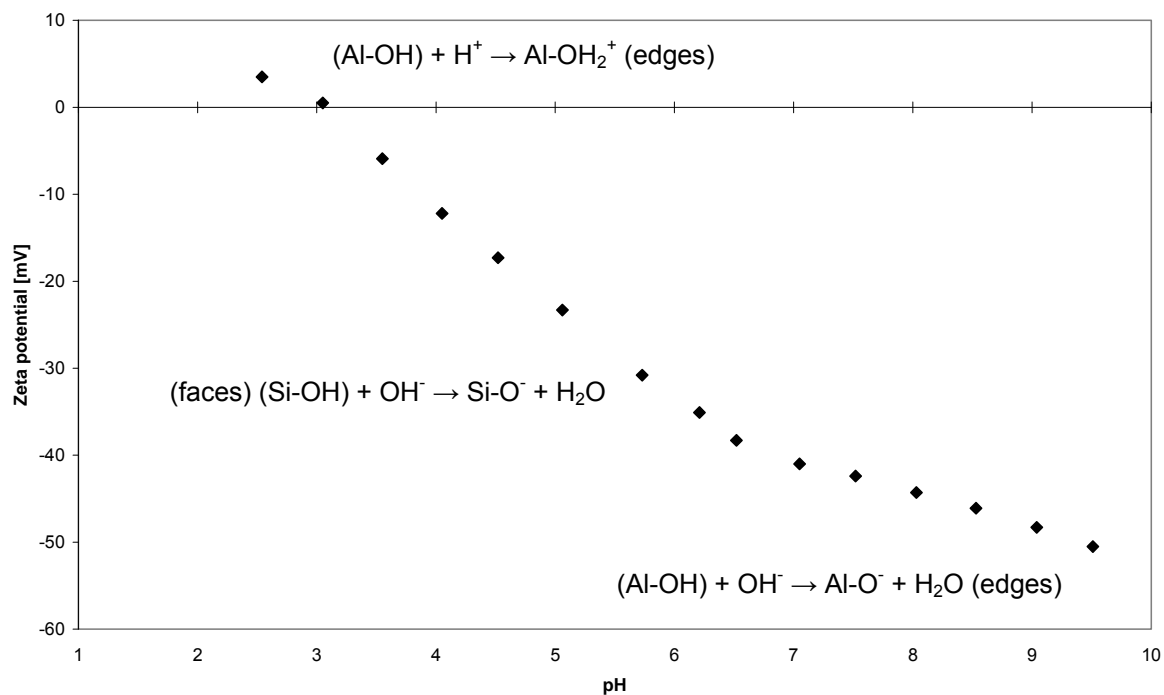
Figure 4.34 *Zeta potential of the kaolin mineral FK-8489 as a function of pH.*
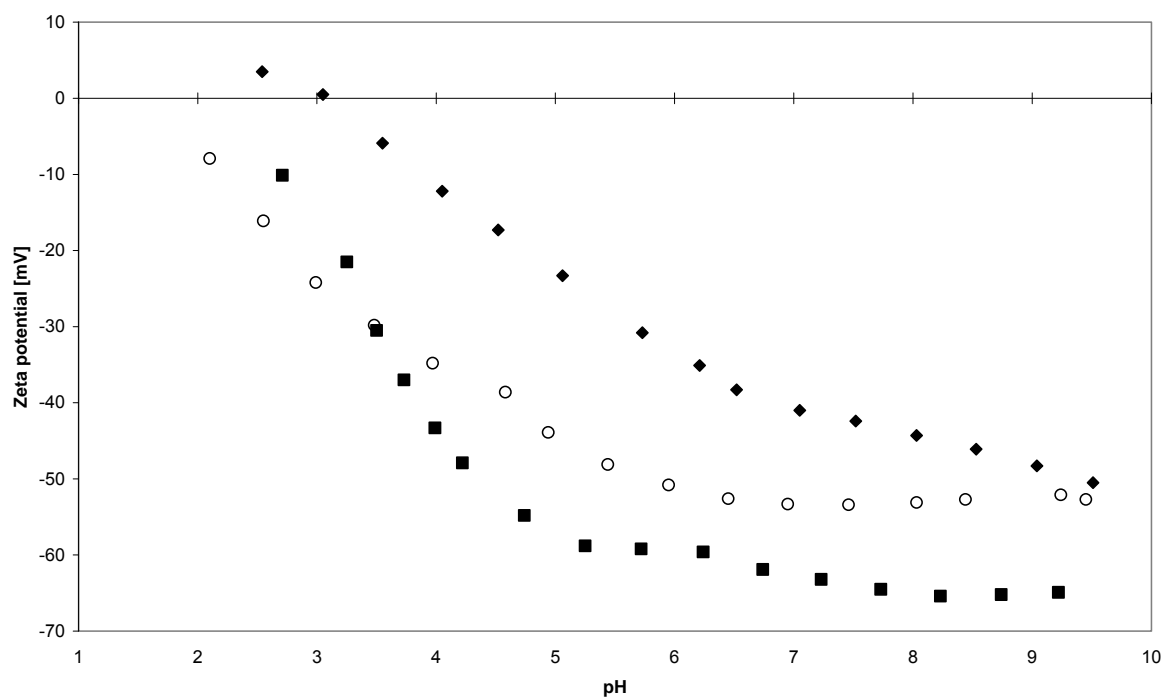
Figure 4.35 *Zeta potential of kaolin minerals: FK-8489 (♦) IK-3939 (○) and PE471-HC (■) as a function of pH.*

The zeta potential of the kaolins are shown as average plots as a function of pH, but there were significantly different zeta potentials among the three kaolin samples when measured under the same conditions. In the broad range of pH, the zeta potential of the Cornish kaolin was less negative than that of the US and Brazilian kaolins. The isoelectric point (iep) for the Cornish kaolin was at pH 3.1. An isoelectric point was not determined for the samples from the United States or Brazil but could be extrapolated from the data in Figure 4.35. Variance in the zeta potential was dependent on the solution pH, ionic strength of the suspension and surface properties of kaolin particles. The ionic strength of the suspension was expected to be closely dependent on the contents of the mineral phases, the crystal imperfections, chemical composition, crystal forms and crystal surface structure. Higher negative zeta potentials values sometimes related to a higher level of exchangeable or soluble ferrous ions in clay [Hu, et al. 2003]. Kaolinite clays from various sources were also reported to display different electrokinetic behaviour despite having similar mineral composition [Teh, et al. 2009].

Most significantly, it has been determined through electroacoustic experiments that the kaolin samples characterised exhibit a sufficient zeta potential to remain stable between pH 6 and 8. A zeta potential greater than -30 mV (>pH 6) should improve plate confirmation at the charged cationic PS surface during the shell formation process. With a zero point of charge of the edges for kaolin at approximately pH 7.3 it was expected that the kaolin plates will form a face-to-face orientation as a shell structure is formed.

4.4.5. Composition and chemical analysis

XRD analyses were conducted using a PANalytical X'Pert Pro MRD powder diffractometer, solid state detector and Cu radiation source (λCu $K\alpha$ = 1,54060 Å) at 40 kV and 40 mA were

utilised. Back-filled kaolin pressed sample mounts were made to minimise transparency and sample displacement effects. The powder diffraction patterns with a 0.05º precision of d-spacing measurements were conducted from $10º ≤ 2θ ≤ 60º$ with a fixed time of 10 seconds for each step. A total of 3236 intensity data points were obtained. Quantification of elements was accomplished by analysing fused kaolin powder discs with a PANalytical Magix-Pro X-ray fluorescence spectrometer.
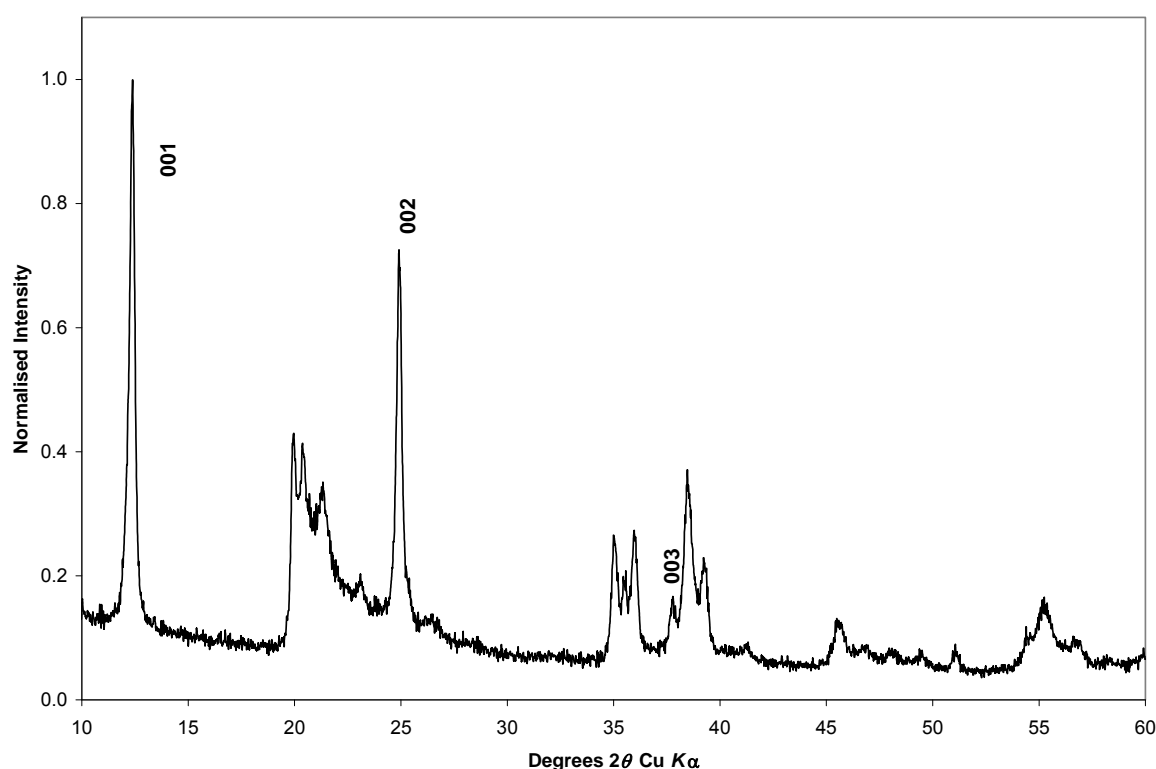
Figure 4.36 *A characteristic diffraction pattern of a kaolin mineral sample (FK-8489).*

The X-ray powder diffraction pattern of a fine kaolin mineral sample (FK-8489) is shown in Figure 4.36. The X-ray diffraction reflections are sharp and distinct and the peaks are characteristic of a pure kaolin mineral [Hanawalt, et al. 1936; Hu, et al. 2003; Chen et al. 2004; Maia, et al. 2007; Hosseini et al. 2011]. Broadening of the peaks can be contributed to crystal size and is representative of the thickness of the lamellar particles, this is evident

between 21 and 22º in 2θ. No sample contamination was evident in the diffraction pattern. As the diffraction pattern showed no identifiable peaks either at 20.7º (100) or at 26.6º (011) in 2θ which would have revealed the presence of α-quartz with the *d* values of 4.27 Å and 3.342 Å respectively. It can be concluded from the XRD diffraction pattern in Figure 4.36 and the d-spacing data in Table 4.8 that the mineral sample FK-8489 is typical of a well ordered kaolinite. The resolution between closely spaced reflections in an X-ray pattern can also be used as an indicator of the relative degree of crystallinity. The closely spaced reflections of kaolin with a considerably high degree of crystallinity are also well resolved and exemplified by the reflections at 20.0º (020) and 37.8º (003) in 2θ as exhibited in Figure 4.36. These closely spaced reflections become indistinct with lower degree of crystallinity.

The XRD technique can be used to determine the order-disorder arrangement for the kaolinite sample FK-8489. The basal spacing indicates a measure for the relative degree of crystallinity of the kaolin sample, in Table 4.8 the basal spacing values are compared to two well-ordered kaolinite samples from Cornwall [Brindley, et al. 1946] and from Georgia [Takahashi, 1958]. Alternatively, the order − disorder arrangement of kaolinite crystals can be evaluated according to the Hinckley Index [Aparicio, et al. 2004; Costa, et al. 2009], determined from the $\left(1\bar{1}0\right)$ and $\left(11\bar{1}\right)$ reflections of the X-ray diffraction pattern in Figure 4.36. Kaolinite structural orders can range from poorly ordered (HI=0.33) to well ordered (HI=1.10), the Hinckley index for the kaolin sample (FK-8489) was determined to be 0.81 compared with a reported Hinckley index of 0.88 for a kaolin mineral from Cornwall [Aparicio, et al. 2004]. Therefore, the structural order of the kaolin sample FK-8489 can be considered to be reasonably well ordered.

Diffraction patterns for the other kaolin mineral samples were not required for characterisation purposes as the purity of the kaolin samples were at least 99 % as represented in Table 4.8 and no notable variance was expected.

Table 4.8 *Degree of crystallinty for kaolin sample FK-8489.*

Cornwall (UK)	Georgia (US)	Kaolin mineral (FK-8489, UK)			
d-spacing	*d-spacing*	*Intensity*	*2 θ*	*hkl*	*d-spacing*
7.15	7.15	1.00	12.4	001	7.14
4.45	4.45	0.42	20.0	020	4.44
4.35	4.36	0.41	20.4	$1\bar{1}0$	4.35
4.17	4.17	0.34	21.3	$11\bar{1}$	4.17
4.12	4.13	0.29	21.5	$1\bar{1}\bar{1}$	4.12
3.56	3.57	0.72	24.9	002	3.57
2.55	2.56	0.26	35.0	$20\bar{1}$, $1\bar{3}0$, 130	2.56
2.52	2.53	0.21	35.6	$13\bar{1}$, $1\bar{1}2$	2.52
2.48	2.49	0.27	36.0	$1\bar{3}1$, 200, 112	2.49
2.37	2.38	0.16	37.8	003	2.37
2.33	2.34	0.37	38.5	$20\bar{2}$, $1\bar{3}1$, $11\bar{3}$	2.34
2.28	2.29	0.23	39.2	$1\bar{1}\bar{3}$, 131	2.29

The slight variance in d-spacing values between the kaolin sample FK-8489 and the reference material in Table 4.8 may be attributed to the following reasons; (i) the presence of water between neighbouring unit layers in the kaolin mineral with lower degree of crystallinity; and/or (ii) the disorder in the unit layer and looseness of the stacking variations of the kaolin unit layers which should be greater in the specimens with lower degree of crystallinity [Takahashi, 1958]. However, this would be indicated by a much greater variance in the d-spacing values of the fine kaolin sample compared with the reference minerals. XRD

reflections for kaolinite (001) samples have been reported indicating a low degree of crystallinity with d-spacing values as low as 7.11 Å and as high as 7.24 Å [Castellano, et al. 2010]. Classification and purity of the powder samples by XRD are shown in Table 4.9. All mineral samples showed high concentrations of kaolinite (at least 99 mass %); trace elements of mica are identified in the K-8489 and UFK-8489 samples. A trace element of anatase was evident in the PE471-HC sample.

Table 4.9 *Composition and purity of kaolin minerals (mass %) by XRD.*

Mineral Composition	Kaolin K-8489	Kaolin FK-8489	Kaolin UFK-8489	Kaolin PE471-HC	Kaolin IK-3939	Reference kaolin
Kaolinite	100	100	99	100	100	88
Mica	<0.1	0	1	0	0	7
Anatase	0	0	0	<0.5	0	1
Quartz	0	0	0	0	0	0
Feldspar	0	0	0	0	0	2
Tourmaline	0	0	0	0	0	0
Albite	0	0	0	0	0	0
Montmorillonite	0	0	0	0	0	2

The composition of a reference kaolin (Cornwall) is shown in Table 4.9, the major components of the kaolinite sample were SiO_2 (46.8 mass %) and Al_2O_3 (37.8 mass %). Table 4.10 lists the content values of Fe_2O_3 and TiO_2 which are considered important as high concentrations of these elements can affect the colour hence the commercial value of the minerals. High concentrations of the alkali elements can also affect the fluxing and melting temperatures of the kaolin minerals.

Table 4.10 *Composition of kaolin minerals (mass %) by XRF.*

Mineral Sample	Al_2O_3	SiO_2	K_2O	Fe_2O_3	TiO_2	CaO	MgO	Na_2O	LOI
Kaolin K-8489 (UK)	38.46	45.97	0.12	0.62	0.79	0.07	<0.01	0.25	13.80
Kaolin FK-8489 (UK)	37.81	45.78	0.11	1.09	1.42	0.08	<0.01	0.02	13.75
Kaolin UFK-8489 (UK)	39.40	42.80	0.11	1.08	1.41	0.21	0.01	0.39	14.62
Kaolin PE471-HC (BR)	40.40	43.40	<0.01	0.31	1.04	0.07	<0.01	0.26	14.63
Kaolin IK-3939 (US)	40.10	44.60	0.07	0.54	0.42	0.08	0.03	0.27	13.93
Average	39.23	44.51	0.08	0.73	1.02	0.10	0.01	0.24	14.15
Reference Mineral									
Kaolin Cornwall (UK)	37.79	46.77	1.49	0.56	0.02	0.13	0.24	0.05	12.79
Kaolin Georgia (BR)	38.16	44.72	0.06	1.03	1.33	0.04	0.02	0.05	13.65
Kaolin Amazon (US)	38.38	45.30	0.04	0.30	1.44	0.05	0.25	0.27	13.97
Average	38.11	45.60	0.53	0.63	0.93	0.07	0.17	0.12	13.47
Kaolin Theoretic	39.50	46.54	-	-	-	-	-	-	13.96

The composition of the reference kaolin minerals listed in Table 4.10 has been reported elsewhere [Costa, et al. 2009]. Chemical compositions obtained by XRF analysis of the different kaolins are apparently similar, with SiO_2/Al_2O_3 ratios ranging from 1.07 (PE471-HC) to 1.21 (FK-8489) compared to the theoretical value of 1.179 [Grim, 1968]. SiO_2/Al_2O_3 ratios ranging from 1.10 to 1.69 have been reported for various kaolin minerals by Costa, et al. [2009]. The Fe_2O_3 values in Table 4.10 range from 0.31 to 1.09 wt%, which suggests that iron, could be a part of the kaolinite structure, since iron oxy-hydroxides (hematite, maghemite or goethite) were not observed. TiO_2 content varies between 0.42 and 1.42 wt%, an average content ranging from 1.3 to 1.9 wt% has been reported respectively [Costa, et al. 2010; Schroeder, et al. 2003]. Conversely, TiO_2 content in kaolin as low as 0.02 and as high as 3.27 wt% have been reported [Prasad, et al. 1991; Costa, et al. 2010; Schroeder, et al. 2003].

Fe_2O_3 and TiO_2 concentrations above 2 wt% are considered to be detrimental to the brightness of kaolin [Sousa, 2000]. The Fe_2O_3 and TiO_2 concentrations reported in Table 4.10 are both in the same value order, which may indicate that they are part of the crystalline structure of kaolinite. However, it is not known how significant the classification (primary or secondary deposits) influences the composition of the kaolin sample under review.

4.4.6. Characterisation of the kaolin surface

X-ray Photoelectron Spectroscopy (XPS) is a surface characterisation technique which is capable of removing core level electrons from the surface of a sample by X-ray. XPS allows the identification of elements present in the first atomic layer under the surface [Durand, et al. 1998]. Ejected electrons from various elements have characteristic kinetic energies. The energies of the photoelectrons are usually measured by a hemispherical energy analyser system, which uses a channeltron to detect electrons at different energies. The process is conducted under ultra high vacuum conditions, at this pressure few of the electrons collide with any other particle on their way to the energy analyser. Only electrons ejected from atoms close to the surface are less likely to escape the solid without colliding with another particle [Hallam, 2007]. All XPS experiments were conducted at the Interface Analysis Centre (University of Bristol, UK).

Kaolin samples were washed, filtered and dried at 60 ºC overnight using a Carbolite laboratory oven prior to surface analysis. The powder samples were pressed onto adhesive conductive carbon tape. Analysis was performed using a VG Escascope system with a base pressure of $2x10^{-10}$ mbar. The spectra were collected using Al $K\alpha$ radiation (1486.6 eV), the maximum X-ray power used was 280 W. The binding energies are accurate to ±0.2 eV.
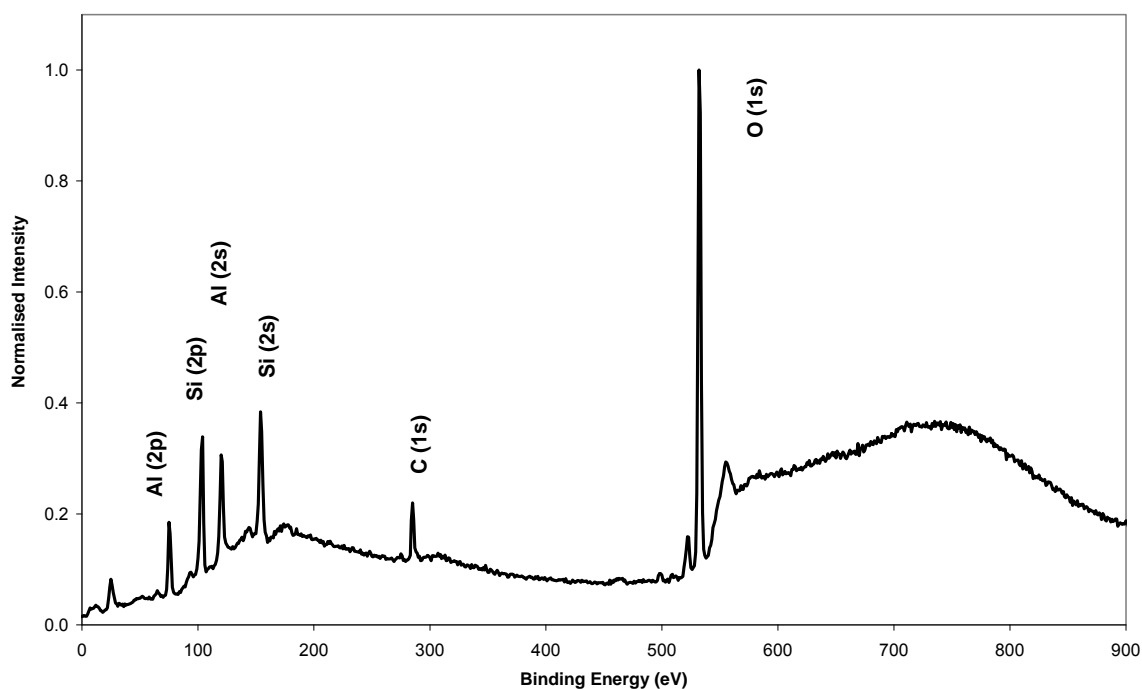
Figure 4.37 *XPS survey of the kaolin mineral surface (FK-8489).*

Figure 4.37 shows a wide scan XPS spectrum of the kaolin sample (FK-8489). The C1s peak, which is due to adventitious carbon on the sample, was used as the binding energy reference (284.8 eV) for the spectrum. The remarkable aspect of the spectrum is the purity, since only Al, Si and O signatures are present in Figure 4.37. The purity of the sample can be compared to XPS spectrums that have identified Na and Ca in measurable quantities in kaolin [Kim, et al. 1995]. Mg, Ca and Na impurities have also been reported [Barr, et al. 1995]. Otherwise, the Al, Si and O peak binding energies of the kaolin sample as shown in Figure 4.37 and Table 4.11 are in agreement with the results published [Wagnes, et al. 1982; Kim, et al. 1995; Barr, et al. 1995; Lombardi, et al. 2002].

106

Table 4.11 *Photoelectron binding energies for kaolin.*

		Photoelectron binding energies (eV)		
Mineral	**Classification**	*Si(2p)*	*Al(2p)*	*O(1s)*
Kaolin	FK-8489 (UK)	103.1	75.3	532.2
Kaolin	[Castle, et al. 1979; 1980]	105.2	73.4	533.3
Kaolin	[Wagner, et al. 1982]	102.8	74.5	532.0
Kaolin	[Barr, et al. 1995]	102.5	74.3	531.5
Kaolin	[Sánchez, et al. 1999]	n.r	74.8	532.0
Kaolin	[Lu, et al. 2009]	102.8	74.6	531.9

4.4.7. Thermogravimetry analysis of kaolin

Heating an industrial mineral at a steady rate can produce chemical changes, degradation and physical changes. Thermal analysis is used to complement the X-ray characterisation techniques and scanning electron microscopy, the technique can be used to define the temperature and energy changes associated with a structure change and provide a characteristic 'fingerprint' trace of a specific mineral. The various techniques of thermal analysis measure one or more physical properties of a sample as a function of temperature, change in mass, and energy flow. A variety of clay minerals contain various amounts of kaolinite (86 to 100%) as a mineral phase and by heating, transformation of kaolinite to metakaolin and mullite can be observed. This transformation can be identified by two endothermic peaks, firstly due to the removal of physically absorbed moisture. Secondly, due to the loss of structural water and an endothermic relating to the crystallisation of the Al-Si spinel phase, these observations are well known [Chakraborty, 2003].

A Netzsch STA-449EP thermogravimetric instrument has been used to determine the mass change and calorimetric effects simultaneously of kaolin. All mineral samples were received

in powder form, and were washed, filtered and dried at 60 ºC, samples were kept in a dehumidifier for approximately 12 hr prior to heating. A 35 mg representative sample was taken from each mineral and placed in an alumina crucible within the furnace system of the thermogravimetric instrument. Care was taken to ensure the mineral samples were of similar weight to ensure reproducible results. The reference material was α-Al_2O_3, the rate of heating was 10 ºC per min and the sensitivity was ± 50 µV. Reproducibility was in the range of ±5%.
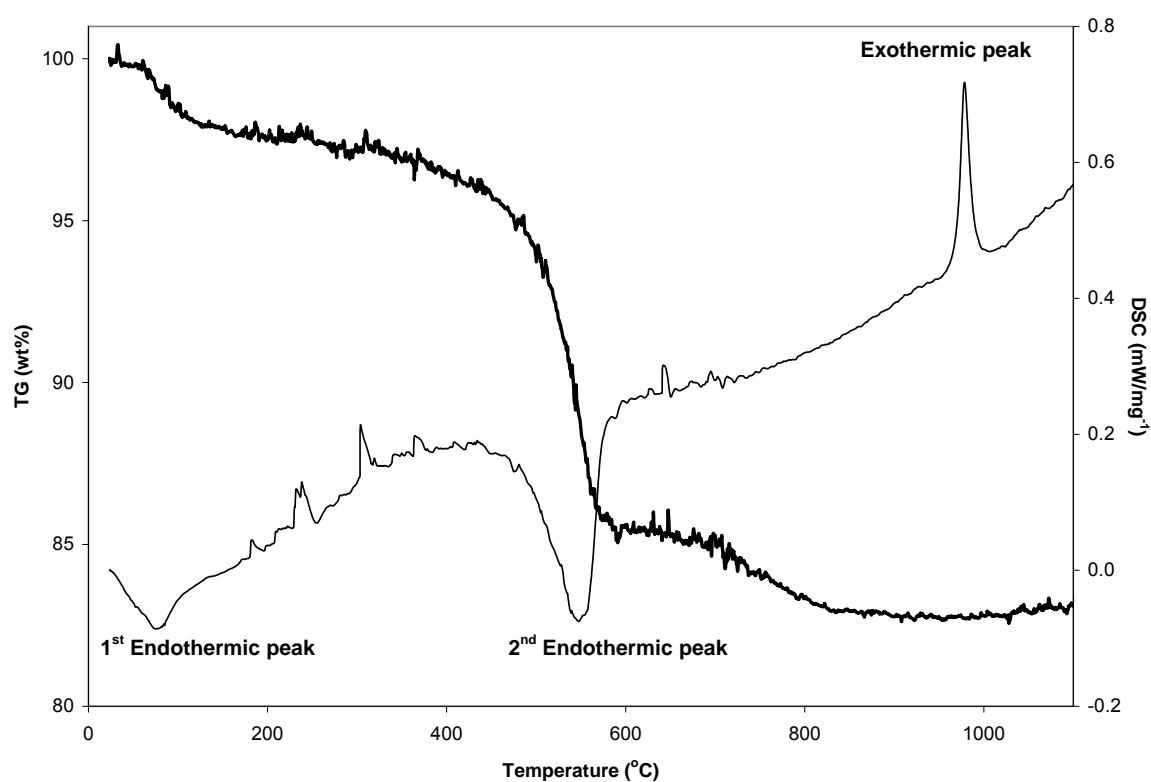
Figure 4.38 *Thermal decomposition of fine kaolin sample FK-8489.*

The TG (bold line) and DSC curves shown in Figure 4.38 represent the thermal degradation of kaolin and was representative of all the kaolin samples under review. From room temperature to 100 ºC adsorbed water is lost from the surface of the kaolin sample; from 400 to 575 ºC organic material is removed from the sample. The endothermic peak at 547 ºC represents the dehydroxylation of the kaolin sample forming metakaolin.

Dehydroxylation results in the collapse of the kaolinite crystal structure. At approximately 978 ºC the transformation of metakaolin to the spinel phase takes place as identified by the exothermic peak. The total decomposition of kaolin is finished around the temperature 1200 ºC by formation of cristobalite [Dohnalová, 2008], this exothermic effect was not detected within this thermal decomposition study or shown in Figure 4.38 as the measurement temperature interval was 23 to 1100 ºC. The residual mass of kaolin after heating to 1000 ºC is 82.9%. The loss is in agreement with values reported in the literature [Castelein, et al. 2001; Heide, et al. 2006; Castellano, et al. 2010; Zhou, et al. 2010] and is attributed to loss of adsorbed water identified by the first endothermic peak centred at 76 ºC and mainly to the endothermic dehydroxylation of kaolin. In the thermogravimetric studies a discrepancy between thermogravimetric weight loss was frequently reported. The variance is often attributed to numerous factors, such as degree of structural ordering, particle size and shape, adsorbed ions and substituted ions, and instrumental conditions [Heide, et al. 2006]. This was evident in Table 4.12, where loss on ignition (LOI) values at 1000 ºC for various kaolin samples are compared, LOI values at 1000 ºC from X-ray diffraction analysis are also stated.

Table 4.12 *Thermogravimetric analysis of kaolin mineral samples.*

Mineral Sample	1st Endothermic peak (ºC)	2nd Endothermic peak (ºC)	Exothermic peak (ºC)	LOI (TGA)	LOI (XRF)
Kaolin K-8489	77	569	981	15.28	13.80
Kaolin FK-8489	76	547	978	17.10	13.75
Kaolin UFK-8489	79	571	999	13.28	14.62
Kaolin PE471-HC	70	537	998	13.56	14.63
Kaolin IK-3939	69	551	992	13.99	13.93
Average	74 ± 4	555 ± 15	990 ± 10	14.64 ± 1.57	14.15 ± 0.44

4.5. *Conclusions*

The hollow PS microsphere product was considered the most favourable. After cleaning the hollow PS remained stable in suspension at pH 6.6 ±0.2 with a zeta potential measured at -51.1 ±1.1 mV. Its particle size (d_{50}) was measured to be 0.90 μm, which represents a sufficient diameter enabling fine mineral particles to form a shell structure. If the actual particle size of the PS template were smaller in diameter a smooth shell formation by finer particles may not be possible. No actual size ratio between the template material and the shell forming material was evident in the published literature.

The thermal degradation of the PS template material was important, excess amounts of volatile material from a solid PS product may be detrimental during the calcination process; removal of polystyrene from within a shell formation may result in numerous capillaries and collapse of the microsphere shell. From thermogravimetric analysis the difference in decomposition of hollow and solid PS microspheres has been reviewed, a fast rate of decomposition of the hollow PS composite may be more favourable when fabricating hollow microspheres. Complete removal of the template material at the lowest possible temperature may be significant when considering end use applications. XPS identified elements at the hollow PS microsphere surface which in turn determined the quality of the PS product. It is also important to note that the product was batch manufactured by Rohm & Haas, therefore, each batch, approximately 18 L samples at approximately 26 wt% solids, were characterised to ensure condition and quality.

The kaolin mineral classified as FK-8489 was considered the most appropriate shell forming material. The fine mineral was chosen based on a number of important characteristic

properties including: particle size, size distribution and particle shape. Further analyses of the kaolin sample confirmed the mineral surface characteristics and composition.

The average particle size (d_{50}) of the fine kaolin mineral was 0.13 μm, and showed no form of aggregation or contamination. The kaolin mineral exhibited a platy structure which may be advantageous when forming a shell structure on a template core material. A platy kaolin structure is expected to form a face-to-face orientation of particles and form an over-lapping of particles within the shell structure resulting in a stronger shell arrangement. However, a blocky kaolin mineral is likely to form a shell with weak bonds between the kaolin plates and hence the microsphere shell structure is likely to collapse during calcination as the volatile material is removed.

The stability and the zeta potential of the mineral particles in suspension were determined, at pH 7.5 ±0.4 the zeta potential was measured at -45.0 ±1.0 mV.

All mineral samples showed high concentrations of kaolinite (at least 99 mass %); in the kaolin mineral grades -8489, no trace elements of quartz or anatase were evident. The composition ratio SiO_2/Al_2O_3 of FK-8489 was calculated to be 1.21 which is in good agreement with the theoretical value of 1.179 [Grim, 1968]. The Fe_2O_3 and TiO_2 concentrations for the fine kaolin sample are both in the same value order, 1.09 and 1.42 wt% respectively, which may indicate that they are part of the crystalline structure of kaolinite. Concentrations above 2 wt% are considered to be detrimental to the brightness of kaolin. The brightness value for kaolin sample FK-8489 was measured at 87.2%.

The XRD technique was also used to determine the order – disorder arrangement for the kaolinite sample FK-8489, the basal spacing values indicated a measure for the relative degree of crystallinity of the sample. The sample FK-8489 can be considered to be reasonably well-ordered when compared to two well-ordered reference kaolinite samples [Brindley, et al. 1946; Takahashi, et al. 1958]. Finally, XPS identified elements present in the kaolin sample. Since only Al, Si and O signatures were present in the XPS spectrum and Mg, Ca and Na impurities were not identified in measurable quantities the purity of the kaolin sample is confirmed.

During the early stages of characterisation a number of mineral samples including; calcium carbonate and zeolite were removed from the selection process due to their large particle size and evidence of aggregation within the sample. Two fine kaolin mineral samples including; UFK-8489 and PE471-HC both measured low shape factors indicating a blocky particle plate structure which is likely to be detrimental when forming a shell structure. A possible economic alternative to a polystyrene template material could also be considered in the future. Alternatives may include; yeast cells [Weinzierl, et al. 2009], carbon black [Li, et al. 2010], natural beeswax [Wang, et al. 2008], biological gelatin [Huang, et al. 2008], and/or gas bubbles [Hadiko, et al. 2005; Yan, et al. 2007].

The next chapter will describe the experimental process to modify the anionic PS template material resulting in a cationic charged surface. Adsorption isotherm experiments will try to quantify the amount of cationic charged PE required to modify the polystyrene surface. Further experiments will determine the amount of kaolin required to form a shell structure on the hollow PS microspheres.

4.6. *References*

Adamczyk, Z., Warszyński, P. *Adv. Colloid Sci.* 63 (**1996**) 41.

Alkan, M., Demirbas, Ö., Duğan, M. *Microporous Mesoporous Mater.* 83 (**2005**) 51.

Aparicio, P., Bernal, J.L.P., Galán, E., Bello, M.A. *Clay Miner.* 39 (**2004**) 75.

Barr, T.L., Seal, S. He, H., Klinowski, J. *Vacuum* 46 (**1995**) 1391.

Bates, T.F. *Am. Mineral.* 44 (**1959**) 78.

Bolland, M.D.A., Posner, A.M., Quirk, J.P. *Clays Clay Miner.* 28 (**1980**) 412.

Brady, P.V., Cygan, R.T., Nagy, K.L. *J. Colloid Interface Sci.* 18 (**1996**) 356.

Brindley, G.W., Robinson, K. *Trans. Farad. Soc.* 42 (**1946**) 198.

Brunauer, S., Emmett, P.H., Teller, E. *J. Am. Chem. Soc.* 60 (**1938**) 309.

Brunauer, S., Emmett, P.H., Teller, E. *J. Am. Chem. Soc.* 62 (**1940**) 1723.

Cases, J.M., Touret-Poinsignon, C., Vestier, D. *C.R. Acad. Sci., Paris, Ser. C* 272 (**1971**) 728.

Castelein, O., Soulestin, B., Bonnet, J.P., Blanchart, P. *Ceram. Int.* 27 (**2001**) 517.

Castle, J.E., Hazell, L.B., West, R.H. *J. Electron Spectrosc. Relat. Phenom.* 16 (**1979**) 97.

Castle, J.E., West, R.H. *J. Electron Spectrosc. Relat. Phenom.* 18 (**1980**) 355.

Castelano, M., Turturro, A., Riani, P., Montanari, T., Finocchio, E., Ramis, G., Busca, G. *Appl. Clay Sci.* 48 (**2010**) 446.

Chakraborty, A.k. *Thermochim. Acta* 398 (**2003**) 203.

Chassagne, C., Mietta, F., Winterwerp, J.C. *J. Colloid Interface Sci.* 336 (**2009**) 352.

Chen, Y.F., Wang, M.C., Hon, M.H. *J. Eur. Ceram. Soc.* 24 (**2004**) 2389.

Costa, M.L., Sousa, D.J.L., Angélica, R.S. *J. South Amer. Earth Sci.* 27 (**2009**) 219.

Cunha, F.O., Torem, M.C., D'Abreu, J.C. *Miner. Eng.* 19 (**2006**) 1464.

Das, K.K. *Interfacial Electrokinetcs and Electrophoresis.* Surfactant Science Series, vol. 106, Delgado, A.V., (eds.), Dekker, New York, **2002**.

Dohnalová, Ž., Svoboda, L., Šulcová, P. *J. Min. Metall. Sect. B* 44 (**2008**) 63.

Durand, C., Beccat, P. *J. Pet. Sci. Eng.* 20 (**1998**) 259.

Durant, Y.G., Sundberg, D.C. *Macromolecules* 29 (**1996**) 8466.

Durant, Y.G., Sundberg, D.C. *ACS Symposium Series* 663 (**1997a**) 44.

Durant, Y.G., Sundberg, E.J., Sundberg, D.C. *Macromolecules* 30 (**1997b**) 1028.

Faridi-Majidi, R., Sharifi-Sanjani, N. *J. Magn. Magn. Mater.* 31 (**2007**) 55.

Ferris, A.P., Jepson, W.B., *J. Colloid Interface Sci.* 51 (**1975**) 245.

Fitch, R.M., McCarvill, W.T. *J. Colloid Interface Sci.* 66 (**1978**) 20.

Ford, J.R., Morfesis, A.A., Rowell, R.L. *J. Colloid Interface Sci.* 105 (**1985**) 516.

Gates, L.F., Webb, T.W. (ECC Inter., Ltd.) **1992**. Aspect ratio measurements. United States patent application 5128606.

Goodwin, J.W., Hearn, J., Ho, C.C., Ottewill, R.H. *Br. Polym. J.* 5 (**1973**) 347.

Goodwin, J.W., Hearn, J., Ho, C.C., Ottewill, R.H. *Colloid Polymer. Sci.* 252 (**1974**) 464.

Greenwood, R., Bergström, L. *Eur. Ceram. Soc.* 17 (**1997**) 537.

Greenwood, R. *Adv. Colloid Interface Sci.* 106 (**2003**) 55.

Greenwood, R. *Personal communication*, University of Birmingham, May (**2005**).

Greenwood, R., Lapčíková, B., Surýnek, M., Waters, K., Lapčík, Jr., L. *Chem. Pap.* 61 (**2007**) 83.

Grim, R.E. *J. Geol.* 50 (**1942**) 225.

Hadiko, G., Han, Y.S., Fuji, M., Takahashi, M. *Mater. Lett.* 59 (**2005**) 2519.

Hallam, K. *Personal communication*, University of Bristol, February (**2007**).

Hanawalt, J.D., Rinn, H.W. *Ind. Eng. Chem. Anal. Ed.* 8 (**1936**) 244.

Harvey, C.C., Murray, H.H. *Appl. Clay Sci.* 11 (**1997**) 285.

Hauser, E.A. *Chem. Rev.* 37 (**1945**) 287.

Hearn, J., Wilkinson, M.C., Goodall, A.R. *Adv. Colloid Interface Sci.* 14 (**1981**) 173.

Heide, K,. Földvari, M. *Thermochim. Acta* 446 (**2006**) 106.

Herrington, T.M., Clarke, A.Q., Watts, J.C. *Colloids Surf.* 68 (**1992**) 161.

Hosseini, S.A., Niaei, A., Salari, D. *J. Phys. Chem.* 1 (**2011**) 23.

Hu, Y., Liu, X. *Miner. Eng.* 16 (**2003**) 1279.

Huang, Z., Tang, F. *Colloid Polym. Sci.* 282 (**2004**) 1198.

Huang, C.C., Liu, T.Y., Su, C.H., Lo, Y.W., Chen, J.H., Yeh, C.S. *Chem. Mater.* 20 (**2008**) 3840.

Hul, van den, H.J., Vanderhoff, J.W. *J. Colloid Interface Sci.* 28 (**1968**) 336.

Hunter, R.J. *Zeta Potential in Colloid Science: Principles and Applications*, Academic Press, London, **1988**.

Hunter, R.J. *Colloids Surf. A* 141 (**1998**) 37.

Hunter, R.J., Alexander, A.E. *J. Colloid Sci.* 18 (**1963**) 820.

Hunter, R.J., Alexander, A.E. *J. Colloid Sci.* 18 (**1963b**) 833.

James, A.E., Williams, D.J.A. *Adv. Colloid Interface Sci.* 17 (**1982**) 219.

Jayasuriya, R.M., El-Aasser, M.S., Vanderhoff, J.W. *J. Polym. Sci. Part A: Polym. Sci.* 23 (**1985**) 2819.

Jepson, W.B., *Philos. Trans. R. Soc. Lon. A* 311 (**1984**) 411.

Johnson, S.B., Franks, G.V., Scales, P.J., Boger, D.V., Healy, T.W. *Int. J. Miner. Process.* 58 (**2000**) 267.

Kawaguchi, H. *Prog. Polym. Sci.* 25 (**2000**) 1171.

Kesler, T.L. *Econ. Geol.* 51 (**1956**) 541.

Khan, A.K., Ray, B.C. Dolui, S.K. *Prog. Org. Coat.* 62 (**2008**) 65.

Kim, K.S., Winograd, N. *Chem. Phys. Lett.* 30 (**1975**) 91.

Kim, J.H., Chainey, M., El-Aasser, M.S., Vanderhoff, J.W. *J. Polym. Sci. Part A: Polym. Chem.* 27 (**1989**) 3187.

Kim, Y., Cygan, R.T., Kirkpatrick, R.J. *Geochim. Cosmochim. Acta* 60 (**1996**) 1041.

Kim, S.D., Boczar, E.M., Klien, A., Sperling, L.H. *Langmuir* 16 (**2000**) 1279.

Kosmulski, M., Dunkhin, A.S., Priester, T., Rosenholm, J.B. *J. Colloid Interface Sci.* 263 (**2003**) 152.

Kowalski, A., Vogel, M., Blankenship, R.M. (Rohm and Haas Co.) **1984a**. Sequential heteropolymer dispersion and a particulate material obtainable therefrom, useful in coating composition as a thickening and/or opacifying agent. United States patent application 4427836.

Kowalski, A., Vogel, M., Blankenship, R.M. (Rohm and Haas Co.) **1984b**. Sequential heteropolymer dispersion and a particulate material obtainable therefrom, useful in coating composition as a thickening and/or opacifying agent. United States patent application 4468498.

Kowalski, A., Vogel, M. (Rohm and Haas Co.) **1984c**. Sequential heteropolymer dispersion and a particulate material obtainable therefrom, useful in coating composition as an opacifying agent. United States patent application 4469825.

Lascelles, S.F., Malet, F., Mayada, R., Billingham, N.C., Armes, S.P. *Macromolecules* 32 (**1999**) 2462.

Lee, D.I. *Prog. Org. Coat.* 45 (**2002**) 341.

Li, H., Wei, S., Qing, C., Yang, J. *J. Colloid Interface Sci.* 258 (**2003**) 40.

Li, X., Chen, F., Lu, X., Ni, C., Zhan, C., Chen, Z. *J. Porous Mater.* 17 (**2010**) 297.

Lombardi, K.C., Guimarães, J.L., Mangrich, A.S., Mattoso, N., Abbate, M., Schreiner, W.H., Wypych, F. *J. Braz. Chem. Soc.* 13 (**2002**) 270.

Lu, Z., Ren, M., Yin, H., Wang, A., Ge, C., Zhang, Y., Yu, L., Jiang, T. *Powder Technol.* 196 (**2009**) 122.

Luckham, P.F., Rossi, S. *Adv. Colloid Interface Sci.* 82 (**1999**) 43.

Lyklema, J. *Colloidal Dispersion,* Goodwin, J.W., (eds.), Dorset Press, Amsterdam, **1982**.

Madaeni, S.S., Ghanbarian, M. *Polym. Int.* 49 (**2000**) 1356.

Maia, A.A.B., Saldanha, E., Angélica, R.S., Souza, C.A.G., Neves, R.F. *Cerâmica* 53 (**2007**) 319.

Manning, D.A.C., Hill, P.I., Howe, J.H. *J. Geol. Soc. London* 153 (**1996**) 827.

McCarvill, W.T., Fitch, R.M. *J. Colloid Interface Sci.* 64 (**1978**) 403.

McDonald, C.J., Devon, M.J. *Adv. Colloid Interface Sci.* 99 (**2002**) 181.

Michaels, A.S., Bolger, J.C. *Ind. Eng. Chem.* 3 (**1964**) 14.

Michaels, A.S., Morelos, O. *Ind. Eng. Chem.* 47 (**1955**) 1801.

Mpofu, P., Addai-Mensah, J., Ralston, J. *J. Colloid Interface Sci.* 261 (**2003**) 349.

Murray, H.H. *Inter. J. Mineral Process.* 7 (**1980**) 263.

Murray, H.H. *Appl. Clay Sci.* 5 (**1991**) 379.

Murray, H.H. *Appl. Clay Sci.* 17 (**2000**) 207.

Nicole, S.K., Hunter, R.J. *Aust. J. Chem.* 23 (**1970**) 2177.

O'Brien, R.W. *Personal communication*, Colloidal Dynamics/University of Sydney, June (**2005**).

Ohshima, G., Kondo, T. *J. Colloid Interface Sci.* 130 (**1989**) 281.

Okubo, M., Ikegami, K., Yamamoto, Y. *Colloid Polym. Sci.* 267 (**1989**) 193.

Okubo, M., Ahmad, H. *J. Polymer Sci. A* 34 (**1995**) 3147.

Okubo, M., Izumi, J. *Colloid Surf., A* 153 (**1999**) 297.

Olphen, van, H. *J. Colloid Sci.* 19 (**1964**) 313.

Ottewill, R.H., Shaw, J.N. *Kolloid Z. Z. Polym.* 215 (**1967a**) 161.

Ottewill, R.H., Shaw, J.N. *Kolloid Z. Z. Polym.* 218 (**1967b**) 34.

Parks, G.A. *Chem. Rev.* 65 (**1965**) 177.

Prasad, M.S., Reid, K.J., Murray, H.H. *Appl. Clay Sci.* 6 (**1991**) 87.

Pulobesova, T., Rytwo, G., Nir, S., Serban, C., Margulies, L. *Clays Clay Miner.* 45 (**1997**) 834.

Sánchez, R.M.T., Basaldella, E.I., Marco, J.F. *J. Colloid Interface Sci.* 215 (**1999**) 339.

Schroeder, P.A., Melear, N.D., Pruett, R.J. *Appl. Clay Sci.* 23 (**2003**) 299.

Smith, R.W., Narimatsu, Y. *Miner. Eng.* 6 (**1993**) 753.

Somasundaran, P., Healy, T.W., Fuerstenau, D.W. *J. Phys. Chem.* 68 (**1964**) 3562.

Sondi, I.J., Milat, O., Pravdic, V. *J. Colloid Interface Sci.* 189 (**1997**) 66.

Sondi, I.J., Pravdic, V. *Interfacial Electrokinetics and Electrophoresis*, Surfactant Science Series, vol. 106, Delgado, A.V., (eds.), Dekker, New York, **2002**.

Sousa, D.J.L., Varajão, A.F.D.C., Yvon, J., Scheller, T., Moura, C.A.V. *J. South Amer. Earth Sci.* 24 (**2007**) 25.

Street, N. *J. Colloid Sci.* 12 (**1957**) 1.

Stumm, W. *Colloids Surf. A* 73 (**1993**) 1.

Stumm, W. *Colloids Surf. A* 120 (**1997**) 143.

Swartzen-Allen, S.L., Matijevic, E. *Chem. Rev.* 74 (**1974**) 385.

Tadros, T.F. *Adv. Colloid Interface Sci.* 21 (**1980**) 141.

Takahashi, H. *Bull. Chem. Soc. Jpn.* 31 (**1958**) 275.

Tang, E., Liu, H., Sun, L., Zheng, E., Cheng, G. *Euro. Polym. J.* 43 (**2007**) 4210.

Tauer, K. *Colloids and Colloid Assemblies*, Caruso, F., (eds.), Wiley-VCH Verlah GmbH & Co. KGaA, Weinham, **2004**.

Teh, E.J., Leong, Y.K., Liu, Y., Fourie, A.B., Fahey, M. *Chem. Eng. Sci.* 64 (**2009**) 3817.

Thiessen, P.A. *Z. Elektrochem. Angew. Phys. Chem.* 48 (**1942**) 675.

Tombácz, E., Szekeres, M. *Appl. Clay Sci.* 34 (**2006**) 105.

Undabeytia, T., Nir, S., Rytwo, G., Morillo, E., Maqueda, C. *Enviro. Sci. & Technol.* 36 (**2002**) 2677.

Vanderhoff, J.W. *Pure Appl. Chem.* 52 (**1980**) 1263.

Vasel, A. *Colloid Polym. Sci.* 33 (**1923**) 178.

Wagner, C.D., Passoja, D.E., Hillery, H.F., Kinisky, T.G., Six, H.A., Jansen, W.T., Taylor, J.A. *J. Vac. Sci. Technol.* 21 (**1982**) 933.

Wang, Z. W., Yi, X.Z., Li, G.Z. *Chem. Phys.* 274 (**2001**) 57.

Wang, Z.W., Li, G.Z., Guan, D.R., Yi, X.Z., Lou, A.J. *J. Colloid Interface Sci.* 246 (**2002**) 302.

Wang, Z., Chen, M., Wu, L. *Chem. Mater.* 20 (**2008**) 3251.

Weinzierl, D., Lind, A., Kunz, W. *Cryst. Growth Des.* 9 (**2009**) 2318.

Westall, J., Hohl, H. *J. Colloid Interface Sci. 12* (**1980**) 265.

Williams, D.J.A., Williams, K.P. *J. Colloid Interface Sci.* 65 (**1978**) 79.

Wypych, F., Satyanarayana, K.G. *Clay Surfaces: Fundamentals and Applications.* Interface Science and Technology, vol. 1, Elsevier Academic Press, London, **2004**.

Xu, Y., Higgins, B., Brittain, W.J. *Polym.* 46 (**2005**) 799.

Yan, C.L., Xue, D.F. *J. Alloys Compd.* 431 (**2007**) 241.

Yates, D.E., Ottewill, R.H., Goodwin, J.W. *J. Colloid Interface Sci.* 62 (**1977**) 356.

Yuan, J., Pruet, R.J. *Miner. Metall. Process.* 15 (**1998**) 50.

Zhou, J., Zhang, X., Wang, Y., Larbot, A., Hu, X. *J. Porous Mater.* 17 (**2010**) 1.

Zhu, X., Jiang, D., Tan, S., Zhang, Z. *J. Eur. Ceram. Soc.* 21 (**2001**) 2879.

Chapter Five: Adsorption studies of polyelectrolyte and kaolin fine particles on polystyrene

5.1. Introduction

Polyelectrolytes are used as flocculants, surface modifiers or stabilisers in numerous industrial applications and processes. It is therefore important to understand the behaviour of polyelectrolytes in solution and when adsorbed on to a substrate. In these applications the interaction between polyelectrolytes and colloidal particles plays a major role [Andelman, et al., 2000]. The physical properties of charged macromolecules in contact with a solid surface are fundamentally different from those of similar layers consisting of uncharged polymers. In contrast, the structure and properties of polyelectrolyte layers are dominated by electrostatic interactions.

In general, two different pathways for attaching polyelectrolytes to a solid surface are known; firstly, where the chains are physically bound (physisorption) and another where the chains are attached through establishment of a covalent bond between the substrate and the polyelectrolyte (chemisorption). With physisorption the amount of adsorbed polyelectrolyte and the conformation of the layer structure are governed by parameters such as charge density of the polymer, the density of the surface charge, and the ionic strength of the medium from which the polyelectrolyte is adsorbed [Papenhuijzen, et al. 1986; Cohen Stuart, et al. 1991]. Because the electrostatic repulsion between charged molecules in aqueous medium opposes the accumulation of the polyelectrolyte at the surface, highly charged polyelectrolytes typically adsorb in small amounts to a solid substrate, this can be overcome

if electrostatic forces are screened. One way to achieve this is the addition of low molecular weight electrolytes to the medium from which the molecules are adsorbed.

Adsorption layer formation is influenced by three steps: (1) transport of the polymer molecules to the interface, (2) the primary adsorption step, (3) arrangement of the adsorbed molecules. Once at the interface, the rearrangement of the macromolecules becomes important. This rearrangement is a complex process and very often determines the time required to reach equilibrium conditions. In contrast to small molecules, the polyelectrolyte chains change their conformation at the surface. This means that the adsorbed amount at a fully covered surface can differ because of different conformations depending on the concentration of polyelectrolytes and salt additives [Klitzing, et al. 2002].

The different parts of adsorbed chains are distinguished by the adsorption strength of the monomer units at the surface. As shown in Figure 5.1, *trains* are adsorbed with all segments to the substrate, *loops* consist of non-adsorbed segments and connect two trains, and the free chain ends are called *tails*. Indirectly, the volume fraction profile gives information about tail, train, and loop distributions.
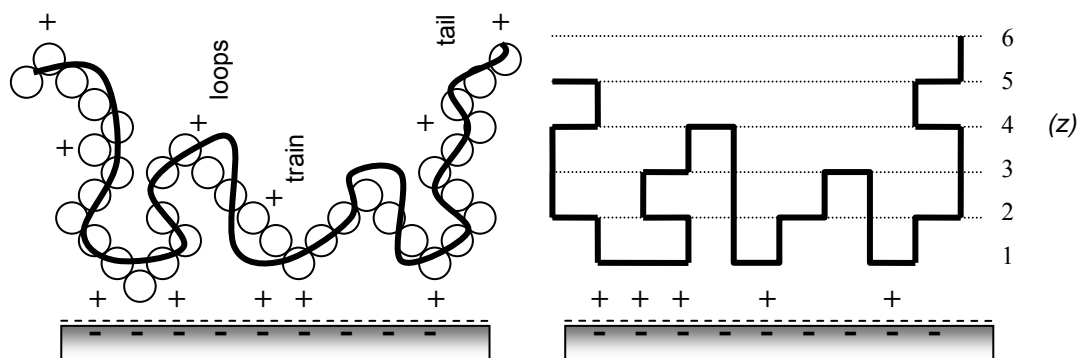
Figure 5.1 *Schematic for the conformation of an adsorbed polyelectrolyte chain at a negatively-charged substrate.*

5.2. *Background*

A number of theories of polymer adsorption and chain conformation at the interface have been reported [Flory, 1942; Huggins, 1942; Frish, et al. 1953; Scheutjens, et al. 1979, 1980; de Gennes, 1981; Binder, 1983; Evers, et al. 1985; Lvov, et al. 1999; Netz, et al. 1999; 2003; Andelman, et al. 2000; Castelnovo, et al. 2000; Dobrynin, et al. 2005]. Polymer configuration profiles can also be measured by several spectroscopic methods, these include; infrared (IR), nuclear magnetic resonance (NMR), and electron spin resonance (ESR) [Cohen Stuart, et al. 1986; Cosgrove, et al. 1985; 1990]. In addition to the polyelectrolyte concentration, the concentration of salt (i.e. NaCl) changes the adsorbed amount. In solutions of low ionic strength the charges along a polyelectrolyte chain are more stretched (large radius of gyration).

After adsorption the chains form trains at low polyelectrolyte concentration and long tails toward the solution at high polyelectrolyte concentration. At high ionic strength the charges along a chain are screened and the chains become more coiled (decrease in radius of gyration). The chains become more flexible (decrease in persistence length) and show more loops after adsorption. In addition to diminishing intrachain screening, interchain interactions play an important role. Both effects lead to more a densely formed polyelectrolyte layer with increasing ionic strength. At high polyelectrolyte concentration and high ionic strength, the number of binding sites per molecule depends on the local adsorption conditions; when a molecule adsorbs to an empty substrate it finds the space to form more binding sites than a molecule that adsorbs to a half covered substrate. Therefore, it will adsorb with fewer binding sites. Since the adsorption energy of a monomer unit is independent of the chain length, the chains with many binding sites increase the number of

adsorption sites to decrease their free energy. This takes place at the expense of polymer chains with fewer binding sites, which desorbs back into the solution.

A classical method of measuring the adsorption isotherm is by adding various amounts of the polyelectrolyte to a known surface area, allow the system to equilibrate, separate the supernatant either by filtration or centrifugation, and analyse for the amount of polyelectrolyte remaining in the supernatant. The amount of polyelectrolyte adsorbed to the surface is then determined from a mass balance. The centrifugation method exploits separation forces based on the density differences between the substrate particles and the medium. However, this technique assumes that the centrifugation does not influence the adsorption process and that any polymer that becomes trapped within the sediment is in equilibrium with the polymer on the particle surface. The filtration method will work only if the hydrodynamic radius of the polymer is smaller than the pore size of the membrane and if the diameter of the particles is larger than the pore size of the membrane. This is not always true with associative polymers, because they can build networks that approach the colloidal range, and usually it is not possible to know at what concentrations the associative polymer network will become too large to pass through the membrane. The filtration technique may be difficult to apply to polystyrene that are associative polymers for two reasons: first, the cake of the polystyrene particles may entrap the associative polymer molecules; and second, at high concentrations of polyelectrolyte, the viscosity of low molecular weight polymers is extremely high, making it essentially difficult for the associative polymers to pass through the cake of particles. However, with reference to the research being conducted, centrifugation is not a viable means of separation due to the low density of the hollow PS microspheres, 1.02 g cm^{-3}.

5.3. **Experimental Process**

5.3.1. Materials

The properties of the hollow anionic PS microspheres were described in the previous chapter. As the majority of PE adsorption research which has been published was conducted using solid microsphere substrates, solid PS samples were produced using a free radical polymerisation technique [Greenwood, 2007; Luckham, 2007]. The solid template material classified as Imperial PS was used to ensure that the hollow PS adsorption isotherm experiments were reliable.

Solid PS microspheres were produced using the following procedure: Initially, a styrene monomer was passed through an inhibitor removal column before entering the reaction flask. The 4-neck round-bottom flask was fitted with mechanical stirrer, condenser, thermometer, and nitrogen inlet. Mechanical stirring was required to keep the droplets of styrene dispersed before they polymerise. The flask and its contents are heated in a water bath with the liquid level in the flask submerged below the level of the water in the bath. Nitrogen was passed through the suspension at a low flow rate to ensure an inert atmosphere and prevent the oxidation of the reactants. Oxygen inhibits free radical polymerisations. 0.8 molar v/v of styrene in a $1.33 \times 10^{-2} \, gdm^{-3}$ of sodium chloride (NaCl) solution was added to the reaction flask containing 1750 ml of water. The reaction flask temperature was maintained at approximately 80 ºC and the mixture stirred at 350 rpm for 60 min. When the temperature achieved an equilibrium state, the reaction was initiated by adding 100 ml of 2.22×10^{-3} gdm^{-3} ammonium persulphate to the flask. 100 ml of purified water was then added to the flask and the reaction was allowed to proceed for approximately 24 hr.

The resultant mixture was then allowed to cool to room temperature and passed through glass wool to remove any coagulated particles. The mixture was then dialysed in purified water within well boiled dialysing tubes for 3 weeks. The purified water was subject to daily changes. Prior to use, the solid PS microspheres were washed, filtered and resuspended using the membrane ultrafiltration system described previously. The PS particles were characterised and the properties are described in Table 5.1.

Table 5.1 *Properties of solid Imperial PS microspheres.*

Polystyrene Product	Particle Structure	Particle Size (nm)	Density (g/cm^3)	pH	Zeta Potential (mV)
Imperial PS-1	Solid	325 ± 24	1.05 ± 0.01	6.7 ± 0.1	-43.2 ± 2.0
Imperial PS-2	Solid	340 ± 28	1.05 ± 0.01	6.7 ± 0.1	-44.1 ± 3.4
Imperial PS-3	Solid	363 ± 13	1.05 ± 0.01	6.8 ± 0.1	-43.1 ± 3.6

Sodium chloride (NaCl) (analytical grade) and poly(diallyldimethylammonium chloride) (polyDADMAC; $C_8H_{16}ClN$; M_W =70,000 to 100,000 g mol, 20 wt% in water) were purchased from Sigma-Aldrich Co., Ltd. (Dorset, UK) and used without further purification.

Gel permeation chromatography (GPC) experiments were carried out on the polyDADMAC to determine the molecular weight and molecular weight distribution. All experiments were conducted by Rapra Technology Ltd., (Shropshire, UK). Analysis was carried out using Plaquagel-OH columns with a buffer solution of 0.2 M $NaNO_3$ and 0.5 M CH_3COOH at a flow rate of 1.0 mL min. Four samples from two different stock solutions were submitted for analysis.

From the computed molecular weights and the distributions, it was apparent that the samples were similar. All samples had a broad distribution polymer component and a narrow

distribution low molecular component. Results are summarised in Table 5.2 as the calculated molecular weight averages and polydispersity (*Mw/Mn*) for the polymer component. In Appendix C, Figure C.1 represents the molecular weight distribution of polyDADMAC, the narrow distribution peak identifies the low molecular component.

Table 5.2 *Characteristics of the polyelectrolyte polyDADMAC by GPC.*

Polyelectrolyte Product	Sample Reference	Molecular Weight (Mw)	Molecular Average (Mn)	Polydispersity
polyDADMAC	RTL8379/1-17	59,400	11,900	5.0
polyDADMAC	RTL8379/1-19	59,300	12,000	4.9
polyDADMAC	RTL8378/2-18	59,300	12,000	4.9
polyDADMAC	RTL8379/2-20	59,300	12,000	4.9

For the adsorption isotherm experiments, known concentrations of cationic polyelectrolyte were dissolved in ultra pure water without any further adjustment of pH and were magnetically stirred for at least 5 min. to improve dispersity. Concentration spectra for the polyelectrolyte polyDADMAC are presented in Appendix C, Figure C.2. The water used in all experiments and for dialysis was laboratory grade distilled water.

5.3.2. Membrane ultrafiltration system

For pressure filtration, Amicon 8200 stirred cells (Amicon Bioseparations, Bedford, US) were used to wash PS samples and perform adsorption isotherm experiments. A number of reaction vessels were used in parallel. The stirred cells were used at a pressure of 3 bar maximum. The filtration can be performed continuously, controlling the sequential addition of the PE as well as the addition of water during the washing and resuspension cycles.

Membrane filters of the following type were used: Polyethersulfone (PBMK06210, diameter 63.5 mm) with a nominal molecular weight limit (*NMWL*) ≥ 300,000. Prior to use, the membrane filters were cleaned to remove glycerine ($C_3H_5(OH)_3$) and sodium azide (NaN_3) which are used as additives. The membrane filters were submerged in distilled water for 60 min, changing the solution water every 20 min. The membrane filters were then rinsed by filtering distilled water for 20 min. at 2 bar pressure. The filtrate samples were then analysed for traces of UV-absorbing material causing interference. This procedure was sufficient to render the membrane material clean and did not result in influencing the adsorption process.

5.3.3. Analytical methods

5.3.3.1. *Molecular absorption spectroscopy*

Molecular absorption spectroscopy is concerned with the measured absorption of radiation as it passes through a gas, liquid or a solid. Absorption of incident radiation by bonding and non-bonding electrons represents a high energy transition corresponding to an absorption band which is observed at 190 to 800 nm in the ultraviolet (UV) and visible (Vis) range of detection. The quantised internal energy E_{int} of a molecule in its electronic ground or excited state can be approximated:

$$E_{\text{int}} = E_{el} + E_{vib} + E_{rot} \qquad [5.1]$$

where E_{el} is the electronic, E_{vib} the vibrational and E_{rot} the rotational energy, respectively. Absorption of a photon results in a change of electronic energy accompanied by changes in the vibrational and rotational energies. Each particular electronic and vibrational transition corresponds to an absorption band, in liquid and solids the rotational lines may be broad and

overlap. For a solution absorbing substance, an absorptivity ratio at a monochromatic wavelength is defined as: (incident light, I_0)/(transmitted, I) and this is logarithmically related to concentration and optical path-length by the Beer Lambert law:

$$(A) = \log_{10}\left(I_0 \big/ I\right) = k.c.l. \qquad\qquad [5.2]$$

where A is the absorbance, c is the amount concentration of solute, l the absorption path length between parallel optical faces of a suitable cell and k is a proportionality constant.

Molecular absorption spectroscopy was used to determine absorption isotherms, polyelectrolyte concentrations and residence of unreacted monomer or surfactant in the filtrate from clean and conditioned polystyrene. UV-Vis spectra were collected using a Lambda 25 spectrometer (Perkin-Elmer Ltd., UK) with a scan rate of 120 nm min. A pair of quartz sample cells was used in all measurements, radiation was passed simultaneously through the cells, one cell is the sample cell while the other, the reference cell contains the solvent or a reference solution. To obtain precision in the absorption measurement it is necessary to adjust the sample concentration to bring the absorbance into the range 0.1 to 1.0. The theoretical minimum error occurs at a best precision absorbance of approximately 0.8.

5.3.3.2.   *Nuclear magnetic resonance*

The solvent relaxation nuclear magnetic resonance (NMR) technique takes advantage of the fact that protons within water molecules bound at an interface have a shorter spin-spin magnetic relaxation time, T_{2b}, than the time for those free in solution, T_{2f}. The T_{2f} value for protons within free water molecules is around 2 s, but at the interface spin-spin relaxation

processes are efficient enough to give T_{2b} values typically <1 ms. Provided there is fast exchange of solvent between the two states, a single overall relaxation time, T_{2obs} or simply T_2, is observed, which is linked to the fraction of protons in the bound environment, P_b.

$$\frac{1}{T_{2obs}} = \frac{1-P_b}{T_{2f}} + \frac{P_b}{T_{2b}}$$

[5.3]

The dynamics may alternatively be viewed in terms of the correlation time τ_c, which is proportional to the reciprocal of T_2 and describes the lifetime of a dynamic process, for example, rotation or translation. In the bulk molecular motions are fast and τ_c is short, while at the interface the opposite is true; restricted motion leads to a long τ_c and facilitates more efficient spin-spin relaxation processes [Nelson et at., 2002].

Results are commonly expressed in terms of the relaxation rate constant, R_2, which is the reciprocal of T_2, or the specific relaxation rate constant, R_{2sp}, which is the relaxation rate relative to the relaxation rate, R_2°, of a suitable reference sample, which in this case is the filtrate from a clean PS latex suspension.

$$R_{2sp} = \frac{R_2}{R_2^\circ} - 1$$

[5.4]

An increase in R_{2sp} implies that there is either more solvent or more strongly bound solvent at the interface and hence that there is a higher surface polyelectrolyte coverage (θ). NMR was used to provide insight into the portion of the adsorbed polyelectrolyte layer close to the PS particle surface. Plots of the specific relaxation rate of the solvent, R_{2sp}, against polyelectrolyte concentration are in some ways comparable to adsorption isotherms,

providing information on the density of the polyelectrolyte train layer and a measure of the total adsorbed amount.

A Bruker MSL 300 MHz NMR spectrometer (Bruker Corp., UK) has been used to plot the specific relaxation rate of the solvent, R_{2sp}, against polyelectrolyte concentration, in some ways comparable to adsorption isotherms.

5.3.4. Preparation of polystyrene samples

Prior to the adsorption of polyelectrolyte all PS samples were dialysed in purified water. Amicon ultrafiltration cells were used to rinse, wash and redisperse PS samples to the required concentrations. In Appendix C, Figure C.3 shows the reduction in absorbance of PS supernatants after washing. The graph indicates that after the fourth and fifth wash cycle, the majority of absorbing material has been removed. However, an increase in absorbance is evident after conditioning of PS and this increase is likely to influence the adsorption kinetics of a cationic polyelectrolyte. Figure 5.2 compares the absorbance peaks for both hollow and solid PS supernatants.
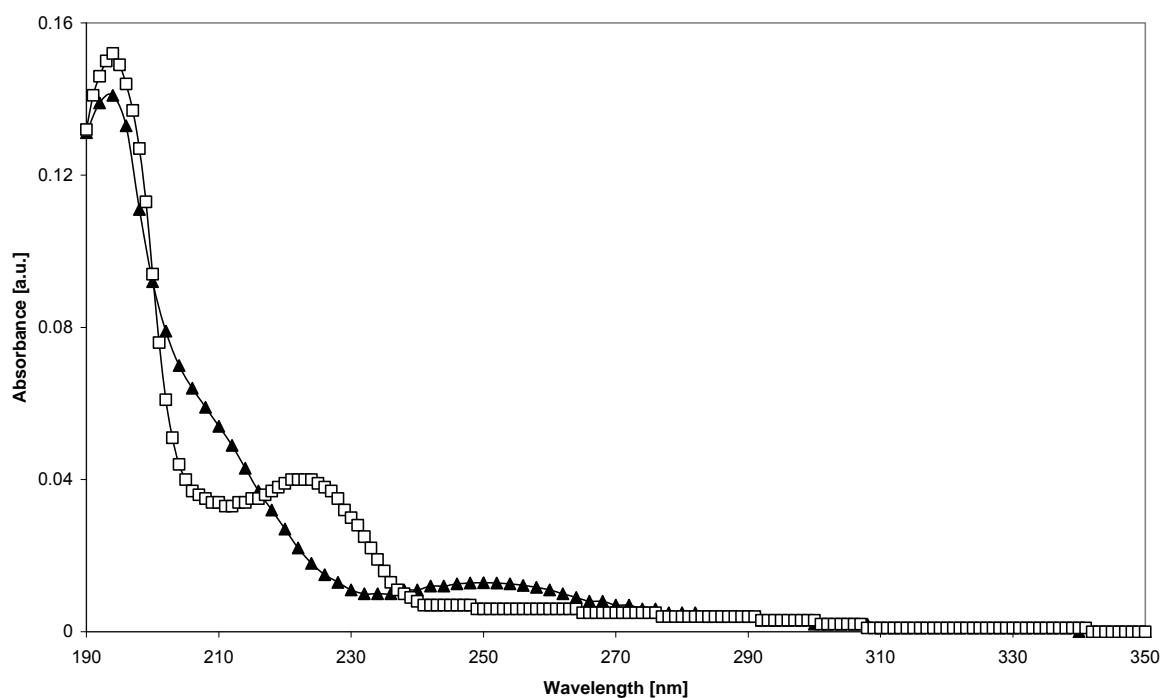
Figure 5.2 *Comparison of UV-vis absorbance values for supernatant from hollow PS (□) and solid PS (▲). 24 hr conditioning after wash cycle n=4.*

The UV-Vis spectra in Figure 5.2 have a number of important attributes; firstly, it is possible to determine which chemical groups are evident within the supernatant by verifying the wavelength of specific peaks. Secondly, the required number of wash cycles can be determined which would result in a clean PS system. Finally, a reference sample can be determined which will be used when analysing supernatants from adsorption isotherm experiments. In Figure 5.2, the absorbance curve for hollow PS exhibit two specific peaks at wavelength 194 nm and 223 nm, these are be attributed to the release of alkane groups (C_nH_{2n+2}) from the polystyrene surface and ether compounds (C-O-C) possibly attributed to the polymerisation process of polystyrene respectively [Binks, 2002; He, et al. 2005]. The absorbance profile for solid PS exhibit a well defined initial peak at wavelength 194 nm again attributed to alkane groups within the solvent and a broad peak at 250 nm due to halocarbons (haloalkane groups exhibiting C-C bonds).
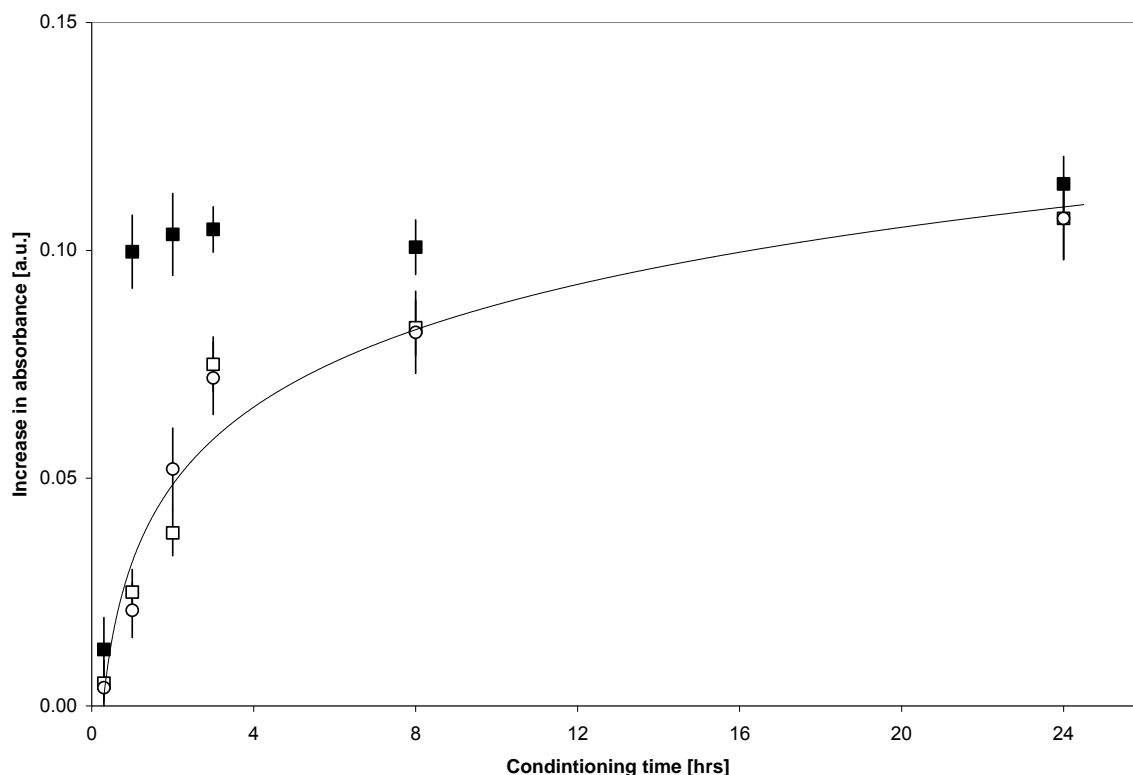
Figure 5.3 *Increase in UV-Vis absorbance due to 24 hr conditioning of hollow PS. Wash cycle n=3 (■); n=4 (□); and n=5 (○).*

Even after dialysis of the hollow PS, the microspheres required further wash cycles to remove unreacted monomer and excess surfactants. Figure 5.3 identifies that during conditioning molecules are released from either the PS surface or from within the PS void area. The third wash cycle shows an immediate release of absorbing material within the first hour of conditioning, whereas the fourth and fifth wash cycle indicates a gradual release during the initial four hours of conditioning. Increase in absorbance is important as the adsorption isotherm experiments are conducted over a 20 min and 24 hr period. The release of surfactant over this period will certainly influence the adsorption kinetics of added polyelectrolyte concentration.
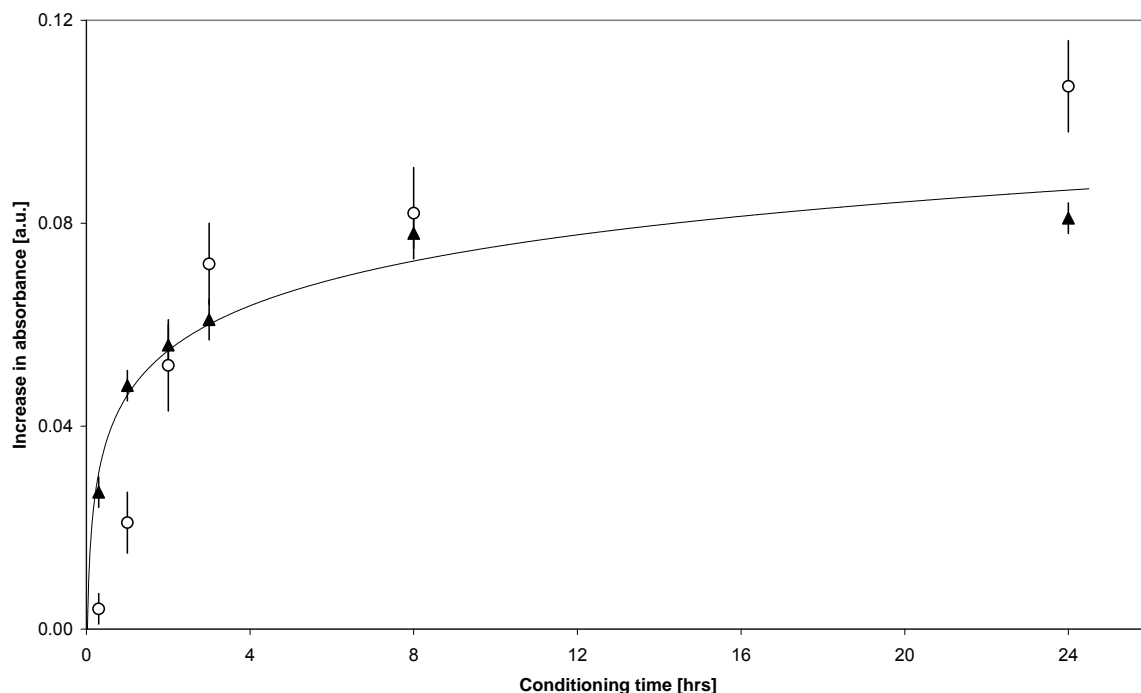
Figure 5.4 *Increase in UV-vis absorbance after final wash due to 24 hrs conditioning of hollow PS (○) and solid PS (▲). Wash cycle n=5.*

A comparison of conditioning of hollow and solid PS samples is shown in Figure 5.4. The graph shows an increase in absorbance for both PS samples during the initial four hours of conditioning. The gradual release of chemical groups from the hollow PS samples during conditioning may result from surfactant moving from the internal void area of the hollow PS microsphere into the medium. Whereas, weak-bonded chemical groups from the solid PS surface are expected to detach from the surface during conditioning.

5.3.5. Adsorption of polyelectrolyte on hollow PS surface

Amicon 8200 stirred cells were used to conduct the adsorption isotherm experiments. Prior to any adsorption experiment, all PS samples were treated with ultrasound for at least 2 min. resulting in a deflocculated suspension. In the initial adsorption isotherm experiments, 100 ml aqueous solution with appropriate concentrations of the cationic polyelectrolyte

polyDADMAC were added to dispersed hollow PS (1 wt% solids) suspensions, with no added NaCl. A concentration profile for the polyelectrolyte samples is shown in Figure C.2, Appendix C.

The polyelectrolyte solutions were added drop wise to the PS suspensions by using a burette. The resulting solutions were magnetically stirred at room temperature for 20 min. The experiments were repeated with the polyelectrolyte concentrations in a 0.1 M NaCl solution with an adsorption process of 20 min.

Adsorption isotherm experiments were repeated and the adsorption process time was extended to 24 hr to compensate for depletion of weakly attached polymer at the interface. The scopes of these experiments were repeated at various NaCl concentrations in the range of 0.1, 0.2 and 0.5 M NaCl. Experiments are listed in Tables 5.3 and 5.4.

After polyelectrolyte adsorption, all samples were filtered under pressure using Amicon stirred cells resulting in the supernatant containing non-adsorbed polymer to be removed. The adsorbed amounts were determined from the difference between the initial polymer concentration and the concentration in the supernatant by UV-Visible spectroscopy. A solvent spectrum was subtracted from all spectra. All isotherm experiments were repeated at least five times to ensure reproducibility of the adsorption isotherm procedure.

Table 5.3 *Initial adsorption isotherm experiment variables.*

PS Structure	Concentration PS (wt%)	Concentration PE (g L)$^{-1}$	Concentration NaCl (M)		Adsorption time (min.)	
			(a)	*(b)*	*(a)*	*(b)*
Hollow	1.0 ± 0.1	0.1	0	0.1	20	1440
Hollow	1.0 ± 0.1	0.2	0	0.1	20	1440
Hollow	1.0 ± 0.1	0.4	0	0.1	20	1440
Hollow	1.0 ± 0.1	0.8	0	0.1	20	1440
Hollow	1.0 ± 0.1	1.6	0	0.1	20	1440
Hollow	1.0 ± 0.1	3.2	0	0.1	20	1440
Hollow	1.0 ± 0.1	6.4	0	0.1	20	1440

Table 5.4 *Adsorption isotherm experiments with extended NaCl concentration range.*

PS Structure	Concentration PS (wt%)	Concentration PE (g L)$^{-1}$	Concentration NaCl (M)				Adsorption time (min.)
			(a)	*(b)*	*(c)*	*(d)*	
Hollow	1.0 ± 0.1	0.4	0	0.1	0.2	0.5	1440
Hollow	1.0 ± 0.1	2.0	0	0.1	0.2	0.5	1440
Hollow	1.0 ± 0.1	4.0	0	0.1	0.2	0.5	1440
Hollow	1.0 ± 0.1	6.0	0	0.1	0.2	0.5	1440
Hollow	1.0 ± 0.1	8.0	0	0.1	0.2	0.5	1440
Hollow	1.0 ± 0.1	10.0	0	0.1	0.2	0.5	1440
Hollow	1.0 ± 0.1	12.0	0	0.1	0.2	0.5	1440

5.3.6. Adsorption of polyelectrolyte on solid PS surface

Solid Imperial PS samples were used as anionic substrates to adsorb polyDADMAC. The experiments were conducted to ensure the reliability of the adsorption isotherm filtration method. The solid PS latex samples were produced using the free radical polymerisation technique as described previously. 100 ml aqueous solution with appropriate concentrations of the cationic polyelectrolyte polyDADMAC were added to dispersed solid Imperial PS

suspensions at 1 wt% solids, with no added NaCl. The polyelectrolyte solutions were added drop wise to the PS suspensions by using a burette. The solutions were magnetically stirred at room temperature for 20 min. The adsorption times were extended to 24 hr and were again repeated with polyelectrolyte concentrations in a 0.1 M NaCl solution. Adsorption isotherm experiments are outlined in Table 5.5. After polyelectrolyte adsorption, all PS samples were filtered under pressure; the resulting supernatants were analysed using UV-Vis spectrometry to determine the remaining polyelectrolyte concentration in solution.

Table 5.5 *Adsorption isotherm experiments using solid Imperial PS.*

PS Structure	Concentration PS (wt%)	Concentration PE (g L)$^{-1}$	Concentration NaCl (M)		Adsorption time (min.)	
			(a)	*(b)*	*(a)*	*(b)*
Solid	1.0 ± 0.1	0.1	0	0.1	20	1440
Solid	1.0 ± 0.1	0.2	0	0.1	20	1440
Solid	1.0 ± 0.1	0.4	0	0.1	20	1440
Solid	1.0 ± 0.1	0.8	0	0.1	20	1440
Solid	1.0 ± 0.1	1.6	0	0.1	20	1440
Solid	1.0 ± 0.1	3.2	0	0.1	20	1440

5.3.7. Adsorption of kaolin on hollow PS surface

The Amicon 8200 stirred cells were used again to conduct kaolin adsorption experiments. Prior to any adsorption experiments, all kaolin samples were washed to remove excess dispersant and treated with ultrasound for at least 2 min to improve dispersity. SEM was used to ensure that no aggregated kaolin structures were evident. The kaolin grade used in all adsorption experiments was the KF-8489.

Hollow AF1055 PS microspheres were used as a substrate; all PS samples were cleaned and rendered cationic in surface charge using polyDADMAC. The PS surface was saturated using a 2 g L^{-1} polyelectrolyte stock solution. The polyelectrolyte adsorption process was conducted over a 24 hr period. Excess polyelectrolyte was removed by filtration under pressure at 3 bar.

The cationic PS microsphere samples were resuspended using laboratory grade distilled water. Under gentle stirred conditions kaolin concentrations were added to the 100 ml PS suspension using a burette. The resulting solutions were magnetically stirred at room temperature for 20 min. Kaolin concentrations were varied to enable an optimum coverage to be determined. Kaolin adsorption experiments are listed in Table 5.6, the ratio values for kaolin to PS are based on weight values. Kaolin specific surface area measurements were based on the BET gas adsorption method described in Chapter 4.2.5, values represent the actual specific surface area of KF-8489 available to adsorb at the PS interface.

Table 5.6 *Kaolin adsorption experiments using hollow PS template.*

PS Structure	PS Surface	Concentration PS (wt%)	Ratio Kaolin : PS	Kaolin specific surface area (m^2)	Adsorption time (min.)
Hollow	Positive	1.0 ± 0.1	0.40:1	5.6	20
Hollow	Positive	1.0 ± 0.1	0.50:1	7.1	20
Hollow	Positive	1.0 ± 0.1	0.75:1	10.6	20
Hollow	Positive	1.0 ± 0.1	1.25:1	17.7	20
Hollow	Positive	1.0 ± 0.1	1.50:1	21.2	20
Hollow	Positive	1.0 ± 0.1	1.75:1	24.8	20

After kaolin adsorption, 20 ml samples were removed from the Amicon stirred cells using a pipette and were immediately prepared for SEM. Coverage of PS by fine kaolin particles were observed using a JOEL JSM 6700-F SEM instrument.

Finally, particle adsorption isotherms were determined from sediment volume measurements. In this case, a series of 100 ml glass measuring cylinders, with uniform bore capillary tubing at their bottom end, were used for measuring the sediment volume. To each of these measuring cylinders, a suspension containing positive PS latex, fine kaolin particles in sodium chloride (where required) were added. The ratios of fine kaolin particles to PS are listed in Table 5.6. All samples were mildly agitated for 20 min to ensure the adsorption of fine kaolin particles to PS particles prior to being allowed to stand for 7 days. The sediment height in the measuring cylinder was monitored, hence the sediment volume, V, could be easily calculated. The reduced sediment volume is equal to V/V_{hex}, where V_{hex} is the volume that would be occupied by an equivalent number of hexagonally close-packed particles [Vincent, et al. 1978; Skuse, et al. 1986]. Therefore, V_{hex} represents the volume of the measured kaolin sediment and V represents the volume of the measured sediment formed by coated PS particles. A number of assumptions have been made with regards to measuring the sediment height; (i) when kaolin particles sediment they form a face-to-face orientation (no face-to-edge interactions occur resulting in a house-of-cards effect); (ii) when coated PS microspheres sediment they form a close-packed array. In some cases, after the sediment height was measured and calculated, the layer of liquid above the sediment in the capillary was discarded and a sample of the plug carefully removed. The sample was then sputter coated with gold and examined in a JOEL JSM 6700-F SEM instrument.

5.4. *Results and Discussion*

Classification of isotherms is considered necessary to their theoretical treatment and interpretation. A classification system of isotherms has been described by C.H. Giles and colleagues [Giles, et al. 1960; 1974a; 1974b]. This divides adsorption isotherms by their initial slope, into four main classes, termed Langmuir (*S*, *L*), high affinity (*H*) and constant

partition (*C*) and further into several sub-groups. The isotherm shape is largely determined by the adsorption mechanism and can be therefore be used to diagnose the nature of the adsorption. Classification and explanation of relevant isotherms can be referenced to in Appendix C.

The primary mechanism for adsorption is the ionic attraction between an oppositely charged substrate and polymer. However, owing to the distinct nature of various molecules employed to produce polyelectrolyte charged layers, other secondary interactions such as H-bonding and dispersion forces may also influence the adsorption process. With such a variety of possible mechanisms and dependency on experimental conditions for adsorption, it is not surprising that no single theory can account for all experimental observations made for different systems. Nevertheless, there have been several attempts to explain important features or aspects of adsorption mechanisms and their resulting properties [Scheutjens, et al. 1974; Vincent, 1974; Cohen Stuart, et al. 1980; 1996; Papenhuijzen, et al. 1984; Decher, et al. 1992; Netz, et al. 1999a; 1999b; Joanny, et al. 2000; Aoki, et al. 2006;].

For adsorption governed by ionic interactions, much can be learned from decades of research on the mechanisms of adsorption of polyelectrolytes, a review of experimental results and theoretical models have been published [Fleer, et al. 1993; Tripathy, et al. 2002]. Polyelectrolyte adsorption depends on the molecular weight of the polymer, its linear charge density, the charge distribution along the chain, the ionic strength of the solution, substrate charge, and nonelectrostatic affinity between the substrate and the polyelectrolyte [Shubin, et al. 1997]. The self-consistent field lattice model developed by Scheutjens and Fleer can account for the major observations in the adsorption experiments [Scheutjens, et al. 1979; 1980; Evers, et al. 1986; Böhmer, et al. 1990]. The molecular weight is an important

parameter because small molecules are the first to be adsorbed and as the equilibrium is reached for the adsorption process, larger molecules replace the small molecules.

The charge of the polyelectrolyte usually compensates or even over compensates for the surface charge. The adsorbed amount should then decrease with the ionic strength of the solution, owing to the screening of the attractive ionic force [Muthukumae, et al. 1987; Cohen Stuart, et al. 1991]. For strong polyelectrolytes, the attraction dominates the adsorption process; the adsorption process is referred to as screening-reduced [Steeg, et al. 1992]. When there are specific interactions of the polymer with the surface, adsorption is generally screening enhanced, with adsorption increasing with the ionic strength. This is expected to occur for the majority of polymers adsorbed. For weak polyelectrolytes, the charge density is affected by pH and ionic strength and may vary, depending on the adsorption system [Blaakmeer, et al. 1990].

In spite of the difficulties of treating theoretically the adsorption mechanisms for various types of polyelectrolytes, a qualitative understanding can be achieved by summarising the driving forces. Thin adsorbed layers are usually obtained for polymers with high levels of segmental repulsion of the ions distributed along the polymer chain [Stockton, et al. 1997]. The adsorbed chains then adopt a more extended configuration on the surface. Thicker layers are produced if the ionic repulsion is reduced and a greater fraction of the polymer will be adsorbed as loops and tails. Such reduction may be achieved by increasing the ionic strength of the polymer solution or reducing the charge density of the polymer [Shiratori, et al. 2000].

The ionic strength of the solution is an additional factor to consider, since it determines the solvent quality in aqueous polyelectrolyte solutions. In polyelectrolyte solutions the ionic

strength results from the combined concentration of the polyelectrolyte and whatever low molar mass salts are also present. Only when the salt concentration is much higher than the polyelectrolyte concentration may the latter be neglected. Considering the above classification, various limiting cases have been distinguished [Schmidt, et al. 2002; Dukhin, et al. 2005]: (a) highly charged polyelectrolyte at low ionic strength of the solution; (b) lowly charged polyelectrolyte at low ionic strength of the solution; (c) highly charged polyelectrolyte at high ionic strength of the solution; and (d) lowly charged polyelectrolyte at high ionic strength of the solution. Whereas the polyelectrolyte behaviour of (a) and (b) is determined by electrostatic interactions, the electrostatic contributions are screened in cases (c) and (d). Therefore, physiochemical parameters such as molar mass become important and in the majority of cases the surface chemistry has an additional influence on the adsorption process [Schmidt, et al. 2002]. If electrostatic adsorption of a polyelectrolyte is enhanced by a chemically mediated surface affinity (H-bonding), the system is likely to become less sensitive to the ionic strength [Wiegel, 1977; Muthukumar, 1987]. However, for solutions with a relatively high ionic strength ($C_s \geq 1.0$ M), the adsorption is a function of the ionic strength and the polyelectrolyte molecular weight [Blaakmeer, et al. 1990]. This multitude of influencing factors may be the reason for the frequently contradictory experimental findings.

5.4.1. Determination of polyelectrolyte coverage on hollow PS

The reverse in surface charge of the anionic PS was performed by the adsorption of PE from known concentration solutions. Useful information on the adsorption can be obtained from the adsorption isotherm which represents the plot of adsorbed amount (Γ) as a function of equilibrium polyelectrolyte concentration in the supernatant (C_{eq}). Under standard conditions commonly employed for polyelectrolyte layer formation, the time for polymer adsorption is often chosen between 10 and 20 min [Rehmet, et al. 1999; Trotter et al. 2005; Rusu, et al.

2006]. The time required for adsorption saturation of various assemblies including organic and inorganic materials has been reported elsewhere [Lvov, et al. 1998; Ariga, et al. 1999]. The initial polyelectrolyte adsorption time of 20 min was chosen based on published literature [Caruso, et al. 1998; 1999]. However, the adsorption time was extended to compensate for the possible depletion of weakly-attached polymer chains at the PS surface.
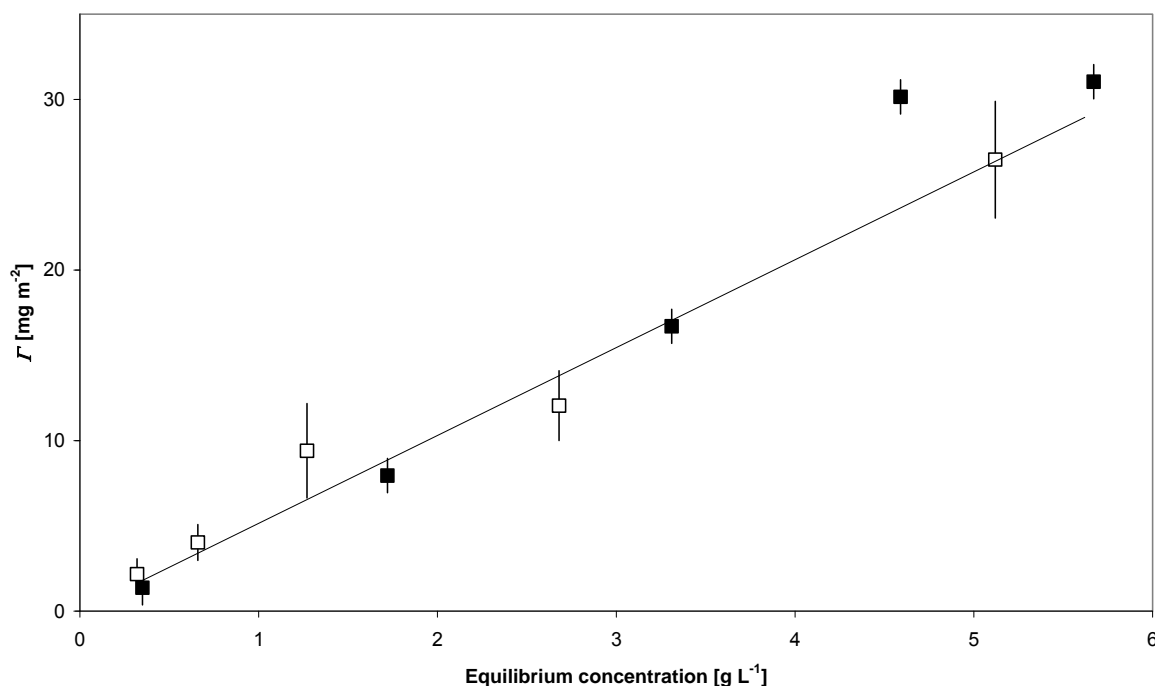
Figure 5.5 *Isotherm for polyelectrolyte adsorption on hollow PS; adsorption time 20 min (□) and 24 hr (■). With no added NaCl in aqueous solution.*

In Figure 5.5 the adsorption times of 20 min and 24 hr are compared for polyDADMAC on hollow PS. A linear line is plotted for 20 min adsorption experiments for ease of interpretation. The 24 hr isotherm indicates no significant increase in adsorbed polymer. The adsorbed amount is linearly increasing with polyelectrolyte concentration for both processes; however no plateau region can be identified although at the high concentration range the total adsorbed amounts are similar.

The initial slopes for both adsorption isotherm experiments can be compared to the Langmuir model expressing an increase in adsorption as concentration increases, at low concentration one would expect a slope to represent high affinity, i.e. when all polymer chains in the sample are adsorbed are low concentrations until saturation is reached. Accordingly, it has been reported that by increasing the ionic strength of the polyelectrolyte solution, the configuration of the polymer chain is changed from a flat to a coil configuration [Blaakmeer, et al. 1990]. This change in configuration is expected to result in an increase of adsorbed polyelectrolyte at the PS surface. This increase in absorbed polyelectrolyte due to the addition of NaCl is represented in Figure 5.6.
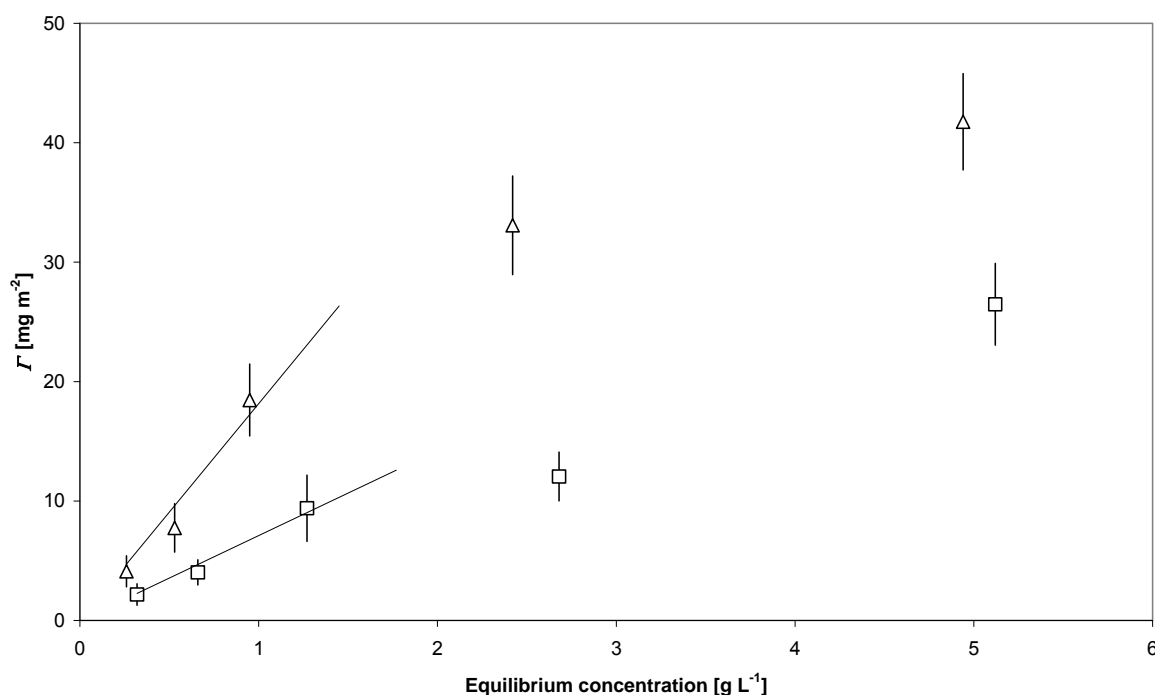
Figure 5.6 *Isotherm for polyelectrolyte adsorption on hollow PS. With no added NaCl (□) and in a 0.1 M NaCl (Δ) aqueous solution. Adsorption time 20 min.*

Figure 5.6 represents an isotherm for polyDADMAC adsorption on hollow PS after 20 min at two different ionic strengths. The initial slope for both adsorption processes are similar, both slopes indicate an linear increase in adsorption at low concentrations, the slopes are

representative of a Langmuir (*L*-curve) model which is the result of ease with which molecules can find vacant sites at the surface. The slope is expected to decrease with rise in PE concentration.

With the addition of 0.1 M NaCl the angle gradient of the slope was increased signifying an increase in PE at the PS surface. It was reported that polyelectrolyte formation was affected by the ionic strength of the solution [Clark, et al. 1997; Kovacevic, et al. 2002]. At low charge densities or at high ionic strengths due to the addition of salt, polyelectrolyte chains have more or less coiled conformations. As the ionic strength is decreased, the polyelectrolyte coil is expanded due to electrostatic repulsion, which can be regarded as a kind of excluded volume effect [Kitano, et al. 1980]. In Figure 5.6 an increase of the adsorbed amount is observed, a result due to the formation of more loops and tails of the adsorbed polymer chain at the PS surface.

Two important features are also evident; firstly, no plateau region was evident, representing surface saturation, and secondly, the adsorbed amounts of polyelectrolyte per surface area are higher than one would expect. This may be a result due to either interpolymer complexes forming in the solution or multilayer formations being formed at the PS surface between the cationic polyelectrolyte and anionic surfactant.

Initially, no significant increase in polymer adsorption was observed when the process was conducted over a 24 hr period. However, due to the change in polymer chain configuration and the increase in adsorption, an adsorption time of 24 hrs was chosen. With these experiments it was demonstrated that a further increase in the adsorbed amount of polyDADMAC was possible due to the addition of NaCl.
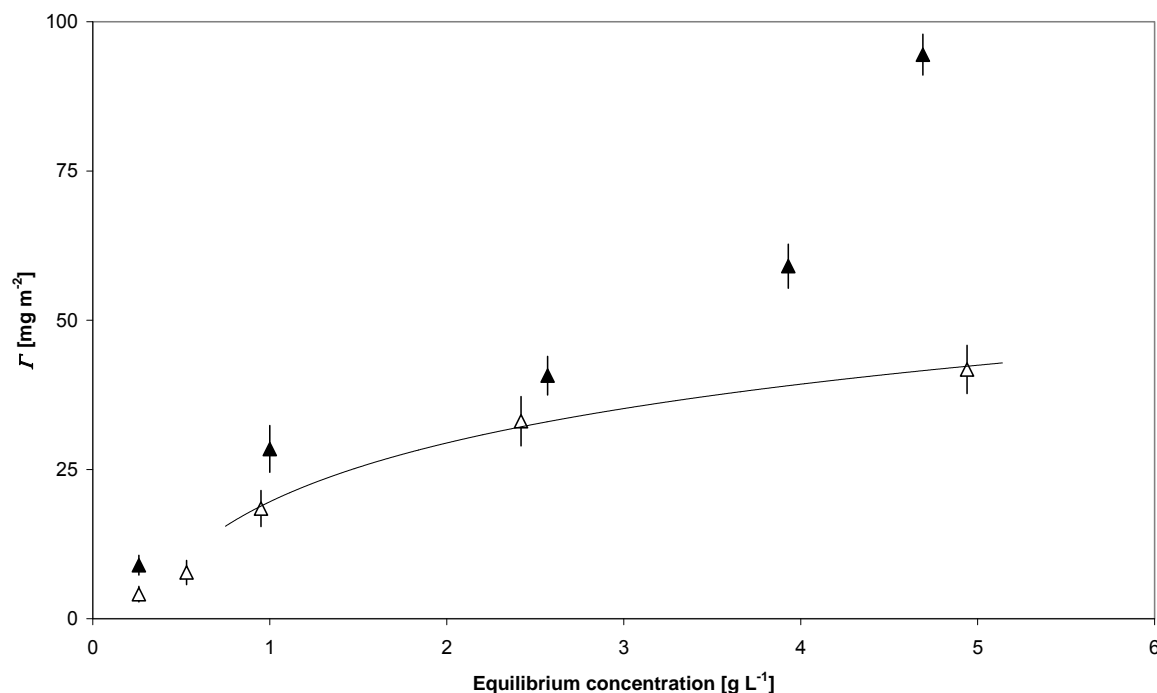
Figure 5.7 *Isotherm for polyelectrolyte adsorption on hollow PS. Adsorbed amounts after 20 min (Δ) and 24 hr (▲) in a 0.1 M NaCl aqueous solution.*

Figure 5.7 shows an isotherm for polyelectrolyte adsorption after an adsorption time of 20 min and 24 hrs. A slight increase in polyelectrolyte adsorption at the low concentration range is evident after 24 hrs when compared to the 20 min adsorption process. The curve in the graph indicates a possible plateau region for the 20 min adsorption process; this will likely be confirmed if the concentration range is extended. However, what was more apparent, at the high end of the concentration profile is a steep increase in polymer adsorption after 24 hr. This increase may be the result of the exchange process between short polymer chains being displaced by longer chains.
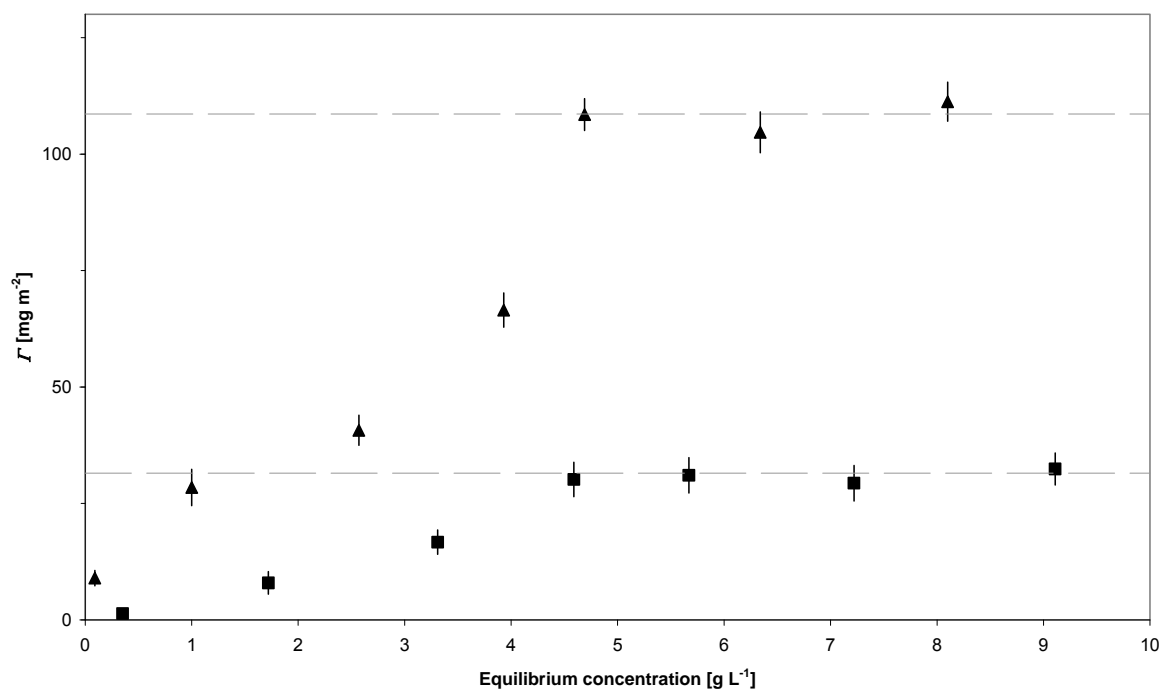
Figure 5.8 *Isotherm for polyelectrolyte adsorption on hollow PS with no added NaCl (■) and in a 0.1 M NaCl (▲) aqueous solution. Adsorption time 24 hrs.*

In Figure 5.8 an increase of the adsorbed amount of polyelectrolyte due to the addition of NaCl is observed. The adsorption time has remained at 24 hr to compensate for cooperative adsorption and the relatively strong attractive forces between polyelectrolyte molecules and the PS surface. At increased polyelectrolyte concentrations a plateau region which represents polyelectrolyte surface saturation was evident. It was understood, that at low ionic strength the conformation of the polyelectrolyte layer is flat, caused by the repulsive segment-segment interaction. This leads to a comparable low adsorbed amount as shown in Figure 5.8, because extended loops and tails do not exist. As the concentration of NaCl becomes increased, screening of the macro ions takes place. The adsorbed amount increases, because loops and tails occur, which increase the adsorbed amounts. Plateau regions are indicated at the high-end of the polyelectrolyte concentration range in Figure 5.8, with the addition of 0.1 M NaCl the adsorbed amount over a 24 hr period increased from 31.5 to 108.8 mg m^{-2}.

Most polyelectrolyte adsorption isotherms in the semi-dilute range show well defined plateaux [Lyklema, 1984]. The plateau amounts adsorbed of highly charged polymers are often comparable and amount to a few mg m^{-2} [Garvey, et al. 1974; Cosgrove, et al. 1990; Rehmet, et al. 1999; Trotter, et al. 2005], however adsorbed amounts in the range of 20 to 25 mg m^{-2} have been reported [Rusu, et al. 2006].

The significance of a long plateau must be that a high energy barrier has to be overcome before additional adsorption can occur at the surface, after the substrate has been saturated to the first degree. The solute has high affinity for the solvent, but low affinity for the layer of solute molecules already adsorbed. It is significant that adsorptions of cationic polymers give isotherm curves with long plateau; in this case the surface of the PS, when covered, will repel other cationic polymer molecules holding the same charge. A short plateau, which has not been observed, must mean that the adsorbed polymer molecules expose a surface which has nearly the same affinity for more solute as the original surface had.

At higher ionic strength the adsorbed amount achieves surface saturation at lower polyelectrolyte concentrations as loops and tails of longer polymer chains contribute more to the adsorbed amount. Figure 5.9 indicates a further increase in polyelectrolyte adsorption due to an increase in NaCl concentration.
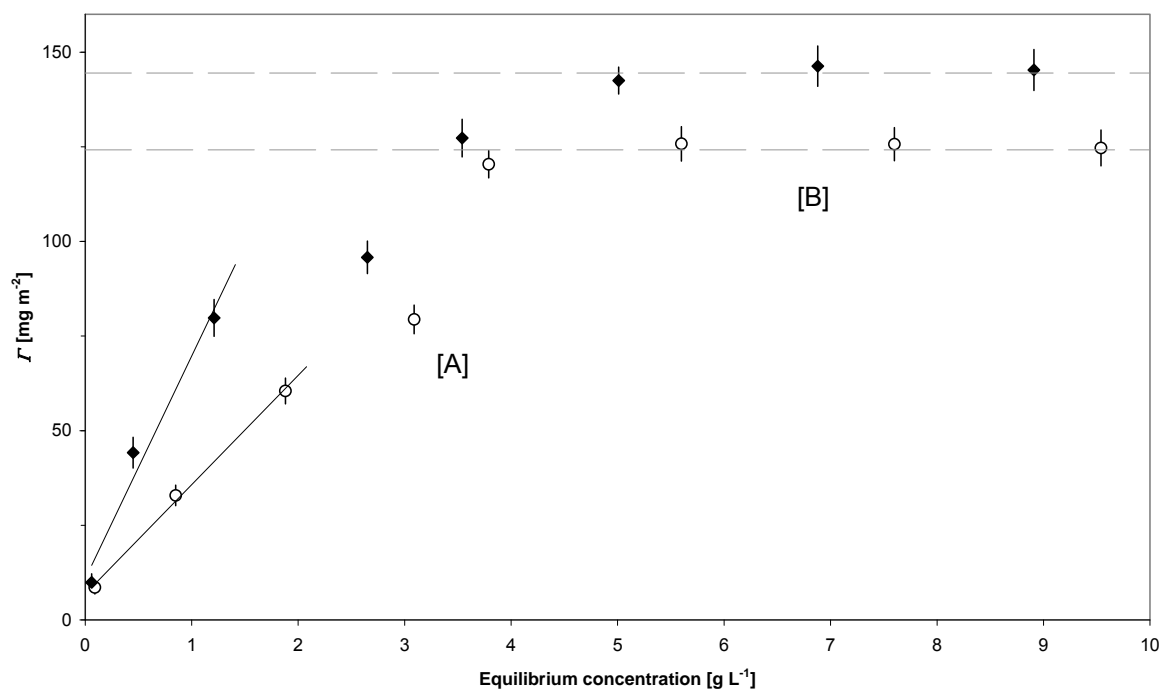
Figure 5.9 *Isotherm for polyelectrolyte adsorption on hollow PS in 0.2 M (○) and 0.5 M NaCl (♦) in aqueous solution. Adsorption time 24 hr.*

Isotherm experiments conducted at higher concentrations exhibit two possible plateau regions, this is more evident in Figure 5.9. The initial plateau region is indicated by the letter [A] and the final plateau region by [B]. Initially, it was believed that as PE saturation of the PS surface was achieved, adsorption of an anionic surfactant molecule (detached from the PS surface during the early stages of conditioning into the solution) formed a second polymer layer as shown in Figure 5.10. Free cationic polyelectrolyte polymer chains then formed a third layer and this process may have continued until all the free surfactant molecules are adsorbed. This process may be represented by the second slope of the curve prior to saturation.

Pairs of oppositely charged electrolytes in aqueous solution are well-known to form complexes [Koetz, 1986; Decher, et al. 1991; Hoogeveen, et al. 1996]. The complexation is mainly due to the attractive electrostatic interaction between the chains. This process could

contribute to high adsorption values if these complexes are formed either in solution or at the PS interface. If in solution, these complexes may not be removed during the filtration stage. This multilayer formation of polyelectrolyte-surfactant chains would compensate for the reported high adsorption values representing surface saturation as shown in Table 5.7. However, with adsorption values greater than 100 mg m^{-2} the number of polymer layers formed at the PS surface would be in the range of 50 to 70. It has been reported that the measured adsorbed amount of approximately 2 mg m^{-2} is sufficient to saturate a PS surface and form a polyelectrolyte monolayer, a polyDADMAC layer thickness has been measured between 1.5 and 2 nm by a single particle light scattering technique [Caruso, et al. 1998a; Caruso, 2000; Rusu, et al. 2006]. This complex formation at the PS interface would increase the diameter of PS microspheres by almost 75 to 100 nm and could also result in a bridging effect between colloidal particles. Detailed information on the polyelectrolyte formation at the PS surface should be further investigated using small-angle neutron scattering (SANS) and photon correlation spectroscopy (PCS) techniques [Flood 2008; Qiu, et al. 2008]. SANS can provide detailed structural information on polymers adsorbed on colloidal particles [Marshall, et al. 2004].
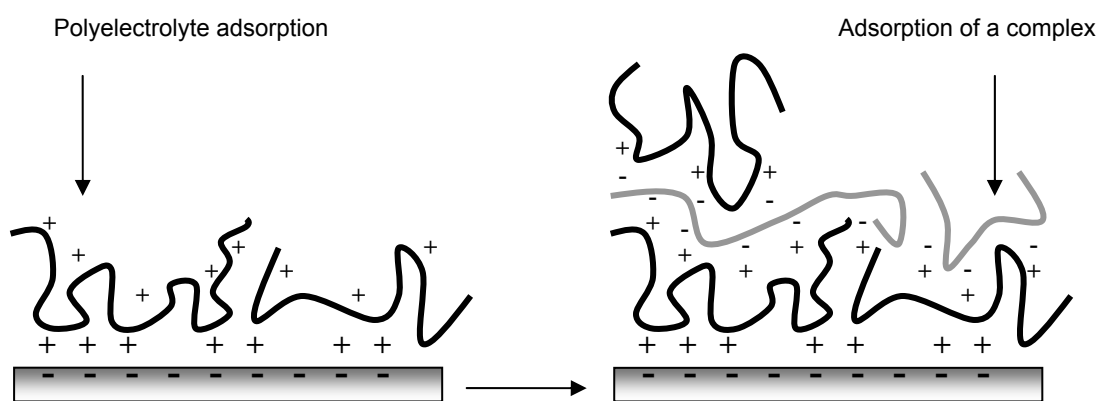
Figure 5.10 *Complex formation of an anionic surfactant polymer with a cationic polymer at the substrate. When both polymers are highly charged, the complex formation remains strongly bound to the substrate; stable multilayers can be formed.*

Table 5.7 *Adsorption isotherm values for plateau regions.*

PS Structure	Polyelectrolyte	Adsorption time (hrs.)	Ionic strength NaCl (M)	Adsorption Γ (mg m^{-2})
Hollow	PolyDADMAC	24	0.0	31.5 ± 3.6
Hollow	PolyDADMAC	24	0.1	108.6 ± 4.2
Hollow	PolyDADMAC	24	0.2	124.2 ± 4.3
Hollow	PolyDADMAC	24	0.5	144.5 ± 4.9

However, the exchange of short polyelectrolyte chains by long chains at the PS surface may be the process that was determined by the second slope of the isotherm curve, as exhibited in Figure 5.9. Even though polymers may not easily desorb in solvent, they may readily exchange against polymer molecules coming from the solution. At least two kinds of exchange can occur: between chemically identical chains, where long polymer chains displace shorter chains and between different molecules where strongly adsorbing polymer displaces weakly bound chains [Cohen Stuart, et al. 1986; 1996]. The kinetics between the exchange processes can be distinguished by several different steps; *(a)* transport of displacer through the solution; *(b)* attachment of the displacer; *(c)* conformation changes of the displacer chain; *(d)* detachment of the displaced chain; and *(e)* transport of the displaced chain away from the surface. In particular, the surface processes *(c)* and *(d)* are of interest. If the displacer and displaced polymer chains are identical or very similar, it is expected that they would interact with the same kind of surface sites. The displacer polymer chains can only occupy these sites if the displaced chain detaches from them at the same time. If the chains are chemically different, it is conceivable that they attach to different surface sites and may coexist on the surface.

In all adsorption isotherm experiments a commercial PE was used, GPC experiments identified a wide distribution in the molecular weight distribution of the polymer; see Figure

C.1. Therefore, within the polymer solution short (defined as low M_w) and long (high M_w) polymer chain lengths exist and their adsorption behaviour will influence the shape of the isotherm curve.
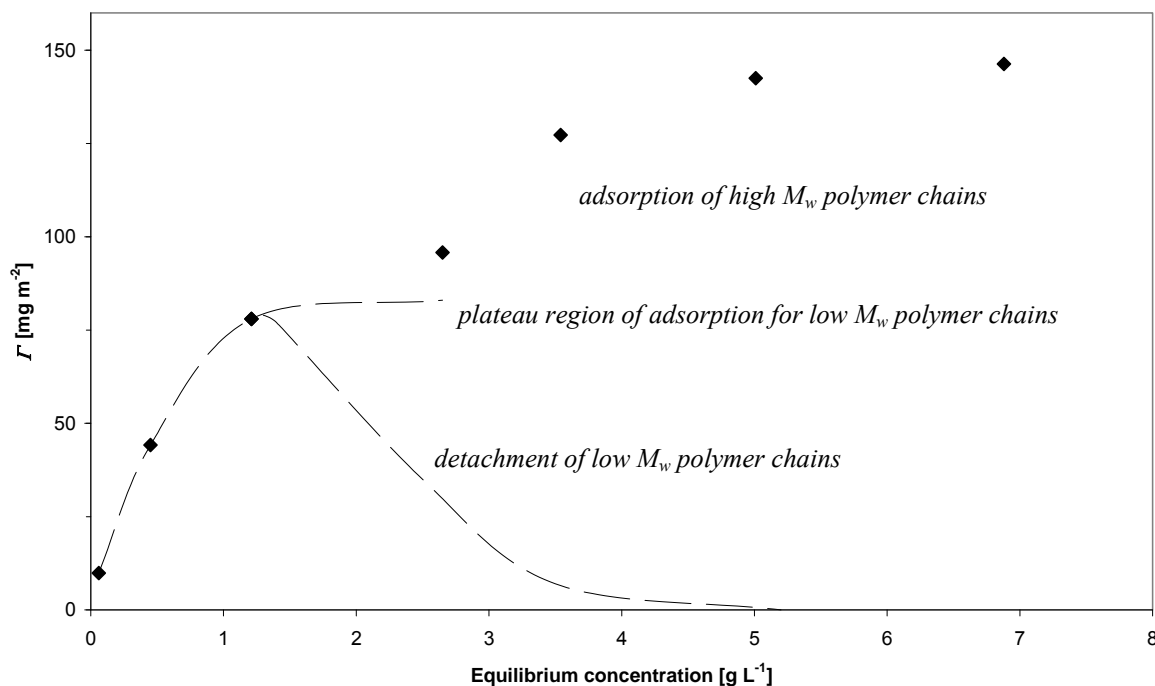
Figure 5.11 *Exchange kinetics between low M_w (dashed lines) and high M_w polymer chains in a 0.5 M NaCl (▲) aqueous solution.*

The possible exchange of low M_w polyDADMAC by high M_w chains can be observed in Figures 5.11 using the isotherm for PE adsorption previously shown in Figure 5.9. The kinetics between the processes is hypothetical. The isotherm curve at low PE concentration indicates a constant adsorbed amount, characteristic of low M_w chains, at low concentration. The adsorbed amount then increases to reach saturation value, characteristic of that of high M_w chains. Figure 5.11 suggests that two adsorption processes occur; (*i*) high M_w polymer chains compete for vacant surface sites as concentration increases; and (*ii*) low M_w polymer chains are dominate at the surface and high M_w polymer chains remain in the solution until a concentration favours their attachment and low M_w chains are displaced.

151

These adsorption processes of PE polymer chains at low concentrations can be investigated if the M_w of the polymer chains in solution are very similar [Furusawa, et al. 1982; 1983a; 1983b; Cohen Stuart, et al. 1986]. Therefore, adsorption of low and high M_w polymer chains in low and high concentrations can be plotted independently.

In Figure 5.11, the overall adsorption can be decomposed into the contributions of low and high M_w polymer chains. The low M_w chains adsorb initially, equilibrium concentrations below 3 g L^{-1}, they desorb such that the total adsorbed amount mass remains constant as long as desorption is incomplete. This may be an important observation because it suggests that both high and low M_w polymer chains occupy the same area per unit mass. The exchange process is also expected to take place rapidly so as to maintain equilibrium between the surface layer and the adsorbed chains. This also implies that the rate of exchange may be controlled by the supply of free high M_w chains from solution. All the isotherms that have been presented within this chapter have indicated a gradual increase in adsorption and only when the concentration range has been extended has it been possible to identify surface saturation. As shown in Figure 5.11, polymers with a wide molecular weight distribution give rounded isotherms with an apparent plateau depending on the average molecular weight and ionic strength [Garvey, et al. 1974; Cohen Stuart, et al 1986].

Considering the possible exchange of the low and high M_w chains at the PS surface, a number of interesting questions have arisen: how strong is the competition between chains of different molecular weight? How fast is the exchange? Is the adsorption preference complete or not? Further experiments should include the analysis by GPC of the adsorption supernatants and the determination of the molecular weight distribution of the unadsorbed polymer.
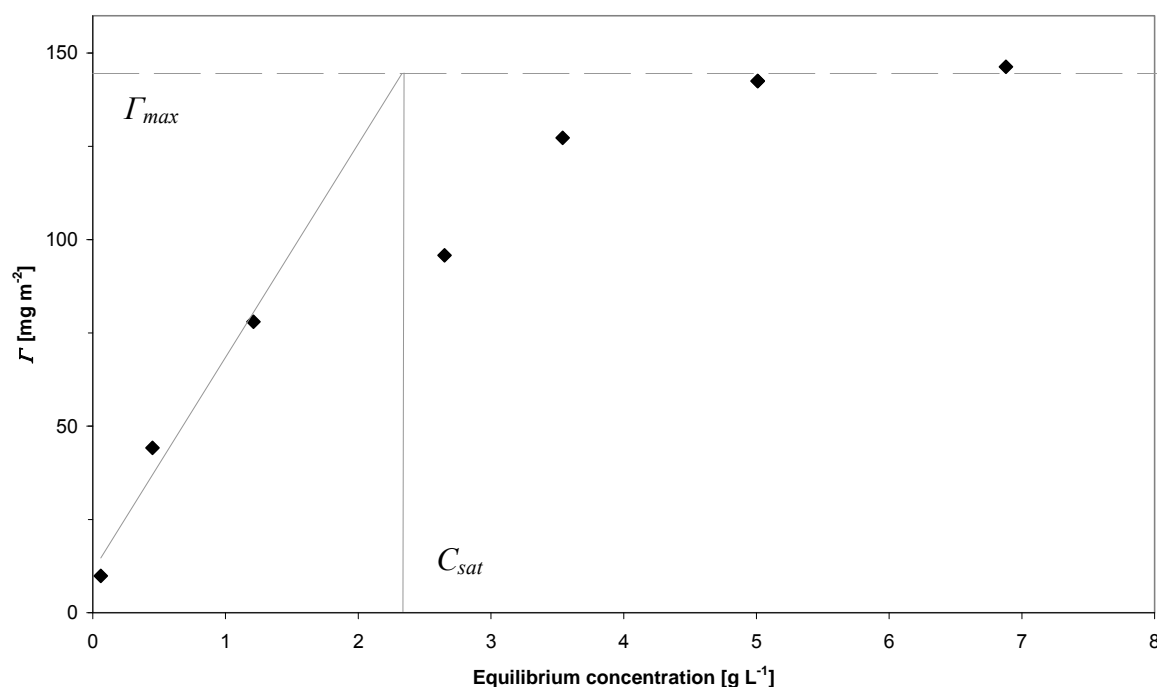
Figure 5.12 *Adsorption of low M_w polymer chains in a 0.5 M NaCl (♦) aqueous solution. Adsorption time 24 hrs.*

It is possible to determine the surface saturation by the fraction of low M_w polymer chains by defining a concentration (C^*) corresponding to the intersection of the extrapolated initial section with the line Γ_{max}. For example, a polymer with a narrow molecular weight fraction would exhibit a so-called high affinity isotherm, characterised by low C_{sat}. In Figure 5.12 the linear plot of short polymer chain adsorption at low concentration can indicate a saturation of the PS surface using a well-defined narrow fraction PE solution. If the polyDADMAC was fractionalised, surface saturation of the PS would be achieved at lower concentration.

To ensure the reliability of the isotherm experiments conducted using hollow PS as a substrate and the Amicon stirred cells process, adsorption experiments were conducted using solid Imperial PS. At present, it is understood that no published results are available with regards to the adsorption of polyDADMAC on hollow PS. The use of solid PS should determine the reliability of the results.
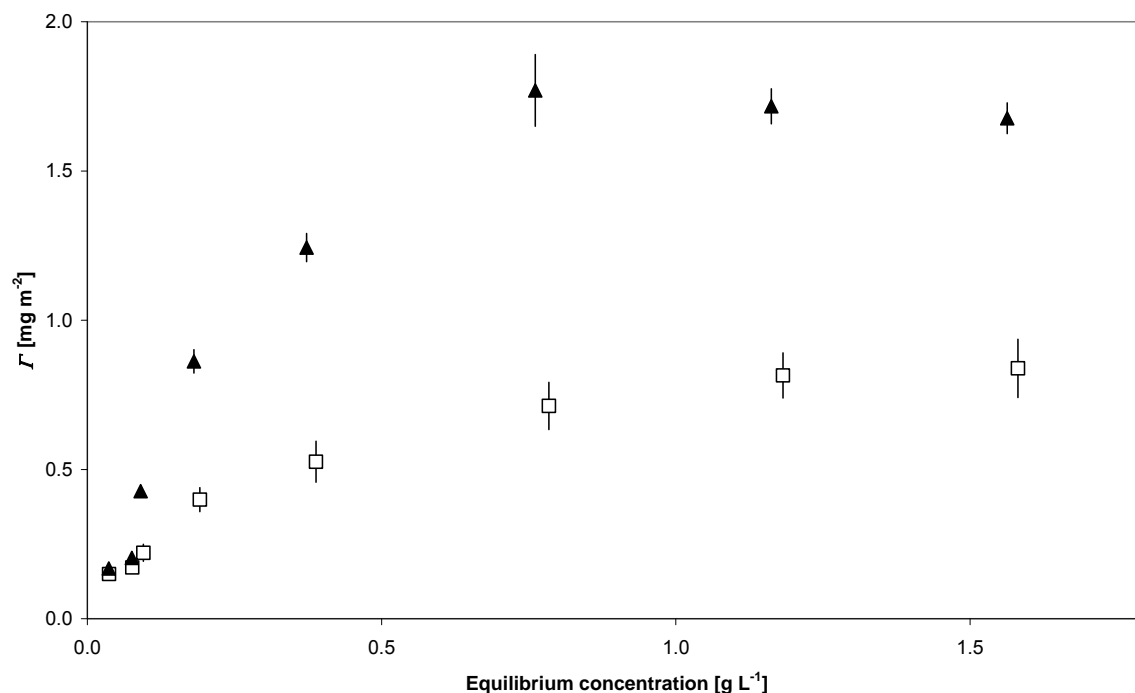
Figure 5.13 *Adsorption of polyelectrolyte on solid Imperial PS. With no added NaCl (□) and in a 0.1 M NaCl (▲) aqueous solution. Adsorption time 20 min.*

All isotherm experiments were conducted in a similar manner as previously described. The adsorption time was 20 min at two different NaCl molar concentrations. The results are presented in Figure 5.13. The results for the adsorption of polyDADMAC on solid PS are in good agreement with published literature data [Cohen Stuart, et al. 1996; Rehmet, et al. 1998; Trotter, et al. 2005; Rusu, et al. 2006]. The isotherm curve in Figure 5.13 has a typical shape with a steep increase at low polymer concentration, especially when the NaCl content was increased. The increase in ionic strength results in additional polymer being adsorbed at the surface with the adsorbed amount being calculated at 1.7 ±0.1 mg m^{-2}. PE concentration required to achieve surface saturation was measured at approximately 1 g L^{-1}.

5.4.2. Determination of polyelectrolyte at the PS surface by NMR

The properties of the surface layers formed by polymers at a substrate depend on factors such as the adsorbed amount, the hydrodynamic thickness, and the number of polymer trains, loops, and tails [Somasundaran, 1997]. These factors can be altered by subtle changes in concentration and even by mixing the components in a different order. In recent years, more detailed information on many polymer systems has been found using a range of more powerful techniques. Small-angle neutron scattering (SANS), dynamic light scattering (DLS), and NMR studies have shown interesting facets in polystyrene or silica and polymer systems [Mears, et al. 1998; Hone, et al. 2002; Dai, et al. 2005].

A Bruker MSL 300 MHz NMR spectrometer, using a Carr-Purcell-Meiboom-Gill (CPMG) pulsed gradient sequence, was used to obtain relaxation decay curve for each sample. The CPMG method is a spin-echo technique and is reported elsewhere [Carr, et al. 1954; Meiboom, et al. 1958]. The time between each pulse was 2 ms, and the recycle delay was 17 s. A total of 4057 data points were collected in each scan, and the signal was averaged over 32 scans for each sample. The T_2 value for each decay curve, $M_y(t)$ against time *(t)*, was then obtained by fitting data to Equation 5.5 using a nonlinear least-squared algorithm, where $M_y(0)$ is the transverse magnetisation immediately after the 90° pulse. All experiments were conducted at the Bristol Colloid Centre, University of Bristol.

$$M_y(t) = M_y(0)e^{-t/T_2}$$ [5.5]

All clean hollow PS microspheres and PE samples were made up from stock solutions, a series of calibrations were also carried out. The study of PS-water-PE interactions had to be preceded by a series of calibrations involving various components alone and in pairs.
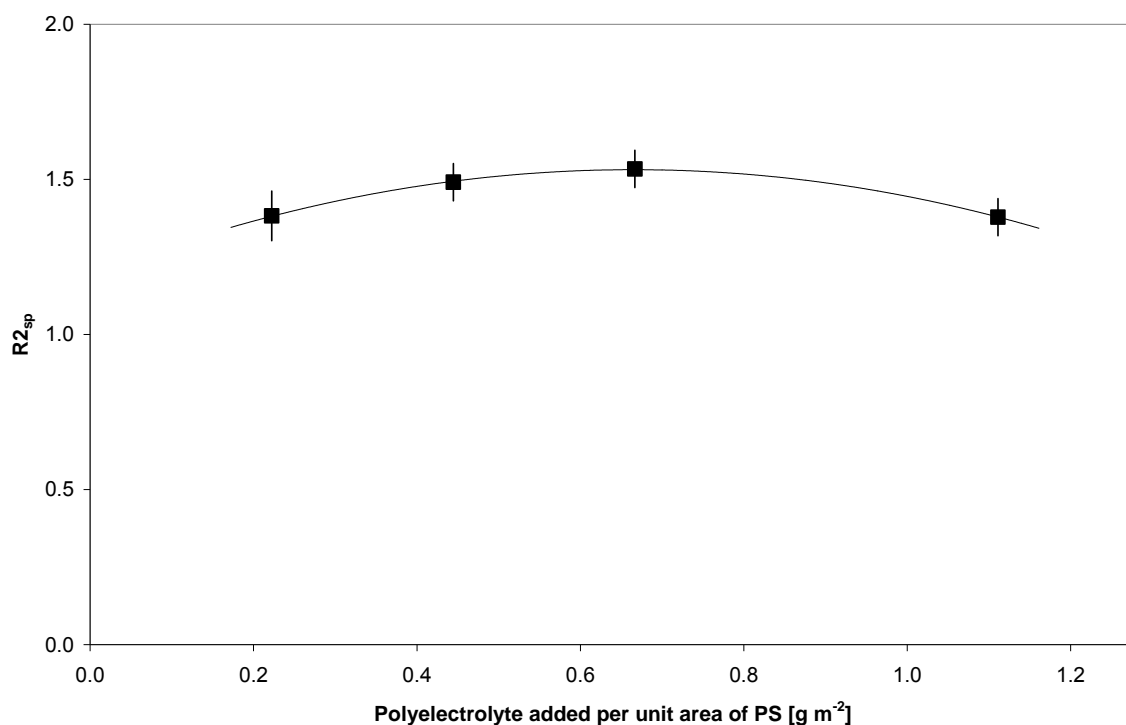
Figure 5.14 *Specific relaxation rate as a function of added polyelectrolyte per unit area of PS in a 0.1 M NaCl aqueous solution.*

PolyDADMAC interactions have been studied in the presence of anionic PS, Figure 5.14 confirms that PE has been adsorbed at the PS surface, this is represented by an increase in the R_{2sp} value. An increase in R_{2sp} implies that either more solvent molecules are bound at the PS surface or those that are bound have remained attached, which suggests a denser, less mobile polymer train layer. Background experiments for the polyelectrolyte dispersed in a 0.1 M NaCl solution measured a specific relaxation rate of $R2_{sp}$ =0.08 ±0.04.

From Figure 5.14 the saturation level of adsorption could be achieved by the addition of ≥0.2 g m^{-2} of polyelectrolyte. Unfortunately, experiments at PE concentrations lower than shown in Figure 5.14 were not conducted due to limited access to the NMR instrument. What was most significant from the NMR experiments was the confirmation of surface saturation by the cationic PE.

Samples containing PS-PE-NaCl were not prone to flocculation or phase separate during the NMR experimental procedure, therefore the data obtained can be considered reliable. Published data with reference to polyDADMAC adsorption at the PS surface is extremely limited, the majority of work being conducted used poly(ethylene oxide) on silica [Flood, et al. 2006; 2007a; 2007b]. However, from the experiments conducted it was possible to verify an increase of water molecules at the PS surface indicating that a PE layer present. It is possible that with the addition of polyelectrolyte (>1.0 g m^{-2}), R_{2sp} decreases, suggesting a weakening of solvent binding within the train layer, corresponding to a gradual desorption of polymer. However, to confirm this phenomenon the concentration range would need to be extended. Although the binding of PE at the PS surface was confirmed, the NMR technique gives no direct information with regards to the polymer structure of the adsorbed layer. Using SANS a full surface volume fraction profile of the adsorbed polymer and detailed information on the size, structure and location of the polyDADMAC molecules could be obtained.

5.4.3. Determination of polyelectrolyte adsorption by electroacoustics

Adsorption isotherm experiments were conducted as previously described, hollow and solid PS substrates were used. Isotherm experiments were conducted over a 24 hr period at two different ionic concentrations, PE was added to PS stock samples with no added NaCl, and experiments were repeated with the addition of 0.1 M NaCl. All samples were transferred to the AcoustoSizer and zeta potential measurements were recorded for each sample. This process was considered more favourable than conducting titration measurements as any excess or free polymer was removed from the sample.
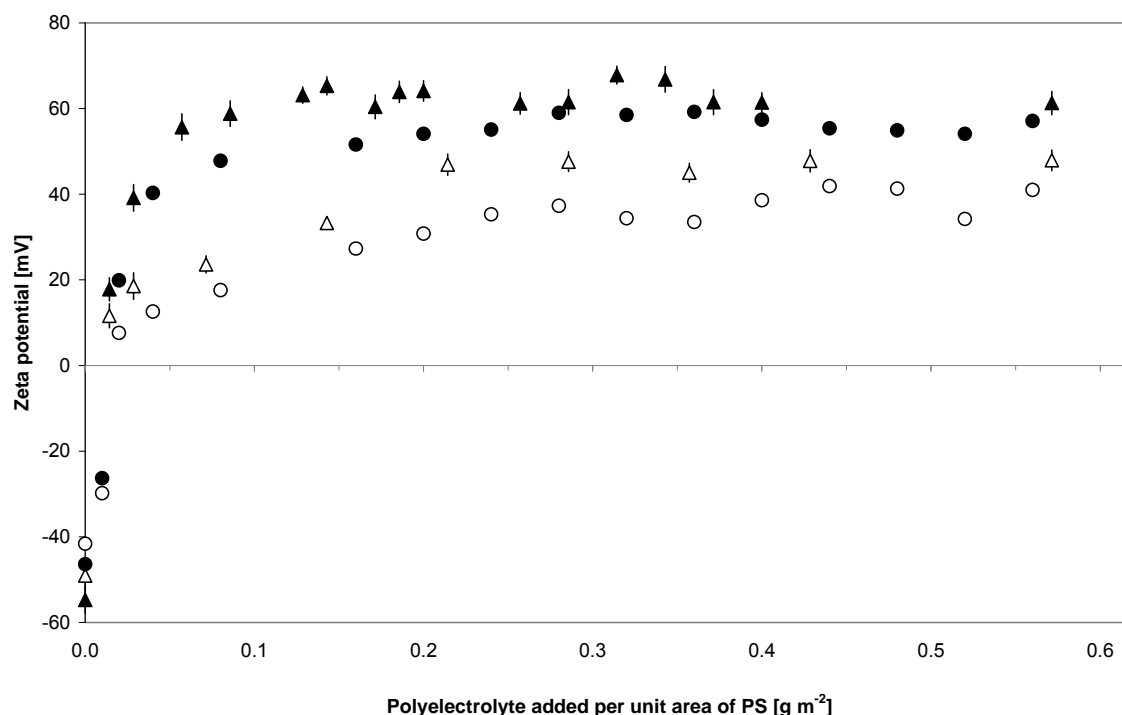
Figure 5.15 *Zeta (ζ) potential as a function of added polyelectrolyte for hollow and solid PS – polyDADMAC systems. Hollow PS; polyelectrolyte with no added NaCl (Δ) and in 0.1 M NaCl (▲); Solid PS; polyelectrolyte with no added NaCl (○) and in 0.1M NaCl aqueous solution (●).*

Figure 5.15 represents ζ-potential as a function of added polyDADMAC and shows the increase of ζ-potential with the amount of added PE, mean data points are shown with the error bars for the hollow PS experiments for ease of interpretation. The abscissa values are calculated by dividing the amount of added PE by the surface area of the PS particles. The initial ζ-potential for the PS substrates and the saturation values are shown in Table 5.8.

Table 5.8 *Adsorbed plateau amounts of polyDADMAC on hollow and solid PS.*

PS Structure	Initial ζ-potential [mV]	Initial pH	Ionic strength NaCl (M)	Adsorption time (hrs.)	ζ-potential at plateau [mV]	pH plateau
Hollow	-49.1 ± 4.3	7.2 ± 0.1	0.0	24	48.1 ± 2.0	6.6 ± 0.1
Solid	-46.4 ± 2.1	7.7 ± 0.1	0.0	24	37.8 ± 3.4	6.2 ± 0.1
Hollow	-54.7 ± 3.2	7.4 ± 0.1	0.1	24	63.5 ± 2.6	6.8 ± 0.1
Solid	-41.6 ± 1.8	7.6 ± 0.1	0.1	24	56.9 ± 1.9	6.4 ± 0.1

As shown in Figure 5.15, the ζ-potential for all samples changed from negative to positive with an increase in PE, the required PE amount added to change ζ-potential of all samples was less than 0.1 g m^{-2}. This change in ζ-potential was evident for both hollow and solid PS in a 0.1 M NaCl environment; this was likely due to the increased amounts of PE at the PS surface. Increasing the NaCl concentration to 0.1 M would lead to a screening effect of the charges along the PE chain, causing the PE to take up a coil configuration in solution [Blaakmeer, et al. 1990; Cohen Stuart, et al. 1991; Decher, et al. 1992]. When adsorbed at the PS surface, the PE chain adsorbs with a loops and tails configuration rather than a flat formation. Hence, more of the PE was adsorbed onto the surface. For PS in a salt free environment (no NaCl added) ζ-potential reached a plateau at a polymer dosage of 0.3 g m^{-2} at 48.1 ± 2.0 mV and 37.8 ± 3.4 mV for hollow and solid PS, respectively. With the addition of 0.1 M NaCl the ζ-potential indicating complete saturation of PS surface was measured at 63.5 ± 2.6 mV and 56.9 ± 1.9 mV for hollow and solid PS, respectively, the added amount of PE required to achieve saturation for both surfaces was approximately 0.15 g m^{-2}. One interesting point worth noting, all zeta potential values are approximately 10 mV higher for hollow PS when compared with solid PS, this may be due to the fact that hollow PS has a lower density value at 1.02 g cm^{-3} compared to 1.05 g cm^{-3} for solid PS.

Based on ζ-potential measurements, approximately 0.2 g m^{-2} of PE would be sufficient to achieve saturation of the hollow PS surface. At a certain concentration of PE the zeta potential no longer increases as the PS particles are now completely covered in polymer. This then is taken to be the optimum amount of PE required to modify the PS surface for kaolin particle adsorption. Any increase in PE amount added after this point does not affect the zeta potential, as the PE remains unadsorbed in solution; hence the zeta potential remains as a plateau. As shown in Figure 5.15, the plateau regions for all the PS systems are not

exactly level, this is because weakly attached PE chains may deadsorb from the PS surface into solution and the resultant zeta potential decreases [Greenwood, 2003; 2007].

5.4.4. Determination of kaolin coverage on hollow PS

Most colloidal particles have a three dimensional shape such as a sphere, the adsorption of inorganic materials that have other shapes such as sheets or plates have not been extensively reported. Inorganic materials that have been adsorbed on to colloidal particles generally include silica [Lvov, et al. 1997; 1998; Caruso, et al. 2001b], montmorillonite [Lvov, et al. 1996], molybdenum oxide [Ichinose, et al. 1998], and laponite [Caruso, et al. 2001c].

A single step shell growth technique was developed for the preparation of kaolin-PS composites. PolyDADMAC would act as the linker between kaolin particles and the PS colloid surface in the preparation of kaolin spherical particles. Based on the functional characteristic properties of the cationic PE at the PS surface, kaolin particles were immobilised on the modified PS surface. The coverage of the shell was controlled by the changing mass ratio of kaolin to PS. By changing the coverage of kaolin, the properties of the core-shell colloids could be changed. Figures 5.16 to 5.21 indicated the change in surface coverage by the increase ratio of kaolin.

Figure 5.16 *Adsorption of fine kaolin particles on PS substrate. Kaolin – PS ratio 0.4:1*

Figure 5.17 *Adsorption of fine kaolin particles on PS substrate. Kaolin – PS ratio 0.5:1*
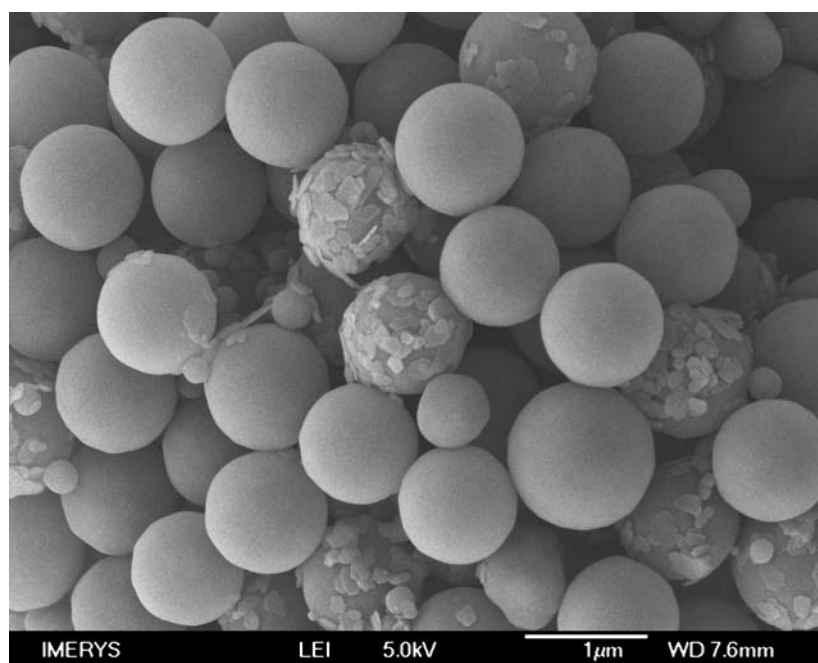
Figure 5.18 *Adsorption of fine kaolin particles on PS substrate. Kaolin – PS ratio 0.75:1*
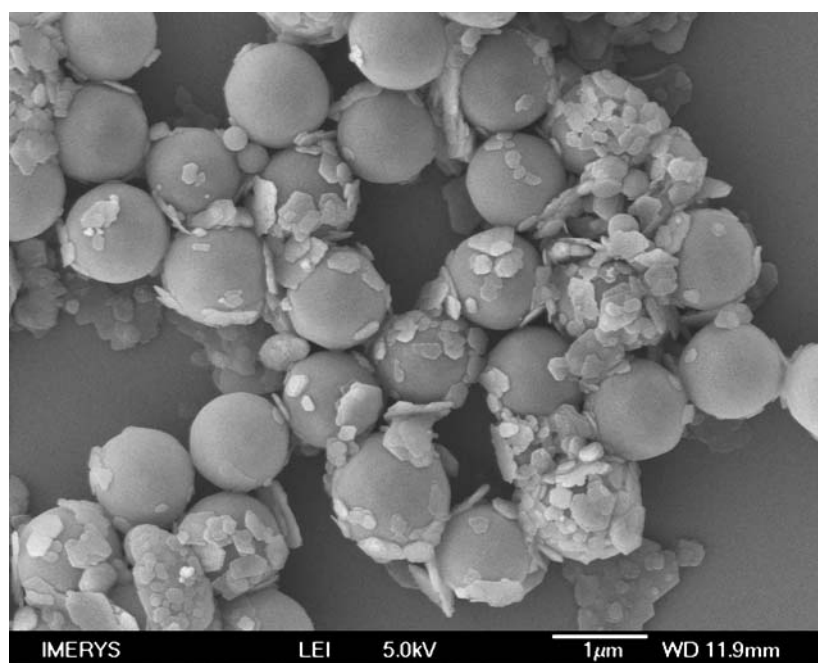
Figure 5.19 *Adsorption of fine kaolin particles on PS substrate. Kaolin – PS ratio 1.25:1*
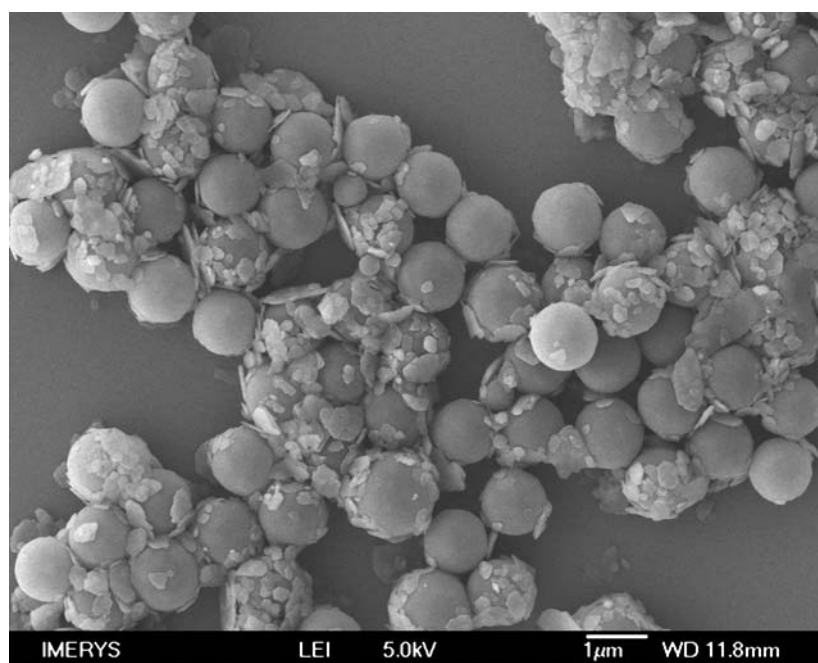
Figure 5.20 *Adsorption of fine kaolin particles on PS substrate. Kaolin – PS ratio 1.5:1*
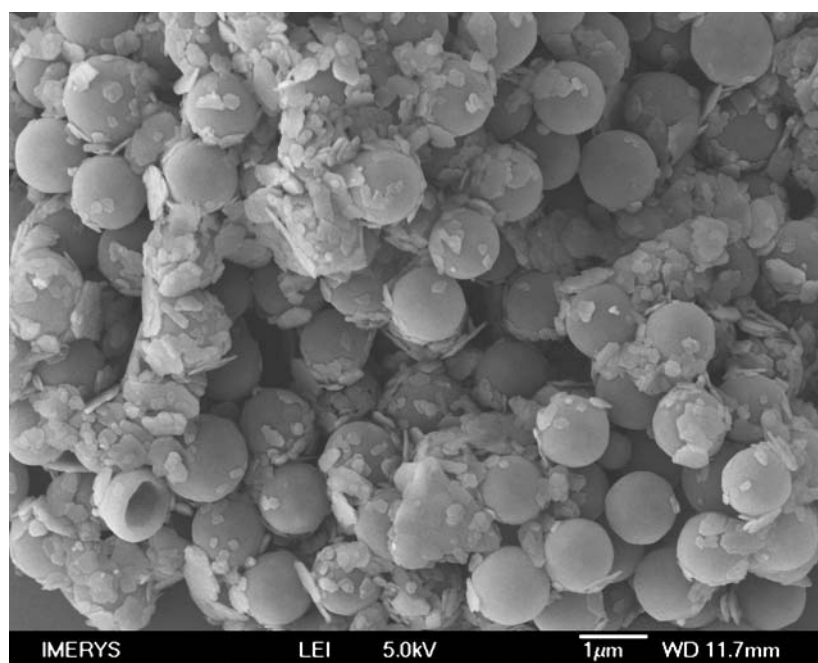
Figure 5.21 *Adsorption of fine kaolin particles on PS substrate. Kaolin – PS ratio 1.75:1*

Kaolin adsorption and surface coverage of the PS surface by fine kaolin particles was determined by SEM. Figures 5.16 to 5.21 are representative images for the kaolin adsorption experiments conducted. Initially, it was observed that all PS-kaolin-NaCl systems were cloudy white. Given time they began to phase separate, the lower phase was grey-white presumably consisted of flocculated PS coated with small kaolin particles, while the upper phase was cloudy white and hence mainly uncoated PS.

Adsorption between rigid components such as clay microplates and colloidal particles has often reported to be unsuccessful [Ariga, 2002]. However, due to the effective surface charge at the PS surface, SEM images indicate the effective electrostatic adsorption of fine kaolin particles. The flat texture of the clay plate may induce efficient contact with the underlying polycations at the PS surface resulting in a stable kaolin formation. The adsorption behaviour of kaolin microplates at the PS surface was expected to be similar to that of organic polyelectrolytes [Iler, 1966; Asano, et al. 1993; Ferreira, et al. 1995; Ramsden, et al. 1995; Ariga, et al. 1997; Lvov, et al. 1998]. The adsorbed plates may reorient at the PS surface to give the most stable arrangement. Adsorption times greater than that of spherical particles are attributed to the rearrangement process. The planar shape of kaolin can produce tight contact with an oppositely charged surface as shown in the SEM images, whereas the spherical shape of silica and gold particles may have limited contacts with a pre-adsorbed PE surface. The limited interaction of spherical particles with the oppositely charged surface leads to fast rearrangement.

The SEM preparation method has obvious influence on the feature of the kaolin-PS structure. In the mentioned method, the PE rendered the PS surface positive enabling the adsorption of kaolin particles. It can be observed that the coverage of the PS surface increased with

increase in kaolin concentration. At a low kaolin ratio value of 0.4 and 0.5:1, no excess kaolin particles were evident, from Figures 5.16 and 5.17 it can be determined that all kaolin particles are adsorbed at the PS surface. There was evidence from Figures 5.19 to 5.21 of kaolin particles bridging between the PS particles resulting in aggregation. However, it was difficult to determine whether this was a feature of the SEM preparation process.

The adsorption of kaolin microplates at the PS surface may resemble a dye assembly [Ariga, et al. 1997]. Most of the dye molecules possess rigid non symmetrical shapes, and their slow adsorption times, 15 to 20 min for saturation, arises from rearrangement of the adsorbed species to attain stable arrangements and effective electrostatic attraction.

Due to aggregation during the sample preparation process, sediment volume experiments were conducted to determine the coverage of PS particles by fine kaolin particles. Sediment volume can be used as an indication of adsorption of small particles onto large particles of opposite charge [Luckham, et al. 1980; Skuse, et al. 1986].
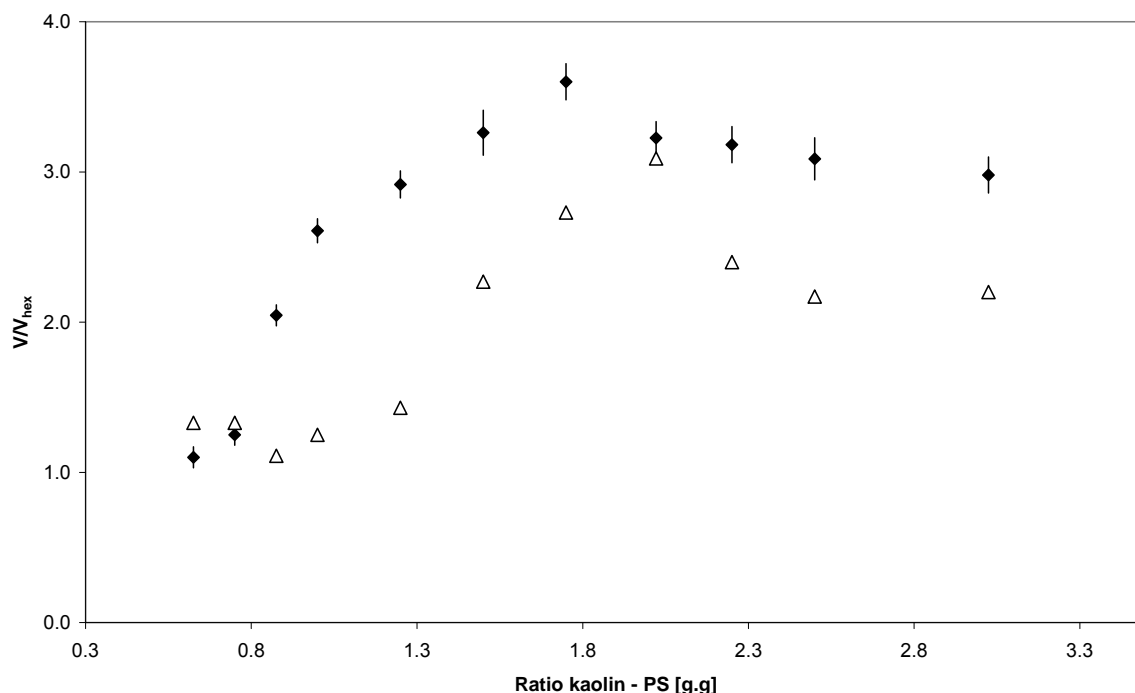
Figure 5.22 *Reduced sediment volume versus ratio for fine kaolin particles adsorbed on PS system. Kaolin in a solution (Δ) and in a solution containing 0.1 M NaCl ($\blacklozenge$).*

The sediment volumes results shown in Figure 5.22 are plotted in a reduced form, where V was the volume occupied by the sedimented large PS particles and V_{hex} was the volume that the same number of particles would occupy in a hexagonally close-packed array [Luckham, et al. 1983]. In Figure 5.22, a maximum occurs for V/V_{hex} at a value corresponding to a coverage of small particles on large particles ~3.6 in a solution containing 0.1 M NaCl, in theory corresponding to a coverage condition where no small particles are in the bulk solution. This would signify surface saturation by small particles, thereafter the value V/V_{hex} decreased and very little further adsorption of small particles take place due to the effect of repulsion between adjacent small particles. An interesting feature with regards to the sediment volume results was that the sediment volumes seem dependent strongly on electrolyte concentration. At lower ionic strength, with no added NaCl, small kaolin particles are adsorbed but only initiate at a higher ratio >1.3, the maximum value of V/V_{hex} was

166

reduced from ~3.5 to ~3. This may reflect the fact that in the absence of NaCl the kaolin particles in solution are more aggregated due to face-to-edge interactions.

At high ionic strength, in the presence of 0.1 M NaCl, the shape of the V/V_{hex} curve changes markedly, corresponding to a high infinity particle adsorption isotherm [Luckham, et al. 1980]. With increasing small particle concentration, adsorption was almost constant until a maximum V/V_{hex} value was obtained. Surface saturation by small particles was affected by the ionic strength of the kaolin solution due to the moderate shielding of the kaolin surface charge, which may provide highly ordered close-packed layered structures. Loose packing within layers was reported for the assembly at none or very little NaCl [Ariga, 2002]. Concentrations as high as 0.5 M NaCl have been reported in the well-layered formations of SiO_2 particles at the PS surface [Caruso, et al. 1998]. With regard to the results presented in Figure 5.22, the large PS and small kaolin particles were mixed directly, by adding kaolin to a PS solution by pipette, thus there will be three competing processes: (i) adsorption of the small particles on the PS; (ii) interactions between the PS particles; and (iii) interactions between the small particles. Since the number of PS particles was, in general, less than that of the small kaolin particles, it can be assumed that adsorption equilibrium would be established at the PS surface before a significant number of particle collisions between them occurred. The role of bridging flocculation by polymer becomes more significant at high NaCl concentrations, at 0.1 M NaCl [Luckham, et al. 1983]. For example particle adsorption determined by V/V_{hex} show values that may imply that multilayer adsorption takes place. With partial coverage by polyDADMAC of the PS surface, bridging flocculation of the smaller particles may occur even in dilute dispersions. Under such conditions, the flocs become adsorbed onto the PS particles which in turn indicate an increase in V/V_{hex} to large values prior to saturation.
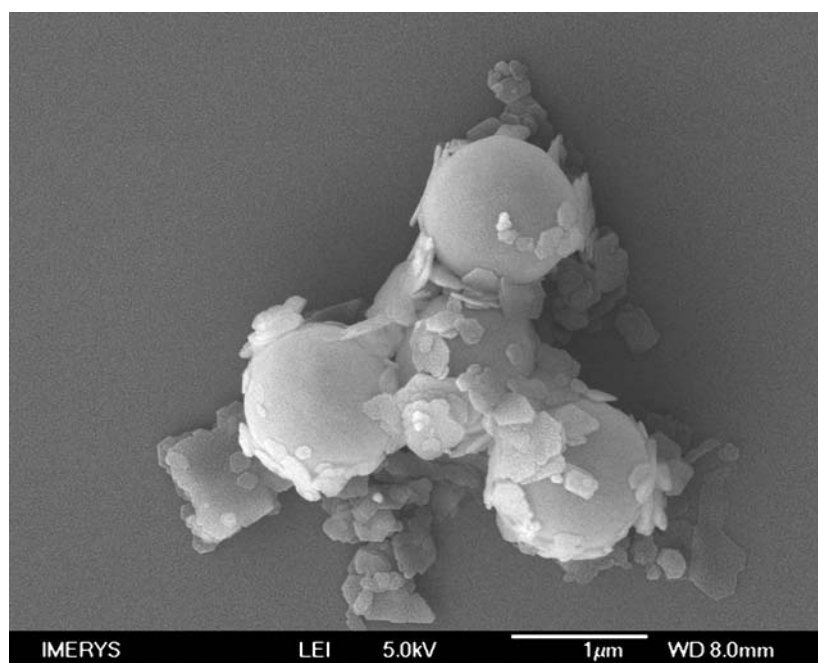
Figure 5.23 *Adsorption of fine kaolin particles on PS substrate. Kaolin – PS ratio 1.25:1*
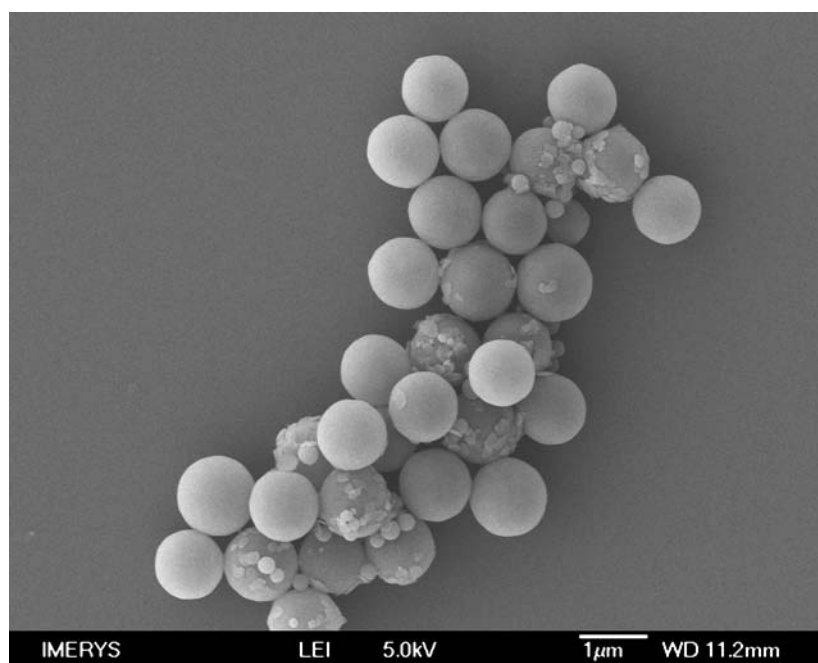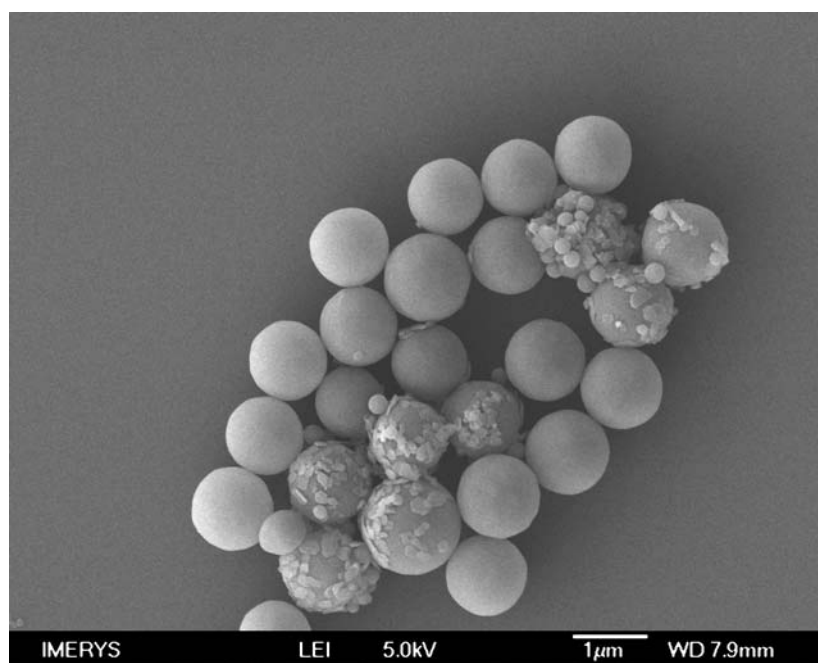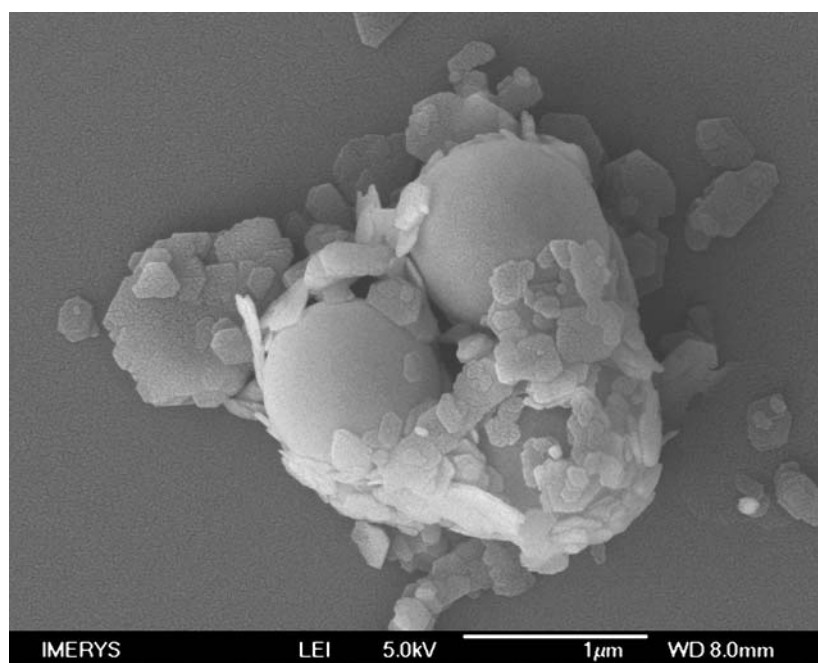

Figure 5.24 *Adsorption of fine kaolin particles on PS substrate. Kaolin – PS ratio 1.5:1*
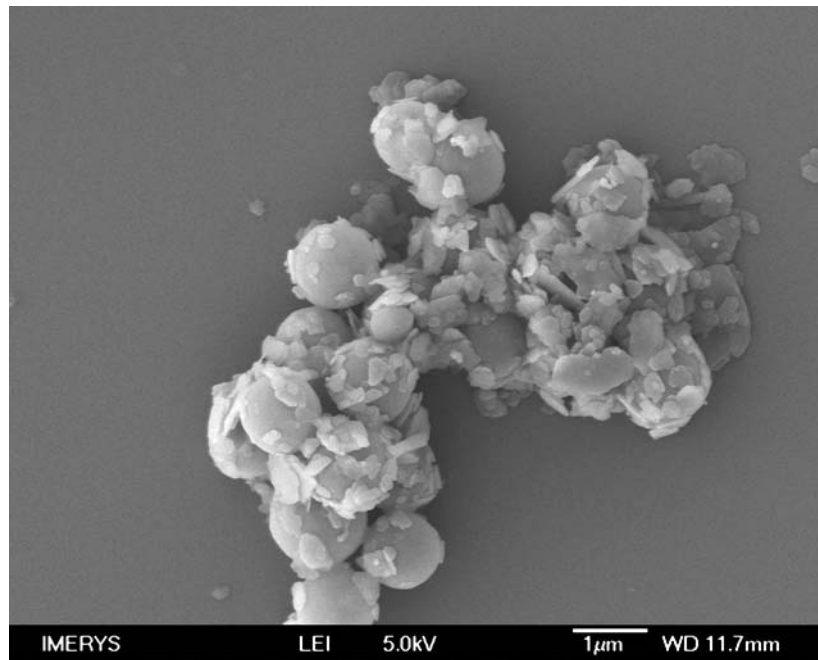
Figure 5.25 *Adsorption of fine kaolin particles on PS substrate. Kaolin – PS ratio 1.75:1*

Figures 5.23 to 5.25 show SEM images of the sediment removed from the measuring cylinders after the sediment volume measurements were conducted. The samples correspond to kaolin adsorption experiments. The images refer to a series in which the concentration of fine kaolin particles are increasing and indicate the open floc structure within the sediment. In Figures 5.23 and 5.24, the kaolin-PS structure exhibited free kaolin at the base of the structure; this may be associated with the breaking of the structure in preparation for the SEM. Unfortunately, it was difficult to draw any real conclusions about the 'openness' of the sediment structures from the SEM images. However, an extended SEM scope of the sediment structures at different kaolin and NaCl concentrations may be more useful in this regard.

5.5. *Conclusions*

Numerous theories predict polymer adsorption isotherms with an initial steep rise, followed by a horizontal plateau. However, the experimental isotherms presented within this chapter with regards to hollow PS usually showed a gradual increase of the adsorbed amount, while a well defined plateau was only observed at high polymer concentrations. It has been recognised that most theories apply only to monodispersed polymers, whereas the experiments conducted, used a commercial polydisperse polyelectrolyte which influenced the isotherm curve. Most isotherm curves presented showed a second slope which was a result of the polymer chain length distribution.

During the polymer adsorption process the surface is covered with short polymer chains. Long chains arrive at the surface, attach, and subsequently spread out to cover to a maximum number of adsorption surface sites. By this process they displace the short chains. If the spreading process occurs quickly, the adsorbed amount will remain low (saturation level of the short chains) as long as long chains are present; the adsorbed layer is in equilibrium. As soon as the short chains have been completely removed, the adsorbed mass increases up to the saturation level for the long chains. This level is higher because longer chains, competing with each other for surface sites, make more loops thereby increasing the adsorbed amount. Adsorption isotherms showed that the presence of NaCl increased the final adsorbed amount but noticeably increased the affinity of the isotherms most specifically at low polyelectrolyte concentrations. Polyelectrolyte adsorption at the PS surface was determined by NMR, an increase in the specific relaxation rate constant R_{2sp} implies an increase in solvent at the PS interface and hence surface polyelectrolyte coverage. By conducting NMR experiments it was possible to determine that with the addition of approximately 0.2 g m^{-2} of polyelectrolyte, the PS surface was saturated and hence cationic in nature. This was

determined by the fact that the specific relaxation rate constant $R2_{sp}$, did not significantly increase with the further addition of polyelectrolyte. The change in surface potential was determined by electroacoustic experiments, bare PS exhibited an initial negative zeta potential, the potential for all the PS samples changed from negative to positive with an increase in polyelectrolyte. As little as 0.1 g m^{-2} of polyelectrolyte was required to change the PS surface potential, however, the zeta potential values indicated surface saturation at 0.3 g m^{-2} for PS in a NaCl free environment. With the addition of 0.1 M NaCl the amount of PE required to achieve saturation was reduced to 0.15 g m^{-2}. The zeta potential of the PS surface in 0.1 M NaCl compared to PS in a NaCl free environment was measured at 63.5 ± 2.6 mV at pH 6.8 ±0.1 to 48.1 ± 2.0 mV at pH 6.6 ±0.1, respectively. This increase of zeta potential can be attributed to the increase of PE at the PS surface.

Kaolin adsorption and surface coverage of the hollow PS surface was determined by SEM images, due to the effective surface charge at the PS surface, SEM images indicated the effective electrostatic adsorption of fine kaolin particles. It was observed that the coverage of the PS surface increases with increase in kaolin concentration. However there was evidence of kaolin particles bridging between PS particles resulting in aggregation. Unfortunately, it was difficult to draw any real conclusions from the SEM images presented as the preparation method was expected to be detrimental to final SEM images obtained. Therefore, sediment volume experiments were conducted to determine the kaolin concentration required to achieve full coverage of the PS surface. The kaolin ratio to achieve surface saturation was dependant upon electrolyte concentration. At low ionic strength, with no added NaCl, kaolin saturation was achieved at a ratio of 2:1 however, in the presence of 0.1 M NaCl, the kaolin ratio required to achieve saturation was reduced to 1.7:1. This change in ratio was likely due

to the moderate shielding of the kaolin surface charge, which may provide highly ordered closed-packed layered structures.

The next chapter discusses the experiments conducted to produce large scale quantities of free-flowing material for calcination. The calcination process would remove the sacrificial core material resulting in hollow microsphere structures.

5.6.   References

Andelman, D., Joanny, J.F. *Surfaces, Interfaces & Films* 5 (**2000**) 1153.

Aoki, K., Adachi, Y. *J. Colloid Interface Sci.* 300 (**2006**) 69.

Ariga, K. Handbook of Polyelectrolytes and Their Applications, Tripathy, S.K., Kumar, J., Nalwa, H.S., (Eds.) American Scientific Publishers, New York, **2002**, p. 127-148.

Ariga, K., Lvov, Y., Kunitake, T. *J. Am. Chem. Soc.* 119 (**1997**) 2224.

Ariga, K., Lvov, Y., Ichinose, I., Kunitake, T. *Appl. Clay Sci.* 15 (**1999**) 137.

Asano, K., Miyano, K., Ui, H., Shimomura, M., Ohta, Y. *Langmuir* 9 (**1993**) 3587.

Binder, K. *J. Chem. Phys.* 79 (**1983**) 6387.

Binks, B.P. *J. Curr. Opin. Colloid Interface Sci.* 7 (**2002**) 21.

Blaakmeer, J., Böhmer, M.R., Cohen Stuart, M.A., Fleer, G.J. *Macromolecules* 23 (**1990**) 2301.

Böhmer, M.R., Evers, O.A., Scheutjens, J.M.H.M. *Macromolecules* 23 (**1990**) 2288.

Borukhov, I., Andelman, D. *Macromolecules* 31 (**1998**) 1665.

Brunauer, S., Emmett, P.H., Teller, E. *J. Amer. Chem. Soc.* 60 (**1938**) 309.

Carr, H.Y., Purcell, E.M. *Phys. Rev.* 94 (**1954**) 630.

Caruso, F. *Chem. Eng. J.* 6 (**2000**) 413.

Caruso, F., Caruso, R.A., Möhwald, H. *Science* 282 (**1998a**) 1111.

Caruso, F., Lichtenfeld, H., Giersig, M., Möhwald, H. *J. Am. Chem. Soc.* 120 (**1998b**) 8523.

Caruso, F., Caruso, R.A., Möhwald, H. *Chem. Mater.* 11 (**1999**) 3309.

Caruso, F., Möhwald, H. *Langmuir* 15 (**1999**) 8276.

Caruso, F., Shi, X., Caruso, R.A., Susha, A. *Adv. Mater.* 13 (**2001a**) 740.

Caruso, F., Spasova, M., Susha, R., Giersig, H., Caruso, R.A. *Chem. Mater.* 13 (**2001b**) 109.

Caruso, R.A., Susha, M., Caruso, F. *Chem. Mater.* 13 (**2001c**) 400.

Castelnovo, M., Joanny, J.F. *Langmuir* 16 (**2000**) 7524.

Clark, S.L., Montague, M.F., Hammond, P.T. *Macromolecules* 30 (**1997**) 7237.

Cohen Stuart, M.A., Cosgrove, T., Vincent, B. *J. Colloid Interface Sci.* 24 (**1986**) 143.

Cohen Stuart, M.A., Fleer, G.J. *Annu. Rev. Mater. Sci.* 26 (**1996**) 463.

Cohen Stuart, M.A., Fleer, G.J., Lyklema, J., Norde, W., Scheutjens, J.M.H.M. *Adv. Colloid Interface Sci.* 34 (**1991**) 477.

Cosgrove, T., Obey, T.M., Vincent, B. *J. Colloid Interface Sci.* 111 (**1985**) 409.

Cosgrove, T., Crowley, T.L., Ryan, K., Webster, J.R.P. *Colloids Surf. A* 51 (**1990**) 255.

Dai, S., Tam, K.C. *J. Colloid interface Sci.* 292 (**2005**) 79.

Decher, G., Hong, J.D., Schmitt, J. *Thin Solid Films* 210 (**1992**) 831.

Decher, G., Hong, J.D. *Makromol. Chem. Macromol. Symp.* 46 (**1991**) 321.

Dobrynin, A.V., Rubinstein, M. *Prog. Polym. Sci.* 30 (**2005**) 1049.

Dukhin, A., Dukhin, S., Goetz, P. *Langmuir* 21 (**2005**) 9990.

Evers, O.A., Fleer, G.J., Scheutjens, J.M.H.M., Lyklema, J. *J. Colloid Interface Sci.* 111 (**1985**) 446.

Ferreira, M., Rubner, M. *Macromolecules* 28 (**1995**) 7107.

Fleer, G.J., Cohen Stuart, M.A., Scheutjens, J.M.H.M., Cosgrove, T., Vincent, B. Polymers at Interfaces. Chapman & Hall, London, **1993**.

Flory, P.J. *J. Chem. Phys.* 10 (**1942**) 51.

Flood, C. *PhD thesis*, University of Bristol, January, **2008**.

Flood, C., Cosgrove, T. *Langmuir* 22 (**2006**) 6923.

Flood, C., Cosgrove, T., Espidel, Y., Howell, I., Revell, P. *Langmuir* 11 (**2007a**) 6191.

Flood, C., Cosgrove, T., Qiu, D., Espidel, Y., Howell, I., Revell, P. *Langmuir* 23 (**2007b**) 2408.

Frish, H.L., Simha, R., Eirich, F.R. *J. Chem. Phys.* 21 (**1953**) 365.

Furusawa, K., Yamashita, K., Konno, K. *J. Colloid Interface Sci.* 86 (**1982**) 35.

Furusawa, K., Yamamoto, K. *Bull. Chem. Soc. Japan* 56 (**1983a**) 1958.

Furusawa, K., Yamamoto, K. *J. Colloid Interface Sci.* 96 (**1983b**) 268.

Garvey, M.J., Tadros, Th.F., Vincent, B. *J. Colloid Interface Sci.* 49 (**1974**) 570.

Gennes, P.G. *Macromolecules* 14 (**1981**) 1637.

Giles, C.H., MacEwan, T.H., Nakhwa, S.N. *J. Chem. Soc.* 786 (**1960**) 3973.

Giles, C.H., Smith, D. *J. Colloid Interface Sci.* 47 (**1974a**) 755.

Giles, C.H., S'Silva, A.P., Easton, I.A. *J. Colloid Interface Sci.* 47 (**1974b**) 766.

Giles, C.H., Tolia, A.H. *J. Appl. Chem.* 14 (**1964**) 186.

Gravely, M.J., Tadros, TH.F., Vincent, B. *J. Colloid Interface Sci.* 49 (**1974**) 57.

Greenwood, R.W. *PhD thesis*, Imperial College, London (**1995**).

Greenwood, R.W. *Adv. Colloid Interface Sci.* 106 (**2003**) 55.

Greenwood, R.W. *Private communications*, University of Birmingham, July (**2007**).

He, X., Ge, X., Wang, M., Zhang, Z. *Polymer* 46 (**2005**) 7598.

Hone, J.H.E., Cosgrove, T., Saphiannikova, M., Obey, T.M., Marshall, J.C., Crowley, T.L *Langmuir* 18 (**2002**) 855.

Hoogeveen, N.G., Cohen Stuart, A., Fleer, G.J., Böhmer, M. *Langmuir* 12 (**1996**) 3675.

Huggins, M.L. *J. Phys. Chem.* 46 (**1942**) 151.

Ichinose, I., Tagawa, H., Mizuki, S., Lvov, Y., Kunitake, T. *Langmuir* 14 (**1998**) 187.

Iler, R.K. *J. Colloid Interface Sci.* 21 (**1966**) 569.

Joanny, J.F. *Eur. Phys. J. B.* 9 (**1999**) 117.

Joanny, J.F., Castlenovo, M., Netz, R. *J. Phys. Condens. Matter* 12 (**2000**) 1.

Kitano, Taguchi, A., Noda, I., Nagasawa, M. *Macromolecules* 13 (**1980**) 57.

Klitzing R., Steitz, R. Handbook of Polyelectrolytes and Their Applications, Tripathy, S.K.,

Koetz, J., Linow, K.J., Philipp, B., Hu, L.P., Vogl, O. *Polymer* 27 (**1986**) 1574.

Kumar, J., Nalwa, H.S., (Eds.) American Scientific Publishers, New York, **2002**, p. 313-334.

Kovacevic, D., van der Burgh, S., de Keizer, A., Cohen Stuart, M.A. *Langmuir* 18 (**2002**) 5607.

Langmuir, I. *J. Amer. Chem. Soc.* 38 (**1916**) 2221.

Luckham, P. *Private communications*, Imperial College, London, July (**2007**).

Luckham, P., Vincent, B. *Colloids Surf.* 1 (**1980**) 281.

Luckham, P., Vincent, B. *Colloids Surf.* 6 (**1983**) 119.

Lvov, Y., Ariga, K., Onda, M., Ichinose, I., Kunitake, T. *Langmuir* 12 (**1996**) 3038.

Lvov, Y., Ariga, K., Onda, M., Ichinose, I., Kunitake, T. *Langmuir* 13 (**1997**) 6195.

Lvov, Y., Rusling, J.F., Thomsen, D.L., Papadimitrakopolus, F., Kawakami, T., Kunitake, T. *Chem. Comm.* 11 (**1998**) 1229.

Lvov, Y., Ariga, K., Onda, M., Ichinose, I., Kunitake, T. *Colloids and Surf.* 146 (**1999**) 337.

Lyklema, J. *Colloids Surf.* 10 (**1984**) 33.

Marshall, J.C., Cosgrove, T., Leemakers, F., Obey, T.M., Dreiss, C.A. *Langmuir* 20 (**2004**) 4480.

Mears, S.J., Cosgrove, T., Obey, T., Thompson, L., Howell, I. *Langmuir* 14 (**1998**) 4997.

Meiboom, S., Gill, D. *Rev. Sci. Instrum.* 29 (**1958**) 688.

Muthukumar, M. *J. Chem. Phys.* 86 (**1987**) 7230.

Netz, R.R., Joanny, J.F. *Macromolecules* 32 (**1999a**) 9013.

Netz, R.R., Joanny, J.F. *Macromolecules* 32 (**1999b**) 9026

Netz, R.R., Andelman, D. *Physics Reports* 380 (**2003**) 1.

Papenhuijzen, J., van der Schee, H.A., Fleer, G.J. *J. Colloid Interface Sci.* 104 (**1985**) 540.

Papenhuijzen, J., van der Schee, H.A., Fleer, G.J. *J. Colloid Interface Sci.* 111 (**1986**) 446.

Qiu, D., Flood, C., Cosgrove, T. *Langmuir* 24 (**2008**) 2983.

Ramsden, J., Lvov, Y., Decher, G. *Thin Solid Films* 254 (**1995**) 246.

Rehmet, R., Killmann, E. *Colloids and Surf. A* 149 (**1999**) 323.

Rusu, M., Kuckling, D., Möhwald, H., Schönhoff, M. *J. Colloid Interface Sci.* 298 (**2006**) 124.

Scheutjens, J.M.H.M., Fleer, G.J. *J. Phys. Chem.* 83 (**1979**) 1619.

Scheutjens, J.M.H.M. Fleer, G.J. *J. Phys. Chem.* 84 (**1980**) 178.

Schmidt, B., Wandrey, C., Freitag, R. *J. Chromatogr. A* 944 (**2002**) 149.

Shiratori, S.S., Rubner, M.F. *Macromolecules* 33 (**2000**) 4213.

Shubin, V., Linse, P. *Macromolecules* 30 (**1997**) 5944.

Skuse, D.R., Tadros, T.F., Vincent, B. *Colloids Surf.* 17 (**1986**) 343.

Somasundaran, P., Krishnakumar, S. *Colloids Surf. A* 491 (**2002**) 123.

Steeg,van der, H.G.M., Cohen Stuart, M.A., Keizer, de, A., Bijsterbosch, B.H. *Langmuir* 23 (**1990**) 2301.

Stockton, W.B., Rubner, M.F. *Macromolecules* 30 (**1997**) 2717.

Tripathy, S.K., Kumar, J., Nalwa, H.S. Handbook of Polyelectrolytes and Their Applications. American Scientific Publishers, New York, **2002**.

Trotter, H., Zaman, A., Partch, R. *J. Colloid Interface Sci.* 286 (**2005**) 233.

Vincent, B. *Adv. Colloid Interface Sci.* 4 (**1974**) 193.

Vincent, B., Young, C.A., Tadros, Th.F. *Faraday Discuss. Chem. Soc.* 65 (**1978**) 296.

Weigel, F.W. *J. Phys. A: Math. Gen.* 10 (**1977**) 299.

Chapter Six: Removal of sacrificial core material by calcination

6.1.   Introduction

Spray drying technology possesses the advantage that microsphere products can be obtained in a less complicated step, the fabrication process can be easily controlled and the size distribution of the product is relatively narrow, in recent years, this method has been widely used to produce dry powders, granules or agglomerates.

In this chapter, low-density hollow microspheres are prepared by a two-step process, the process is optimised and the final product is characterised. The initial process is to spray dry a kaolin-PS slurry, followed by a calcination process to remove the PS sacrificial core material. This process has a number of advantages when preparing hollow microsphere structures including; the fabrication process can be controlled easily, the morphology can be controlled, the size distribution is narrow and the efficiency of the fabrication process is high. Initial experiments reported in Chapter 3 indicated that drying the kaolin-PS suspension in a Carbolite fanned laboratory oven at 80°C for 24 hr resulted in aggregated particles. After calcination at a high temperature, approximately 1000 °C, and sonification the samples showed very few discrete microspheres. The challenge therefore was to prepare a free-flowing material for calcination. For the purpose of economising resources and requiring high efficiency, spray drying technology was used to fabricate a microsphere free-flowing material that once calcined would fabricate hollow microspheres.

6.2. *Background*

When the aim is to obtain good spherical microspheres, templating or layer-by-layer self assembly technology is necessary, by contrast, when the aim is to gain high efficiency, high temperature liquid feed spray pyrolysis may be more appropriate. However, the wide applications of hollow microspheres have been limited, mainly because of the disadvantages associated with the process techniques, such as the high cost, time-consuming or relatively complex fabricating systems. Spray drying, which has been applied in many regions of industry as a facile one-step continuous suspended particle processing operation, is a simple technique for preparing solid and hollow microspheres. Compared with these methods mentioned, it has numerous advantages. For example, the size distribution of the product is relatively narrow and the requiring size of the products can be controlled by adjusting the spray drying parameters. Several articles describing the spray drying process have been published in recent years [Corrigan, 1995; Luo, et al. 1995; Cao, et al. 2000; Tsapis, et al. 2002; Muzzarelli, et al. 2004; Soottitantawat, et al. 2007; Du, et al. 2008; Sun, et al. 2008; Wang, et al. 2009; Kho, et al. 2010].

The spray drying method converts a solution or suspension containing solids, into a powder in a one step process. Spray driers consist of the following components: the feed delivery system, an atomiser, a heated air supply, drying chamber(s), solid-gas separators and product collection system [Corrigan, 1995]. The rate of feed delivered to the atomiser is adjusted to ensure that each spray droplet is completely dried before it comes in contact with the collection chamber. Appropriate adjustment of the drying air temperature and flow rate is also essential. The physical properties of the product produced are also dependent on the type of the atomiser used. Drying chambers may also be designed to provide a specific air stream that results in the mixing of the drying air with feed droplets. Separation of the solid

material from the gas is usually accomplished by means of a cyclone separator. Product may be recovered not just from the cyclone separator but also from the drying chamber and from the filter. In some cases the final dried product may have different properties depending where the sample is collected. The chamber product will have been subjected to longer heat exposure in a less dry environment.

Spray dryers are mainly classified by the air-flow type and by the atomiser type. The three common configurations are co-current, counter-current, and mixed flow, describing the relationship between directions of air and product flow through the drying chamber. Three commonly used atomisers are rotary or wheel, which create droplets using a rapidly spinning disk; pressure, in which liquid is pumped at high pressure through a nozzle; and pneumatic or two-fluid, where a high pressure air jet disintegrates a stream of liquid that is pumped at low pressure. Atomiser performance directly influences the particle size of the dried particles. Typical droplet mass median diameters range from less than 10 μm to upwards of 100 μm, which translates to a typical dry particle diameter range of 0.5 to 50 μm [Vehring, 2008].

Particle morphology can vary with different conditions of the spray drying process, the exact relationship between the influencing factors and the morphology of the products have been discussed by numerous authors [Walton, et al. 1999a; 1999b; Liang, et al. 2001; Bertrand, et al. 2005; Wang, et al. 2009]. However, the effect of process variables upon particle morphology, for example, the residence time of particles within the drying chamber, the method and conditions of atomisation, the type of spray-air contact, drying temperature and feed parameters such as concentration, temperature and the degree of feed aeration, are difficult to assess in general terms. This is due to the lack of information within the literature (a result of commercial confidentiality) and the specific drying nature of most materials.

Morphological phenomena may be difficult to classify with respect to the spray drying operation, as the physical and chemical nature of the particle shell or crust formed during drying determines the type of particle drying behaviour. For given drying conditions particles may inflate, distort, shrivel or fracture depending upon the rheological properties, porosity or non-porosity of the particle shell or crust.

High temperature (inlet air temperature) accelerates the droplet evaporation and so the solvent on the surface is removed quickly. Likewise, the liquid flow is too slow to maintain uniform solid concentration, so the inner voids of granules form easily and increase with the temperature increasing. Therefore, increasing inlet air temperature causes a reduction in bulk density due to the hollow structure forming easily. However, some irregular structures, such as porous and fractured structures, will appear as evaporation rates are so fast at extremely high temperature. But if the inlet temperature is relatively low, the liquid cannot be evaporated completely, so the moisture of the granule products will increase.

Atomised pressure plays an important role in controlling the product morphology. In general, the larger the atomised pressure, the smaller the mean particle. In addition, moisture of products decrease with increase of atomised pressure due to its effect on the mean particle size. This may be explained by two reasons, large surface area and a short diffusing distance of the small particle. High atomised pressure usually causes irregular morphology, while a low atomised pressure may make the slurry accumulate on the internal wall of the spray dryer. Therefore, appropriate atomisation pressure should be controlled in order to obtain the regular morphology.

The feed rate has a direct relationship with the size of the powders. In general, the more enhancing the feed rate is, the bigger the droplet size, and thus the larger the powder size is. It is known that the tendency of obtaining hollow microsphere structures increases with the initial droplet radius increasing and thus larger droplets are favourable for the formation of hollow structures. The reason is that the migration distance of bigger droplets for the liquid or particles is larger, and thus solid concentration is not uniform with the highest on the surface of the droplet.

The slurry concentration at a low solid content usually forms hollow structures because the solvent in the droplets moves to the surface more easily at this condition. However, other morphologies usually appear under this condition due to surface tension. By contrast, the spherical shape of the powders is good with high solid content slurry [Cao, et al. 2000; Wang, et al. 2007], but the tendency of forming hollow structures decreases. The flow ability of slurry is also affected by the size of the primary powders. Generally, the smaller the primary particle, the more easily the internal voids forms. This is because the flow ability of larger powders is better than that of smaller size, so the slurry with small powders diffuses more slowly and forms hollow structure more easily.

Different additives have different characteristics, so they are considered to have different roles in controlling the powder morphology. Adding the correct additive to the slurry may modify its dispersion and viscosity and thus result in obtaining powders with different characteristics. Consequently, appropriate additives are often selected carefully for different materials [Walker, et al. 1999; Wang, et al. 2007].

Selecting the correct spray drying parameters is crucial to obtaining the required morphology, the relationship between the influencing factors and the morphology is generally understood but the exact relationship between them is not a part of this research thesis. Based on the internal reports by Imerys Minerals Ltd., the process parameters can be selected based on previous industrial projects [Hamer, 2006].

In recent years, increasing attention has been focused on spray drying to prepare hollow microspheres and numerous structures have been prepared successfully. A direct synthesis of silica-coated Fe_2O_3 hollow spherical particles has been reported [Tartaj, et al. 2001]. A nozzle atomiser was used to obtain fine and uniform powders, the solvent evaporated from the surface of the droplets at the temperature of 250 °C. It shows that the preparing process has some advantages, such as reproducibility, simplicity, continuity and rapidity. In addition, the characteristics of the products can be modified by changing the silicate content or by controlling the drying temperature.

A spray drying technique was developed to synthesise hydroxyapatite (HA) with a nanocrystalline structure [Luo, et al. 1995]. The method involved the initial preparation of an aqueous solution using inorganic water-soluble compounds. The precursor powder mixture was subsequently formed by atomisation by spray drying the aqueous solution. Calcination of the spray dried powder resulted in HA spherical particles with an approximate 2 μm diameter.

A systematic study was performed to determine how the characteristics of granules prepared by spray drying aqueous alumina slurries are influenced by processing parameters: binder type, solids loading, deflocculant level and spray-dryer type [Walker, et al. 1999]. The study

was extensive and described how yield stress was dependent on deflocculant level, solids loading, and binder type. The viscosity limit was dependent on solids loading and binder type. Granules containing the more-highly-adsorbed binder (PEG Compound 20M) were of lower density than those containing PEG-8000. For fixed slurry solids loading, granules of lower density were produced as the slurry yield stress increased. Granules prepared using a deflocculant which corresponded to high slurry yield stress, were of solid morphology, whereas, for higher deflocculant levels, hollow granules that contained a single large open crater were formed. Spray-dryer type did not influence whether granules were hollow or solid.

Particles were also prepared in a spray dryer from carbohydrates with different solubility and crystallisation propensity, including lactose, mannitol, and sucrose/dextran [Elversson, et al. 2005]. The droplet size during atomisation (7 to 19 μm), the concentration of the feed solution as well as the solubility of the solute affected the particle size during the spray drying of carbohydrate solutions. Furthermore, the particle formation was also reported to be influenced by the crystallisation propensity of the carbohydrate, thus indicating that hollow particles are more likely to be formed by amorphous carbohydrates, such as lactose and sucrose/dextran whereas porous particles are more likely to be obtained from crystalline carbohydrates, such as mannitol.

Opened hollow microspheres of organoclays were prepared via spray drying the suspension of modified Na^+-montmorillonite (Na^+-MMT) with alkylsulfonate [Du, et al. 2008]. Spray drying conditions were kept constant: inlet air temperature 180 °C, outlet air temperature 80 °C, feed rate 1.3 kg/hr. The formation of the novel structure is related to the intercalated structure of the organoclays. When the organoclays have a large interlayer spacing, the

aggregates can intercalate across each other to form a solid shell around droplets during spray drying, and the opened hollow microspheres were formed. However, for the organoclays with small interlayer spacing and pure Na^+-MMT, the aggregates only overlap each other to form a porous shell during spray drying, thus no hollow microspheres were formed.

Hollow spherical aggregates of biocompatible silica particles are also reported to have been manufactured by a spray drying method [Cheow, et al. 2009]. The factorial design approach was employed to determine the spray drying formulation parameters to produce an ideal morphology. The feed concentration, the feed pH, and the ratio of the gas atomising flow rate to the feed rate were identified as the three parameters with the most significant effect on the granule morphology. In general, it was reported that spray drying at a low feed, less than 1% w/w, concentration results in a smaller particle size (d_{50} ~3 μm) and relatively uniform particle size distribution, particularly at a low pH. Spray drying at a higher feed concentration, greater than 1% w/w, results in a larger particle size (d_{50} ~5 μm) and negatively affects the particle size distribution. However, it can be considered non-economical to commercially manufacture hollow microspherical structures at a low concentration feed.

6.3.   Experimental Process

6.3.1. Materials

For the spray drying experiments kaolin FK-8489, hollow PS microspheres and polyDADMAC were used as in previous experiments.

6.3.2. Spray Drying System

The suspension was spray dried in a Niro Mobile Minor™ Spray Dryer (GEA Niro Inc., Soeborg, DK) equipped with a pneumatic rotary atomiser. Atomisation was created by the feed of compressed air at a pressure of 7.5 bar. The air-flow within the spry dryer was in a co-current direction. The rotating disk size was of 50 mm diameter and 14 mm height. The rotating disk contained 24 vanes, dimensions 4 mm diameter. The spray dryer was composed of a cylindrical chamber with 800 mm inside diameter and 620 mm height, followed by a conical chamber of 650 mm height with a 60° angle. The inlet air temperature was controlled at 125 ±10 °C. The rotational speed of the atomiser was controlled at 30,000 rpm. The feed rate of the solution was approximately 29 ±2 mL/min, and the outlet temperature was recorded at 314 ±6 °C. The finished outlet powder collected was stored at room temperature until calcined.

6.3.3. Characterisation of microsphere product

After calcination, powder samples were kept in a humidifier until characterised. From the final yield samples were characterised by using the techniques previously mentioned.

Bulk density and specific gravity measurements were conducted following a standard laboratory procedure as outlined by ASTM C29/C29M and D854. Specific gravity of the calcined microspheres was measured using water displacement in a pcynometer with special care taken to remove all air from the sample. The bulk density was determined by filling the powder into a 5 mL measuring cylinder. The particle bulk density that can help characterise the degree of hollowness was determined by a continual tapping process of the measuring cylinder for a period of 2 min. The tap density was measured using five replicates of 4 mL

each. The measured tap density was corrected by a factor of 0.79^{-1} to obtain the effective bulk density (ρ_{eff}) taking into account the imperfect particle packing of the powder samples. The effective bulk density values allow the determination of the Carr's compressibility index (CI), where Carr's index values below 25 indicate free-flowing particles and values above 40 indicate cohesive particles having poor flowability [Vanbever, et al. 1999; Kho, et al. 2010].

$$CI = \left(\frac{\rho_{eff} - \rho_{bulk}}{\rho_{eff}} \right) \times 100\% \qquad [6.1]$$

Apart from determining the flowability of the powder, the bulk density values presented in the results section represent the tap bulk density that is comparable to published commercial data.

6.3.4. Spray drying of kaolin slurry

Control experiments were conducted using the FK-8489 kaolin powder, the fine kaolin material was spray dried with and without the addition of the cationic polymer solution. The experiments were designed to determine the effect of the polymer as a binder within the kaolin slurry during the spray drying process. A number of control experiments were conducted to determine the effect of the polyelectrolyte within the slurry. Kaolin fine particles were also spray dried without the addition of hollow PS microspheres, this enabled a comparison of final bulk density values and resulting structures. The process parameters of the experiments are shown in Table 6.1. Fine kaolin particles were washed, filtered and dispersed in distilled water and magnetically stirred. A known amount of kaolin was added to solution while under agitation. The suspension containing fine kaolin particles was magnetically stirred for 60 min to ensure the mixing of the polymer and kaolin particles. This

process was repeated with the addition of polyDADMAC, a 2 g L^{-1} solution was prepared and added to the kaolin suspension. The suspension was magnetic stirred for 60 min and was feed into the spray dryer at a constant speed, the rotational speed of the atomiser, the inlet and outlet temperature were kept constant. Product recovery was measured at 84 ±4%.

Table 6.1 *The process parameters for spray drying of kaolin microspheres.*

Inlet Air Temperature (ºC)	Addition of Polyelectrolyte	Slurry Concentration (wt%)	Slurry Feed Rate (rpm)	Ratio (K:PS)	
				Kaolin	*PS*
125 ± 10	Yes	20	15 ± 1	1	0
125 ± 10	No	20	15 ± 1	1	0

The formation of hollow microspheres is schematically illustrated in Figure 6.1 [Sun, et al. 2008]. The process was identical with regards to the fabrication of low density kaolin microspheres where the slurry contained specific concentrations of PS material.
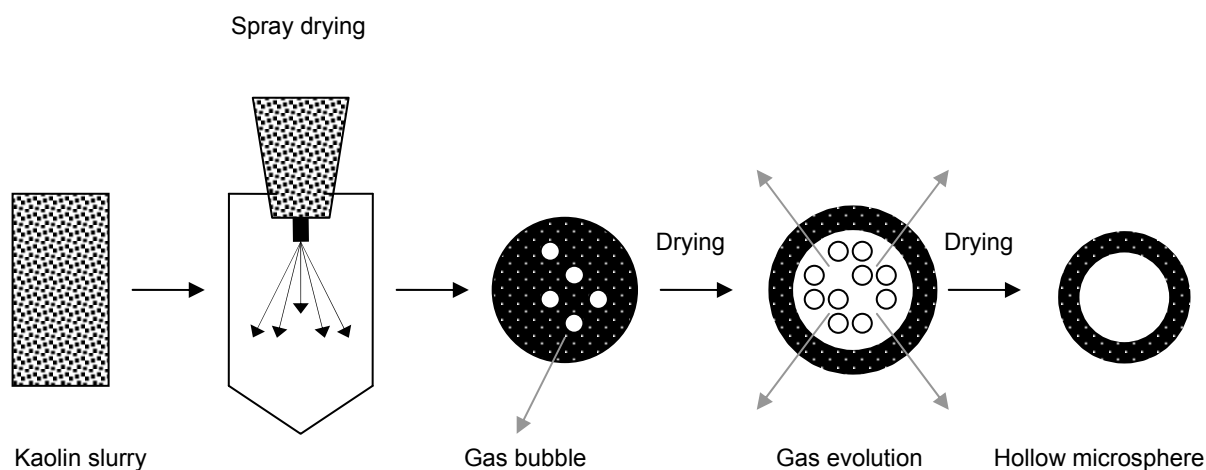
Figure 6.1 *Schematic illustration of the formation of hollow microspheres by spray drying.*

6.3.5. Spray drying of kaolin-PS slurry

The particle suspension was prepared by blending and rehydrating the kaolin powder, FK-8489, in a suspension containing dispersed hollow PS microspheres. Firstly, hollow PS microspheres were cleaned by ultrafiltration and redispersed by using distilled water. The anionic PS microspheres were rendered cationic by the addition of a 2 g L^{-1} of polyDADMAC solution. The suspension was magnetically stirred for 60 min. Fine kaolin particles were washed, filtered and dispersed in distilled water and magnetically stirred. A known amount of kaolin in suspension was added to the PS microsphere solution while under agitation. The suspension containing hollow PS microspheres and fine kaolin particles were magnetically stirred for 60 min to ensure the adsorption of kaolin at the PS surface. The slurry feed was fed into the spray dryer at a constant speed, the rotational speed of the atomiser, the inlet and outlet temperature were kept constant. This process removed the liquid phase and resulted in a free-flowing powder. The process parameters of the experiments are shown in Table 6.2. Product recovery was mainly determined by powder collection efficiency, measured at 83 ±3%. Material loss was due to attachment of sprayed droplets and dry powder to the wall of the drying chamber.

Table 6.2 *The process parameters for spray drying of kaolin low density microspheres.*

Run	Inlet Air Temperature (ºC)	Slurry Concentration (wt%)	Slurry Feed Rate (rpm)	Slurry Ratio (K:PS)	
				Kaolin	*PS*
1	125 ± 10	20	15 ± 1	1.0	0
2	125 ± 10	20	15 ± 1	1.0	1
3	125 ± 10	20	15 ± 1	1.5	1
4	125 ± 10	20	15 ± 1	2.0	1
5	125 ± 10	20	15 ± 1	3.0	1
6	125 ± 10	20	15 ± 1	4.0	1

6.3.6. Calcination of free-flowing material

The free-flowing material collected was calcined in a Carbolite muffle furnace (Carbolite Ltd., UK) using the standard procedure developed in the previous section. Experiments are listed in Table 6.3.

Table 6.3 *The calcination process parameters of kaolin microspheres.*

Run	Ratio (K:PS)		Calcination Temperature (ºC)			
	Kaolin	*PS*				
1	1.0	0	850	1000	1200	1400
2	1.0	1	850	1000	1200	1400
3	1.5	1	850	1000	1200	1400
4	2.0	1	850	1000	1200	1400
5	3.0	1	850	1000	1200	1400
6	4.0	1	850	1000	1200	1400

6.4.   Results and Discussion

During spray drying, particle formulation occurs in the following steps: (1) atomisation of the feed slurry to droplets, (2) deceleration of the droplets to the speed of the drying air that is circulated through the drying chamber, (3) drying of the droplets, and (4) separation of the dried material from the air stream [Walker, et al. 1999]. Droplet drying occurs in two main stages, after the very brief period required for the droplet temperature to reach equilibrium with the drying air, during which negligible drying occurs, drying proceeds at a constant rate as long as the surface remains saturated with liquid. After some critical point, the drying rate decreases as the liquid-vapour interface recedes into the porous material until almost all liquid is gone. This is sometimes referred to as a shrinking wet core [Mezhericher, et al. 2008; Handscomb, et al. 2009; Handscomb, et al. 2010]. For most types of wet-processed systems, the critical point is considered to be the point where particles come in contact, and shrinkage stops. When drying is very rapid, the surface of a droplet may reach the critical point while particles in the interior remain separated by liquid. For droplets containing solids, the critical point is when solids form at the droplet surface, and a shell is formed. The drying rate decreases because of the lower permeability of the shell. When suspended solids are present, the critical point is less well defined, because a rate-limiting shell may form before particles in the interior of the droplet come into contact with each other.

The temperature of droplets of suspensions of solids in liquids during the constant-rate period is equal to the wet-bulb temperature (interface temperature) [Walton, et al. 1999b; Makkinejad, 2001]. If dissolved solids are present, the temperature is slightly increased because of the decreased vapour pressure. During the decreasing-rate period, the subsurface temperature may increase because of the hindered mass transport. Internal pressure may

increase when the internal temperature increases, depending on the nature of the surface layer, the droplet may expand or rupture [Charlesworth, et al. 1959; Walton, 2002].

For most ceramic systems, ideal granules should be uniform solid or hollow spheres; coalescence of drying droplets can produce granules with an irregular shape or cluster of smaller granules. As droplets break free from the atomised feed stream, the shape oscillates before a stable sphere is formed. Formation of a rigid surface layer before the shape stabilises can lead to elongated, pancake, or donut-shaped granules. If the rigid surface layer forms before atomisation is complete, needle like granules can result [Mahjdjoub, et al. 2003; Bertrand, et al. 2005]. A correlation between apparent surface tension and granule shape has been discussed [Charlesworth, et al. 1960; Lukasiewicz, 1989; Cao, et al. 2000; Mujumdar, 2002] but the apparent surface tension of suspensions is not clearly understood as a physical property and the observed influence upon the particles is still under review.

The specific mechanisms leading to formation of hollow granules [Duffie, et al. 1953; Walker, et al. 1999] include; (1) ballooning, where internal pressure causes the droplet to expand; (2) moisture evaporating at a faster rate than diffusion of solids back into the droplet interior, leaving air voids; (3) suspended solids being drawn to the droplet surface as liquid migrates because of capillary action; and (4) entrained air in the feed slurry persisting as voids. Formation of a partial internal vacuum may accompany the third mechanism. For some materials, this partial vacuum leads to the collapse of granules, leaving irregular, apricot-like shapes. Ballooning can produce thin-walled hollow microspheres that are larger than the original droplets, or eggshell-like fragments [Shaw, 1990]. Of interest, a model review of the spray drying process is presented in Appendix D, describing various simplified

models that can be used to link material properties and process parameters to particle and the resultant product attributes.

One common problem that occurs with ceramic slurries regardless of the atomiser type was that granules often form large craters during the spray drying process. The craters are blowholes formed from the release of internal pressure, and are more likely to form when air temperature was high, binder content or molecular weight was high, and solids loading are low. It has also been suggested that craters formed are due to inward collapse of the granule shell because of partial vacuum created as material moves towards the surface during the third mechanism listed above [Shaw, 1990]. The collapse of the shell has been attributed to the fact that the trailing side of the droplet is less exposed to hot gases, so dries at a slower rate, and has a thinner surface layer. This can be compensated for by reducing particle migration by increasing solids loading, which reduces the constant-rate drying period so more water is removed by vapour-phase transport [Crosby, et al. 1958; Lukasiewicz, 1989].

6.4.1. Control experiments

Suspension preparation is believed to be more important than the operational parameters of the spray dryer to influence the characteristics of the dried powder (Cao, et al. 2000). Control experiments were conducted, initial characterisation of the resulting microsphere structures prepared by spray drying of fine kaolin particles and calcination were determined by SEM, bulk density and particle size measurements. The SEM images in Figures 6.2 to 6.9 present a representative scope of control experiments and the resulting kaolin microsphere structures.
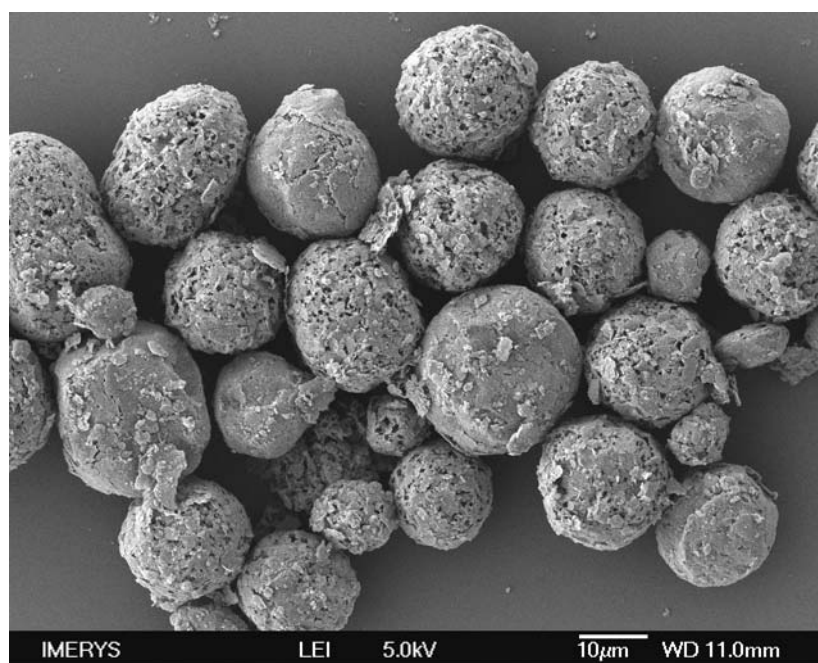
Figure 6.2 *Spray dried kaolin microspheres calcined at 850 ℃ for 60 min.*
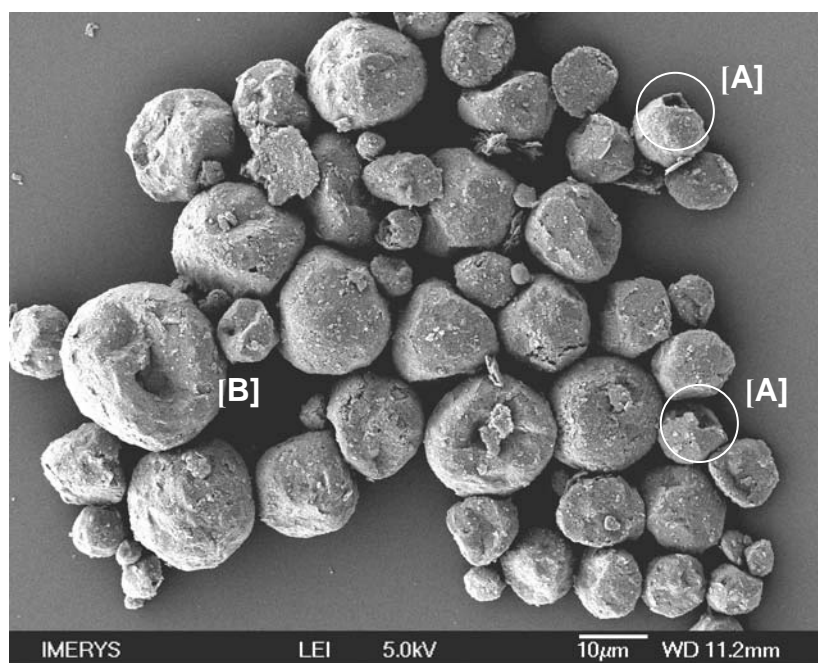
Figure 6.3 *Spray dried kaolin microspheres calcined at 1000 ℃ for 60 min.*
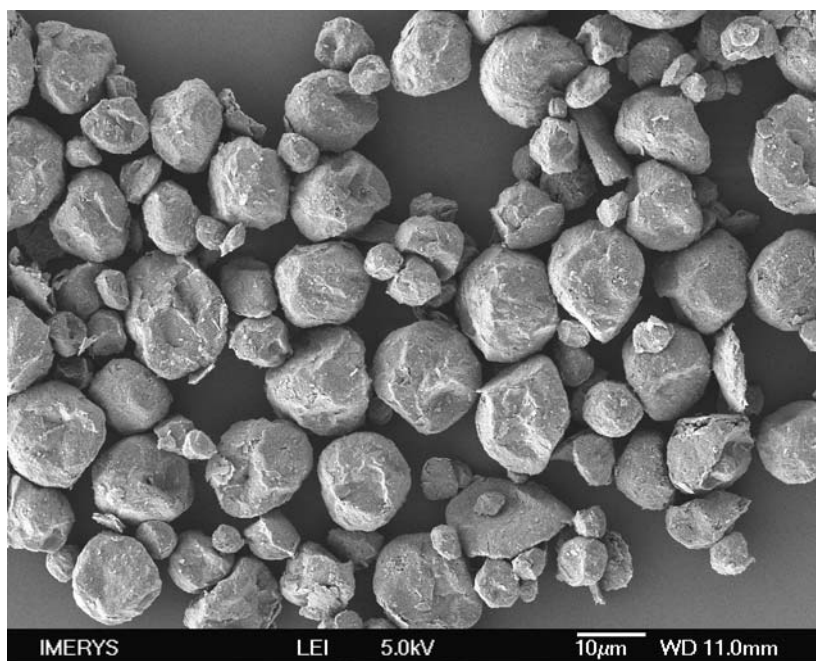
Figure 6.4 *Spray dried kaolin microspheres calcined at 1200 ºC for 60 min.*
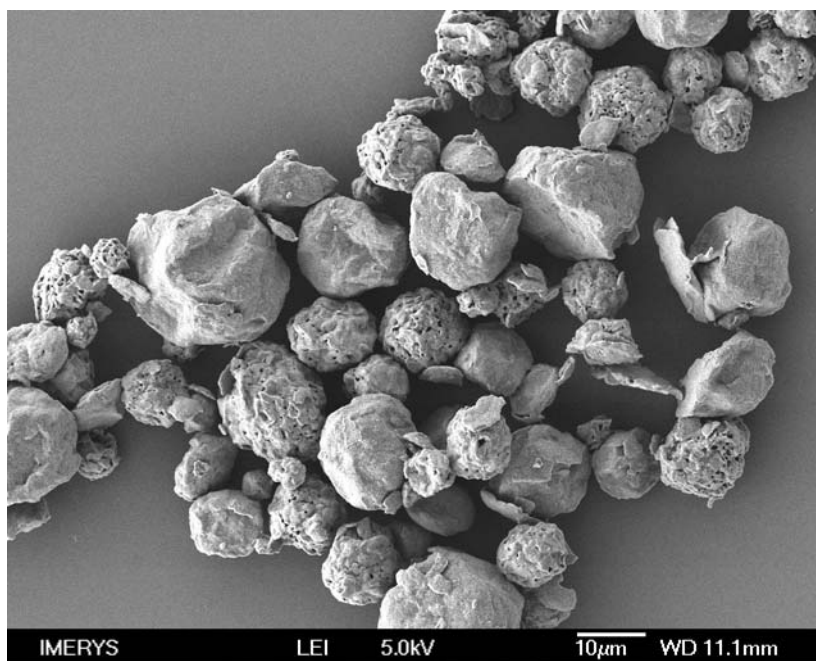
Figure 6.5 *Spray dried kaolin microspheres calcined at 1400 ºC for 60 min.*
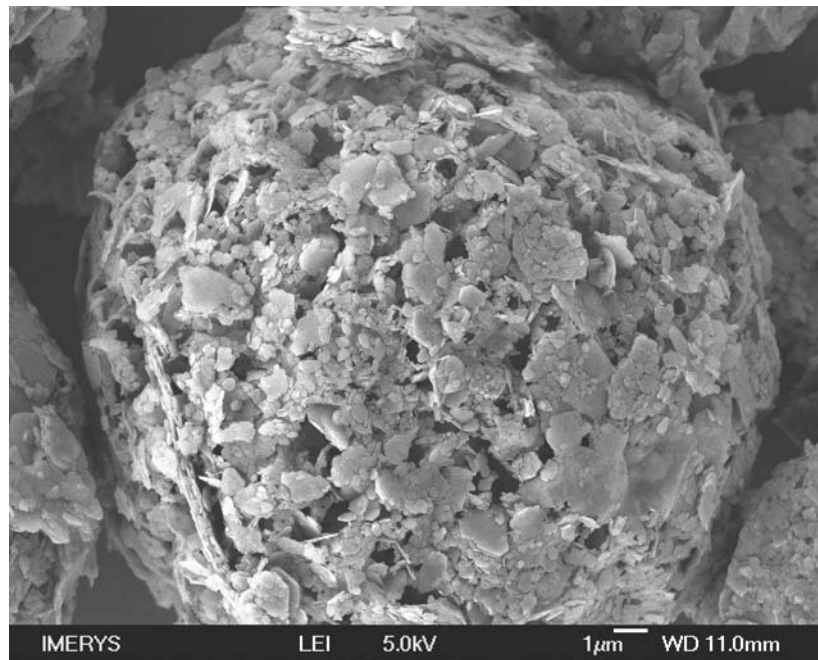
Figure 6.6 *SEM image of kaolin microsphere structure calcined at 850 ºC.*
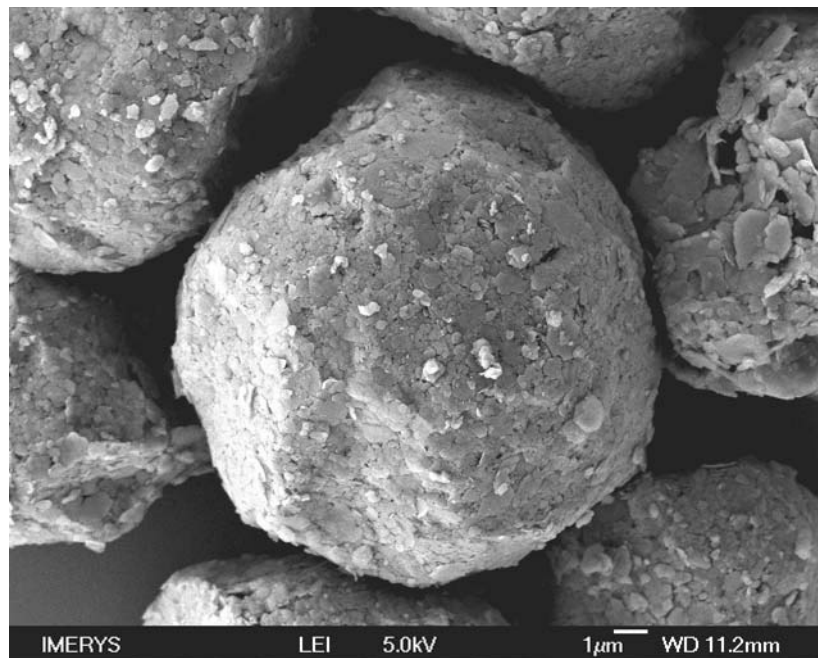
Figure 6.7 *SEM image of kaolin microsphere structure calcined at 1000 ºC.*
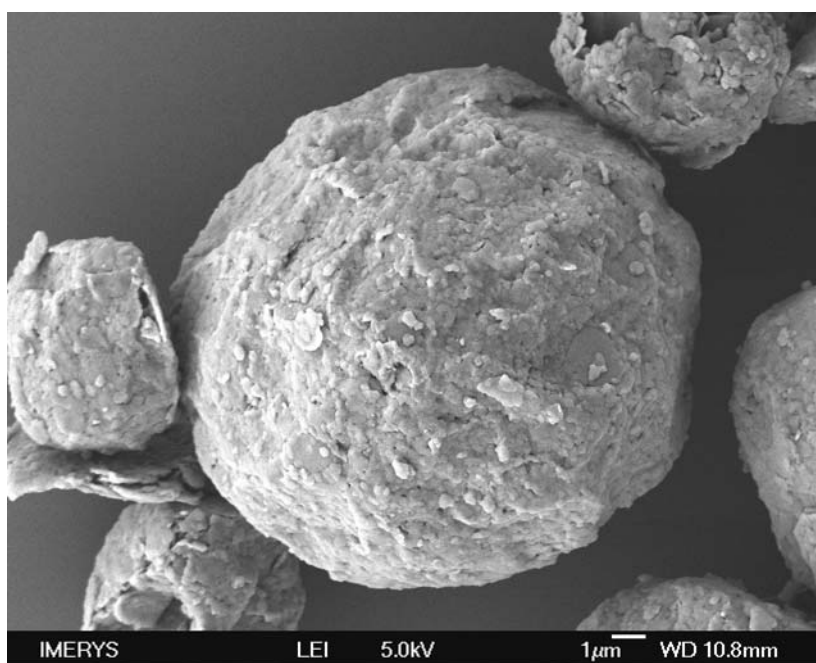
Figure 6.8 *SEM image of kaolin microsphere structure calcined at 1200 ℃.*
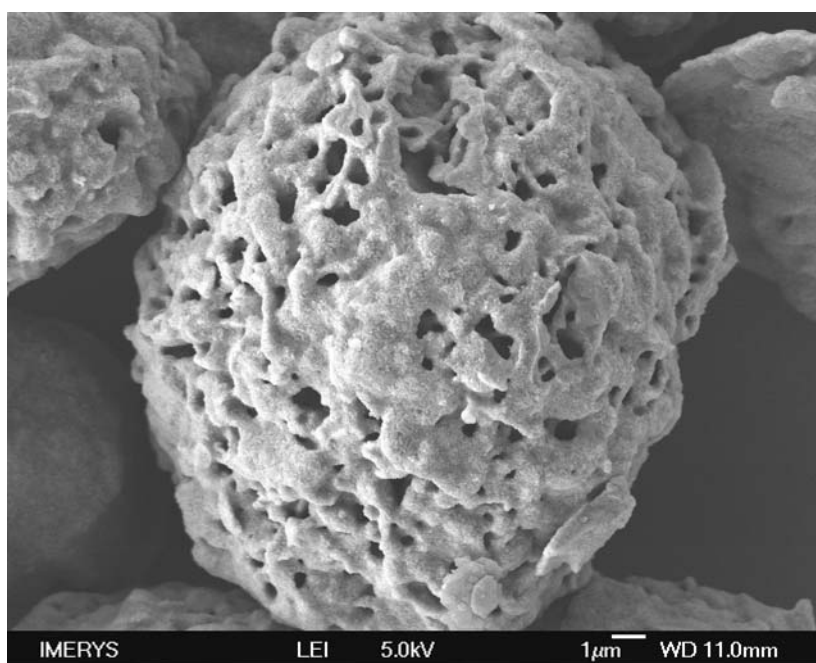
Figure 6.9 *SEM image of kaolin microsphere structure calcined at 1400 ℃.*

Figure 6.2 shows the SEM image of kaolin microspheres prepared by spray drying and calcined at 850 ºC for 60 min. The spray dried and calcined microparticles are spherical and have open pores on the surface. At higher magnification, Figure 6.6, the open pores on the surface of the microsphere are more evident. These open pores may be attributed to the internal pressure building up within the microsphere particle and release through the kaolin shell of the microsphere. Figure 6.3 shows a number of interesting microsphere structures, most particles in the 10 to 15 μm range are roughly spherical, but some have teardrop or dumbbell shapes (indicated by letter B), a common feature of spray dried ceramic materials [Walker, et al. 1999]. Figure 6.3 also shows individual spherical particles exhibiting crater formations (indicated by A) this may be a result of the shell collapsing under high pressure or from the release of gases.

As the calcination temperature was increased the microparticles tend to loose their spherical shape and decrease in particle size. This was likely due to the shrinkage of the microparticles as the calcination temperature reaches 1200 ºC. Figure 6.5 shows a variation in particle structures, large granule particles in the 15 μm range are irregular in shape whereas particles in the 10 μm exhibit an open porous structure. This change in structure was due to the shrinkage of the particles and the possible collapse of the internal matrix structure. Another reason for a decrease in particle size would be the transition phase of the kaolin when calcined above 1000 ºC into α-Al_2O_3.

Figures 6.6 to 6.9 are of a higher magnification and show the changes in the microsphere surface of individual particles due to calcination. Most interesting is the smooth kaolin shell formation of the microspheres when calcined at 1000 and 1200 ºC as exhibited in Figures 6.7 and 6.8. The smooth surface of the spherical particles may be attributed to the addition of the

197

cationic polyelectrolyte resulting in tightly combined kaolin shell formation [Frey, et al. 1984]. This characteristic of the microsphere surface would result in good flowability of the final powder product [Cao, et al. 2000].

Over a wide range distribution of sizes, granule shape was similar. The SEM images have indicated that at the extreme ends of the size distribution highly irregular granules exist. SEM images also showed that most of the microparticles kept their spherical shape after spray drying and calcination.

SEM images showed no significant difference in the final microsphere structures when experiments were conducted without the addition of a cationic polyelectrolyte. However, when used in kaolin spray drying experiments the polyelectrolyte would be expected to act as an organic binder keeping the particles combined with each other during the spray drying process. In ceramic processing polyvinyl alcohol and cellulose derivatives are the most common binders [Whittemore, 1945; Yamashita, et al. 1998]. It has been observed that the addition of binder during the spray drying of ceramic materials results in a decrease in powder density [Wild, 1954]. Bulk density and mean particle size measurements for the spray dried and calcined kaolin microspheres are presented in Table 6.4.

Table 6.4 *Properties of spray dried kaolin microspheres.*

Run	Calcination Temperature (°C)	Addition of Polyelectrolyte	Bulk Density (g/cm³)	Specific Gravity (g/cm³)	Particle Size d_{50} (µm)
1 a	850	Yes	0.30 ± 0.01	2.40 ± 0.03	15.6 ± 0.4
1 b	1000	Yes	0.55 ± 0.02	2.54 ± 0.02	14.2 ± 0.8
1 c	1200	Yes	0.69 ± 0.03	2.65 ± 0.02	13.1 ± 0.4
1 d	1400	Yes	0.80 ± 0.01	2.68 ± 0.02	11.5 ± 0.5
1 e	850	No	0.32 ± 0.01	2.42 ± 0.02	16.8 ± 0.5
1 f	1000	No	0.58 ± 0.01	2.55 ± 0.02	15.1 ± 0.6
1 g	1200	No	0.70 ± 0.02	2.64 ± 0.02	12.0 ± 0.5
1 h	1400	No	0.81 ± 0.03	2.69 ± 0.02	11.9 ± 0.5

In Table 6.4 the relationship between the addition of a binder, bulk density, particle size and the calcination temperature was summarised. The operational parameters which are expected to influence the final structure include; feeding rate, feeding pressure and drying temperature, all these parameters were predetermined and remained constant for all experiments and are listed in Table 6.1.

The effect of a cationic polymer added to the kaolin slurry resulted in a slight decrease in the microsphere bulk density. When calcined at 1000 °C, kaolin microspheres produced with the addition of the polymer exhibited an average bulk density of 0.55 g/cm³ and a mean particle size of 14.2 µm compared to 0.58 g/cm³ and 15.1 µm. The reduction in mean particle size of microspheres resulting from a slurry containing the polymer was likely due to the tight packing of fine kaolin particles as the shell was formed during the spray drying process [Wild, 1954]. However, this phenomenon could not be determined by the use of SEM images. The specific gravity of the kaolin microspheres also changed due to calcination, working with a kaolin starting material having a specific gravity of 2.64 g/cm³, a minimum

value of 2.40 g/cm^3 was measured when calcined at 850 ºC. This reduction may be attributed to the build-up of pressure within the microsphere particle during calcination and the formation of molecular voids within the kaolin shell structure and between kaolin particles. At the temperature 1400 ºC, kaolin microspheres that were formed with and without the addition of polyelectrolyte had measured specific gravity values greater than the starting kaolin powder, 2.68 g/cm^3 and 2.69 g/cm^3 respectively. However, this increase in specific gravity was attributed to the formation of mullite and christobalite, a theoretical specific gravity value of a stoichiometric mixture of mullite and christobalite produced by kaolinite decomposition has been reported at 2.79 g/cm^3 [Reike, et al. 1942; Bridson, et al. 1985].

Even though, the influence of a cationic polymer was not further studied at various concentrations, for the application of spray drying kaolin-PS slurries the addition of a cationic polymer would be considered favourable ensuring homogeneity and, consequently the state of dispersion of the suspension [Takahashi, et al. 1996; Walker, et al. 1999; Fengqiu, et al. 2000; Mahdjoub, et al. 2003; Bertrand, et al. 2005].

6.4.2. Hollow and low density kaolin microspheres

The increase of kaolin fine particles added to a PS suspension would be expected to influence microsphere density to a large extent, with the more-highly loaded slurries producing denser particles. The microsphere structure may also be influenced by the kaolin to PS ratio; higher volumes of PS within the kaolin microspheres structure may affect the internal void and shell formation. Changes in particle structure and surface morphology due to the alterative experimental parameters are shown in Figures 6.10 to 6.24.
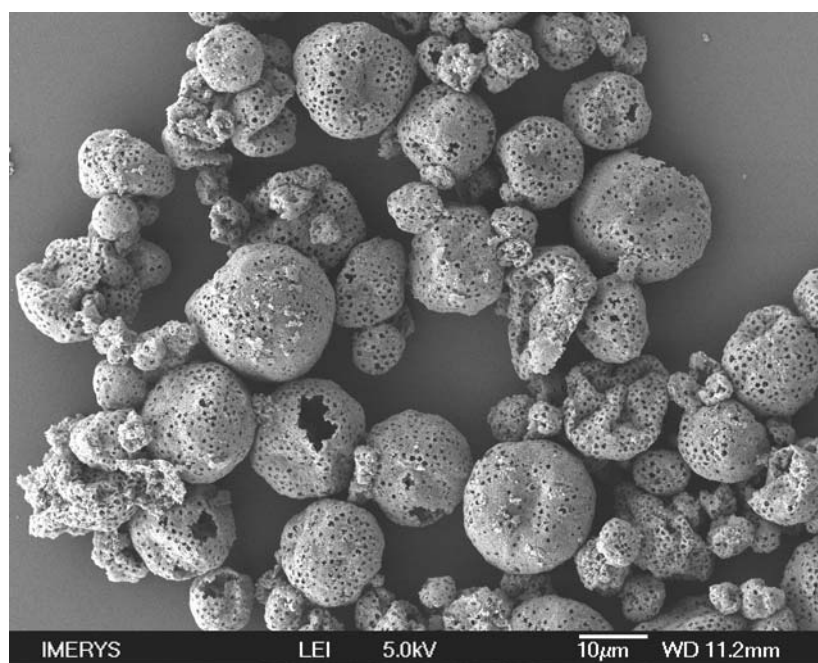
Figure 6.10 *Spray dried kaolin microspheres calcined at 850 ºC, kaolin ratio 1:1.*
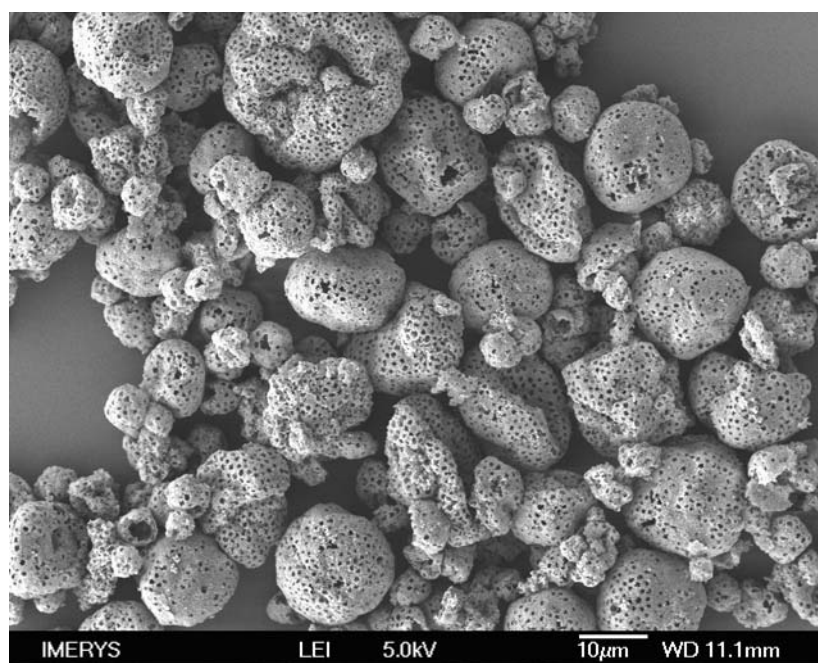
Figure 6.11 *Spray dried kaolin microspheres calcined at 1000 ºC, kaolin ratio 1:1.*
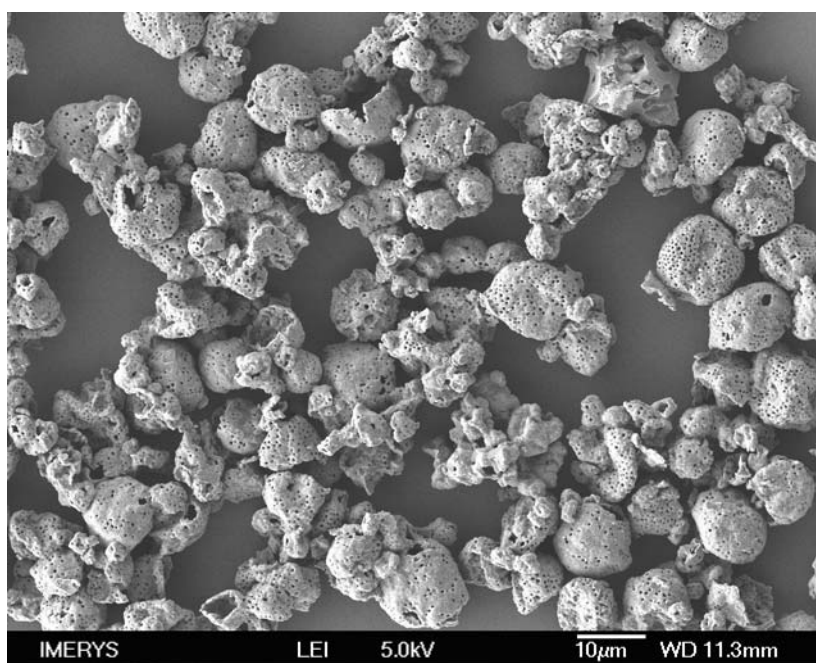
Figure 6.12 *Spray dried kaolin microspheres calcined at 1200 ℃, kaolin ratio 1:1.*
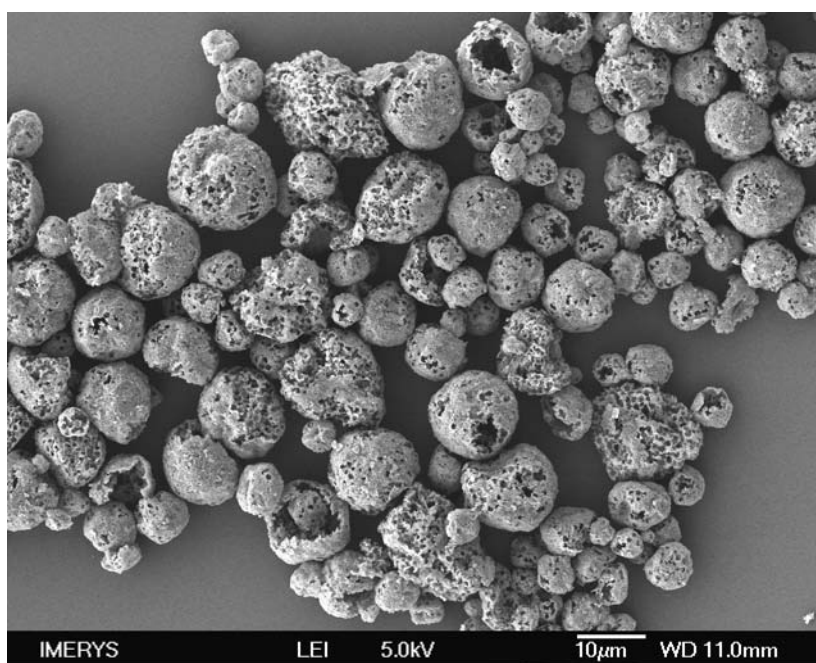
Figure 6.13 *Spray dried kaolin microspheres calcined at 850 ℃, kaolin ratio 1.5:1.*
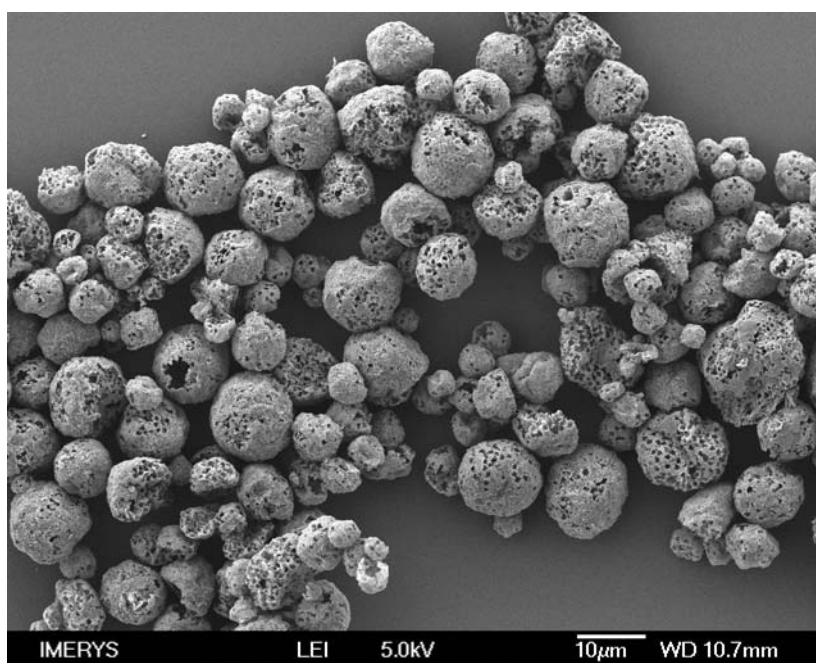
Figure 6.14 *Spray dried kaolin microspheres calcined at 1000 ºC, kaolin ratio 1.5:1.*
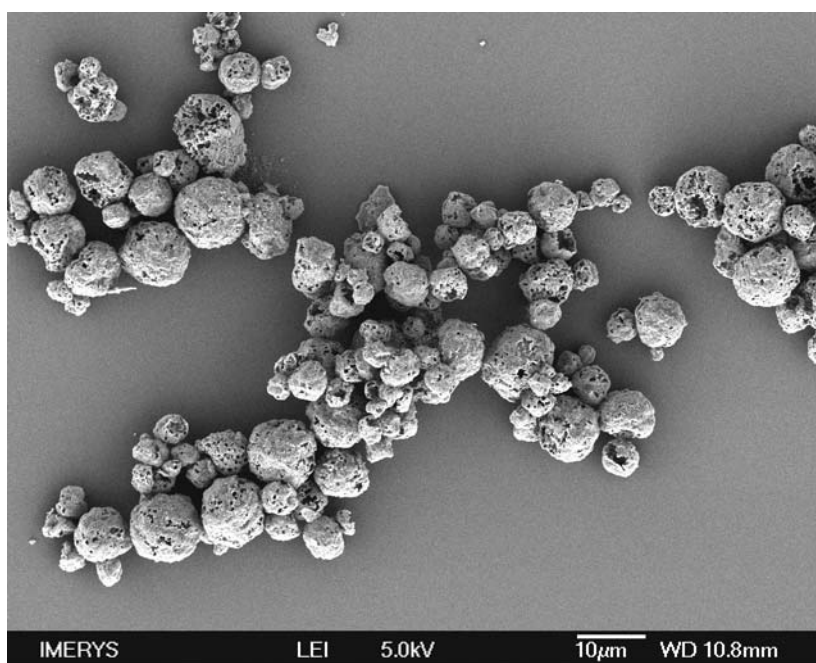
Figure 6.15 *Spray dried kaolin microspheres calcined at 1200 ºC, kaolin ratio 1.5:1.*
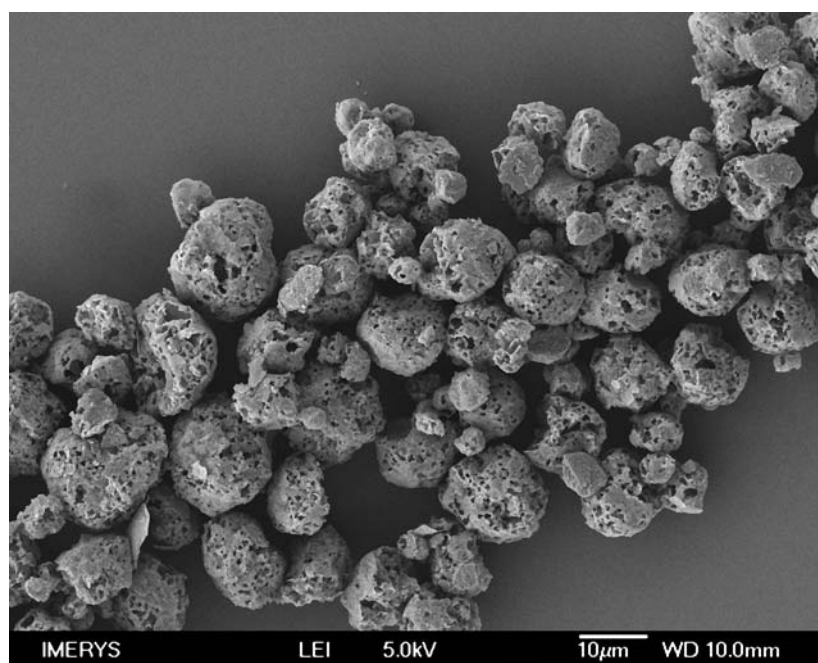
Figure 6.16 *Spray dried kaolin microspheres calcined at 850 ºC, kaolin ratio 2:1.*
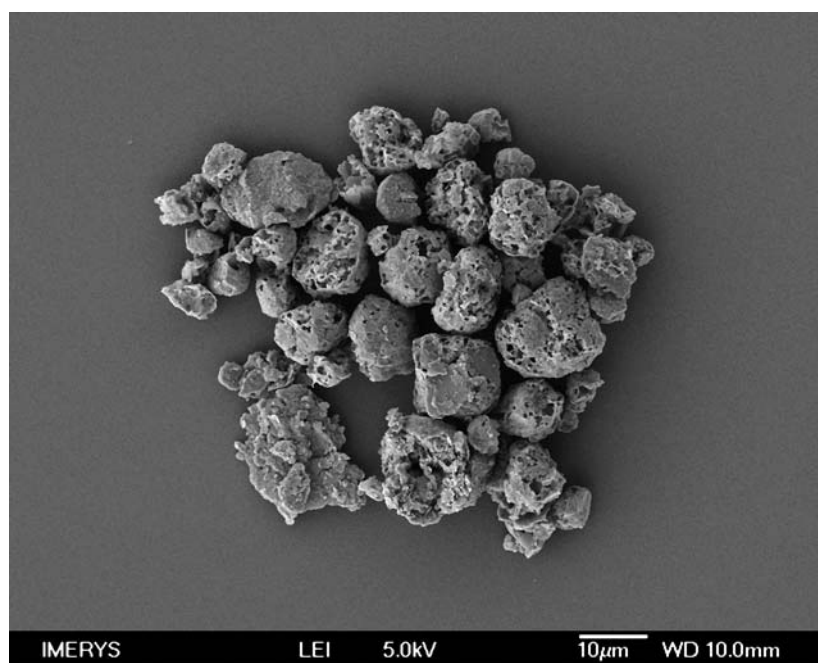
Figure 6.17 *Spray dried kaolin microspheres calcined at 1000 ºC, kaolin ratio 2:1.*
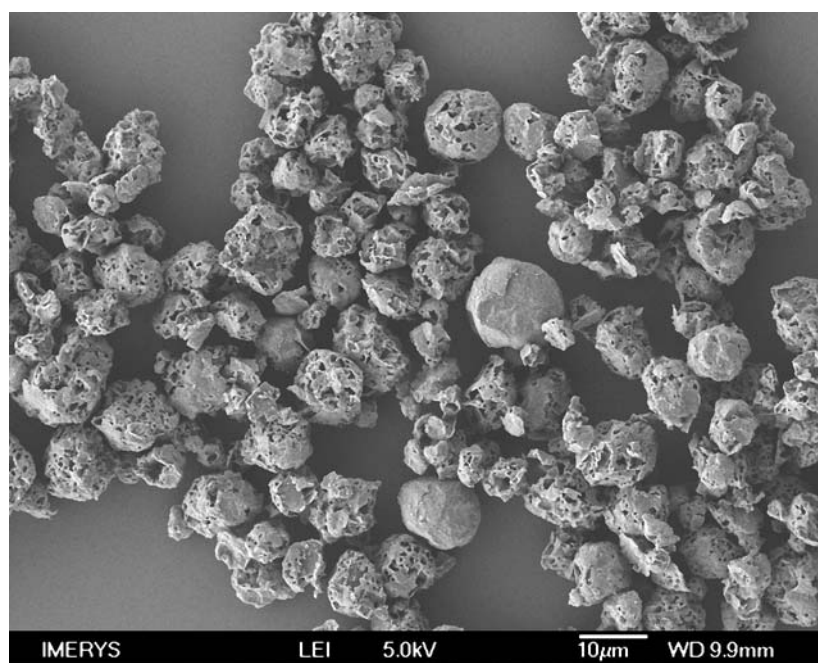
Figure 6.18 *Spray dried kaolin microspheres calcined at 1200 ºC, kaolin ratio 2:1.*
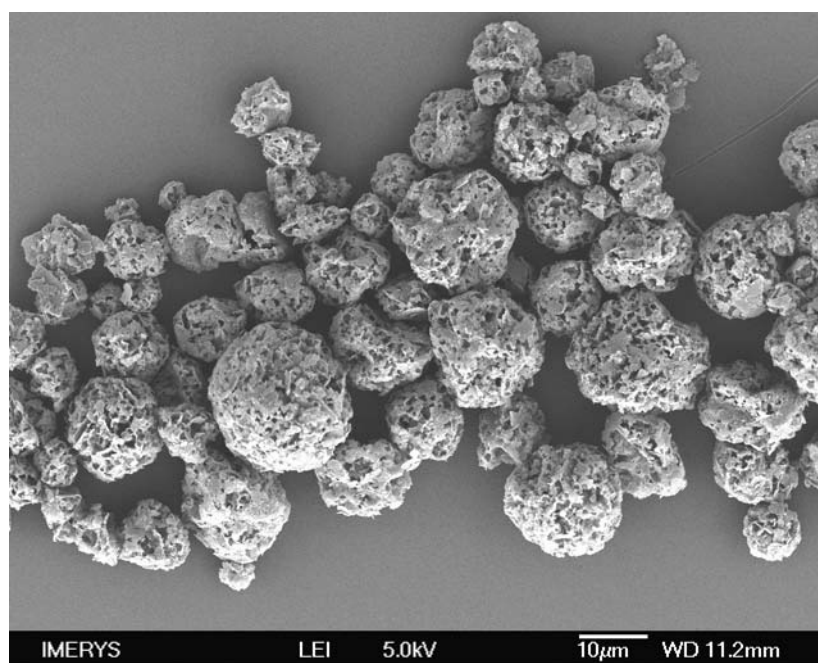
Figure 6.19 *Spray dried kaolin microspheres calcined at 850 ºC, kaolin ratio 3:1.*
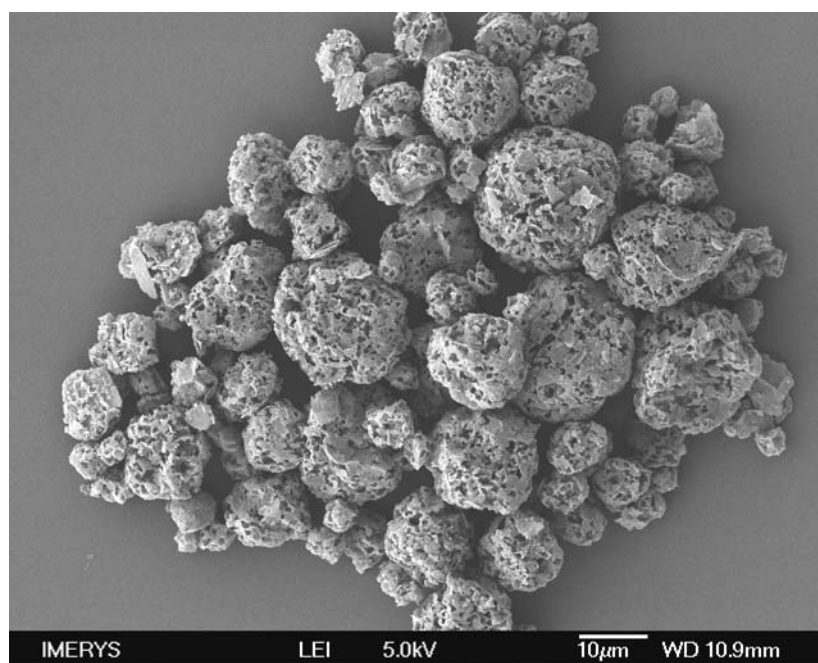
Figure 6.20 *Spray dried kaolin microspheres calcined at 1000 ℃, kaolin ratio 3:1.*
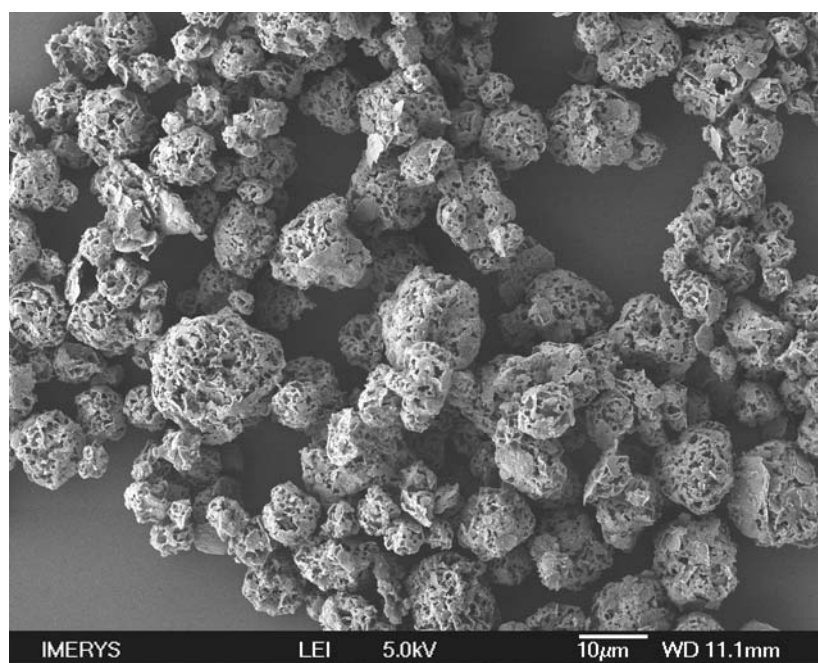
Figure 6.21 *Spray dried kaolin microspheres calcined at 1200 ℃, kaolin ratio 3:1.*
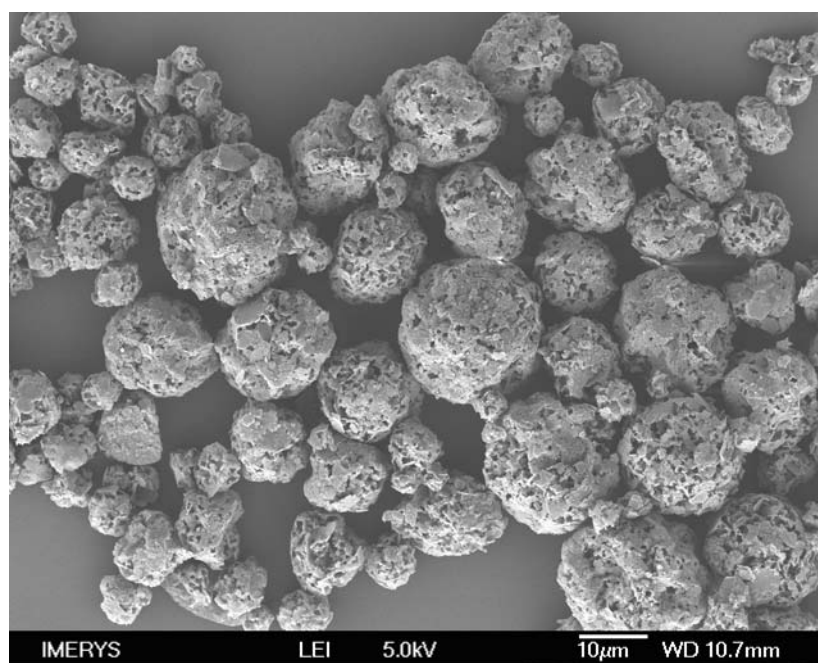
Figure 6.22 *Spray dried kaolin microspheres calcined at 850 ºC, kaolin ratio 4:1.*
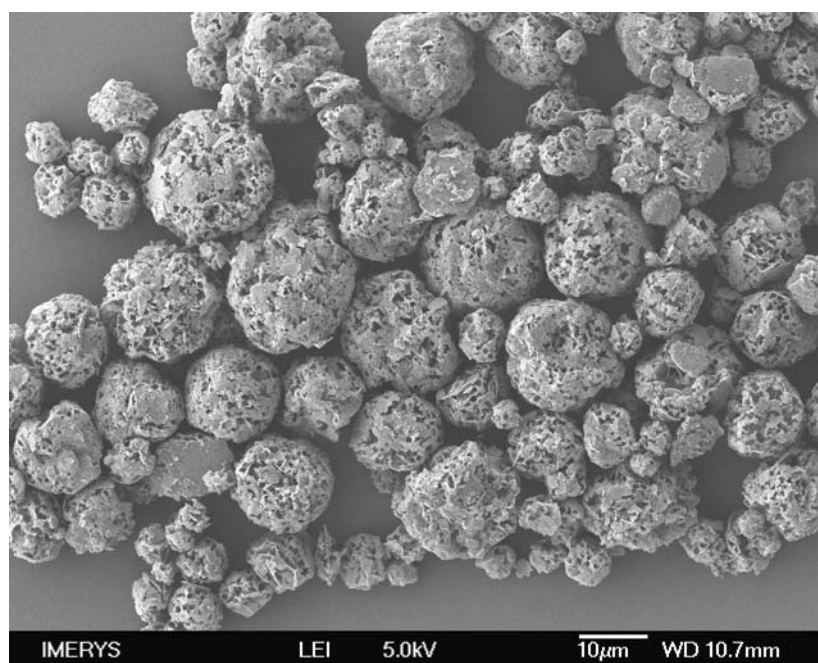
Figure 6.23 *Spray dried kaolin microspheres calcined at 1000 ºC, kaolin ratio 4:1.*
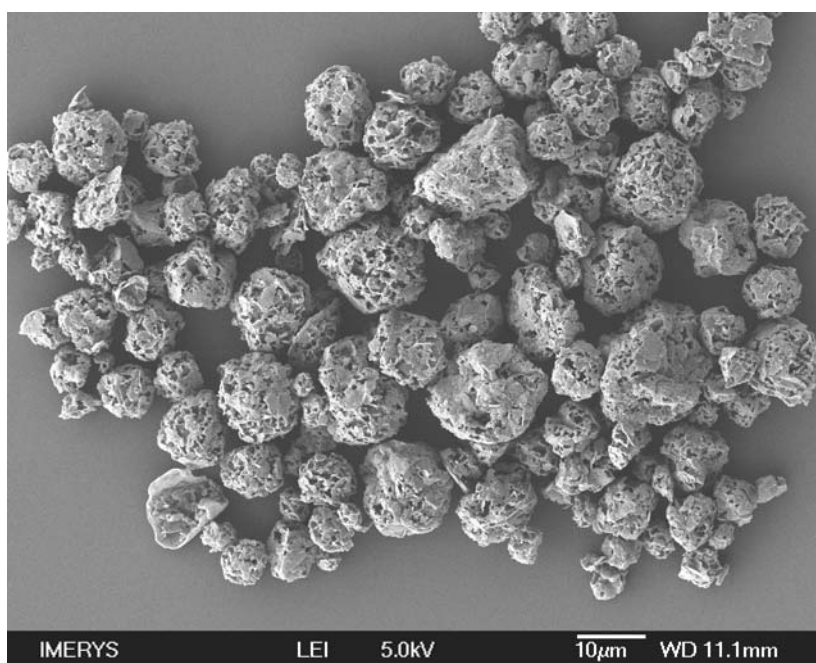
Figure 6.24 *Spray dried kaolin microspheres calcined at 1200 ºC, kaolin ratio 4:1.*

All SEM images are representative of the resulting kaolin particles after calcination. According to the SEM images represented in Figures 6.10 to 6.24, it was confirmed that the formation of hollow microspheres was closely related to the ratio of fine kaolin particles added to the PS suspension. When the kaolin ratio was increased at a value greater than 2:1, no individual hollow microsphere structures were evident. The hollow structure of the microspheres can be clearly observed Figures 6.10 to 6.15. The hollow region became evident due to the collapse or rapture of the microsphere shell during the calcination process.

SEM images have indicated that between the calcination temperatures 850 ºC and 1000 ºC most of the microparticles have kept their spherical morphology after calcination, which indicates that the particles have sufficient strength for further processing. However, when the spray dried samples were calcined at 1400 ºC for 60 min the majority of particles were granular in structure, see Figures 6.25 to 6.27.
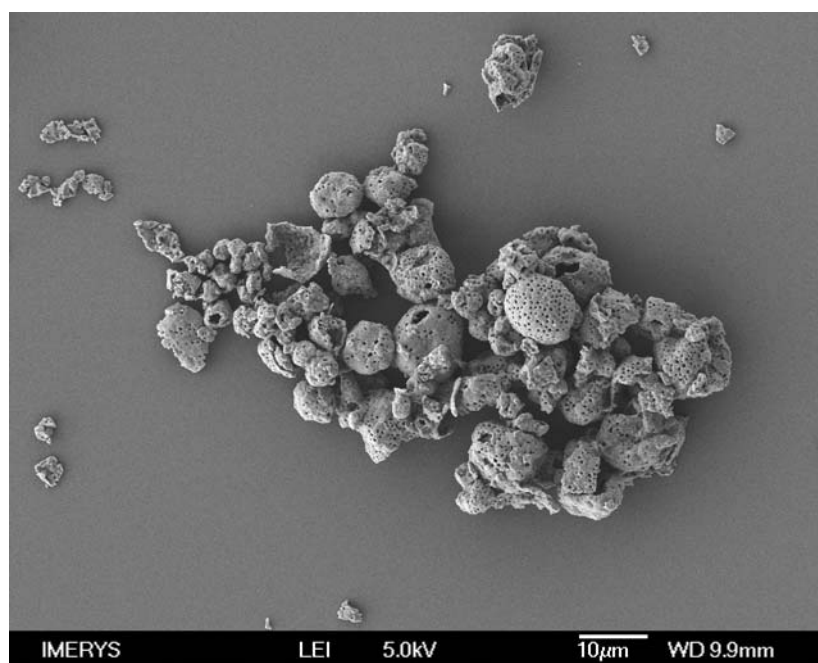
Figure 6.25 *Spray dried kaolin microspheres calcined at 1400 ºC, kaolin ratio 1:1.*
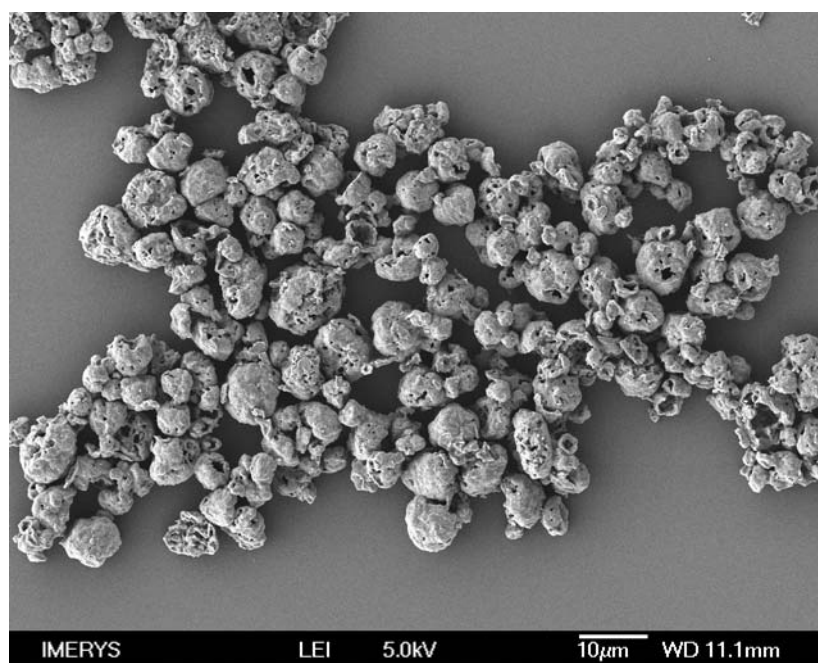
Figure 6.26 *Spray dried kaolin microspheres calcined at 1400 ºC, kaolin ratio 1.5:1.*
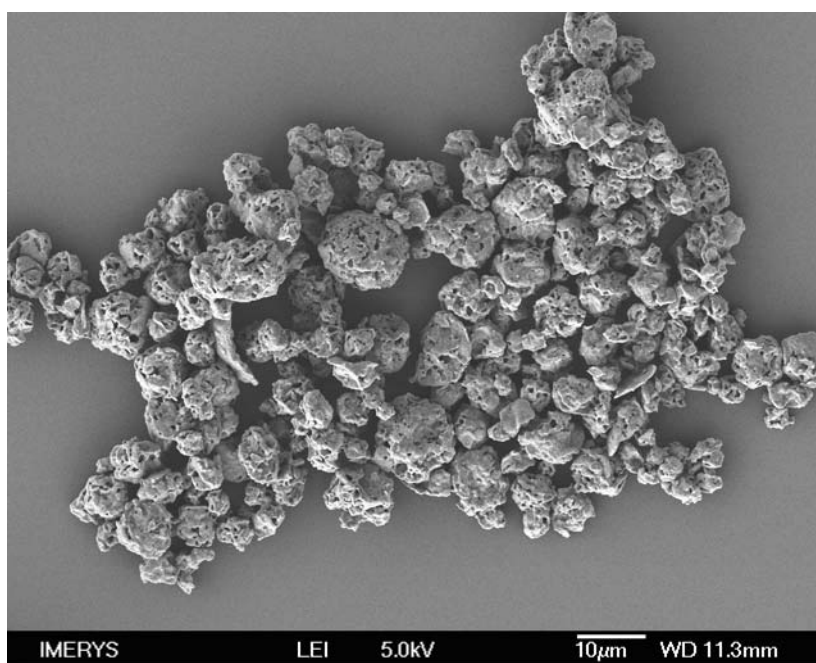
Figure 6.27 *Spray dried kaolin microspheres calcined at 1400 ºC, kaolin ratio 2:1.*

Although hollow microspheres are evident in Figures 6.25 and 6.26 the majority of particles are non-spherical when calcined at 1400 ºC. The loss in spherical shape was attributed to the non-uniform shrinkage of the particles and possibly the change in the transition phase of kaolin when calcined at 1400 ºC. A number of broken shell structures were also evident in Figures 6.25 and 6.26, this was a result of fracturing of the microsphere shell when calcined at a high temperature range. Figure 6.27 shows the final structures of particles when a ratio of 2:1 kaolin slurry was spray dried and calcined at 1400 ºC for 60 min, the structures observed showed a porous surface structure and aggregation between particles was evident when compared to lower calcination temperatures. When experiments were calcined at the high temperature of 1400 ºC the SEM images showed similar spherical particles with regards to the particle surface, open porous surface structures were evident at the ratio values 1:1; 1.5:1 and 2:1. Figures 6.38 to 6.40 represent structures from the three ratio experiments which were calcined at 1400 ºC for 60 min.
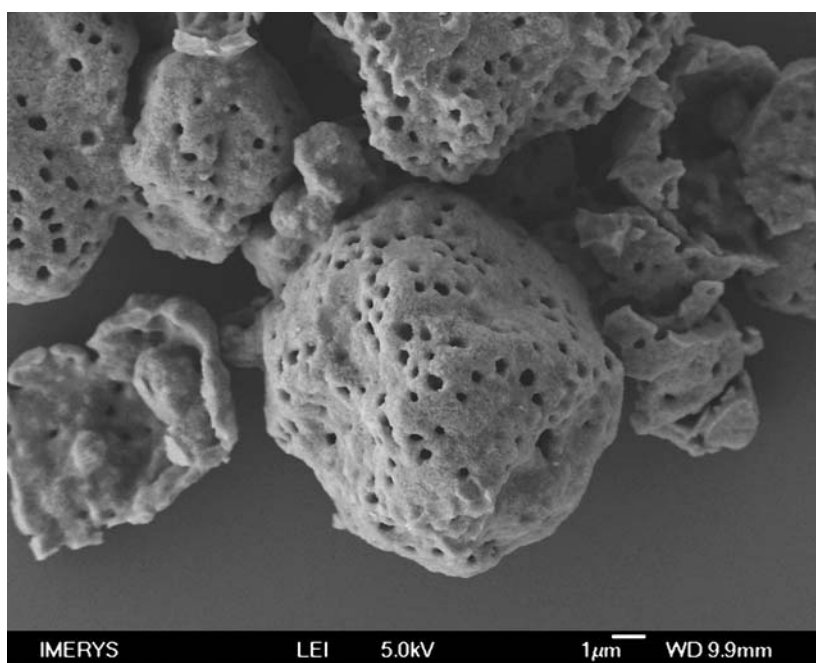
Figure 6.28 *Kaolin microspheres structure, calcined at 1400 ºC, kaolin ratio 1:1*
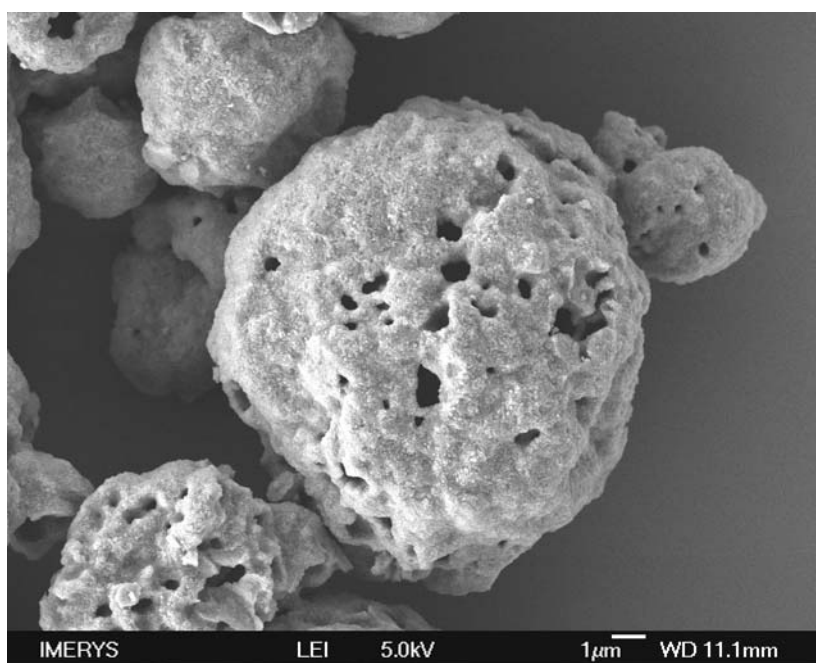
Figure 6.29 *Kaolin microspheres structure, calcined at 1400 ºC, kaolin ratio 1.5:1*
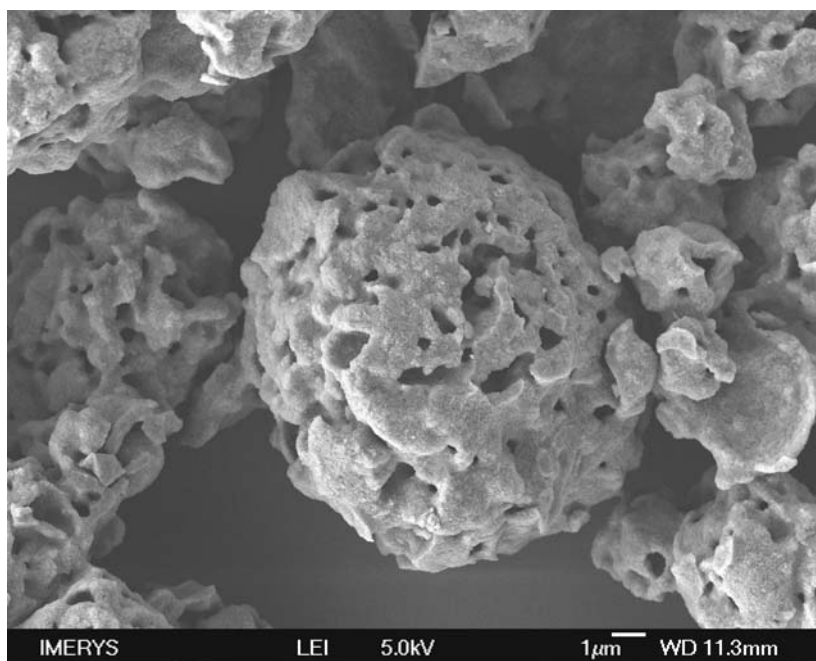
Figure 6.30 *Kaolin microspheres structure, calcined at 1400 ℃, kaolin ratio 2:1*

It was observed that at the high temperature range all the particles showed a fusing of fine kaolin particles. The change in the surface structure was not dependent upon the kaolin ratio. Figure 6.28 showed a kaolin microsphere with a porous shell. A number of shell fragments are also visible; rapture or fracturing of the microsphere shell was often a result of the high calcination temperature for kaolin ratio experiments ≤1.5:1.

Figure 6.29 showed a microsphere particle with an approximate diameter size of 9 μm, the surface had a porous structure. Figure 6.30 represents a microsphere particle from an experiment conducted at a high kaolin ratio of 2:1, the actual surface pores of the particle seem to coalesce due to shrinkage.

The increase in the kaolin ratio and particle shrinkage at high calcination temperature would likely result in a internal structure having an honeycomb structure whereas at a low kaolin

ratio the microsphere particles would likely have a internal void structure. This change in internal structure would influence the resulting bulk density. Kaolin ratio experiments at 3:1 and 4:1 when calcined at 1400 ºC showed no difference in surface structure when compared to the structure in Figure 6.30.

The SEM images do not represent the mean particles size of the final calcined microsphere product; bulk density and mean particles size values for all experiments are shown in Table 6.5. The bulk density of the calcined particles was an important characteristic as it will be used to compare the final material to commercial products. In general, the final particles produced after calcination had bulk densities lower than of the kaolin microspheres produced during the control experiments. Bulk density measurements are shown in Figure 6.31, whereas the specific gravity for the calcined microspheres are plotted as a function of temperature in Figure 6.32.

The d_{50} and particle size distribution were evaluated using CILAS. An overview of the bulk density, specific gravity and d_{50} measurements of the kaolin microspheres calcined between 850 and 1400 ºC are presented in Table 6.5.
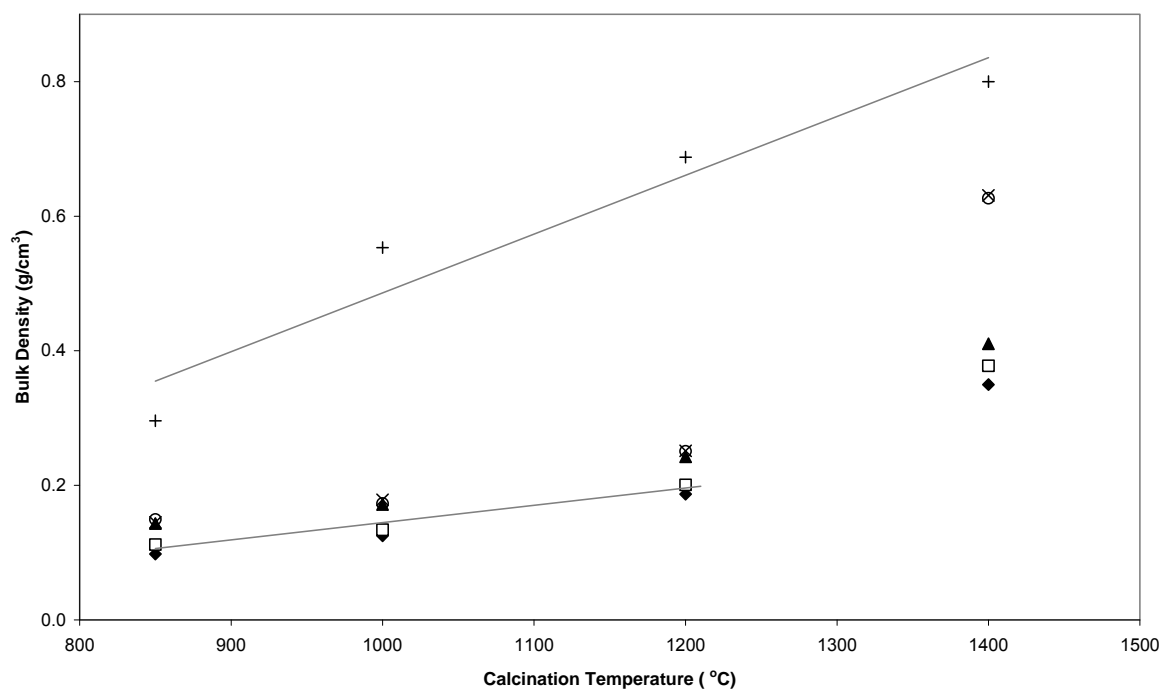
Figure 6.31 *Increase in microsphere bulk density as a result of calcination temperature. Control microspheres (+); kaolin ratio 1:1 (♦); 1.5:1 (□); 2:1 (▲); 3:1; (○); and 4:1 (×).*
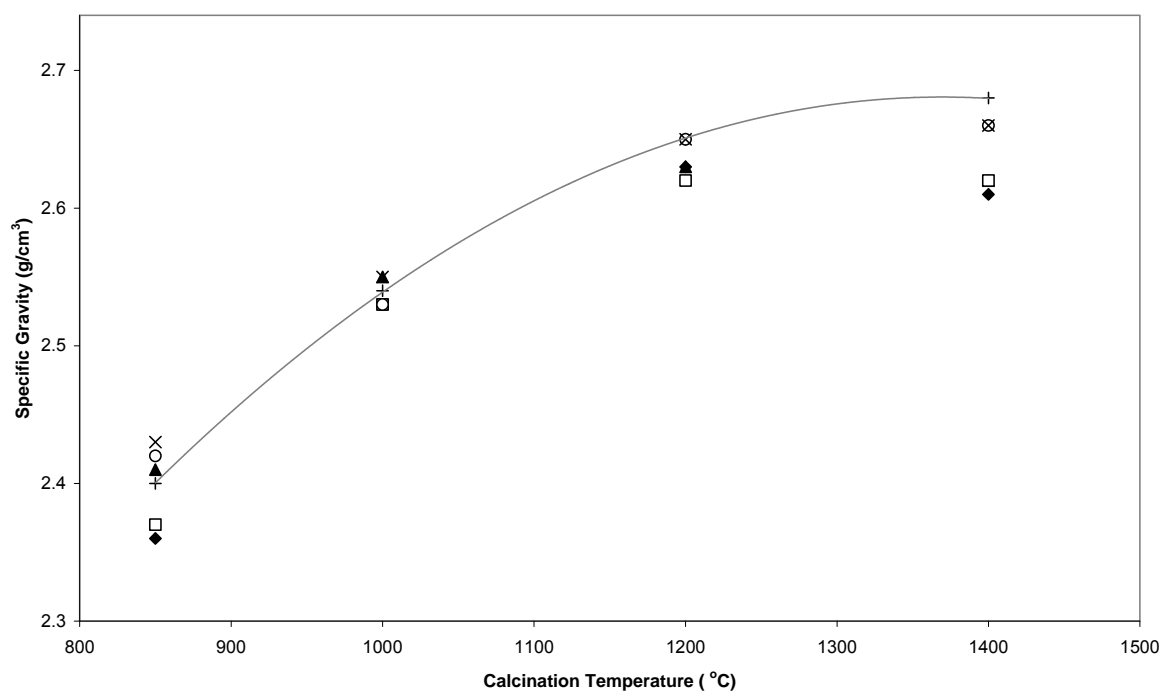
Figure 6.32 *Increase in microsphere specific gravity as a result of calcination temperature. Control microspheres (+); kaolin ratio 1:1 (♦); 1.5:1 (□); 2:1 (▲); 3:1; (○); and 4:1 (×).*

In the majority of experiments, the particle bulk densities of the calcined microspheres exhibited values lower than the original bulk material of 0.62 g/cm^3. Most significantly, all the calcined powder samples had lower bulk densities values when compared to the control experiments. This characteristic of the microsphere bulk densities are shown in Figure 6.31. The straight lines in Figure 6.31 represent a linear fit for the increase in mean bulk density values as a result of calcination of both the kaolin control microsphere and the kaolin ratio 1.5:1 experiments. Error bars are removed for ease of interpretation, however standard deviations are shown in Table 6.5.

If the experimental parameters are favourable, spray dried calcined powders are frequently spherical and hollow in form. A hollow interior imparts a low bulk density of the powder, which will be increased by a narrow size distribution [Elversson, et al. 2005]. In addition, smaller particles are denser and therefore the bulk density of small sized particles will be higher. However, with the addition of PS microspheres it has been possible to further reduce the bulk density of the calcined powders. This reduction was likely due to a number of factors; (i) a larger void to shell thickness ratio is achieved due to the internal volume occupied by the PS microspheres prior to calcination, (ii) the microsphere shell is made of a kaolin honey-comb structure due to PS microspheres within the microsphere shell as a result of the spray drying process, and (iii) the removal of the PS material results in a open-porous microstructure even at high temperatures.

Figure 6.31 shows that bulk density was affected by two factors; (i) the kaolin ratio in the slurry concentration, and (ii) an increase in the calcination temperature. In general, two different ratio concentration profiles could be determined; at a high kaolin concentration where the ratio was ≥3:1 the resulting bulk density signifies an open-porous microsphere

structure, whereas, when the kaolin ratio was ≤2:1 the bulk density was significantly reduced throughout the calcination range. These reduced bulk density values signifying either a hollow or a porous microsphere structure.

The difference in bulk density values at the low kaolin ratios of 1:1 and 1.5:1 was a result of the shell structures formed during the spray drying and calcination process. This was evident in Figures 6.45 to 6.48, where at a low kaolin ratio of 1:1 a single thin shell structure was formed, when the kaolin concentration was increased to a ratio of 1.5:1 a multi-layer or porous shell structure was formed. It has been reported that the specific gravity of kaolin changes during the calcination process [Bridson, et al. 1985]. Figure 6.32 shows the increase in the specific gravity due to the increase in the calcination temperature, the curve represented the increase in specific gravity for the control microsphere experiments. Standard deviations of the mean are shown in Table 6.5. All powder samples showed a decrease in specific gravity when calcined at 850 ºC for 60 min, between 2.36 and 2.43 g/cm^3, when compared to the starting kaolin material, 2.64 g/cm^3. The decrease in specific gravity was due to the formation of closed voids between kaolin particles, either as a result from trapped air within the shell structure and from the removal of the PS component.

As the calcination temperature for all powder samples increased the specific gravity of all the samples also increased, this was due to the collapse of closed voids but also likely due to the formation mixture of mullite and christobalite produced by kaolin decomposition at about 1200 ºC.

Table 6.5 *Properties of calcined low density kaolin microspheres.*

Run	Ratio (*K:PS*)	Calcination Temp. (°C)	Bulk Density (g/cm^3)	Specific Gravity (g/cm^3)	Particle Size d$_{50}$ (µm)
2 a	1:1	850	0.09 ± 0.01	2.36 ± 0.02	15.9 ± 0.9
2 b	1:1	1000	0.12 ± 0.01	2.53 ± 0.01	13.3 ± 0.8
2 c	1:1	1200	0.18 ± 0.01	2.63 ± 0.02	11.6 ± 0.6
2 d	1:1	1400	0.35 ± 0.01	2.61 ± 0.02	n.r.
3 a	1.5:1	850	0.11 ± 0.01	2.37 ± 0.02	12.2 ± 0.4
3 b	1.5:1	1000	0.13 ± 0.01	2.53 ± 0.01	11.2 ± 0.4
3 c	1.5:1	1200	0.20 ± 0.01	2.62 ± 0.01	10.4 ± 0.6
3 d	1.5:1	1400	0.38 ± 0.01	2.62 ± 0.02	n.r.
4 a	2:1	850	0.14 ± 0.01	2.41 ± 0.02	13.1 ± 0.6
4 b	2 :1	1000	0.17 ± 0.01	2.55 ± 0.02	10.7 ± 0.4
4 c	2 :1	1200	0.24 ± 0.01	2.63 ± 0.02	10.1 ± 0.9
4 d	2 :1	1400	0.41 ± 0.02	2.62 ± 0.02	n.r.
5 a	3:1	850	0.15 ± 0.01	2.42 ± 0.02	13.8 ± 0.6
5 b	3 :1	1000	0.18 ± 0.01	2.53 ± 0.01	11.7 ± 0.6
5 c	3 :1	1200	0.25 ± 0.01	2.65 ± 0.01	11.4 ± 0.8
5 d	3 :1	1400	0.63 ± 0.01	2.66 ± 0.02	n.r.
6 a	4:1	850	0.15 ± 0.01	2.43 ± 0.03	12.7 ± 0.8
6 b	4 :1	1000	0.17 ± 0.01	2.55 ± 0.02	11.3 ± 0.6
6 c	4 :1	1200	0.25 ± 0.01	2.65 ± 0.02	10.7 ± 0.6
6 d	4 :1	1400	0.63 ± 0.01	2.66 ± 0.01	n.r.

The results presented in Table 6.4 suggest that a trade-off between bulk density and particle size has to be evaluated to determine the optimum parameters. At the lowest kaolin ratio, 1:1, the lowest bulk density values are measured for the kaolin microspheres throughout the complete calcination range, however the largest d_{50} values are also recorded.

At the higher kaolin ratio vales, 3:1 to 4:1, no significant difference in bulk density at an equivalent temperature can be distinguished. The most favourable properties adhere to experiments conducted using kaolin ratios at 1.5:1 and 2:1, when calcined at 1000 ºC the microsphere products exhibit bulk densities of 0.13 and 0.17 g/cm^3, with d_{50} values of 11.2 and 10.7 μm respectively. Compared to control experiments with the addition of a polyelectrolyte, calcined at the same temperature, exhibiting properties of bulk density at 0.55 g/cm^3 and a d_{50} particle size 14.2 μm.

Another important characteristic of the kaolin microspheres produced by the spray drying and calcination processes was the size distribution. Generally, particle size distributions for spray dried particles have been found to follow the lognormal distribution and solid loading has a pronounced effect on particle size [Walker Jr., et al. 1999]. It has also been reported that particle size increased with the increase in slurry concentration [Wang, et al. 2009]. However, the effect on particle size due to the calcination of spray dried kaolin-PS microspheres has not been previously reported. Particle size distribution data for the microspheres prepared at low ratio concentrations are shown in Figures 6.33 to 6.35.
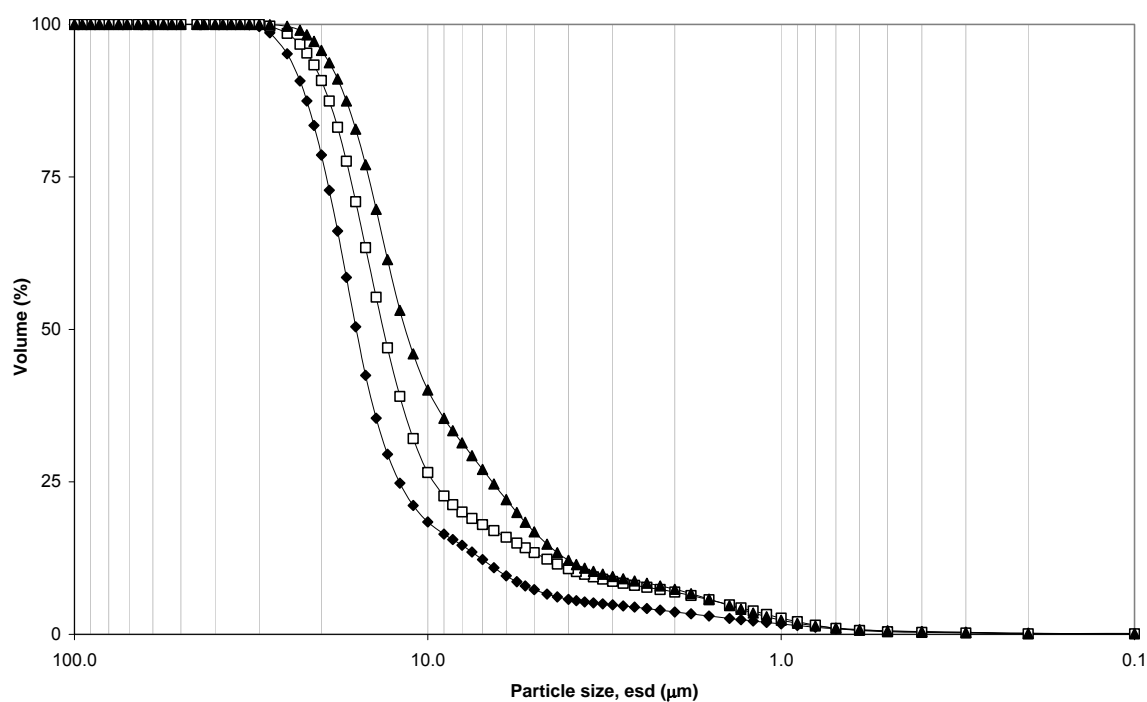
Figure 6.33 *Particle size distributions of kaolin microspheres after calcination at temperatures; 850 ℃ (♦); 1000 ℃ (□); and 1200 ℃ (▲). Kaolin ratio experiments 1:1.*
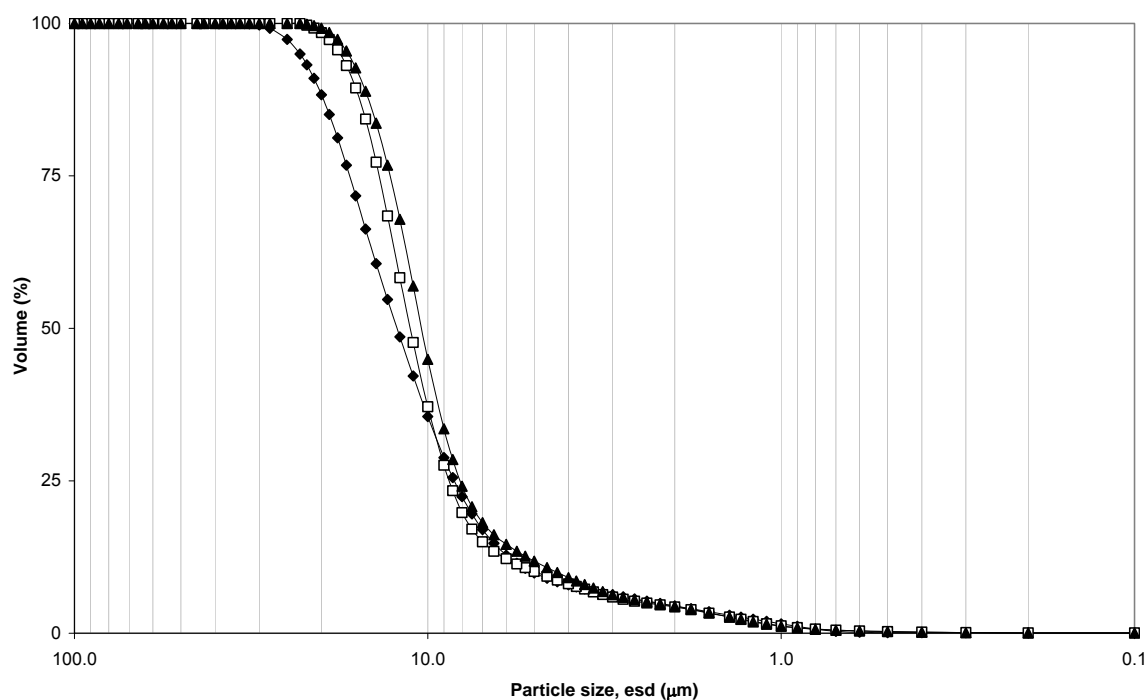
Figure 6.34 *Particle size distributions of kaolin microspheres after calcination at temperatures; 850 ºC (♦); 1000 ºC (□); and 1200 ºC (▲). Kaolin ratio experiments 1.5:1.*
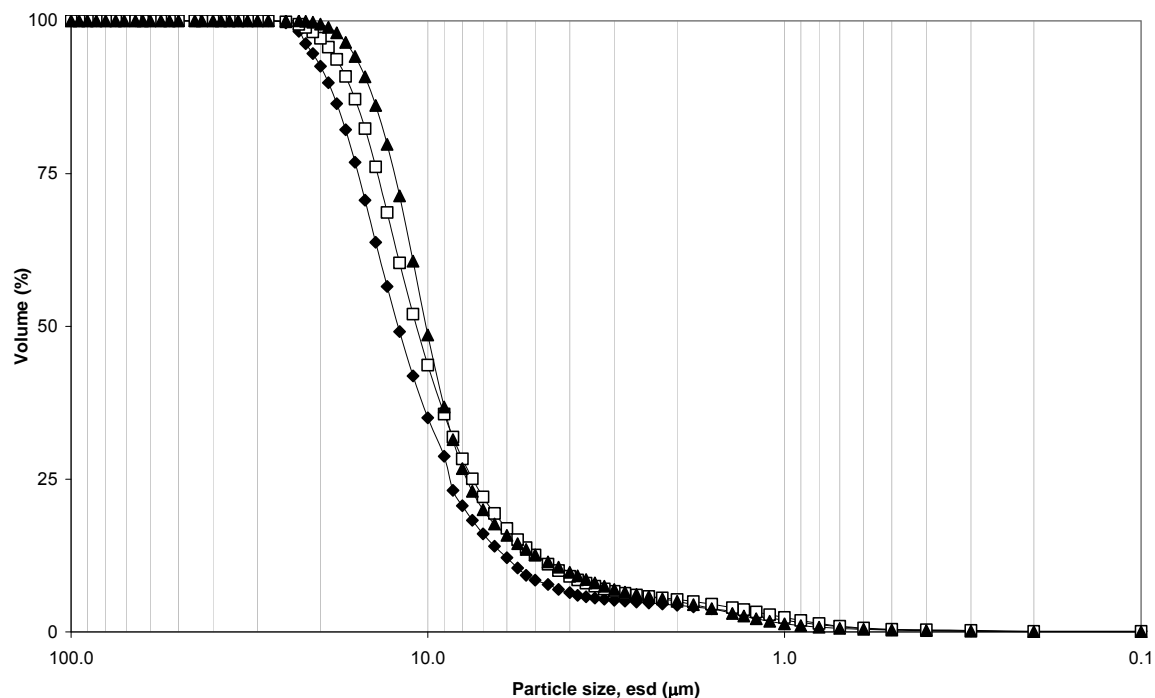
Figure 6.35 *Particle size distributions of kaolin microspheres after calcination at temperatures; 850 ºC (♦); 1000 ºC (□); and 1200 ºC (▲). Kaolin ratio experiments 2:1.*

Figure 6.33 shows the particle size distribution curve of kaolin ratio 1:1 experiments after calcination at three different temperature ranges. The d_{50} particle diameters of the microspheres from each ratio experiment are reported in Table 6.4. The results indicate that most of the particles range in size from approximately 6 to 23 μm after calcination at 850 ºC with a d_{50} of 15.9 μm. As the calcination temperature of the spray dried samples was increased to 1000 and 1200 ºC, the particle size of the microspheres decreased d_{50} values were measured at 13.3 and 11.6 μm, respectively. The decrease in particle size was attributed to the actual shrinkage of the microsphere particles as the temperature increased.

Figures 6.34 and 6.35 indicate the change in the size distribution curves for kaolin ratio experiments 1.5:1 and 2:1, respectively. In both figures, all distribution curves show a shift to the right indicating a decrease in d_{50} particle size as the calcination temperature was increased. A comparison of the mean particle size and the d_{10}, d_{50}, d_{90} range are shown in Table 6.5. At the high kaolin concentration range, ratios 3:1 and 4:1, the particle size distribution plots were similar to the distribution curves for ratio experiments 2:1 as shown in Figure 6.35. A slight increase in particle size was evident as the calcination temperature was increased. The high kaolin ratio samples showed narrow size distribution curves when compared to low kaolin ratios. This may be due to the reduced volume of PS within individual kaolin microspheres and in turn a reduction in the gases released by the thermal decomposition of PS including CO_2, NH_3 and H_2O during the calcination process.

Figure 6.36 represents a comparison of particle size distribution curves for all kaolin ratio experiments calcined at 1000 ºC. These specific size distribution curves were shown as the characteristic properties at this temperature range produced the most favourable results.
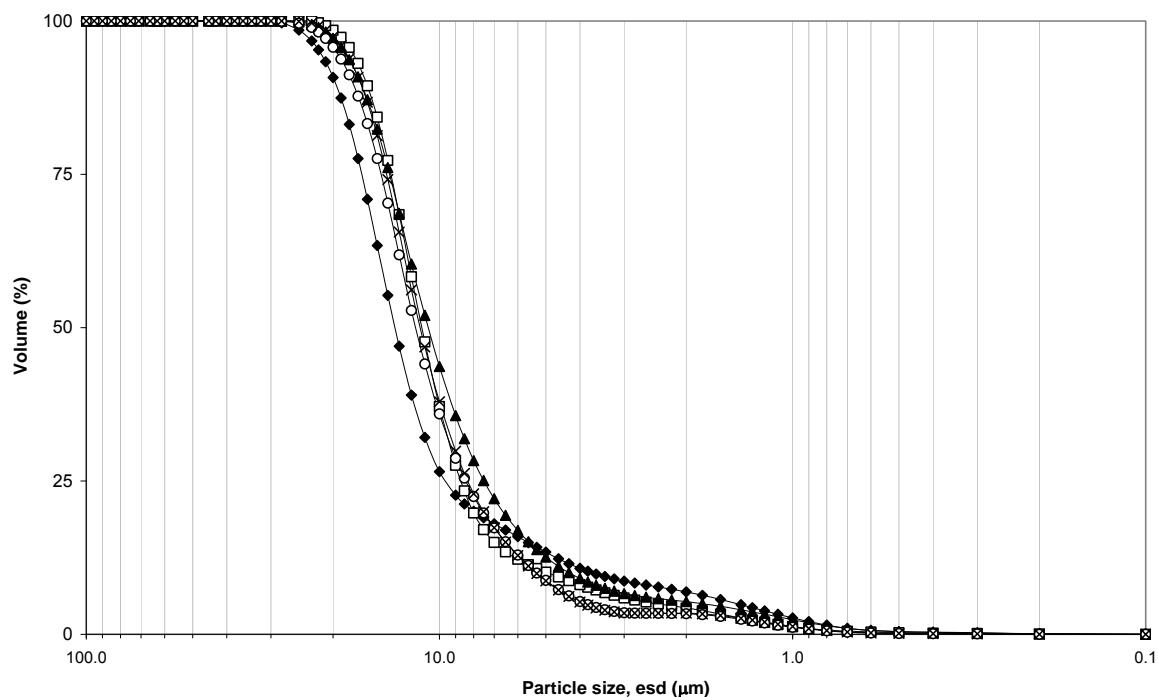
Figure 6.36 *Comparison of particle size distributions of kaolin microspheres after calcination at 1000 ºC. Ratio experiments 1:1 (♦); 1.5:1 (□); 2:1 (▲); 3:1 (○); and 4:1 (×).*

The broadest particle size distribution curve was assigned to the lowest kaolin ratio 1:1. This was due to the larger volume occupied by the PS microsphere material within the kaolin microsphere produced during the spray drying process. As the volatile PS material decomposed during the calcination process, the shell structure expands due to internal pressure and results in a larger particle size when compared to higher ratio values. The two highest kaolin ratio values, 3:1 and 4:1, exhibit similar distribution curves, this was also evident in the SEM images. Table 6.6 lists the important size of the calcined microspheres obtained by calcination of spray dried samples at 1000 ºC. The increase in kaolin ratio within the slurry concentration and the increase in calcination temperature did not significantly increase the mean particle size or d_{50} of the microspheres.

Table 6.6 *Important sizes of calcined kaolin microspheres prepared at different processing parameters.*

Run	Ratio (*K:PS*)	Calcination Temp. (ºC)	Particle Size d_{10} (µm)	Particle Size d_{50} (µm)	Particle Size d_{90} (µm)	Mean Size (µm)
2 b	1:1	1000	3.7 ± 0.8	13.3 ± 0.8	19.8 ± 0.8	14.4 ± 0.8
3 b	1.5:1	1000	4.9 ± 0.7	11.2 ± 0.4	16.2 ± 0.6	13.4 ± 0.4
4 b	2 :1	1000	4.3 ± 0.7	10.7 ± 0.4	16.8 ± 0.6	13.7 ± 0.6
5 b	3 :1	1000	5.3 ± 0.8	11.7 ± 0.6	17.6 ± 0.4	13.9 ± 0.8
6 b	4 :1	1000	5.3 ± 0.6	11.3 ± 0.6	16.8 ± 0.6	13.7 ± 0.8

It has been reported elsewhere that as particle concentration was increased the particle size increased [Wang, et al. 2009]. An increase in calcination temperature was also reported to increase the particle size due to the expansion of the microspheres induced by the release of gases [Sun, et al. 2008].

It was expected that the amount of volatile PS material within the spray dried slurry would be the main influencing factor upon particle size. However, as indicated in Table 6.6, upon calcination very little variance in particle size was noted for kaolin ratio experiments greater than 1.5:1. At a low kaolin ratio of 1:1, the largest microsphere particle size are recorded, d_{50} of 13.3 ±0.8 µm and a mean particle size of 14.4 ±0.8 µm. This large particle size can be attributed to the amount of volatile material within the kaolin microsphere structure. As the kaolin ratio increased the amount of PS material decreased, therefore the amount the volatile material that expanded the microsphere structure during calcination decreased. At a kaolin ratio greater than 2:1, the kaolin concentration within the slurry may well become an influencing factor. Throughout the particle size distribution range for the calcined microspheres, no significant increase in particle size was evident.

To further understand the influence of the kaolin ratio upon resultant particle size additional experiments at higher kaolin ratios should be conducted. It would be interesting to see whether if the particle size significantly increases with kaolin ratio experiments at 6:1, 8:1 and 10:1.

Particle size measurements of powder from the spray drying process prior to calcination was not possible, it was determined that the powder structures were too weak and the mechanical agitation and ultrasonic process used in the particle size analyser method possibly disintegrated aggregates into fragments. These fragments, which are non-spherical would tend to form large-size agglomerates. Particle size measurements for powder samples calcined at 1400 ºC for each ratio experiment are not presented due to aggregation and the formation of agglomerates. This concern has been manifested in the appearance of multiple size distribution curves for the same sample, indicating mean particle size values >60 μm. These aggregated structures were also evident in the SEM images.

When calculating the flowability of the calcined powder samples using the Carr's compressibility index as presented in Equation 6.1, all powder samples measured a low CI value (<23), indicating free-flowing particles. The CI value for the kaolin ratio 1.5:1 when calcined at 1000 ºC for 60 min was calculated at 19, the lowest value was attributed to the kaolin ratio 1:1 when calcined at 850 ºC. In contrast, the highest measurements were recorded for the ratio experiments 3:1 and 4:1 when calcined at 1000 ºC, where CI values were 22 and 23 respectively. Data for all calcined microspheres are presented in the Appendix D, Table D.1.

6.4.3. Structure of calcined microspheres

The optimal spray drying process parameters were determined prior to the control experiments and were based on previous research conditions [Hamer, 2005; 2006], from which low density microspheres were produced. From initial characterisation, two different ratios produced microsphere particles that were of interest because of their low bulk density and particle size.

At a kaolin ratio of 1.5:1, hollow microsphere structures were produced, whereas at a ratio of 2:1, open-porous microsphere structures were evident. Previous SEM images were shown to compare structures from various kaolin ratios, further characterisation by SEM and FIB of calcined microspheres from the kaolin ratios 1.5:1 and 2:1 are shown in Figures 6.33 to 6.60. The images are presented to identify characteristics of the shell and internal structures of the calcined microspheres.
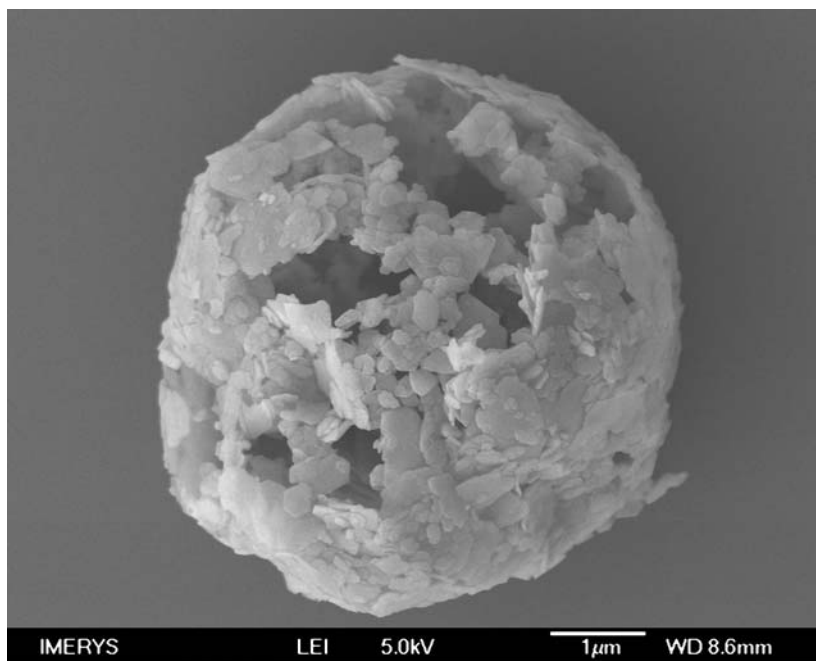
Figure 6.37 *SEM image of an individual kaolin microspheres calcined at 850 ℃, kaolin ratio 1.5:1.*
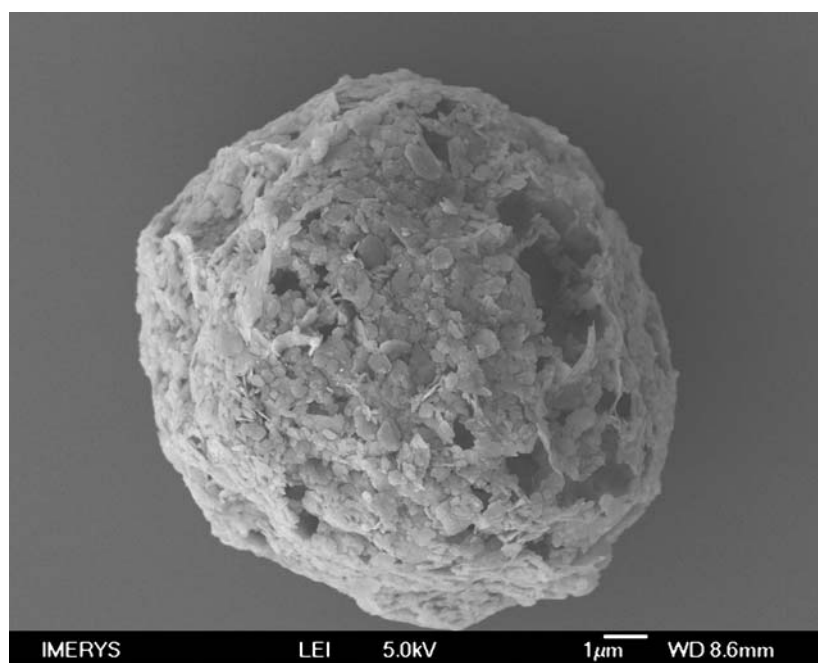
Figure 6.38 *SEM image of an individual kaolin microspheres calcined at 1000 ºC, kaolin ratio 1.5:1.*
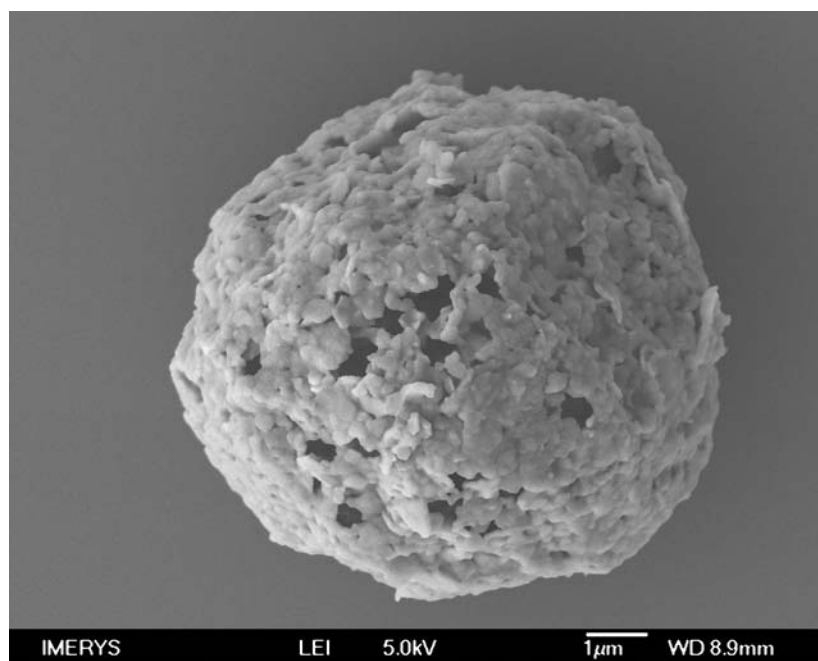
Figure 6.39 *SEM image of an individual kaolin microspheres calcined at 1200 ºC, kaolin ratio 1.5:1.*
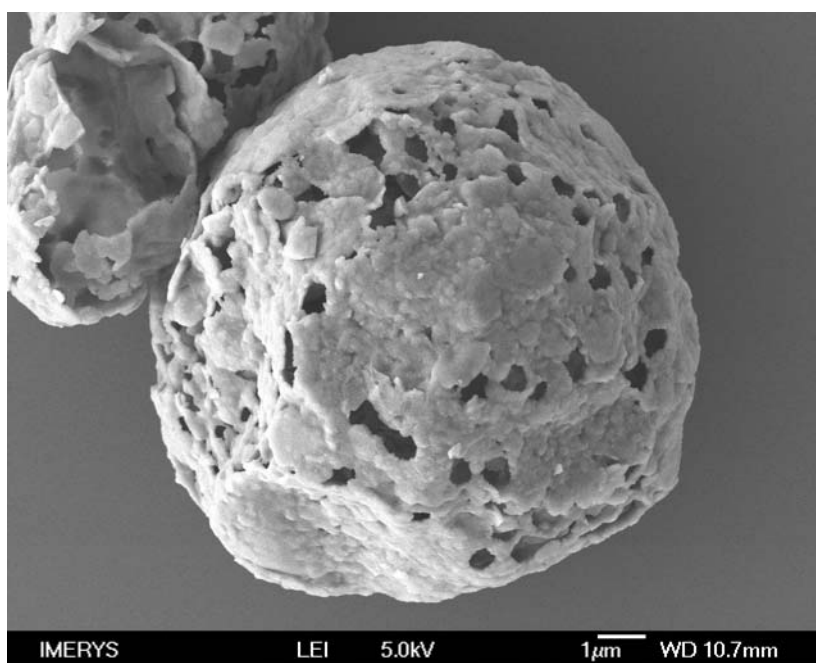
Figure 6.40 *SEM image of an individual kaolin microspheres calcined at 1400 ℃, kaolin ratio 1.5:1.*

The SEM images presented in Figures 6.37 to 6.40 show microsphere structures from kaolin ratio experiments 1.5:1 after calcination. The structures shown are representative of each sample. It can be found that the microsphere structures are built up of numerous kaolin nanoparticles forming a shell structure. In Figures 6.37 and 6.38 the individual kaolin plate structures are easily apparent. As the calcination temperature increases to 1200 ℃ the individual kaolin plates fuse together as shown in Figure 6.39.

The open porous shell structure exhibited in all the images are a result of escaping gases formed due to decomposition of volatile material. In Figure 6.37 the surface pore size varied from 0.5 to 1.4 μm measured by using ImageJ software, a Java-based image processing program [Collins, 2007]. The actual pore size was expected to be dependent upon the strength of the kaolin formed shell structure. As the volatile material escapes through the kaolin shell, loosely packed kaolin plates are likely to be removed resulting in a larger pore

structure. In the Figure 6.39 the pore size decreased as the calcination temperature increased to 1200 ºC, the pores size varied between 0.3 to 0.6 μm. For samples calcined at 1400 ºC the average pore size was measured between 0.3 and 0.5 μm. However, it was evident that coalescence of voids within the microsphere shell structure often resulted in larger pore structures. Figures 6.41 to 6.44 represent microsphere structures formed at a kaolin ratio of 2:1, calcined between 850 and 1400 ºC.
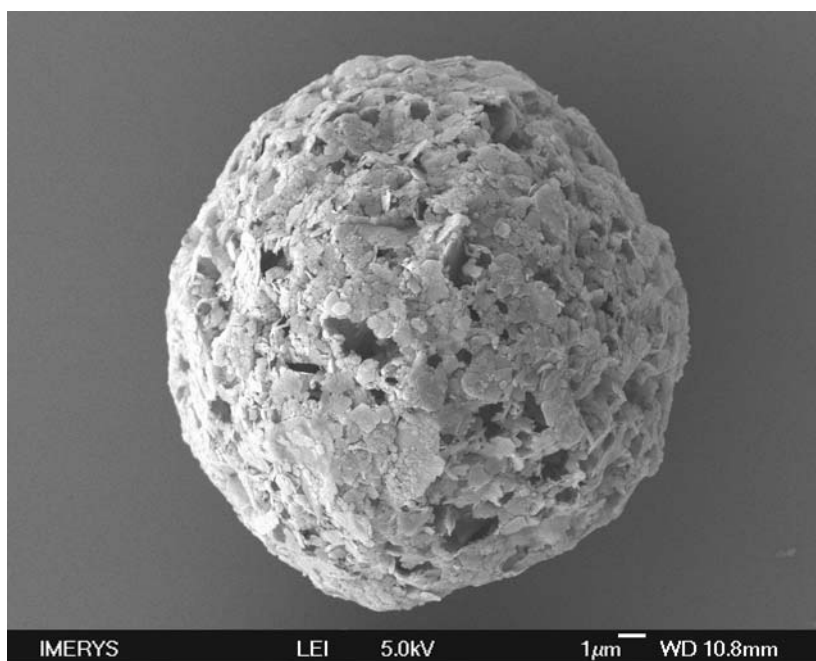
Figure 6.41 *SEM image of an individual kaolin microspheres calcined at 850 ºC, kaolin ratio 2:1.*
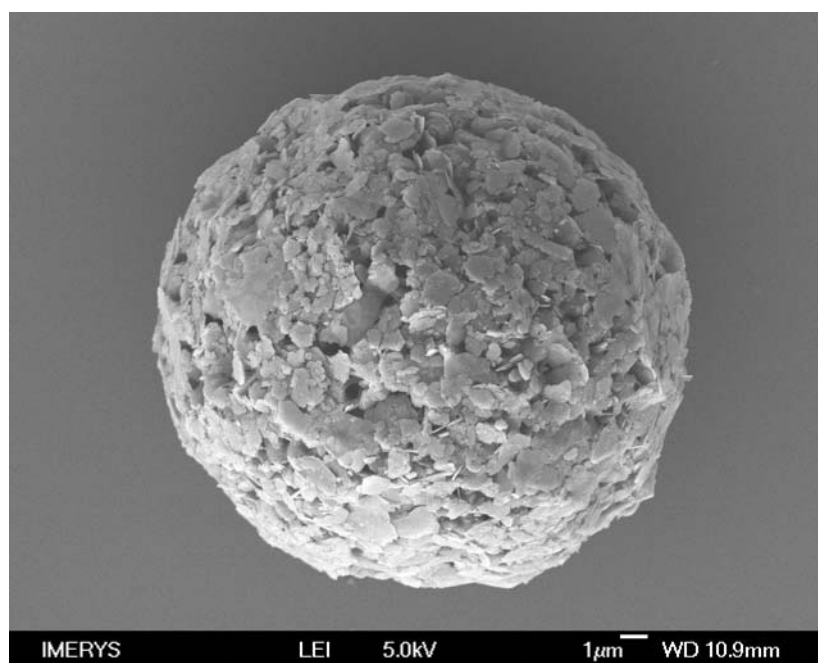
Figure 6.42 *SEM image of an individual kaolin microspheres calcined at 1000 ºC, kaolin ratio 2:1.*
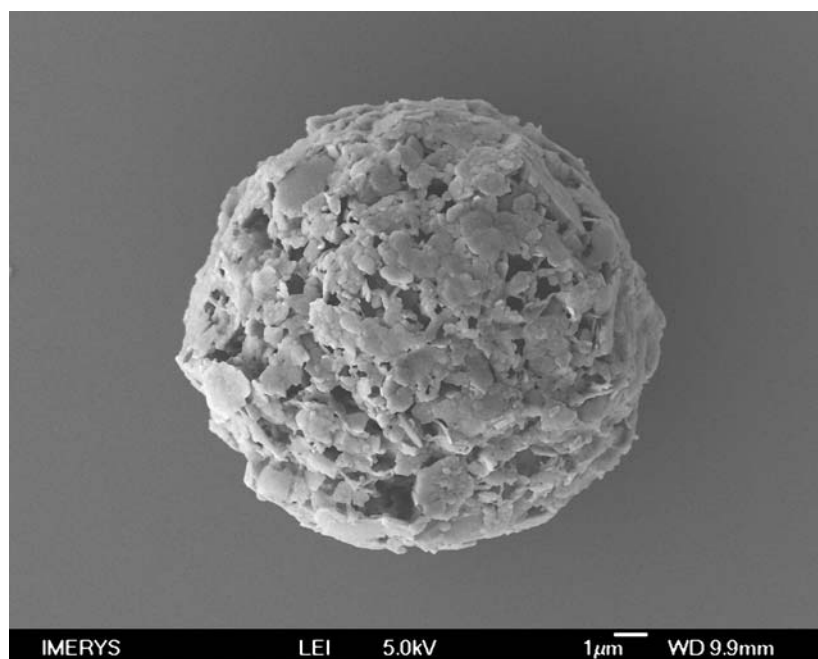
Figure 6.43 *SEM image of an individual kaolin microspheres calcined at 1200 ºC, kaolin ratio 2:1.*
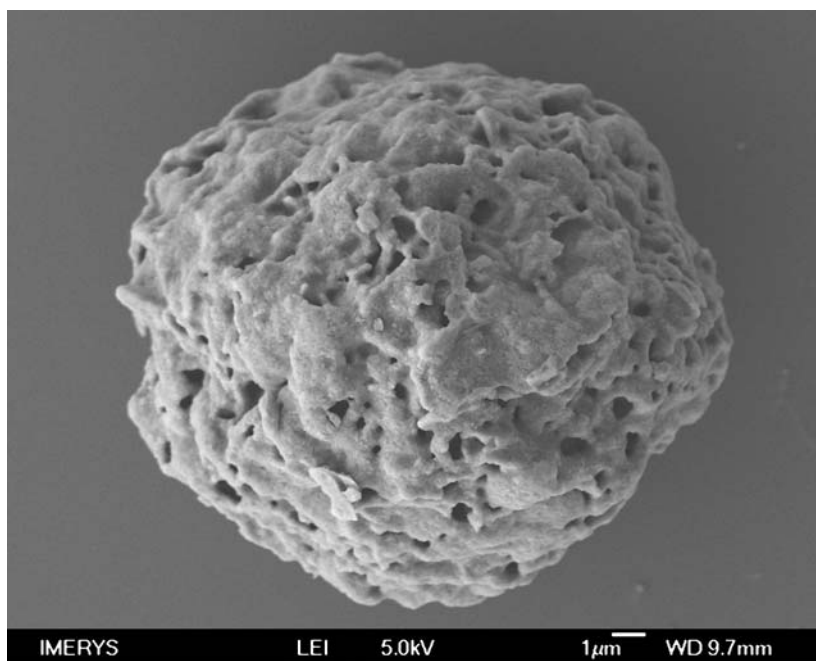
Figure 6.44 *SEM image of an individual kaolin microspheres calcined at 1400 ºC, kaolin ratio 2:1.*

The SEM images in Figures 6.41 to 6.44 represent kaolin microspheres from kaolin ratio experiments 2:1, the majority of microsphere structures observed using SEM were complete in spherical shape and exhibited a smooth surface structure. As the kaolin particle concentration was increased the kaolin plate formation at the surface seemed to be closely-packed. Due to the increase in kaolin concentration the bulk density of the microspheres throughout the calcination range increased when compared to the lower kaolin ratio of 1:1. These resulting denser microsphere particles are likely to be more robust when applied to a commercial application.

Individual kaolin plates are evident in Figures 6.41 and 6.42 after calcination at 850 and 1000 ºC. In Figure 6.43, a fusing of kaolin plates was evident at the microsphere surface after calcination at 1200 ºC forming larger plate structures. As the calcination temperature was increased to 1400 ºC there was no evidence of any individual kaolin particles at the

microsphere surface. Even though not as evident as the previous SEM images, all the samples from the kaolin ratio 2:1 experiments exhibited a porous surface structure. The less significant porous structures may be a result of the reduced amount of volatile material within the sample during calcination. In Figure 6.41 the pore size measured was between 0.5 and 0.9 µm. However, coalescence of surface voids also led to surface pores in the 1.5 µm range. For samples calcined between 1000 and 1400 ℃ the average pore size was measured between 0.3 and 0.6 µm. However, it was evident that coalescence of voids within the microsphere shell structure often resulted in larger pore structures.

The SEM images shown in Figures 6.45 to 6.52 exhibited the change in shell structure. These shell structures are of interest as they signify the formation of the shell structure due to the increase in the kaolin ratio.
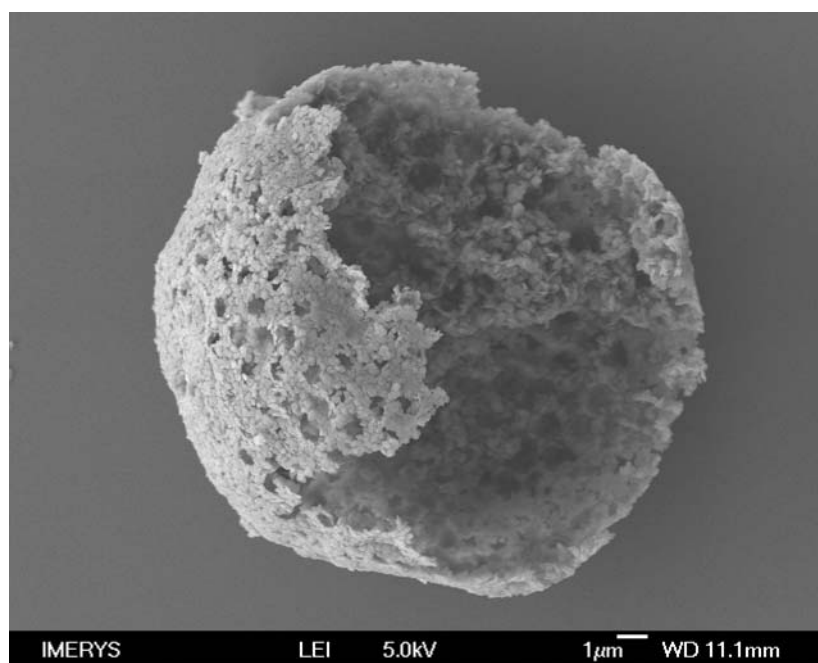
Figure 6.45 *SEM image showing the fractured shell structure of a kaolin microsphere, calcined at 1000 ℃; kaolin ratio 1:1.*
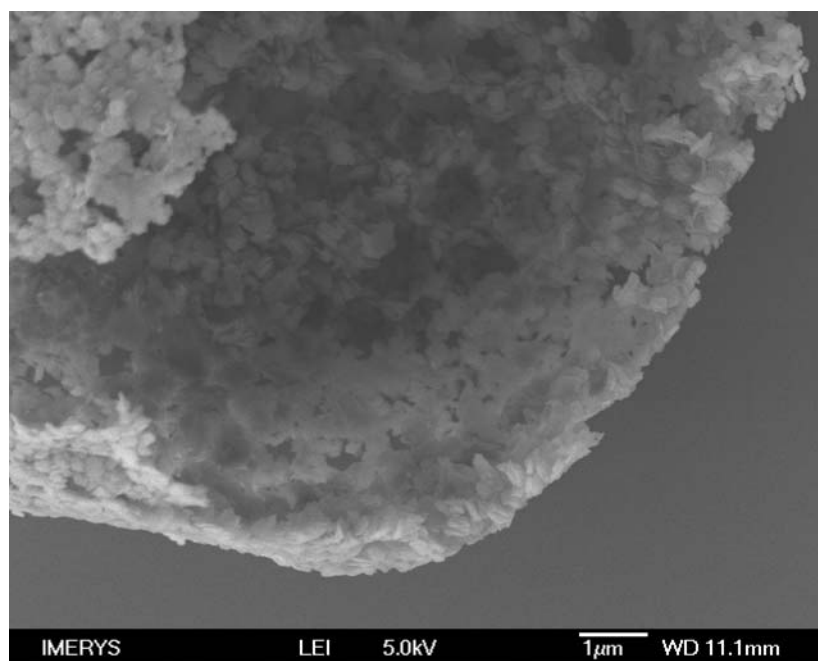
Figure 6.46 *Magnified SEM image of the shell structure of a calcined microsphere.*
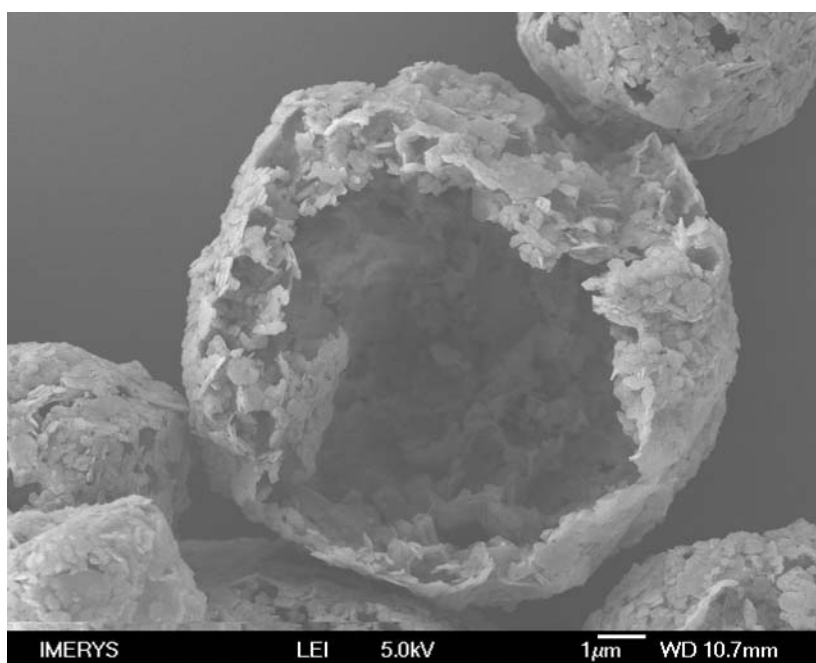
Figure 6.47 *SEM image of a fractured shell structure of a kaolin microsphere, calcined at 1000 ºC; kaolin ratio 1.5:1.*
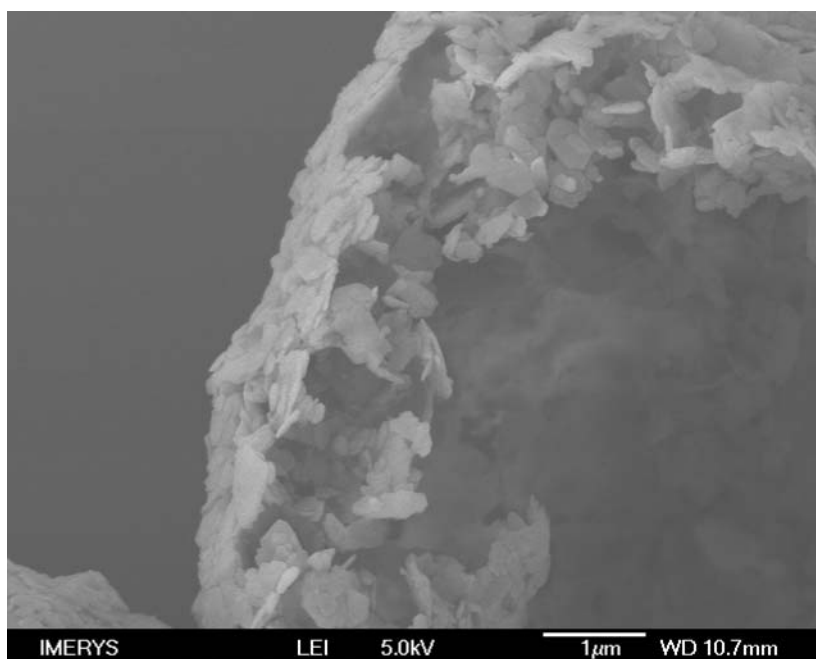
Figure 6.48 *Magnified SEM image of the shell structure of a calcined microsphere.*
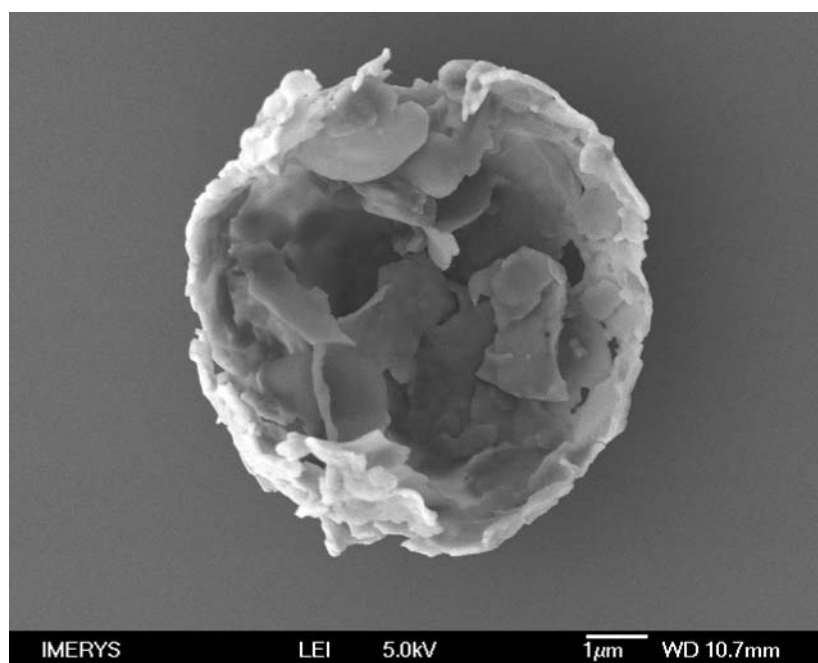
Figure 6.49 *SEM image of a fractured shell structure of a kaolin microsphere, calcined at 1200 ºC; kaolin ratio 1:1.*
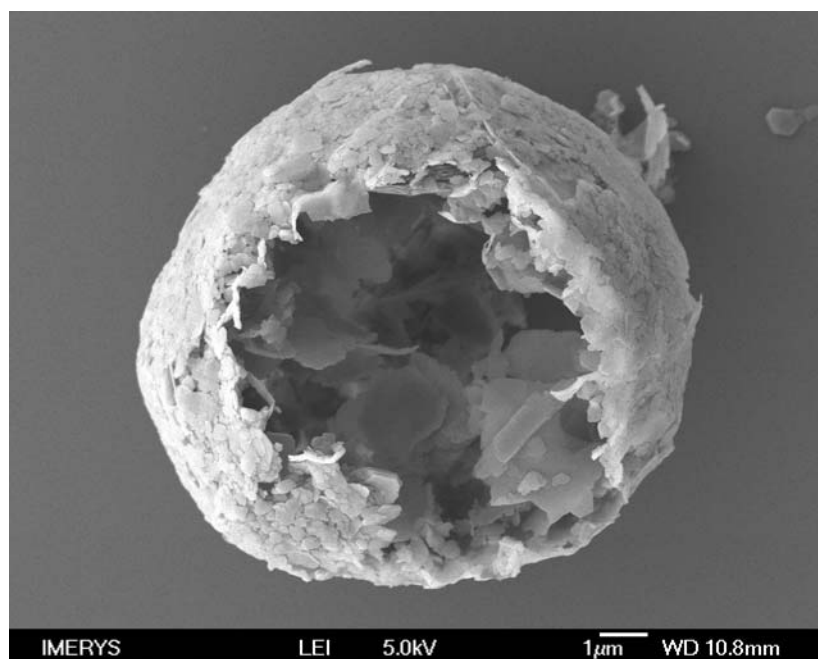
Figure 6.50 *SEM image of a fractured shell structure of a kaolin microsphere, calcined at 1200 ºC; kaolin ratio 1.5:1.*
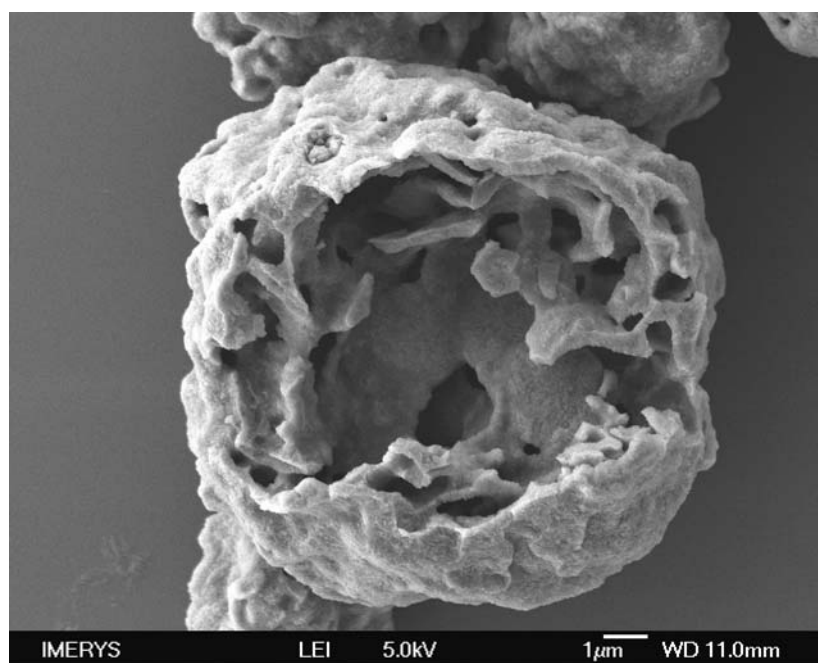
Figure 6.51 *SEM image of a fractured shell structure of a kaolin microsphere, calcined at 1400 ºC; kaolin ratio 1.5:1.*
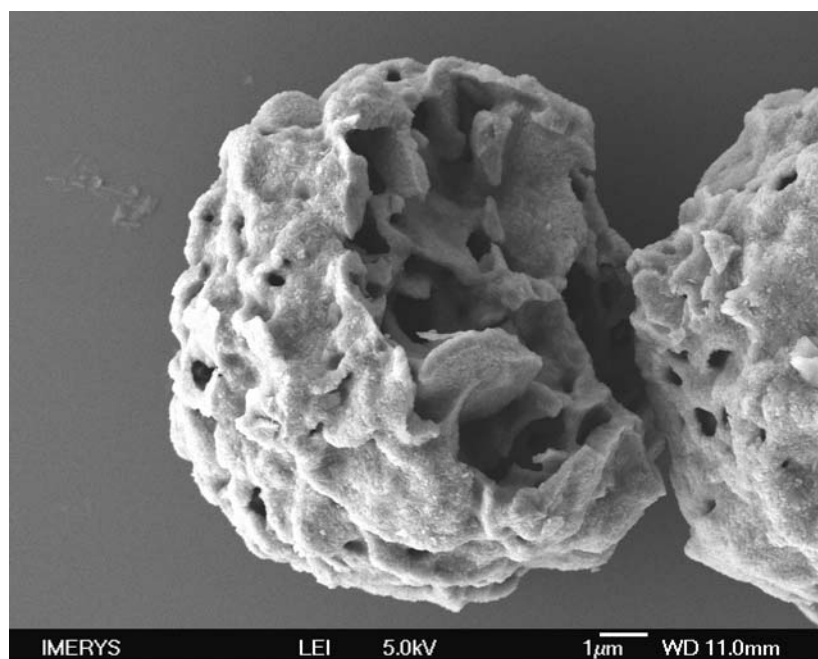
Figure 6.52 *SEM image of a fractured shell structure of a kaolin microsphere, calcined at 1400 ºC; kaolin ratio 2:1.*

Figures 6.45 and 6.46 show the shell structure of a microsphere produced from the kaolin ratio 1:1 experiment and calcined at 1000 ºC for 60 min. The shell structure was representative of the shell structures produced under these experiment parameters. The shell structure was likely damaged during the removal from the oven, storage or during the preparation method. It was possible to determine that microspheres produced from experiments using a low kaolin ratio of 1:1 generally exhibited thin shell structures that measured less than 50 nm. The shell structures of the microspheres were formed by the face-to-face orientation of fine kaolin particles during the spray drying process.

With an increase in the kaolin ratio the resulting microsphere structures after calcination exhibited a multi-layer shell as shown in Figures 6.47 and 6.48. However, thin shell structures were also evident. These multi-layer shell structures were attributed to the increase in kaolin particles that formed the shell during the spray drying process, however it was not clear whether the PS microspheres contributed to the multi-layer shell structures where face to edge kaolin plate configurations formed.

Honeycomb shell structures were evident in samples calcined at 850 and 1000 ºC, when the calcination temperature was increased to 1200 ºC the voids that contributed to the honeycomb structures collapsed. This may attribute to the decrease in microsphere particle size with an increase in calcination temperature. Resulting shell structures from microsphere samples calcined at 1200 ºC are shown in Figures 6.49 and 6.50.

Figures 6.51 and 6.52 were of specific interest because the images showed the internal structures of dense microspheres from kaolin ratio experiments 1.5:1 and 2:1.

As previously discussed the use of a focussed ion beam analyser is a powerful tool for determining the internal structure of a particle. Calcined samples from kaolin ratio experiments 1.5:1 and 2:1 were further characterised using a FIB analyser. The calcined samples from kaolin ratio 1.5:1 were chosen because of their possible hollow structures and samples from ratio 2:1 were chosen because of their low bulk density values, perhaps representative of honey-comb structures.

Even though kaolin ratio experiments 1:1 exhibited hollow microspheres throughout the calcination range, their structures were consider too fragile for further characterisation and any potential commercial use. Kaolin ratio experiments 3:1 and 4:1 were also consider not appropriate for further FIB characterisation due to their increased bulk densities when calcined at the high temperature range.

Figures 6.53 to 6.64 represent microsphere particles from the kaolin ratio experiments 1.5:1 and 2:1 that were cross sectioned using a focussed ion beam to determine the shell and internal structure resulting from calcination.
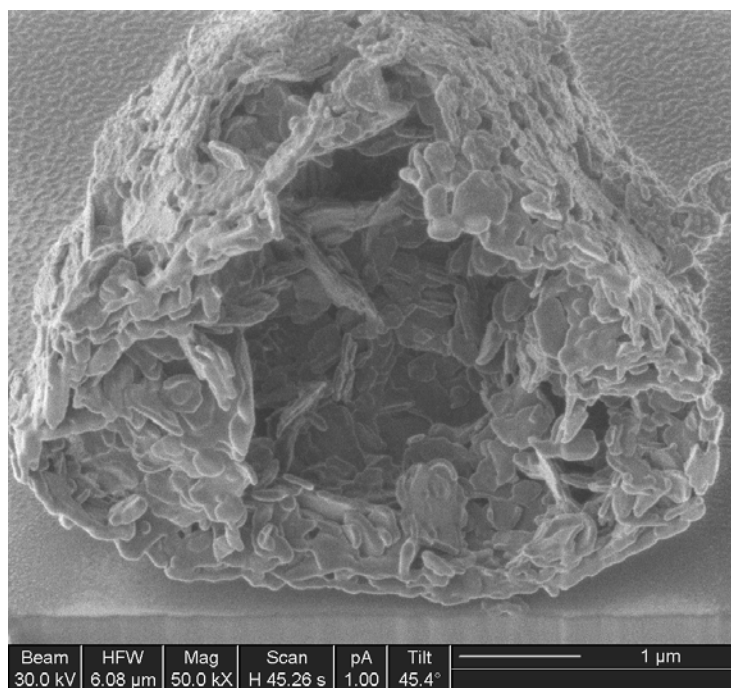
Figure 6.53 *FIB image of a calcined microsphere shell structure, calcination temperature 850 °C; kaolin ratio 1.5:1.*
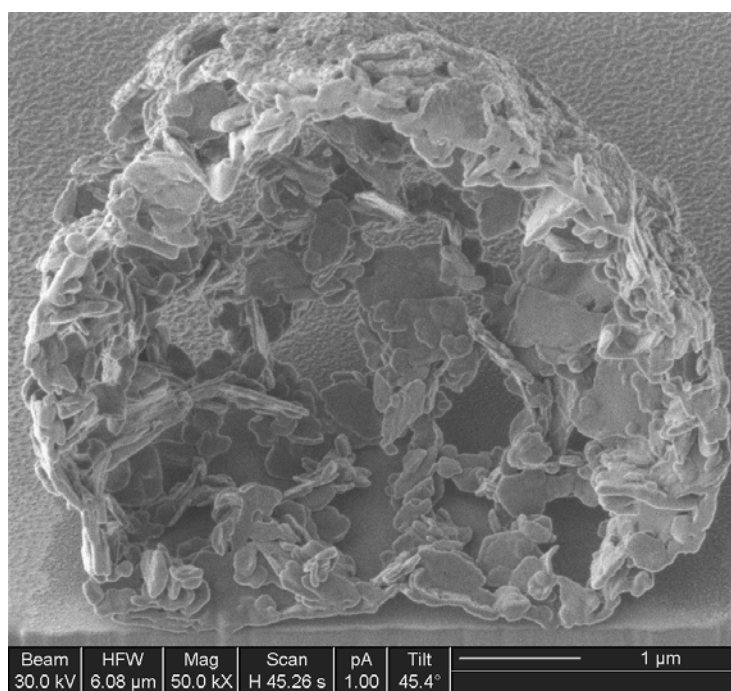
Figure 6.54 *FIB image of a calcined microsphere shell structure, calcination temperature 850 °C; kaolin ratio 1.5:1.*
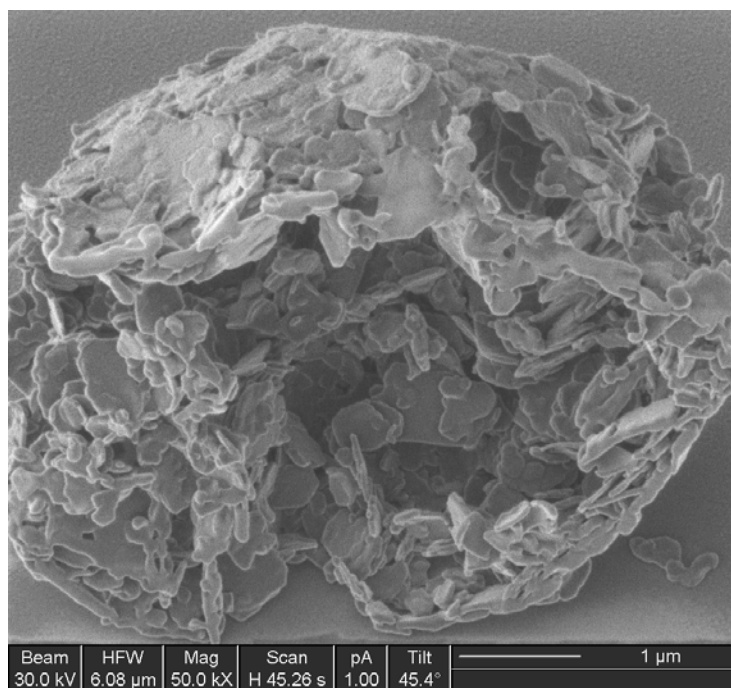
Figure 6.55 *FIB image of a calcined microsphere shell structure, calcination temperature 1000 ºC; kaolin ratio 1.5:1.*
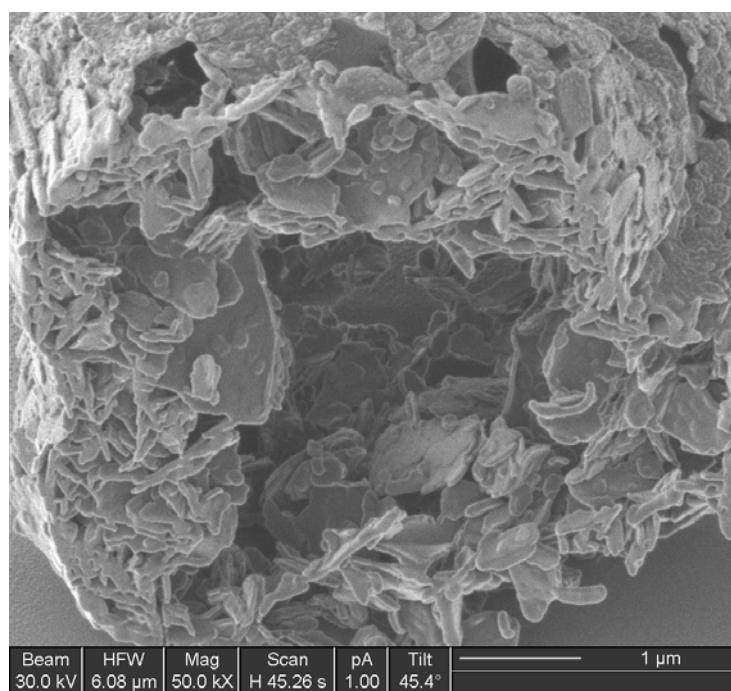
Figure 6.56 *FIB image of a calcined microsphere shell structure, calcination temperature 1200 ºC; kaolin ratio 1.5:1.*
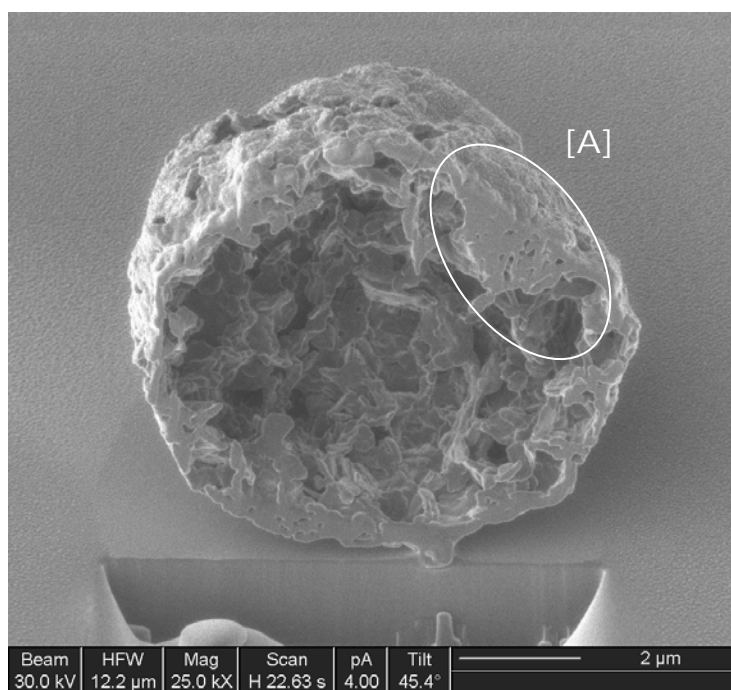
Figure 6.57 *FIB image of a calcined microsphere shell structure, calcination temperature 1400 °C; kaolin ratio 1.5:1.*
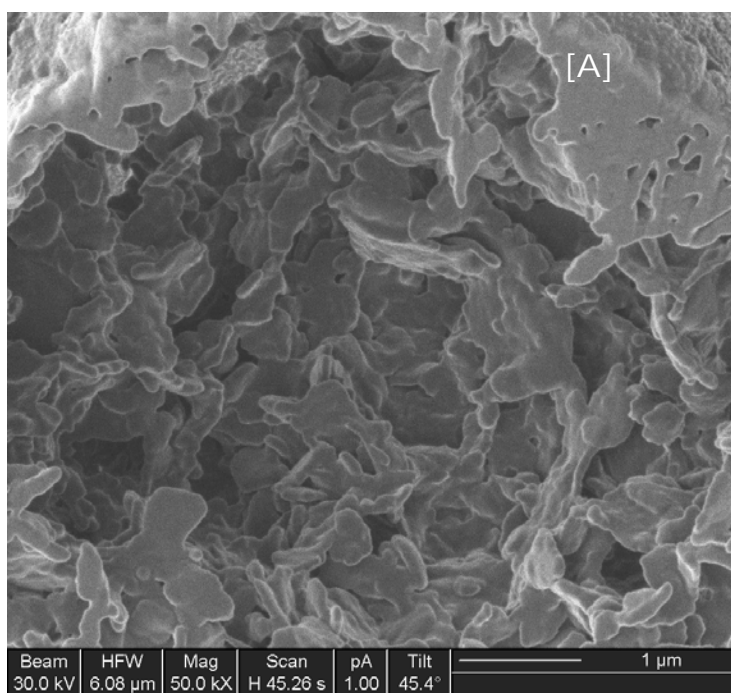
Figure 6.58 *Magnified FIB image of a calcined microsphere shell structure, calcination temperature 1400 °C; kaolin ratio 1.5:1.*

When calcined at 850 ºC for 60 min the resulting microsphere structures exhibited a weak structure likely due to the numerous voids at the surface. This was evident in Figures 6.53 and 6.54 where the particles had lost their spherical symmetry possibly during the preparation process for characterisation. However, both particles exhibited a hollow structure and their shell structures are formed by an aggregation of fine kaolin particles. Their shell structures were non-uniform in dimension as shell thickness varied from approximately 0.1 to 1.1 μm.

Figures 6.55 and 6.56 represent structures from samples calcined at 1000 and 1200 ºC respectively. The internal voids of the microspheres contribute to their low bulk density values and the small closed voids between individual kaolin plates attribute to the reduction in specific gravity. Figure 6.57 shows a cross-section of a microsphere shell structure after calcination at 1400 ºC, an internal void was evident. The kaolin particles that form the shell are fused and numerous closed voids are evident within the kaolin shell structure (indicated by letter A). Figure 6.58 represents a magnified image of the kaolin shell shown in Figure 6.57 where the closed voids within the shell structure are more apparent.

Figures 6.59 to 6.64 represent the cross-section imaging of shell structures from the kaolin ratio experiments 2:1 after calcination. The internal microsphere structure differs from the previous images shown in Figures 6.53 to 6.58.
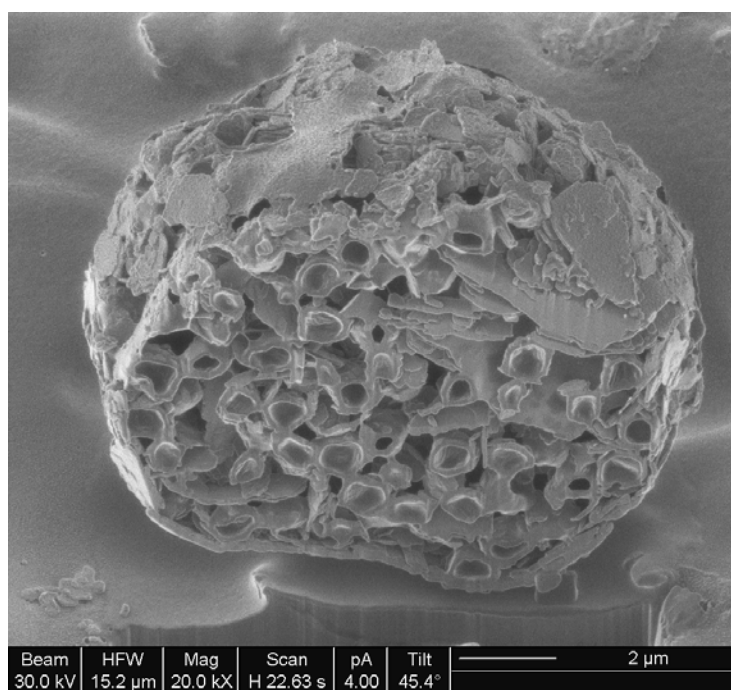
Figure 6.59 *FIB image of the internal structure of a calcined microsphere, calcination temperature 850 ºC; kaolin ratio 2:1.*
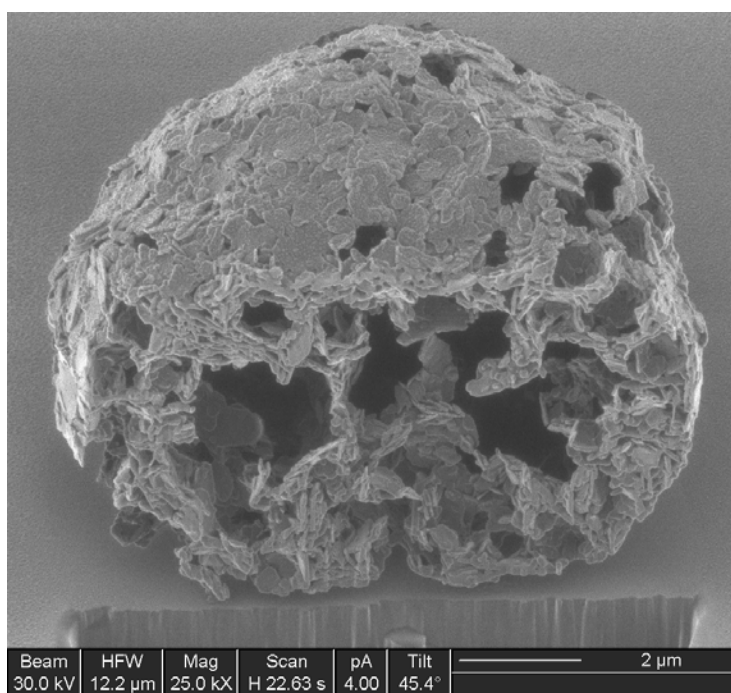
Figure 6.60 *FIB image of the internal structure of a calcined microsphere, calcination temperature 1000 ºC; kaolin ratio 2:1.*
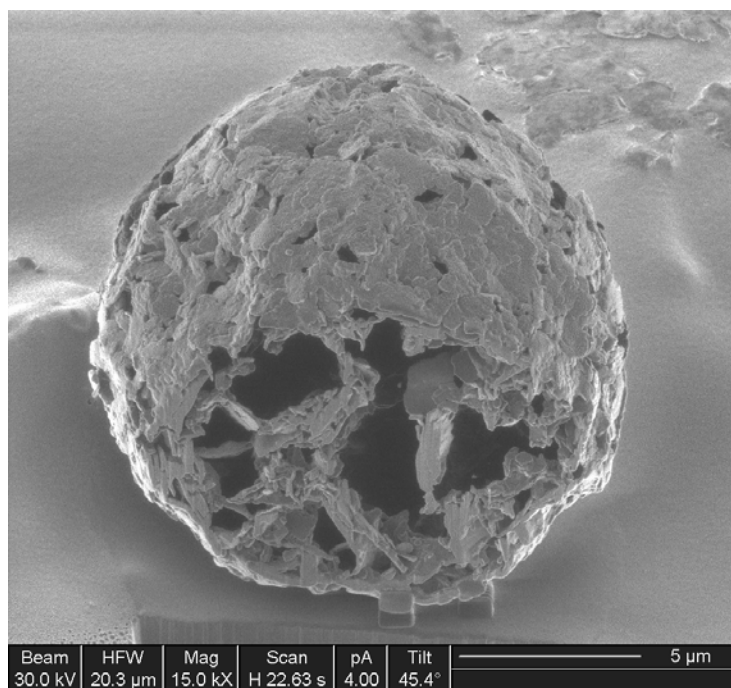
Figure 6.61 *FIB image of the internal structure of a calcined microsphere, calcination temperature 1200 ℃; kaolin ratio 2:1.*
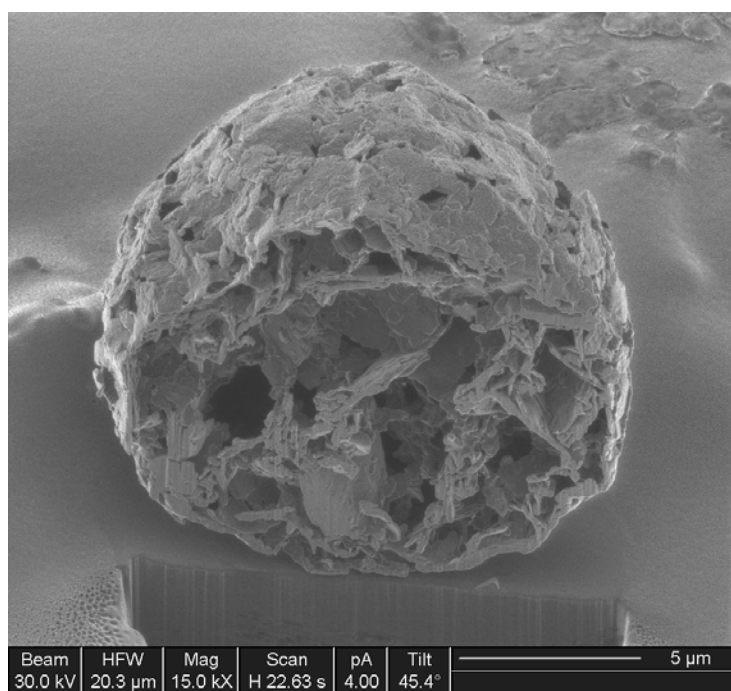
Figure 6.62 *FIB image showing the second cross-section cut of a calcined microsphere structure, calcination temperature 1200 ℃; kaolin ratio 2:1.*
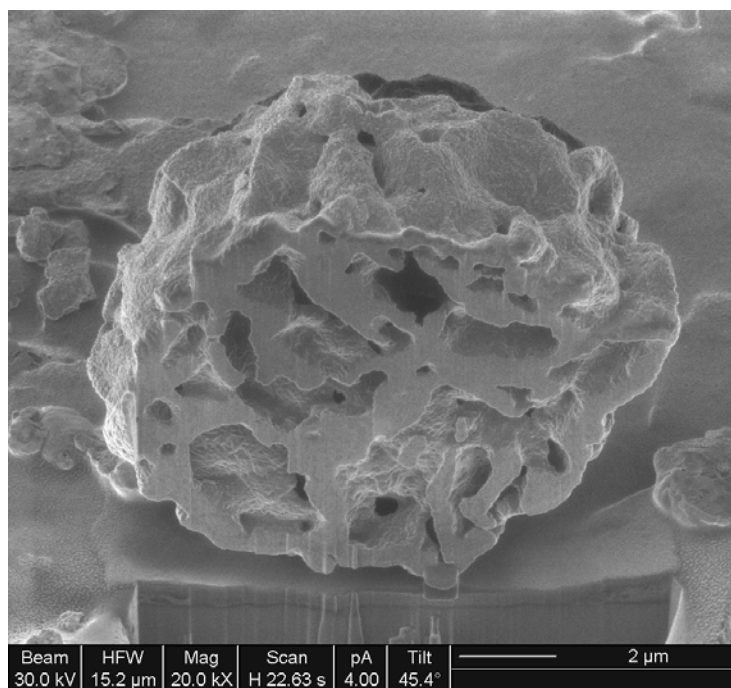
Figure 6.63 *FIB image of the internal structure of a calcined microsphere, calcination temperature 1400 ºC; kaolin ratio 2:1.*
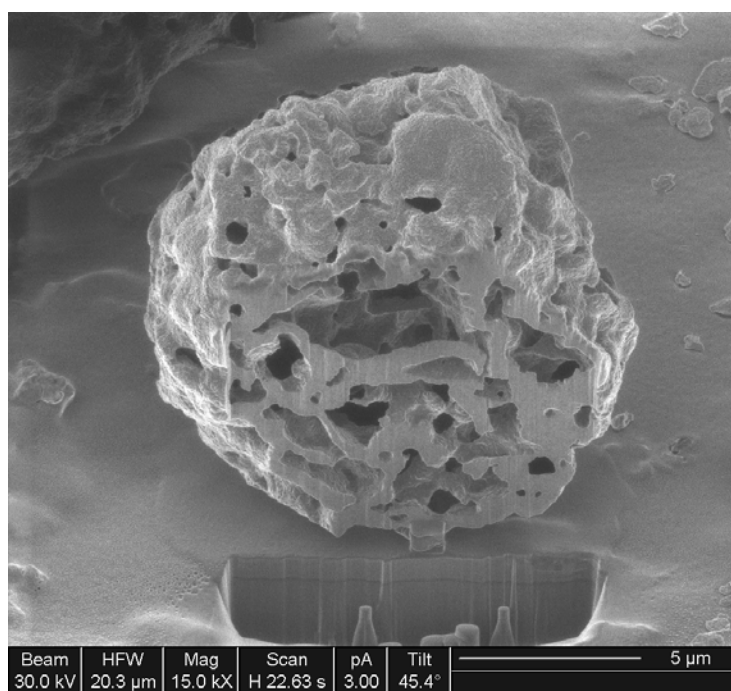
Figure 6.64 *FIB image of the internal structure of a calcined microsphere, calcination temperature 1400 ºC; kaolin ratio 2:1.*

Generally, after calcination at 850 ºC for 60 min the majority of the volatile PS material would be removed from the spray dried samples. Previous TG studies indicated that hollow and solid PS microspheres fully decomposed by approximately 425 and 550 ºC, respectively. However, a number of kaolin microspheres that were cross-sectioned using FIB indicated PS microspheres within the particle structure. Figure 6.59 shows a microsphere particle after calcination at 850 ºC that was cross-sectioned and exhibiting numerous PS microspheres encapsulated within the shell structure. With an increase in the kaolin ratio it was evident that the encapsulated PS material became 'armoured' whereas the kaolin shell structure protects the PS material from thermal decomposition. Figure 6.60 represents a structure after calcination at 1000 ºC. With an increase in temperature the PS material was removed from within the microsphere structure, resulting in numerous internal voids, whereas, single large voids were evident at a low kaolin ratio of 1.5:1.

Figures 6.61 and 6.62 represent the cross-sectioning of a microsphere structure after calcination at 1200 ºC. Figure 6.62 shows the result of a second cross-section cut by the FIB of the microsphere presented in Figure 6.61. The microsphere structure exhibits numerous voids throughout the internal structure due to the removal of the PS material. A scaffolding internal structure was evident due to the aggregation of fine kaolin particles and micro voids are apparent between individual kaolin plates.

Figures 6.63 to 6.64 represent the cross-section imaging of individual microspheres calcined at 1400 ºC. The internal kaolin scaffolding structure seen previous was evident however individual kaolin plates are indistinguishable. The internal structure resulted in numerous internal voids and open pores are evident at the surface.

The surface areas of the calcined microspheres from ratio experiment 1.5:1 were measured to determine the porosity of the shell structures. The surface area measurements were based on the BET gas adsorption method, the technique was described in detail in Chapter 4.2.5. The measurements are presented in Table 6.7, repeatability of measurements were in the range of ±3%.

Table 6.7 *Specific surface area measurements of calcined microspheres.*

Run	Ratio (*K:PS*)	Calcination Temp. (°C)	Bulk Density (g/cm³)	Particle Size d$_{50}$ (μm)	Specific Surface Area (m²/g)
1 a	1:0	850	0.30 ± 0.01	15.6 ± 0.4	4.0 ± 0.5
1 b	1:0	1000	0.55 ± 0.02	14.2 ± 0.8	3.5 ± 0.3
1 c	1 :0	1200	0.69 ± 0.03	13.1 ± 0.4	3.3 ± 0.4
1 d	1 :0	1400	0.80 ± 0.01	11.5 ± 0.5	5.2 ± 0.7
3 a	1.5 :1	850	0.11 ± 0.01	12.2 ± 0.4	19.4 ± 1.5
3 b	1.5 :1	1000	0.13 ± 0.01	11.2 ± 0.4	14.3 ± 1.3
3 c	1.5 :1	1200	0.20 ± 0.01	10.4 ± 0.6	12.4 ± 1.1
3 d	1.5 :1	1400	0.38 ± 0.01	n.r.	10.6 ± 1.5

As shown in Table 6.7 the specific surface area of the hollow microspheres from the kaolin ratio experiments 1.5:1 were higher than that of the control kaolin microspheres. Bulk density and particle size measurements are shown for comparison. The high surface area values for the low density microspheres indicate a higher level of porosity. However, the surface area decreased with an increase in calcination temperature indicating shrinkage of the microspheres and the fusing of fine particle at the shell surface, which in turn resulted in closed voids. Hollow microspheres with high surface area can be used as drug carriers because they can have a high drug loading [Sun, et al. 2008].

6.4.4. Thermogravimetry analysis of spray dried microspheres

Spray drying is frequently used to produce a range of microspherical structures [Broadhead, et al. 1992; Corrigan, 1995]. However, a frequent problem is the understanding and characterising of a complex formation containing more than one component during a heating process. While to date the majority of spray dried and calcined structures are often studied by X-ray diffraction methods [Tsapis, et al. 2002; Liu, et al. 2009; Wang, et al. 2009], the use of thermal methods such as TGA and DSC would be highly appropriate. Thermal methods can identify and quantify the stability, changes in amorphous state and the elimination of a component during a heating process.

Kaolin ratio experiments spray dried were characterised by using a Netzsch STA-449EP thermogravimetric instrument, as described in Chapter 4. The powder samples were taken from the spray dryer, dried in a chamber furnace at 60 ºC and kept in a dehumidifier for approximately 12 hrs prior to heating. Representative samples were placed in an alumina crucible and heated at 10 ºC per min.

Figures 6.65 represents the thermal decomposition of the kaolin ratio experiment 1.5:1, the increase in weight loss of the spray dried samples can be attributed to the removal of the PS material. For clarity, the TG-DSC curve for the kaolin ratio experiment 2:1 is shown in Appendix D, Figure D.9.
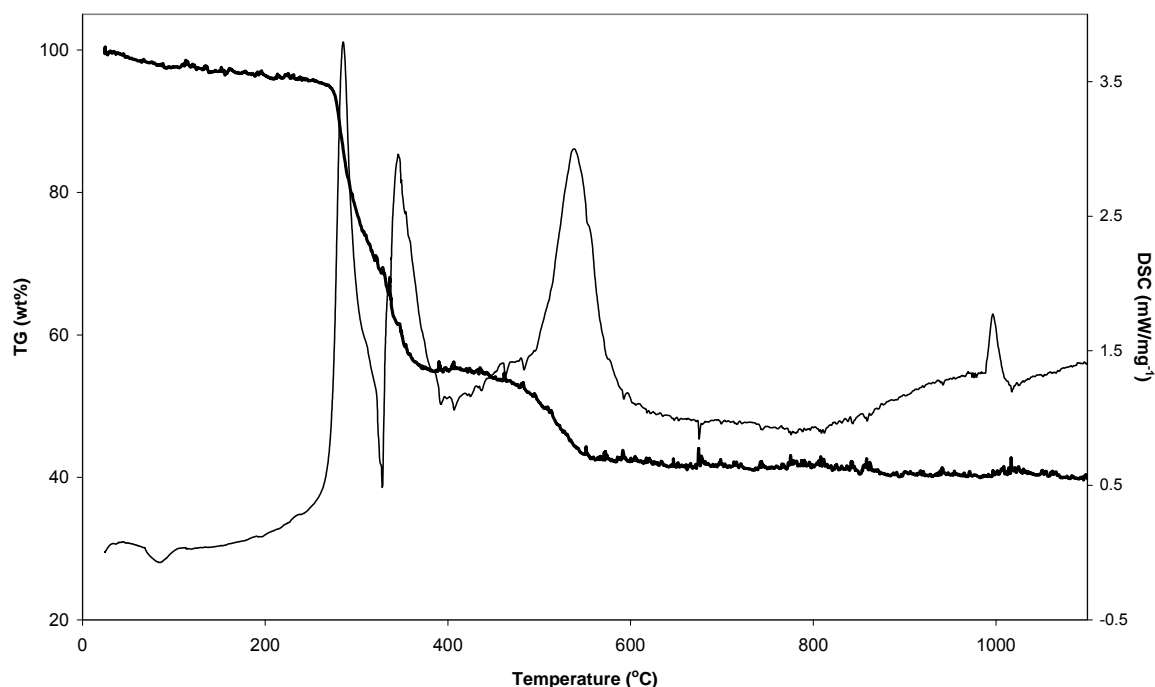
Figure 6.65 *Thermal decomposition studies of spray dried microspheres by TG-DSC. Kaolin ratio experiment 1.5:1.*

The TG (bold line) and DSC curve represent the thermal degradation of both kaolin and PS from a spray dried sample. From the initial thermal characterisation of kaolin it was determine that the average 14.6 ±1.6 wt% loss at 1000 ℃ was due to the removal of moisture, the dehydroxylation and decomposition of kaolin. Therefore, the increase in weight loss to 59.4 wt% as shown in Figure 6.65 was attributed to the removal of PS from the spray dried powder sample and the thermal degradation of the kaolin mineral.

From the TG curve it was possible to identify three significant stages of weight loss; initially from room temperature to 100 ℃ adsorbed water was lost from the powder sample identified by the endothermic peak centred at 84 ℃. This weight loss continued until the thermal decomposition of PS was identified by the second exothermic peak centred at 345 ℃; it was considered that this weight loss was the excess amounts of free PS microspheres that were not encapsulated within the void structure of the kaolin microspheres. The third stage of

weight loss was identified between 450 and 560 ºC at which point the PS material within the kaolin particles was decomposed. The weight loss between 600 and 1000 ºC was measured at approximately 2 wt%. No endothermic peak centred approximately at 547 ºC representing the dehydroxylation of the kaolin was evident in the DSC curve due to the exothermic reaction centred at 538 ºC of the PS material within the kaolin microspheres.

The first and second exothermic peaks, centred at 285 and 345ºC shown in Figure 6.65 have not previously been identified in the thermal decomposition of either kaolin or PS. The spray dried samples investigated showed similar TG and DSC curves, a comparison of the DSC curves for kaolin ratio experiments 1.5:1, 2:1 and 3:1 are shown in Figure 6.66. Data relating to the endothermic and exothermic peaks for the individual samples are shown in Table 6.8.
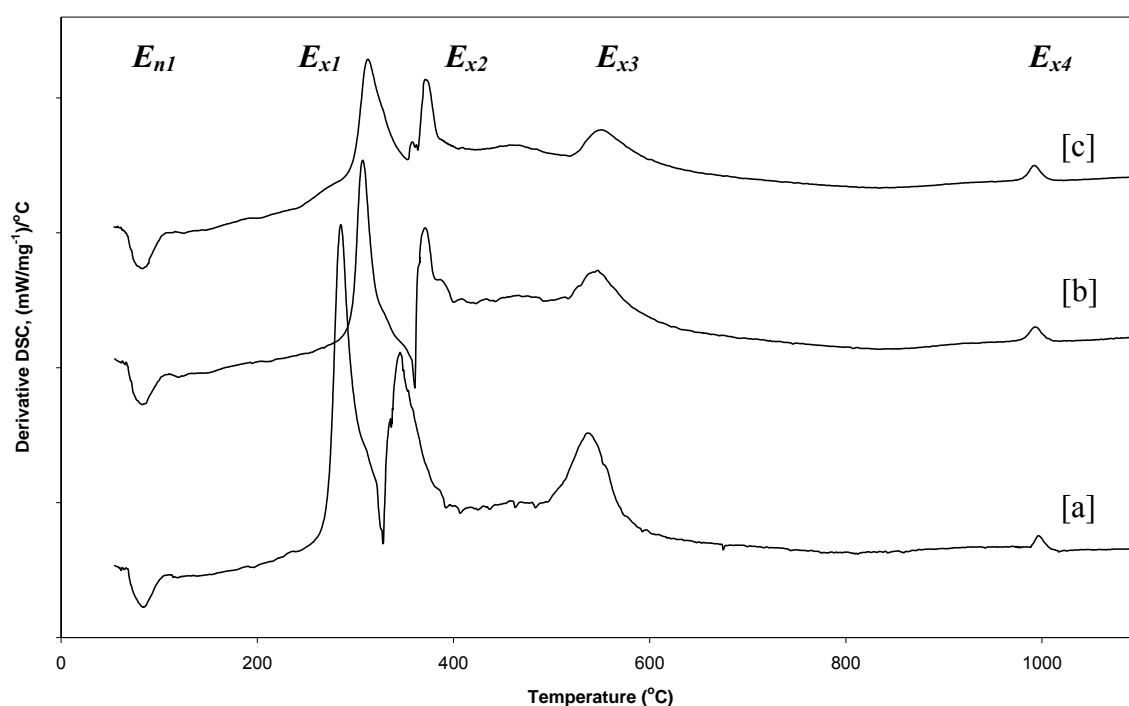
Figure 6.66 *DSC curves for spray dried microspheres from kaolin ratio experiments: 1.5:1 [a]; 2:1 [b]; and 3:1 [c].*

Table 6.8 *Endothermic (E_n) and exothermic (E_x) data relating to thermogravimetric analysis for spray dried microsphere experiments.*

Sample / Ratio	$E_{n\,1}$	$E_{x\,1}$	$E_{x\,2}$	$E_{x\,3}$	$E_{x\,4}$	LOI (wt%)
Kaolin	74	n.r.	n.r.	n.r.	990	14.6 ± 1.6
PS	98	n.r.	n.r.	415	n.r.	98.0 ± 1.1
1.5:1	84	285	345	538	996	60.1 ± 3.8
2:1	90	307	371	547	994	42.3 ± 3.2
3:1	91	312	374	552	992	41.0 ± 2.9

The DSC curves for the thermal study of the spray dried experiments are shown in Figure 6.62. The DSC curves for the kaolin ratio experiments 2:1 and 3:1 show a slight shift to the right indicating an increase in temperature. The temperature for the initial exothermic peak centred at 285 ºC for [a] kaolin ratio experiments 1.5:1 may be attributed to the onset decomposition of the free PS material.

As the amount of PS was reduced within the sample due to an increase in the kaolin ratio, the area of the exothermic peaks decreased, as expected since there was less PS to undergo an exothermic reaction. The endothermic peaks representing the loss of moisture centred between 84 and 91 ºC and the phase transformation of metakaolin to the spinel phase identified by the exothermic peaks centred between 992 and 996 ºC are comparable and are in good agreement with published results [Chen, et al. 2004; Ptáček, et al. 2010].

The endothermic peak ($E_{n\,1}$) for the kaolin starting material centred at 74 ºC identifies the removal of loss of adsorbed water. Endothermic peaks for the spray dried experiments also included the loss of moisture for the PS material within the powder samples. Therefore,

under similar process parameters and storage conditions the increase in loss-of-moisture was related to the increase of PS. However, the effect of spray drying the slurry samples with an inlet and outlet air temperature of 125 ±10 and 314 ±6 ºC respectively, would likely affect the physical properties of the samples and possibly increase the temperature of the endothermic reaction.

The exothermic reactions, E_{x1}, E_{x2} and E_{x3} for the spray dried samples represent the decomposition and removal of the PS and organic material. The removal of the PS material was likely to depend upon the state of the PS. Free PS material within the sample would be removed as the temperature was increased, however, due to the heat profile of the spray drying process complete removal of the free PS would possibly be completed at a lower temperature. Characterisation of the PS material indicated that the PS would decompose between 315 and 425 ºC. The removal of 'armoured' PS material, decomposition of the PS from within the kaolin microsphere structure was indicated by the exothermic reaction E_{x3}. An increase in temperature for the exothermic reactions of the spray dried samples was evident as shown in Table 6.8; this increase corresponds to the increase in the kaolin ratio of the samples.

A second endothermic peak representing the dehydroxylation of kaolin usually identified at around 547 ºC was absent from all the DSC curves shown in Figure 6.66, in all three kaolin ratio experiments a third exothermic peak was present, believed to represent the removal of the PS and organic material from within the kaolin microsphere samples.

A reference point for comparison would be the values for the final exothermic peak, E_{x4}, which signifies the transformation of metakaolin to the spinel phase at around 990 ºC.

The weight loss measured by TG for the spray dried samples are shown in Table 6.6, the average values for the kaolin ratio experiments 1.5:1; 2:1; and 3:1 are 60.1 ±3.8; 42.3 ±3.2; and 41.0 ±2.9 wt%, compared to the calculated average values of 54.6, 47.9 and 39.6 wt%, respectively. The calculated values account for the total removal of the PS and organic material from the kaolin samples. The differences between the TG and calculated weight loss values could be attributed to the particle formation during the spray drying process or the sampling technique used for TG analysis.

6.4.5. Composition and chemical analysis

The phase transformation of calcined kaolin has been reported [Brindley, et al. 1959a; 1959b; 1959c; Bridson, et al. 1985; Chen, et al. 2000; Chen, et al. 2004]. It is general understood that when kaolinite is heated, the adsorbed water is liberated at approximately 100 ºC and the weakest part of the chemical bond is broken. Dehydroxylation takes place at 400 to 500 °C. For kaolinite, dehydroxylation might result in the disturbance of the octahedral sheets by the outer hydroxyls [Gruner, 1932; Freimann, et al. 2001]. After heating at 950 ºC, the SiO_4 of the tetrahedral groups combine with the AlO_6 group to form the Al-Si spinel phase in a short range order structure.

The Al-Si spinel phase general appears around 950 ºC and persists until 1200 ºC [Brindley, et al. 1959a; Chakraborty, 2003; Heide, et al. 2006; Ptáček, et al. 2010]. Mullite formation occurs at 1000 ºC, growth increases and is accelerated by instantaneous nucleation and short distance diffusion. The mullite formation increases with the heating temperature from 1000 to 1300 ºC. The general transformation of kaolin to mullite can be expressed by the following reactions [Chen, et al. 2004; Ptáček, et al. 2010]:

$$Al_2O_3 \cdot 2SiO_2 \cdot 2H_2O(kaolinite) \xrightarrow{400 \sim 500^\circ C}$$
$$Al_2O_3 \cdot 2SiO_2(metakaolinite) + 2H_2O$$

[6.2]

$$2(Al_2O_3 \cdot 2SiO_2)(metakaolinite) \xrightarrow{\sim 950^\circ C}$$
$$Si_3Al_4O_{12}(Al-Si-spinel) + SiO_2(amorphous)$$

[6.3]

$$3Si_3Al_4O_{12}(Al-Si-spinel) \xrightarrow{>1050^\circ C}$$
$$2(3Al_2O_3 \cdot 2SiO_2)(mullite) + 5SiO_2(amorphous)$$

[6.4]

$$SiO_2(amorphous) \xrightarrow{>1200^\circ C}$$
$$SiO_2(cristobalite)$$

[6.5]
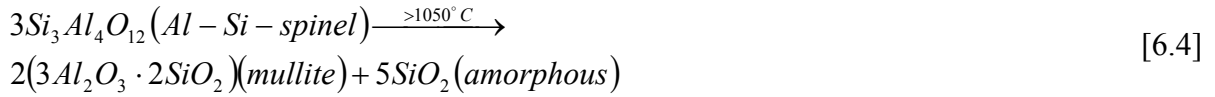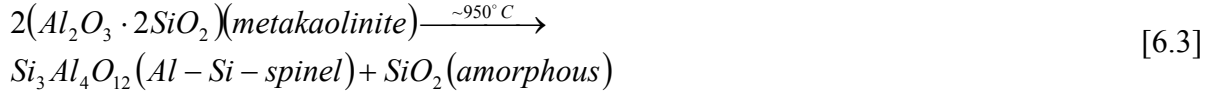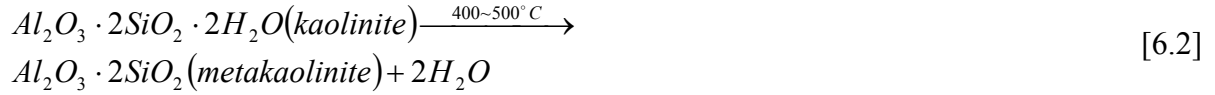
The purpose of this investigation and analysis was to determine and identify discernible impurities of the calcined kaolin microspheres and identify any discrepancies in the mullite transformation. In a commercial application the formation of aluminosilicate fibres are detrimental with associated health hazards. The formation of cristobalite, a crystalline form of silica, has the potential to be carcinogenic [Gantner, 1986; Brown, et al. 1992; Laskowski, et al. 1994].

Due to commercial constraints only the kaolin ratio sample 1.5:1, spray dried and calcined between 850 and 1400 ºC were selected for XRD and XRF analysis. All spray dried and calcination experiments used the same starting kaolin mineral, therefore no variation in the phase composition and element analysis was to be expected.
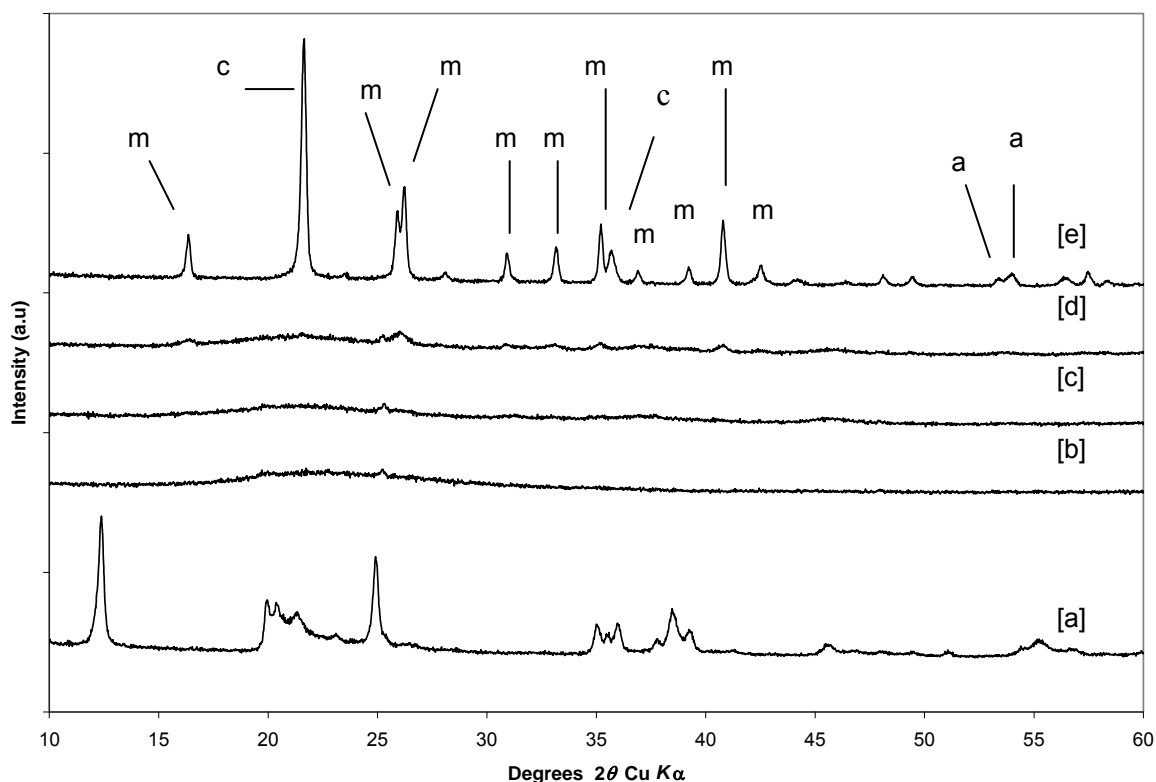
Figure 6.67 *XRD patterns of spray dried and calcined kaolin microspheres; [a]starting kaolin mineral, [b] 850 ℃; [c] 1000 ℃; [d] 1200 ℃; and [e] 1400 ℃; (m: mullite, c: cristobalite, and a: anatase).*

Figure 6.67 shows the XRD patterns of the kaolin microspheres as calcined at specific temperatures. It was found that the minor phase of quartz or mica where not detected by the reflections of (201) and (002) at 2θ= 45.8 and 17.6° in the kaolin starting mineral, respectively. When samples were calcined at 850 and 1000 ℃ for 60 min the Al-Si spinel have been noted to be the major phase as shown in Figure 6.62 [b] and [c] indicating that they were amorphous. The slight diffraction peak at 2θ= 25.25° for both samples represents the collapse of the metakaolinite structure, with a decrease in *d* values from 3.57 to 3.51 Å. No peaks of any impurities were observed.

The mullite phase appears as the microsphere samples were heated at 1200 ℃ as shown in Figure 6.62 [d]. When the calcination temperature was increased to 1400 ℃, the intensity

254

increased and more defined X-ray reflections are observed [e], indicating further development of mullite formation. The (120) and (210) reflections split at $2\theta= 25.91$ and $26.24°$ are characteristic of XRD patterns for mullite and are in agreement with published results [Li, et al. 1991; Chen, et al. 2004]. Cristobalite was identified by the reflections of (111) and (220) at $2\theta= 21.65$ and $35.69°$ in the XRD pattern for samples calcined at 1400 ℃, respectively. Anatase was also identified by the reflections of (105) and (211) at $2\theta= 53.42$ and $54.03°$ as presented in Table 6.7. Data relating to the identification of cristobalite and anatase within the calcined samples correspond to similar results published [Vine, et al. 1984; Wang, et al. 1999; Chen, et al. 2000; Chen, et al. 2004]. The d-spacing values for the calcined sample in Table 6.9 are compared to values for a reference mullite composite from the ICDD database. SEM was used to identify the phase change of the kaolin microspheres. Figure 6.68 exhibits the fibres material at the surface of a microsphere after calcination at 1400 ℃ due to the formation of cristobalite.
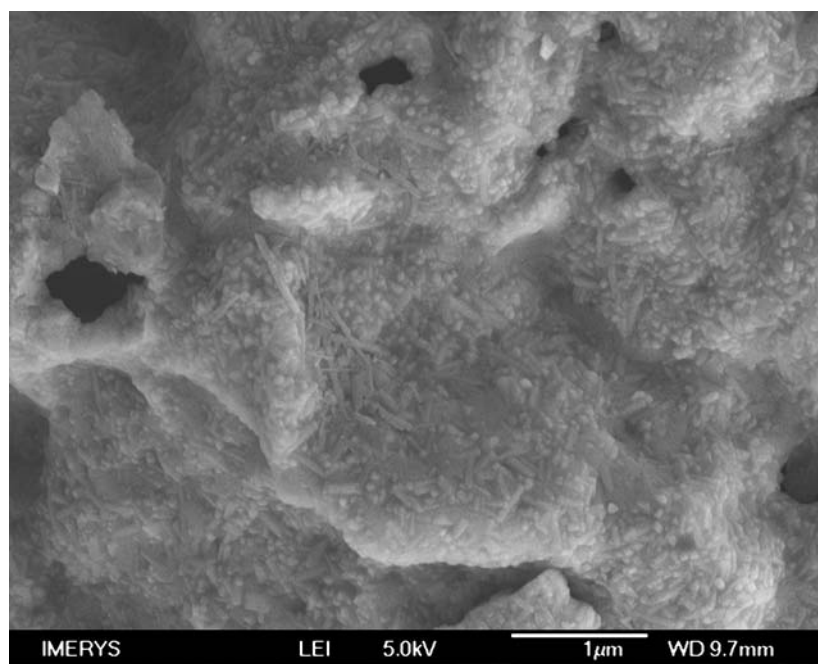
Figure 6.68 *SEM image showing crystallised fibre at the surface of a kaolin microsphere after calcination at 1400 ℃ for 60 min.*

Table 6.9 *Identification of crystallisation phases of kaolin microspheres calcined at 1400 ºC.*

2 θ	*Reflection Indices* *(hkl)*	*Composition*	*Sample* *d-spacing (Å)*	*Reference:* *d-spacing (Å)*
16.36	110	mullite	5.41	5.39
21.65	111	cristobalite	4.10	n.r.
25.91	120	mullite	3.43	3.42
26.24	210	mullite	3.39	3.39
30.93	001	mullite	2.88	2.88
33.16	220	mullite	2.69	2.69
35.21	111	mullite	2.54	2.54
35.69	220	cristobalite	2.51	n.r.
36.90	130	mullite	2.43	2.42
39.21	201	mullite	2.29	2.29
40.79	121	mullite	2.21	2.20
42.54	230	mullite	2.12	2.12
53.42	105	anatase	1.71	n.r.
54.03	211	anatase	1.69	n.r.

The composition and purity of the kaolin spray dried microspheres by XRD are shown in Table 6.10. Individual XRD patterns for the calcined microspheres are shown in Appendix D, Figures D.12 to D.15.

Table 6.10 *Composition and purity of spray dried and calcined kaolin microspheres (mass %) by XRD.*

Composition / Temp. (ºC)	850	1000	1200	1400
Amorphous	99.0	98.9	97.9	0.0
Anatase	1.0	1.0	1.0	2.0
Cristobalite	0.0	0.0	1.0	34.0
Mullite	0.0.	< 0.1	< 0.1	64.0

The composition of the starting kaolin material was 100% kaolinite. Figure 6.62 indicates the composition and growth of mullite, cristobalite and anatase phases as the calcination temperature increases. The most favourable composition was found for microspheres calcined at 1000 ºC where cristobalite had not been formed and mullite was measured at <0.1%. The calcination range could be further investigated by calcining microsphere samples at an interval of 20 ºC between 1000 and 1400 ºC to identify the initiation and growth of cristobalite in more detail. Table 6.11 lists the composition of the calcined microspheres by XRF.

Table 6.11 *Composition of spray dried and calcined kaolin microspheres (mass %) by XRF.*

Sample	Temp. (ºC)	Al_2O_3	SiO_2	K_2O	Fe_2O_3	TiO_2	CaO	MgO	Na_2O	LOI
FK-8489		37.81	45.78	0.11	1.09	1.42	0.08	0.01	0.02	13.75
1.5:1	**850**	44.70	52.40	0.18	0.62	0.88	0.08	0.04	0.45	0.64
1.5:1	**1000**	44.60	52.30	0.18	0.62	0.89	0.63	0.06	0.44	0.23
1.5:1	**1200**	44.70	52.30	0.18	0.62	0.86	0.64	0.06	0.45	0.17
1.5:1	**1400**	45.00	52.70	0.19	0.63	0.88	0.09	0.06	0.45	0.03

The analysis by XRF was to determine the changes in composition due to calcination and identify any discernible impurities. The major components of the kaolin starting material were SiO_2 and Al_2O_3, 45.78 and 37.81 wt%, respectively. The SiO_2/Al_2O_3 ratio was calculated at 1.21 for the kaolin mineral FK-8489. Upon calcination the SiO_2/Al_2O_3 ratio values showed a slight decrease in values but were comparable, for the sample calcined at 1000 ºC the ratio was measured at 1.17. The Fe_2O_3 values in Table 6.9 showed a 43% decrease in wt% after calcination and TiO_2 values showed a decrease between 37 and 39%. The concentrations remained in the same value order, which indicates that they are part of

the kaolinite structure. The elements Fe_2O_3 and TiO_2 are considered to be detrimental to the brightness of kaolin [Sousa, 2000], the brightness values of the resulting microsphere samples after calcination are presented in Table 6.12.

Table 6.12 *ISO brightness values (%) for kaolin microspheres after calcination.*

Sample	Temp. (ºC)	Al₂O₃	SiO₂	Fe₂O₃+TiO₂	ISO Brightness	Yellowness
FK-8489		37.81	45.78	2.51	87.2	5.9
1.5:1	850	44.70	52.40	1.50	86.6	7.2
1.5:1	1000	44.60	52.30	1.51	90.0	5.0
1.5:1	1200	44.70	52.30	1.48	92.5	3.5
1.5:1	1400	45.00	52.70	1.51	91.9	3.6

The important optical properties of the calcined samples include brightness and yellowness and are expressed in ISO units in Table 6.12. During calcination, the kaolinite structure breaks down and the iron containing minerals are converted to free oxides that impart colour to the product. The organic matter released from the kaolinite particles also contribute to a reduction in brightness, therefore the optical properties degrade during the initial heating. As the calcination temperature is increased, the position of iron changes during dehydroxylation and with its incorporation into the mullite structure, the organic matter burns off and the optical properties improve significantly [Stoch, 1987].

As shown in Table 6.12 the calcined samples generally showed an increase in brightness than the starting kaolin mineral. The brightness of the samples calcined above 1000 ºC was measured between 90.0 and 92.5% compared to the 87.2 ±1.0% of the kaolin raw material. The decrease in brightness to 86.6% when calcined at 850 ºC was presumably due to the

conversion phase of iron to free oxides and the release of organic material within the kaolin structure; calcination at 1000 ℃ restored the brightness to 90.0%. In Table 6.10 the combined values of Fe_2O_3 and TiO_2 show a decrease in mass as the samples are calcined compared to the values of the raw mineral. This decrease can be attributed to the removal of some free iron oxide impurities along with the titanoferrous minerals [Chandrasekhar, et al. 2002]. The reduction in Fe_2O_3 and TiO_2 from 2.51 to approximately 1.50% confirms this observation. Identification of elements present at the surface of the calcined samples was conducted by XPS. Surface analysis was accomplished by irradiating a sample with X-rays and analysing the energy spectrum of the electrons emitted.
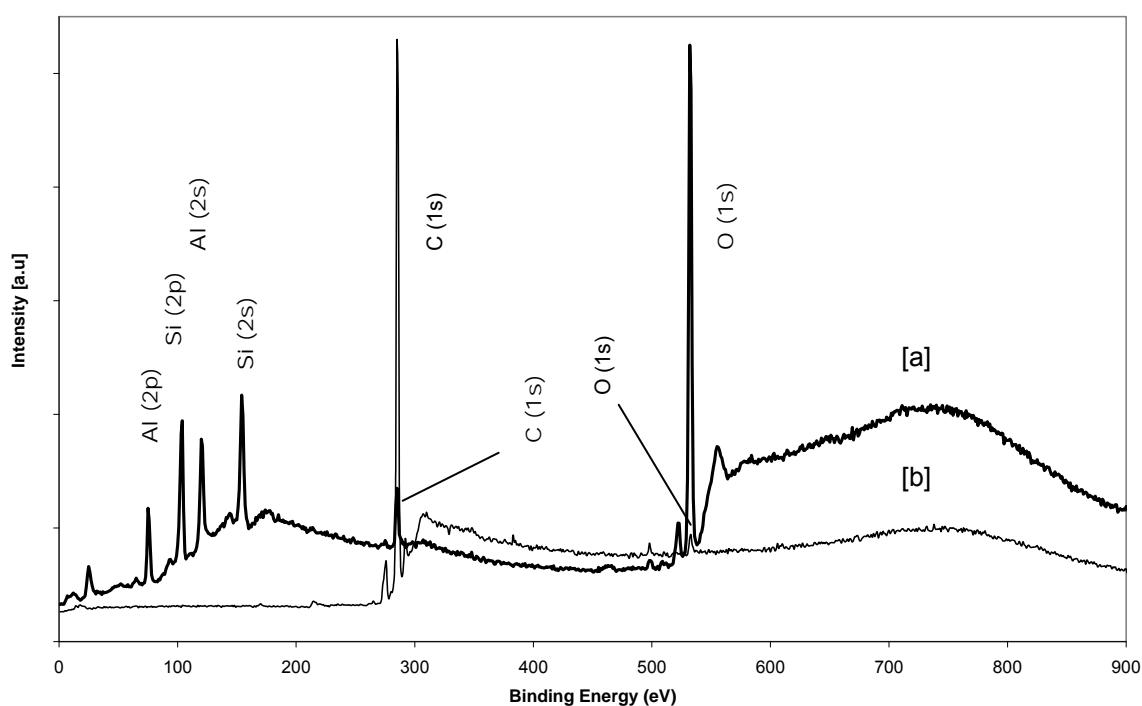
Figure 6.69 *XPS survey of the [a]starting kaolin mineral and [b] PS material.*
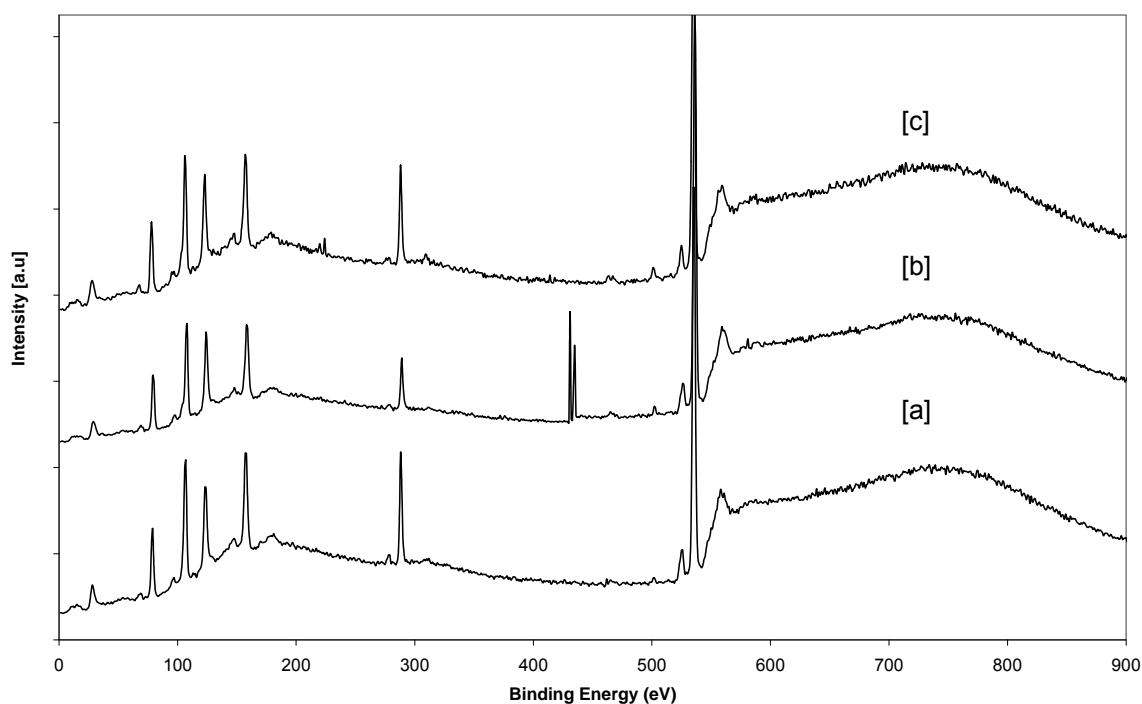
Figure 6.70 *XPS survey of kaolin microspheres; calcined at 850 ℃ [a]; 1000 ℃ [b]; and 1400 ℃ [c].*

The XPS spectra presented in Figures 6.69 and 6.70 identify the elements associated with surface components of the raw materials and samples calcined at 850, 1000 and 1400 ℃. For clarity the spectra for the calcined samples are presented in Figure 6.70, the spectrum for the sample calcined at 1200 ℃ showed no variance in peak positions and was omitted.

The C1s peak at 284.8 eV was used as the binding energy reference for the spectra. Figure 6.70 shows the Al2p, Si2p and O1s peak positions for the calcined kaolin microspheres. Since only Al, Si, and O signatures are present in the spectra presented, the calcined microsphere samples can be considered free from impurities. Fe, Mg, Cr, Ni, Na and Ca in measurable quantities were not evident. The peaks in binding energy 432 and 428 eV for the sample calcined at 1000° C were not designated to either element nut considered an anomaly [Allen, 2007]. Photoelectron binding energy values are shown in Table 6.13 for the calcined microspheres.

Table 6.13 *Photoelectron binding energies for calcined kaolin microspheres.*

		Photoelectron binding energies (eV)			
Sample	**Temp. (ºC)**	*C(1s)*	*Si(2p)*	*Al(2p)*	*O(1s)*
KF-8489		284.8	103.1	75.3	532.2
PS		284.8	n.r.	n.r.	532.0
1.5:1	**850**	284.8	103.1	75.3	532.1
1.5:1	**1000**	284.8	103.3	75.1	531.0
1.5:1	**1200**	284.8	103.4	74.9	531.0
1.5:1	**1400**	284.8	103.1	74.8	530.7

The binding energies of the Al2p and O1s for the calcined samples indicated a slight shift to lower energies shown in Table 6.11. The binding energy of Al2p for calcined kaolin microspheres at 850 ºC was 75.3 eV, however when calcined at 1400 ºC the binding energy decreased to 74.8 eV, this may signify the phase transformation of kaolin to mullite. The decrease in binding energies may be due to the increase in the calcination temperature, where interactions between particles and a phase change may result in an energy shift [Lu, et al. 2009]. Binding energy Al2p values for the Al-Si spinel phase and mullite have been reported at 76.6 and 74.7 eV, respectively. Si2p values of 102.2 eV for mullite have been also reported [Aklouche, et al. 2008]. However, greater variance in the Al2p and Si2p binding energy values were noted in the published results for kaolin [Castel, et al. 1980; Barr, et al. 1996; Sánchez, et al. 1999]. Although XPS clarified the purity of the microspheres samples after calcination, the slight change in the binding energies presented in Table 6.11 can not be determined at present.

6.4.6. Zeta potential measurements

A minimum surface charge is needed for the dispersion of particles in aqueous solution for controlling the dispersion stability of kaolin suspensions. This study was to determine any change in the zeta potential of the kaolin surface due to the calcination process of the spray dried microspheres.

The zeta potentials of the calcined kaolin microspheres are shown in Figure 6.71. The zeta potential of the starting kaolin mineral is also shown as average plots as a function of pH. The standard deviation of each measurement was ±2mV. The pH of the solution was adjusted by the addition of NaOH and HCl.
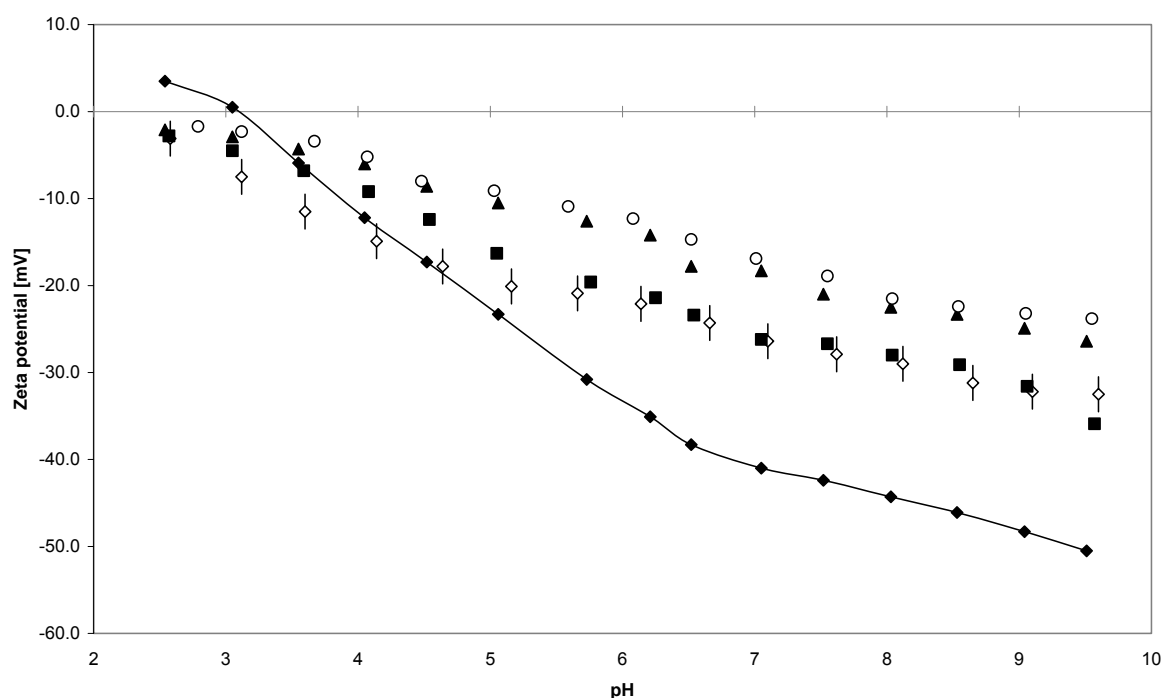
Figure 6.71 *Zeta potential as a function of pH of calcined kaolin microspheres; starting kaolin mineral [♦]; 850° C [■]; 1000 °C [◊]; 1200 °C [▲]; and1400 °C [○].*

The iep for the kaolin raw mineral was measured at pH 3.1. Most clay minerals have an iep between pH 2 and 4 [Braggs, et al. 1994; Yukselen, et al. 2002; Alkan, et al. 2004;

Yukselen-Aksoy, et al. 2011]. As the pH of the solution increased; the zeta potential of the raw kaolin mineral became more negative, as shown in Figure 6.71. This can be ascribed to either the adsorption of OH$^-$ ions onto the positive charge centres of kaolin or the deprotonation of surface hydroxyl groups.

In addition, the change in the zeta potential of the calcined microspheres showed less variance in zeta potential over the pH range. For example, the zeta potential for the raw kaolin powder ranged from 3.5 mV at pH 2.5 to -50.5 mV at pH 9.5, while for kaolin microspheres calcined at 1000 ºC the zeta potential only changed 30 mV, from -3.1 mV at pH 2.6 to -32.5 mV at pH 9.6. The calcined kaolin microsphere samples showed no iep within the pH range.

Furthermore, the obtained zeta potential values for the calcined microspheres showed a variance. For samples calcined at 850 ºC the zeta potential ranged from -2.8 mV at pH 2.6 to -35.9 mV at pH 9.6. Whereas, samples calcined at 1400 ºC the zeta potential ranged from -1.7 mV at pH 2.8 to -23.8 mV at pH 9.6. Table 6.14 reports the maximum and minimum zeta potential values for the kaolin calcined microspheres.

The higher negative zeta potential values may be related to a higher level of exchangeable or soluble ferrous ions in the sample [Hu, et al. 2003]. For the kaolin microspheres, as the calcination temperature was increased the zeta potential measurements showed a decrease in values when compared, possibly due to the removal of ferrous ions at the surface during dehydroxylation and the transformation phase into mullite.

Table 6.14 *Comparison of maximum and minimum zeta potential values for calcined microspheres.*

		Maximum		Minimum	
Sample	Temp. (ºC)	pH	Zeta potential (mV)	pH	Zeta potential (mV)
1.5:1	850	9.57 ± 0.1	-35.9 ± 2.0	2.57 ± 0.1	-2.8 ± 1.1
1.5:1	1000	9.60 ± 0.1	-32.5 ± 1.7	2.58 ± 0.1	-3.1 ± 1.2
1.5:1	1200	9.51 ± 0.1	-26.4 ± 1.6	2.54 ± 0.1	-2.1 ± 1.0
1.5:1	1400	9.55 ± 0.1	-23.8 ± 1.9	2.79 ± 0.1	-1.7 ± 0.9

Significant variations exist among published experimental data regarding the iep and the magnitude of zeta potential for kaolin [Williams, et al. 1978; Smith, et al. 1993; Hotta, et al. 1999; Stephan, et al. 2001; Alkan, et al. 2005; Greenwood, et al. 2007; Teh, et al. 2009]. The differences in the zeta potential are attributed to differences in the mineral phases, chemical compositions, crystal form, preparation and methods used to interpret the data.

However, electroacoustic experiments have determined that the calcined microspheres did not exhibit a sufficient potential charge to remain stable while in suspension. Kaolin microspheres calcined at 1000 ºC for 60 min. exhibited a zeta potential value of -27.9 mV at pH 7.6. The stability of kaolin in water is usually expected at zeta potential values great than -30mV [Dohnalová, et al. 2008]

Further electroacoustic experiments should be conducted to study the stability of the calcined microspheres with the addition of a dispersant agent; also the variation of zeta potential between samples calcined at low and high temperatures should be examined.

6.5. *Conclusions*

This chapter has described the application of a spray drying process followed by a calcination method to fabricate novel hollow and low density microsphere structures and structures of interest. The mechanism of forming hollow microspheres by spray drying and heat treatment has been described.

In general, spray drying at a 20 wt% solids concentration and at a kaolin-PS ratio of 1.5:1, resulted in a free flowing powder that after calcination gave hollow and low density microspheres. When calcined at 1000 ºC the microsphere product measured a bulk density of 0.13 g/cm^3, with a d$_{50}$ value of 11.2 μm. Compared to control experiments calcined at the same temperature exhibiting properties; bulk density at 0.55 g/cm^3 and particle size of 14.2 μm. The properties of the calcined kaolin microsphere compared to commercial microspheres are exhibited in Figure 6.72.
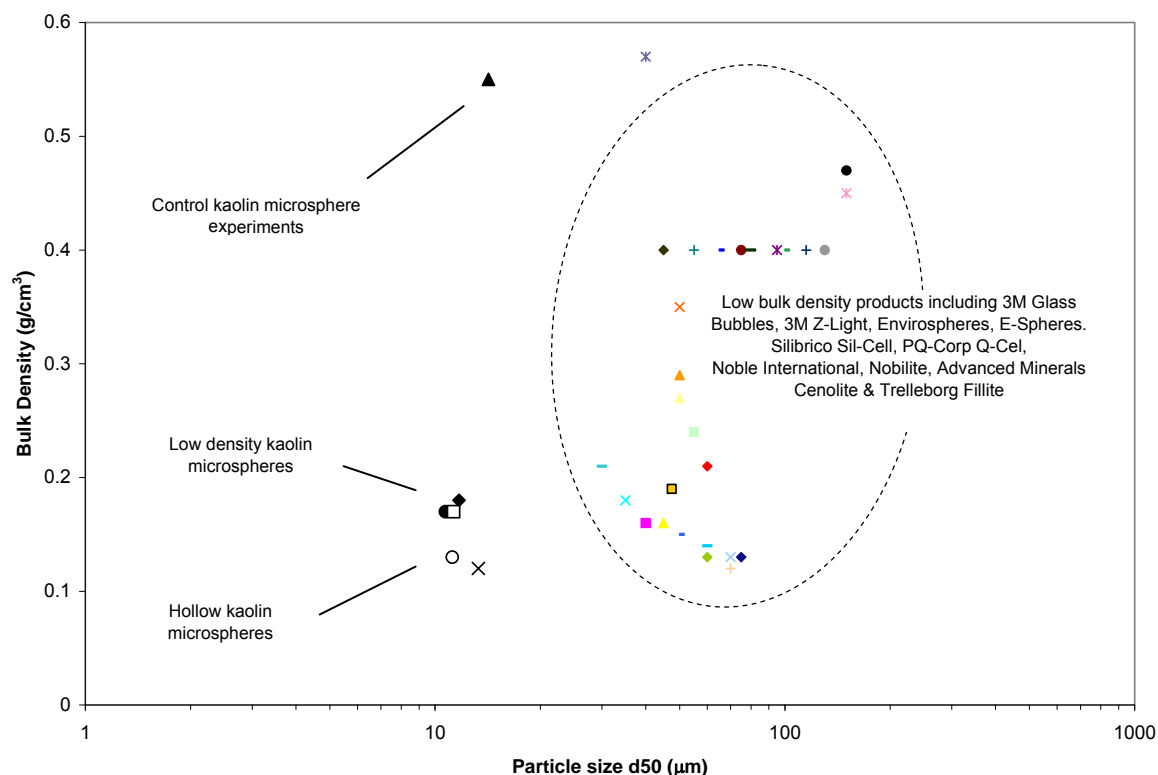
Figure 6.72 *Properties of calcined kaolin microspheres compared to commercial low bulk density microspheres. Control kaolin microspheres [▲]; kaolin ratio experiments; 1:1 (×); 1.5:1 (○); 2:1 [●]; 3:1 [♦]; and 4:1 [□]. Calcined at 1000 ℃.*

It was believed that the limiting factor with regards to reducing the particle size further was the solids content of the kaolin-PS slurry. At 20 wt% solids concentration the resulting particle size d_{50} was measured between 10.1 and 15.9 μm. The mean particle size could be reduced by lowering the solids content of the slurry formulation however; this would increase the cost per tonne of the microsphere product.

SEM and FIB results indicated that the calcined structures were generally spherical in form and at the low kaolin-PS ratio experiments of 1:1 and 1.5:1 exhibited hollow internal structures. FIB images of cross sectioned particles indicated a non-uniform shell structure. At a kaolin ratio of 2:1 the internal structure of the calcined microspheres exhibited a

scaffolding structure with numerous internal voids varying in size, this resulted in an increase in the bulk density values.

High surface area values for the low density microspheres indicated a high level of porosity as already detailed by SEM. At 1000 ºC, surface area measurements for control kaolin microspheres exhibited values of 3.5 m^2/g compared to 14.3 m^2/g for low density microspheres. The surface area for the low density microspheres decreased as the calcination temperature increased indicating shrinkage and fusing of kaolin particles at the shell surface.

XRD results showed that the kaolin microspheres were mainly composed of amorphous phase when calcined at the temperatures of 850, 1000 and 1200 ºC. The mullite phase was identified as the microsphere samples were heated to 1200 ºC and the further development of mullite was observed when the calcination temperature was increased to 1400 ºC. Cristobalite was identified by the reflections of (111) and (220) and anatase was also identified by the reflections of (105) and (211). The most favourable composition was found for microspheres calcined at 1000 ºC where cristobalite had not been identified and mullite was measured at <0.1%.

Analysis by XRF identified no discernible impurities for any of the calcined samples. The Fe_2O_3 and TiO_2 element concentrations were measured in the same value order, indicating that they elements were part of the kaolinite structure. All calcined kaolin microsphere samples measured the Fe_2O_3 and TiO_2 element concentrations at approximately 0.62 and 0.88 wt%, respectively.

The calcined microsphere products were clearly brighter than the raw kaolin mineral. The brightness of the kaolin microsphere samples calcined at 1000 and 1200 ºC was 90.0 and 92.5%, respectively, compared to the approximate 87.2% brightness of the starting mineral. This increase in brightness was due to the removal of some free iron oxide impurities during calcination providing the microsphere product with excellent optical properties.

Identification of elements present at the surface of the calcined surface was conducted by XPS. Since only Al, Si and O signatures were identified the calcined microsphere samples were considered free from impurities. Fe, Mg, Cr, Ni, Na and Ca in measurable quantities were not evident.

The kaolin calcined microspheres have negative zeta potential with the increase in pH of the system without attaining an iep. Significant variation between the zeta potential throughout the pH range of microspheres calcined at 1000 and 1200 ºC was observed, possibly due to the removal of ferrous ions at the surface during dehydroxylation and the transformation phase into mullite. It was determined that the calcined microspheres did not exhibit a sufficient charge to remain stable while in suspension. Kaolin microspheres calcined at 1000 ºC measured a zeta potential of -27.9 ±1.6 mV at pH 7.6 ±0.1.

A costing analysis for the production of low density microspheres with an approximate d_{50} particle size <11 μm can now be conducted based on a number of assumptions. Assuming all relevant equipment was available and full utilisation [Taylor, 2007]. Approximate costing for the kaolin microspheres was calculated at £590 per tonne. The cost analysis and assumptions are listed in Appendix D, Table D.3. The value was considered relatively high but was likely

to increase due to the economic environment and more specifically increases in fixed and variable costs.

The microsphere particles produced as described within this chapter exhibit favourable properties and have potential in numerous industrial sectors and applications. However, there are still several problems associated with these materials that must be solved before they can be brought into large scale industrial use; one example includes the use of PS as a sacrificial core material. For a viable industrial process to succeed an alternative core material may be required to ensure a cost effective product.

6.6. References

Aklouche, N., Achour, S., Tabet, N. *Mater. Research Bull.* 43 (**2008**) 1297.

Alkan, M., Demirbaş, Ö., Doğan, M. *Micro. Meso Mater.* 83 (**2005**) 51.

Barr, T.L., Seal, S., He, H., Klinowski, J. *Vacuum* 46 (**1995**) 1391.

Bertling, J., Blömer, J., Kümmel, R. *Chem. Eng. Technol.* 27 (**2004**) 829.

Bertrand, G., Roy, P., Filiatre, C., Coddet, C. *Chem. Eng. Sci.* 60 (**2005**) 95.

Braggs, B., Fomasiero, D., Ralston, J., Smart, R.S. *Clays Clay Min.* 42 (**1994**) 123.

Bridson, D., Davies, T.W., Harrison, D.P. *Clays Clay Miner.* 33 (**1985**) 258.

Brindley, G.W., Nakahira, M. *J. Am. Ceram. Soc.* 42 (**1959a**) 311.

Brindley, G.W., Nakahira, M. *J. Am. Ceram. Soc.* 42 (**1959b**) 315.

Brindley, G.W., Nakahira, M. *J. Am. Ceram. Soc.* 42 (**1959c**) 319.

Broadhead, J., Rouan, S.K.E., Rhodes, C.T. *Drug Devel. Ind. Pharm.* 18 (**1992**) 1169.

Castle, J.E., West, R.H. *Electron Spectrosc. Relat. Phenom.* 18 (**1980**) 355.

Brown, R.C., Sara, E.A., Hoskins, J.A., Evans, C.E., Young, J., Laskowski, J.J., Acheson, R., Forder, S.D., Rood, A.P. *Ann. Occup. Hyg.* 36 (**1992**) 115.

Cao, X.Q., Vassen, R., Schwartz, S., Jungen, W., Tietz, F., Stöever, D. *J. Eur. Ceram. Soc.* 20 (**2000**) 2433.

Caruso, F., Caruso, R.A., Mohwald, H. *Science* 282 (**1998**) 1111.

Caruso, F., Spasova, M., Salgueiriño-Maceìra, V., Marzán, L.L. *Adv. Mater.* 13 (**2001**) 1090.

Chandrasekhar, S., Ramaswamy, S. *Appl. Clay Sci.* 21 (**2002**) 133.

Chakraborty, A. *Thermochim. Acta* 398 (**2003**) 203.

Charlesworth, D.H., Marshall Jr., W.R. *A.I.Ch.E. Journal* 6 (**1959**) 9.

Chen, C.Y., Lan, G.S., Tuan, W.H. *Ceram. Inter.* 26 (**2000**) 715.

Chen, Y.F., Wang, M.C., Hon, M.H. *J. Eur. Ceram. Soc.* 24 (**2004**) 2389.

Cheow, W.S., Li, S., Hadinoto, K. *Chem. Eng. Res. Des.* (**2009**) Article in Press

Collins, T.J. *BioTechniques* 43 (**2007**) 25.

Corrigan, O.I. *Thermochim. Acta* 248 (**1995**) 245.

Crosby, E.J., Marshall Jr., W.R. *Chem. Eng. Prog.* 54 (**1958**) 56.

Dohnalová, Ž., Svoboda, L., Šulcová, P. *J. Min. Metall.* 44 (**2008**) 63.

Du, X., Jiang, Z., Meng, X., Wang, Z., Yu, H., Li, M., Tang, T. *J. Phys. Chem. C* 112 (**2008**) 6638.

Duffie, J.A., Marshall Jr., W.R. *Chem. Eng. Prog.* 49 (**1953**) 417.

Elversson, J., Millqvist-Fureby, A. *J. Pharm. Sci.* 94 (**2005**) 2049.

Fengqiu, T., Xiaxian, H., Yufeng, Z., Jinkun, G. *Ceram. Int.* 26 (**2000**) 93

Freimann, S., Rahman, S. *J. Eur. Ceram. Soc.* 21 (**2001**) 2453.

Frey, R.G., Halloran, J.W. *J. Am. Ceram. Soc.* 67 (**1984**) 199.

Gantner, B.A., *Am. Ind. Hyg. J.* 47 (**1986**) 530.

Gruner, J.W., *Kristallogr.* 83 (**1932**) 75.

Hamer, B. *Private communications*, Imerys Minerals Ltd., St. Austell, January (**2005**).

Hamer, B. *Private communications*, Imerys Minerals Ltd., St. Austell, September (**2006**).

Handscomb, C.S., Kraft, M. *Chem. Eng. Sci.* 65 (**2010**) 713.

Handscomb, C.S., Kraft, M., Bayly, A.E. *Chem. Eng. Sci.* 64 (**2009**) 228.

He, X.D., Ge, X.W., Wang M.H., Zhang, Z.C. *Polymer* 46 (**2005**) 7598.

Heide, K., Foldvari, M. *Thermochim. Acta* 446 (**2006**) 106.

Hotta, Y., Banno, T., Nomura, Y., Sano, S., Oda, K. *J. Ceram. Soc. Jpn.* 107 (**1999**) 868.

Hu, Y., Liu, X. *Miner. Eng.* 16 (**2003**) 1279.

Károly, Z., Szépvölgyi, J. *Powder Technol.* 132 (**2003**) 211.

Kho, K., Hadinoto, K. *Powder Technol.* 198 (**2010**) 354.

Kim, M., Laine, R.M. *J. Am. Chem. Soc.* 131 (**2009**) 9220.

Laskowski, J.J., Young, J. Gray, R., Acheson, R., Forder, S.D. *Anal. Chim. Acta* 286 (**1994**) 9.

Li, G.C., Zhang, Z.K. *Mater. Lett.* 58 (**2003**) 2768.

Li, Z.Z., Wen, L.X., Shao, L. *J. Control Release* 98 (**2004**) 245.

Liang, H., Shinohara, K., Minoshima, H., Matsushima, K. *Chem. Eng. Sci.* 56 (**2001**) 2205.

Liu, J., Chen, X., Wang, W., Huang, Q., Wang, G., Zhu, K., Guo, J. *Mater. Lett.* 63 (**2009**) 2221.

Lou, X.W., Wang, Y., Yuan, C., Lee, J.Y., Archer, L.A. *Adv. Mater.* 18 (**2006**) 2325.

Lou, X.W., Archer, L.A. Yang, Z. *Adv. Mater.* 20 (**2008**) 3987.

Lu, Z.Z., Ren, M., Yin, H., Wang, A., Ge, C., Zhang, Y., Yu, L., Jiang, T. *Powder Technol.* 196 (**2009**) 122.

Luo, P., Nieh, T.G. *Mater. Sci. & Eng. C* 3 (**1995**) 75.

Lukasiewcz, S.J. *J. Am. Ceram. Soc.* 72 (**1989**) 617.

Mahdjoub, H., Roy, P., Filiatre, C., Bertrand, G., Coddett, C. *J. Eur. Ceram. Soc.* 23 (**2003**) 1637.

Makkinejad, N. *Int. J. Heat Mass Transfer* 44 (**2001**) 429.

Mezhericher, M., Levy, A., Borde, I. *Chem. Eng. Process* 47 (**2008**) 1404.

Mujumdar, A.S. *Dev. Chem. Eng. Mineral Process* 10 (**2002**) 225.

Muzzarelli, C., Stanic, V., Gobbi, L., Tosi, G., Muzzarelli, A.A. *Carbohydr. Polym.* 57 (**2004**) 73.

Park, J.H., Oh, C., Shin, S.I., Moon, S.K., Oh, S.G. *J. Colloid Interf. Sci.* 266 (**2003**) 107.

Ptáček, P., Kubátová, D., Havlica, J., Brandštetr, J., Šoukal, F., Opravil, T. *Thermochim. Acta* 501 (**2010)** 24.

Sánchez, R.M.T., Basaldella, E.I., Marco, J.F. *J. Colloid Interface Sci.* 215 (**1999**) 339.

Shaw, F.S. *Am. Ceram. Soc. Bull.* 69 (**1990**) 1484.

Soottitantawat, A., Peigney, J., Uekaji, Y., Yoshii, H., Furuta, T., Ohgawara, M., Linko, P. *Asia-Pac. J. Chem. Eng.* 2 (**2007**) 41.

Smith, R.W., Narimatsu, Y. *Miner. Eng.* 6 (**1993**) 753.

Stephan, E.A., Chase, G.G. *Sep. Purif. Technol.* 21 (**2001**) 219.

Stoch, L. *Interceram.* 6 (**1987**) 21.

Sun, R.X., Li, M.S., Lu, Y.P. *Mater Rev.* 19 (**2005**) 10.

Sun, R., Lu, Y., Chen, K. *Mater. Sci. & Eng. C* (**2008**) Article in Press

Takahashi, H., Shinohara, N., Uematsu, K. *J. Ceram. Soc. Japan* 104 (**1996**) 59.

Taylor, R. *Private communications,* Imerys Minerals Ltd., St. Austell, June (**2007**).

Teh, E.J., Leong, Y.K., Liu, Y., Fourie, A.B., Fahey, M. *Chem. Eng. Sci.* 64 (**2009**) 3817.

Tartaj, P., González-Carreño, T., Serna, C.J. *Adv. Mater.* 13 (**2001**) 1620.

Tsapis, N., Bennett, D., Jackson, B., Weitz, D.A., Edwards, D.A. *PNAS*. 99 (**2002**) 12001.

Vanbever, R., Mintzes, J.D., Wang, J., Nice, J., Chen, D.H., Batycky, R., Langer, R., Edwards, D.A. *Pharm. Res.* 16 (**1999**) 1735.

Vehring, R. *Pharm. Res.* 25 (**2008**) 999.

Vehring, R., Foss, W.R., Lechuga-Ballesteros, D. *Aerosol Sci.* 38 (**2007**) 728.

Vine, G., Young, J., Nowell, I.W. *Ann. Occup. Hyg.* 28 (**1984**) 356.

Walker Jr., W.J., Reed, J.S. Verma, S.K. *J. Am. Ceram. Soc.* 82 (**1999**) 1711.

Walton, D.E. *Dev. Chem. Eng. Mineral Process* 10 (**2002**) 323.

Walton, D.E., Mumford, C.J. *Trans. IChemE.* 77 (**1999a**) 21.

Walton, D.E., Mumford, C.J. *Trans. IChemE.* 77 (**1999b**) 442.

Wang, A.J., Lu, Y.P., Sun, R.X. *Mater. Sci. & Eng. A* 460-461 (**2007**) 1.

Wang, A.J., Lu, Y.P., Zhu, R.F., Li, S.T., Ma, X.L. *Powder Technol.* 191 (**2009**) 1.

Wang, C.C., Ying, J.Y. *Chem. Mater.* 11 (**1999**) 3113.

Whittemore, J.W. *Bull. Am. Ceram. Soc.* 23 (**1944**) 427.

Wild, A. *Am. Ceram. Soc. Bull.* 33 (**1954**) 368.

Williams, D.J.A., Williams, K.P. *J. Colloid Interface Sci.* 65 (**1978**) 79.

Yamashita, O., Kishimoto, Y. *Powder Metall.* 41 (**1998**) 177.

Yin, J., Qiana, X.F., Shib, M., Zhou, G. *Mater. Lett.* 57 (**2003**) 3859.

Yukselen, Y., Kaya, A. *Water Air Soil Pollut.* 145 (**2003**) 155.

Yukselen-Aksoy, Y.A., Kaya, A. *Environ. Earth Sci.* 62 (**2011**) 697.

Chapter Seven: Conclusions and Extension of Research

7.1. Conclusions

Prior to the self assembly and calcination experiments to fabricate novel microsphere structures, a selection of sacrificial core template and shell forming materials were fully characterised. Hollow PS microspheres were considered the most favourable template material with a zeta potential of -51.1 ±1.1 mV at pH 6.6 ±0.2. Particle size (d_{50}) was measured at 0.90 μm. A kaolin mineral classified as FK-8489 was chosen as the most appropriate shell forming material. The fine mineral was chosen based on a number of important characteristic properties including; particle size, particle size distribution, and particle shape. The kaolin mineral exhibited a platy structure with a particle size (d_{50}) of 0.13 μm.

The logic behind the initial scoping experiments was to determine whether the use of a PS sacrificial core material coated with fine kaolin micro particles would yield hollow kaolin microspheres after heat treatment. Experiments were successfully conducted using a process where the surface of the PS template material was rendered cationic by the use of a polyelectrolyte. Negatively charged fine kaolin particles were than added to the PS solution and mixed. Ideally, the formation of kaolin plates at the PS microsphere surface would form a shell structure. Once dried, the samples were then calcined in a furnace at elevated temperatures to removal the template material. Upon calcination, few discrete microsphere particles were evident and at elevated temperatures the majority of structures were porous non spherical aggregates. A FIB instrument enabled the cross sectioning of specific particles to be investigated revealing internal voids due to the use of PS and upon calcination at an elevated temperature these internal voids collapsed.

Even though the initial experiments reported a few negative results it was evident that under the correct conditions, discrete spherical hollow microspheres could potentially be produced. The next experiments were conducted to determine the amount of polyelectrolyte required to render the PS surface cationic making the surface suitable for kaolin adsorption. The adsorption of polymer at the PS surface was studied using adsorption isotherms, electroacoustics and solvent relaxation NMR. The adsorbed amounts of polyelectrolyte were determined from the difference between initial polymer concentration and the concentration in the supernatant by UV-Vis. spectroscopy. Experimental isotherms showed a gradual increase of adsorbed amount of polyelectrolyte, while a well defined plateau was only observed at high polymer concentrations. The primary mechanism for adsorption was the ionic attraction between the negatively charged PS substrate and polymer. With the addition of 0.1 M NaCl to the polymer solution an increase of the polyelectrolyte was calculated at the PS surface. At low charge densities or at high ionic strength due to the addition of NaCl, polyelectrolyte chains have a more coiled configuration. If the ionic strength is decreased, the polyelectrolyte coil is expanded due to electrostatic repulsion. It was also determined that at higher ionic strengths the adsorbed amount achieved surface saturation at lower polyelectrolyte concentrations as loop and tails of longer polymer chains contribute more to the adsorbed amount. Polyelectrolyte adsorbed at the PS surface at an ionic strength of 0.1 M NaCl was calculated at 108.6 ±4.2 mg m^{-2}.

It was considered that during the adsorption process surfactant molecules were released from the PS surface resulting in polymer complexes, whether these complexes occurred at the PS surface it was not clear. The formation of polyelectrolyte-surfactant complexes at the PS surface would compensate for such high adsorption values. To ensure the reliability of the isotherm experiments conducted using hollow PS microspheres, solid PS microspheres were

produced using a free radical polymerisation technique. Surface saturation by the polymer was achieved at approximately 1 g L^{-1}. Total coverage by the polyelectrolyte adsorbed at the solid PS surface at an ionic strength of 0.1 M NaCl was calculated at 1.7 ±0.1 mg m^{-2}, in good agreement with published literature results. Most isotherm curves presented showed a second slope which may be a result of the polymer chain length distribution. GPC experiments identified a wide distribution in the molecular weight distribution of the polymer. Therefore, within the polymer solution short (low M_w) and long (high M_w) polymer chains exist and their adsorption behaviour are likely to influence the shape of the isotherm curve.

Polyelectrolyte adsorption at the PS surface was determined by NMR, an increase in the specific relaxation rate R_{2sp} implies an increase in solvent at the PS interface and hence surface polyelectrolyte coverage. Plots of the specific relaxation rate of the solvent against polyelectrolyte added per unit area are in some ways comparable to adsorption isotherms. NMR experiments determined that with the addition of 0.2 g m^{-2} of polyelectrolyte the PS surface was saturated and cationic in nature.

Electroacoustic experiments were conducted to determine the change in zeta potential due to polyelectrolyte adsorption. PS microspheres exhibited an initial zeta potential of -51.1 ±1.1 mV, the potential for all the PS samples changed from negative to positive with an increase in polyelectrolyte. As little as 0.1 g m^{-2} of polyelectrolyte was required to change the PS surface potential however, the zeta potential values indicated surface saturation at approximately 0.3 g m^{-2} for PS in a NaCl free environment. With the addition of 0.1 M NaCl the concentration required to achieve saturation was reduced to approximately 0.15 g m^{-2}. The zeta potential of the PS saturated surface in 0.1 M NaCl compared to PS in a NaCl free

environment was measured at 63.5 ±2.6 mV at pH 6.8 ±0.1 to 48.1 ±2.0 mV at pH 6.6 ±0.1, respectively. This increase of zeta potential can be attributed to an increase in adsorption of PE at the PS surface.

Kaolin adsorption and surface coverage of the hollow PS surface was determined by SEM images, due to the effective surface charge at the PS surface, SEM images indicated the effective electrostatic adsorption of fine kaolin particles. It was observed that the coverage of the PS surface increased with increase in kaolin concentration. However there was evidence of kaolin particles bridging between PS particles resulting in aggregation. Reduced sediment volume experiments were conducted to determine the kaolin concentration required to achieve full coverage of the PS surface. Kaolin ratio to achieve surface saturation was dependant upon electrolyte concentration. At low ionic strength, with no added NaCl, kaolin saturation was achieved at a ratio of 2:1 however, in the presence of 0.1 M NaCl, the kaolin ratio required to achieve saturation was reduced to 1.7:1. This change in ratio was due to the moderate shielding of the kaolin surface charge, which may provide highly ordered closed-packed layered structures.

An experimental approach was employed to determine the spray drying formulation parameters to produce aggregates having the ideal morphology, such as a mean particle size diameter <15 μm, a reduced bulk density <0.6 g/cm^3, a narrow size distribution and a high productive efficiency. In general, experiments were conducted by spray drying at a 20 wt% solids concentration at various kaolin-PS ratios, this process resulted in a free flowing powder that after calcination gave hollow and low density microspheres. The optimum ratio was determined to be 1.5:1 when hollow microspheres were produced. At this ratio value and calcined at 1000 ºC the microsphere product had the following properties; a bulk density of

0.13 g/cm^3, with a d$_{50}$ value of 11.2 μm. Compared to control experiments calcined at the same temperature exhibiting properties; bulk density at 0.55 g/cm^3 and particle size of 14.2 μm. At a higher ratio kaolin of 2:1 the microsphere properties were measured at; bulk density of 0.17 g/cm^3, with a d$_{50}$ value of 10.7 μm. It was evident from the result that as the kaolin ratio was increased the bulk density increased. Bulk density also increased with increase in calcination temperate. Specific gravity values for the spray dried microspheres only indicated a slight reduction when compared to the control experiments. Changes in the bulk density and the specific gravity for the calcined microspheres resulted from the removal of the volatile PS material. SEM and FIB results indicated that the calcined structures were generally spherical in form and at the low kaolin-PS ratio experiments of 1:1 and 1.5:1 exhibited hollow structures. FIB images of cross sectioned particles indicated a non-uniform shell structure. At a kaolin ratio of 2:1 the internal structure of the calcined microspheres exhibited a scaffolding structure with numerous internal voids varying in size.

Due to constraints it was not practical to fully characterise every sample, therefore the majority of the results relate to the kaolin ratio experiment 1.5:1, this sample offered the best properties with regards to bulk density, particle size and specific gravity. The surface area of the calcined microspheres was based on BET measurements; high specific surface area values for the low density microspheres indicated a high level of porosity as already detailed by SEM. At 1000 ℃, surface area measurements for control kaolin microspheres exhibited values of 3.5 m^2/g compared to 14.3 m^2/g for low density microspheres produced using a kaolin ratio of 1.5:1. It was also determined that the surface area for the low density microspheres decreased as the calcination temperature increased indicating shrinkage and fusing of kaolin particles at the shell surface.

XRD results showed that the kaolin microspheres were mainly composed of amorphous phase when calcined at the temperatures of 850, 1000 and 1200 ℃. The mullite phase was identified as the microsphere samples were heated to 1200 ℃ and the further development of mullite was observed when the calcination temperature was increased to 1400 ℃. Cristobalite and anatase were identified by the relevant reflections. The most favourable composition was found for microspheres calcined at 1000 ℃ where cristobalite had not been identified and mullite was measured at <0.1 wt%. Analyses by XPS and XRF identified no discernible impurities for any of the calcined samples. XRF identified that the Fe_2O_3 and TiO_2 element concentrations were measured in the same value order, indicating that they elements were part of the kaolinite structure. All calcined kaolin microsphere samples measured the Fe_2O_3 and TiO_2 element concentrations at approximately 0.62 and 0.88 wt%, respectively. The calcined microsphere products were clearly brighter than the raw kaolin mineral. The brightness of the kaolin microsphere samples calcined at 1000 and 1200 ℃ was 90.0 and 92.5%, respectively, compared to the approximate 87.2% brightness of the starting mineral. The increase in brightness was due to the removal of some free iron oxide impurities during calcination providing the microsphere product with excellent optical properties.

Electroacoustic experiments indicated that the kaolin calcined microspheres had negative zeta potential values without attaining any iep. Significant variation between the zeta potential throughout the pH range of calcined microspheres were observed. For samples calcined at 850 ℃ the zeta potential ranged from -2.8 mV at pH 2.6 to -35.9 mV at pH 9.6. Whereas, samples calcined at 1400 ℃ the zeta potential ranged from -1.7 mV at pH 2.8 to -23.8 mV at pH 9.6. The higher negative values may be related to a higher level of exchangeable or soluble ferrous ions in the samples. From experiments it was determined

that the calcined microspheres did not exhibit a sufficient charge to remain stable while in suspension. Kaolin microspheres calcined at 1000 ºC measured a zeta potential of -27.9 mV at pH 7.6 and -24.3 mV at pH 6.6.

7.2. Recommendations for Further Work

Considering the adsorption isotherm experiments, a number of interesting questions have arisen: (i) Are the high adsorption values reported due to polymer complexes being formed at the PS interface? (ii) Are the curves of the isotherm a result of the competition between polymer chains of different molecular weight?

To address these questions further experiments could involve the use of dynamic light scattering, or photon correlation spectroscopy (PCS) techniques to determine the hydrodynamic thickness of the adsorbed polymer layers and the resultant increase in the PS particle size. The techniques utilises light scattering due to the Brownian motion of diffusing particles. Analysis of the spectral width of the scattered light using a correlation function would allow calculation of particle size increase due to polymer adsorption or the formation of polymer complexes at the PS interface. This is, in principle, a fast technique, although it is restricted to dilute dispersions of spherical particles with a reasonable narrow size distribution. Small angle neutron scattering (SANS) is a technique that can provide detailed structural information on polymers adsorbed on colloidal particles. In a SANS experiment, the scattering cross section is measured as a function of the momentum transfer, which itself is a function of the scattering angle and the wavelength of the incident neutrons. SANS will be able to determine the overall size of the polymer chains and the spatial distribution of the chain segments at the PS interface.

Continuing with the solvent relaxation NMR experiments, this is certainly an area on which a great deal more work could be focussed. The initial results illustrate the potential of the technique for studying the attachment of adsorbed polymers. Fractionalised high and low molecular weight polyelectrolytes could be used to investigate the adsorption mechanisms in more detail and the interfacial competition between various molecular weight polymer chains. The study of polymer complexes at the hollow and solid PS interface would be an interesting comparison.

Another interesting experiment would be the characterisation of the adsorption supernatants containing the unadsorbed polymer. Analysis by GPC of the supernatants and the determination of the molecular weight distribution of the chains may signify whether low M_w polymer chains are dominate at the surface until a concentration favours the attachment of high M_w chains.

One significant point of interest worth investigating further is the localised coating phenomena previously aforementioned in Chapter 3. This is understood to occur at low concentrations when individual template particles are favoured by the coating material and near complete individual shell structures are formed. One possible reason for the phenomena is that the surface properties of individual templates are simply more favourable for adsorption. Whether the adsorption process is time dependant it is at present unclear. Experiments could be conducted to confirm the phenomena in other colloidal systems using various template materials including; silica and solid PS microspheres; the coating material could include spherical or platy nanoparticles of gold, silica, or calcium carbonate. Observation of the localised coating phenomena could be confirmed by SEM images.

Several problems associated with the calcined kaolin microspheres must be solved before they can be brought into a large scale industrial use. For a viable industrial process to succeed an alternative core material may be required to ensure a cost effective product, the cost of polystyrene is expected to rise, alternative template materials to PS could include the use of yeast cells, carbon black, natural beeswax, biological gelatin, or gas bubbles.

It would be interesting to expand upon some of the experimental parameters to determine whether specific properties of the calcined microspheres could be improved. The concentration of the slurry and the ratio of kaolin to PS were predetermined to offer microsphere structures that had integrity, but lowering the slurry concentration may result in a much lower mean particle size. However, a reduced mean particle size may also result in a higher bulk density and specific gravity.

Further work with regards to hollow microspheres should also include the application testing of the low density microspheres. Samples have been produced using the experimental procedures outlined; they have been applied to industrial applications and believe to exhibit favourable results however, due to industrial constraints the findings have been excluded from this thesis.

Appendix A:

A.1 Review of Polystyrene Microspheres

Polystyrene (PS) microspheres can be prepared by physical methods, such as emulsification, coacervation, spray drying, and by chemical methods like heterogeneous polymerisation. These preparative methods give a variety of microspheres in terms of size, surface chemistry, composition, surface texture and morphology.

One of the major developments in emulsion polymerisation over the last two decades has been the ability to make hollow PS microspheres. Interest has been increasing in hollow PS particles owing to their direct and potential applications in special coatings, medicine and material composite modification. Ultra-violet (UV) radiation absorption performance of a composition can be improved by adding hollow PS particles to the composite. By the addition of hollow PS particles coating compositions can be formulated to protect plastic or wood [McDonald, et al. 2002]. Voided PS particles, in particular hollow PS particles, have proven to be very useful in coating applications. The void can scatter light contributing to the coating opacity [Lee, 2002] or contribute to the mechanical properties of the coating affecting performance variables such as gloss [Khan, et al. 2008]. Industrial interest in hollow PS particles has grown as the technology has advanced.

The composite PS particles create a class of materials with unique colloidal and physical properties that differ from particles of random copolymers or from polymer blends. By adjustment of the thermodynamic and kinetic variables, a range of particle morphologies are possible. These include structures such as core-shell, hemispherical particles with inclusions

of one polymer within the other, or inverted core-shell particles. One common approach to structuring a PS particle was by a series of consecutive emulsion polymerisations with different monomer types, that is a second monomer stream is added and polymerised in the presence of seed PS particles prepared in an earlier process [Okubo, et al. 1989; Okubo, et al. 1995; Okubo, et al. 1999]. Furthermore, other components in an emulsion polymerisation process such as initiator type, monomer types and surfactant all influence the final morphology. Some of the essential requirements inherent to hollow PS made by osmotic swelling for commercial and industrial applications include [Kowalski, et al. 1984a; 1984b; 1984c; McDonald, et al. 2002]: the swellable core of the particles should be of sufficient volume relative to the volume of the particle to form a void inside the particle sufficient to scatter light efficiently. This efficiency is defined by the diameter of the void relative to the wavelength of visible light and the thickness of the shell. The shell should have the appropriate transport properties as adjusted by the composition and structure to facilitate the transport of ester into the interior of the particle. Finally, the shell must have thermoplastic flow properties at the expansion temperature and be sufficiently cohesive and uniform to maintain the integrity of the particle. It must also be strong enough to avoid collapse during processing or application conditions.

Synthesis of a structured polystyrene particle

The ability to make a hollow PS particle begins with the synthesis of a structured latex particle. This is usually in the form of a particle with concentric domains, the innermost of which is capable of being ionised and expanded by osmotic swelling. The hollow PS microsphere suspension supplied by Rohm & Haas Co. (research grade material classification AF1055) was reported to be synthesised by sequential emulsion polymerisations. The core contains carboxylic acid groups, which are ionised by the addition

of a volatile base. An elevated temperature of 80 to 100 ºC was utilised to soften the shell and allow the base to permeate the core and induce the osmotic swelling. Rohm & Haas Co. utilise sodium hydroxide to swell a particle with a shell having at least 1% carboxylic acid-functionalised polymer in the sheath, and swelling is activated in the presence of a solvent. Thus, a polar component in the shell as well as a plasticiser facilitates the transport and swelling of the core.

The incorporation of high levels of carboxylic acid into an emulsion copolymer has several disadvantages. Polar-ionisable monomer can partition significantly into the water phase of the emulsion, leading to the formation of oligomeric species which can behave as dispersants or flocculants depending on their molecular weight [McDonald, et al. 2002].

Surface chemical properties of polystyrene particles

Factors affecting the surface chemistry of a polystyrene particle include the various reactants of the polymerisation process such as the initiator type, monomer and comonomer functionality, and surfactant used. In a surfactant free polymerisation method, the surface properties of the polystyrene microsphere are mainly dependant on the initiator type [Goodwin, et al. 1973; 1974]. After preparation, the surface chemistry may also be changed by the cleaning method employed (i.e. centrifugation, ion exchange or dialysis) or by prolonged storage. A concerning feature of the cleaning procedure is that different authors, using similar recipes for the polystyrene latex preparation, have observed different surface groups [Yates, et al. 1977]. Using ion-exchange resins to remove ionic impurities have concluded that only strong-acid groups, i.e. sulphate groups arising from initiator fragments, are present on the surface. Those using dialysis as a cleaning procedure, have detected the presence of weak-acid groupings on the surface in addition to the strong-acid groupings

[Goodwin, et al. 1973]. The weak-acid groups could be produced by the hydrolysis of surface sulphate groups to hydroxyl groups followed by oxidation to carboxyl groups.

The ideal polystyrene model would contain only one type of charged end group. However, in the case of an aqueous, surfactant free PS, polymerised, from non-polar styrene monomer using potassium persulphate ($K_2S_2O_8$) as the initiator, it is expected that the reaction would follow the typical steps for a free radical reaction; initiation, propagation and termination [Jayasuriya, et al. 1985]:

$$S_2O_8^{2-} \rightarrow 2S\dot{O}_4^{-} \qquad\qquad [A.1]$$

$$S\dot{O}_4^{-} + HOH \rightarrow \dot{O}H + HSO_4^{-} \qquad\qquad [A.2]$$

In polystyrene microspheres initiated by persulphate ions, hydroxyl and carboxyl endgroups have been reported in addition to the expected sulphate endgroups [Hul, et al. 1968]. The hydroxyl endgroups could form at the expense of sulphate ion-radicals and the –OH radicals could initiate polymerisations such as sulphate ion-radicals to form polymeric radicals, which can terminate to produce hydroxyl chain-ends. Alternatively, the hydroxyl endgroups could be formed by the hydrolysis of sulphate end-groups. The formation of carboxyl endgroups could occur by oxidation of hydroxyl endgroups by residual persulphate ion, especially under the conditions when polymerisations are carried out in air instead of nitrogen [Ottewill, et al. 1967a; 1967b]. The oxidising behaviour of persulphate initiator can be eliminated by the use of different initiators such as azo compounds (i.e. Ar-N=N-Ar′, where Ar and Ar′ indicate substituted aromatic rings) that decompose forming nitrogen rather than oxygen.

Allowing a persulphate initiated PS to age at ambient temperature with the sulphate groups in the H$^+$ form, at a low pH may also lead to the appearance of carboxyl groups, whilst storage at 90 ºC is likely to lead to the formation of hydroxyl endgroups [Vanderhoff, 1980]. However, uncertainty exists as to whether such carboxyl groups should be present due to various oxidative side reactions or cleaning methods [Hearn, et al. 1981].

Industrial emulsion polymerisations commonly use reduction-oxidation initiation systems containing sulphites or metabisulphites in addition to persulphates which form sulphonate radicals and hence sulphonate endgroups, in addition to sulphate end groups [McCarvill, et al. 1978; Fitch, et al. 1978]. In many instances, surface functionality is deliberately introduced by means of the reaction recipe, using a functional monomer, or by using techniques such as copolymerisation. Typical functional monomers include: (meth)acrylic acids, for the introduction of carboxyl groups [Kim, et al. 2000]; styrene sulphonate for the introduction of strong acid groups [Kim, et al. 1989]; and tertiary amines for the generation of quaternary ammonium salts [Upson, et al. 1985; Lascelles, et al. 1999]. Many of these functional monomers are capable of forming polyelectrolytes and, in addition to becoming part of the polystyrene polymer, will be present in the aqueous phase, or weakly bound to the particle surface. In addition to their role as steric stabilisers, surfactants and emulsifiers can also contribute to the stabilising surface charge density due to hydrophilic endgroups which may be either physically or chemically bound to the PS particles surface. The surfactants, sodium dodecyl sulphate ($CH_3(CH_2)_{11}SO_4^-Na^+$) and sodium dodecyl sulphonate ($CH_3(CH_2)_{11}SO_3^-Na^+$) are also expected to contribute significantly towards the surface charge and the number of chemically bound sulphate and sulphonate groups respectively [Fitch, et al. 1978].

287

Stable dispersion of polystyrene particles

Polymer colloids such as PS have a low viscosity compared to solutions containing the same amount of solids. The viscosity of the colloidal suspension is a function of apparent volume fraction of the microspheres. The apparent volume fraction of microspheres can be changed by environmental conditions such as pH and temperature [Ford, et al. 1985]. The viscosity of dispersion of charged polystyrene particles is increased in shear field due to the distortion of the electric double layer around the particles. This phenomenon is referred to as the electroviscous effect and the characteristic value for the electroviscous effect is correction factor p in Equation A.3; which is a function of zeta potential and the electric double layer thickness.

$$\eta_r = 1 + 2.5(1 + p)\phi \qquad [A.3]$$

Where η_r is the relative viscosity of the dispersion to solvent, and ϕ is the volume fraction of particles. In dispersion the microspheres can move macroscopically through the medium by gravity, electric field, etc. and microscopically via Brownian motion. These movements keep a fresh interface between the microspheres and the medium. Particles having a soft surface allow water to penetrate the surface layer and meet less resistance when they move through the medium. Such particles may exhibit high electrophoretic mobility even if they have little charge [Ohshima, et al. 1989].

The potential energy of polystyrene particles in dispersion and, consequently the stability of the PS itself are decided by the contribution of three factors: electrostatic repulsive forces, van der Waals' attractive forces and steric repulsive forces among the particles. Refer to Table A.1 for an overview of the principles of stabilisation of colloidal PS particles. The

Derjaguin, Landau, Verwey and Overbeek (DVLO) theory includes the first two forces, if the particle has a potential energy barrier larger than 15 kT [Kawaguchi, 2000]; it is reported to have a high stability ratio.

The surface potential energy is affected significantly by environmental factors such as ionic strength and pH. The minimum concentration of a salt to flocculate polystyrene microspheres is termed the critical flocculation concentration (CFC). Steric repulsive interactions are a crucial force for microspheres covered with polymer layers protruding in solution [Kawaguchi, 2000]. The Steric stabilisation effect consists of both enthalpy and entropy effort. The overlap of the surface layers of two microspheres results in a shift from the equilibrium state of the layer (i.e. enthalpy gain) and in a decrease in the conformational freedom of solvated polymer chains (i.e. entropy loss).

The high stabilities of polystyrene colloids often result in some difficulty in the separation of microspheres from the dispersed medium. Centrifugation is sometimes useless for dispersions of very fine particles because the sedimentation rate is proportional to the square of the diameter. Ultrafiltration of PS microspheres is an alternative route. Coagulation with salt is one of the most conventional methods to separate microspheres from water. Magnetic or electric fields are sometimes applied for collecting microspheres from the dispersion [Kawaguchi, 2000].

Table A.1 *General principles of stabilisation of colloidal PS particles.*

Stabilisation	Acting forces	Important parameters
Electrostatic	Electrostatic repulsion of equally charged particles; repulsive potential (V_R) around charged particles at distance (d) decays as: $$V_R \propto f(\psi)\exp\left(-\frac{d}{\lambda_D}\right)$$	Charge density at the interface, surface potential (ψ), ionic strength (I_S); Debye screening length (λ_D) $$\lambda_D = \left(\frac{\varepsilon \cdot \varepsilon_0 \cdot \kappa_B \cdot T}{\sum_i (z_i \cdot e)^2 \cdot C_{salt}}\right)^{0.5}$$
Steric	Osmotic and entropic force between overlapping stabiliser layers of approach particles $$V_R \propto \frac{C_{S,L}^2}{v_{c,p} \cdot \rho_{S,L}^2} \cdot (\psi_1 - \chi_{S,cp})$$ $$\cdot \left[\left(\Delta R - \frac{d}{2}\right)^2 \left(3\frac{D}{2} + 2\Delta R + \frac{d}{2}\right)\right]$$	Solution state of stabilising polymer molecules (interaction parameter between stabilising polymer and continuous phase); temperature, ionic strength as far as both influence the solution state of the lyophilic polymer
Electrosteric	Competition between the osmotic pressure induced by counterion condensation inside the polyelectrolyte corona, which stretches the polyelectrolyte chain into the aqueous phase, and the entropic polymer elasticity, which pulls the chains back to the surface, $$\Delta R \propto I_S^a; a = -1/5$$	Ionic strength, conformation and charge density of the polyelectrolyte chain, ratio corona thickness to particle diameter (D); corona shrinks upon increasing ionic strength

C_{salt} is the molar bulk concentration of the ions, $\kappa_B T$ is the thermal energy, ε and ε_0 are the permittivities in the continuous phase, z is the stoichiometric valency of the electrolyte, and e is the element charge; $C_{S,L}$ is the concentration of polymer per unit volume inside the corona; $v_{c,p}$ is the molar volume of the continuous phase, $\rho_{S,L}$ is the density of the polymer, ψ_1 is an entropy parameter for the mixing of the overlap region, and $x_{S,cp}$ is the interaction parameter between the polymer and dispersion medium [Tauer, 2004].

Appendix A: References

Fitch, R.M., McCarvill, W.T. *J. Colloid Interface Sci.* 66 (**1978**) 20.

Ford, J.R., Morfesis, A.A., Rowell, R.L. *J. Colloid Interface Sci.* 105 (**1985**) 516.

Goodwin, J.W., Hearn, J., Ho, C.C., Ottewill, R.H. *Br. Polym. J.* 5 (**1973**) 347.

Goodwin, J.W., Hearn, J., Ho, C.C., Ottewill, R.H. *Colloid Polymer. Sci.* 252 (**1974**) 464.

Hearn, J., Wilkinson, M.C., Goodall, A.R. *Adv. Colloid Interface Sci.* 14 (**1981**) 173.

Hul, van den, H.J., Vanderhoff, J.W. *J. Colloid Interface Sci.* 28 (**1968**) 336.

Jayasuriya, R.M., El-Aasser, M.S., Vanderhoff, J.W. *J. Polym. Sci. Part A: Polym. Sci.* 23 (**1985**) 2819.

Kawaguchi, H. *Prog. Polym. Sci.* 25 (**2000**) 1171.

Khan, A.K., Ray, B.C. Dolui, S.K. *Prog. Org. Coat.* 62 (**2008**) 65.

Kim, J.H., Chainey, M., El-Aasser, M.S., Vanderhoff, J.W. *J. Polym. Sci. Part A: Polym. Chem.* 27 (**1989**) 3187.

Kowalski, A., Vogel, M., Blankenship, R.M. (Rohm and Haas Co.) **1984a**. Sequential heteropolymer dispersion and a particulate material obtainable therefrom, useful in coating composition as a thickening and/or opacifying agent. United States patent application 4427836.

Kowalski, A., Vogel, M., Blankenship, R.M. (Rohm and Haas Co.) **1984b**. Sequential heteropolymer dispersion and a particulate material obtainable therefrom, useful in coating composition as a thickening and/or opacifying agent. United States patent application 4468498.

Kowalski, A., Vogel, M. (Rohm and Haas Co.) **1984c**. Sequential heteropolymer dispersion and a particulate material obtainable therefrom, useful in coating composition as an opacifying agent. United States patent application 4469825.

Lascelles, S.F., Malet, F., Mayada, R., Billingham, N.C., Armes, S.P. *Macromolecules* 32 (**1999**) 2462.

Lee, D.I. *Prog. Org. Coat.* 45 (**2002**) 341.

McCarvill, W.T., Fitch, R.M. *J. Colloid Interface Sci.* 64 (**1978**) 403.

McDonald, C.J., Devon, M.J. *Adv. Colloid Interface Sci.* 99 (**2002**) 181.

Ohshima, G., Kondo, T. *J. Colloid Interface Sci.* 130 (**1989**) 281.

Okubo, M., Ikegami, K., Yamamoto, Y. *Colloid Polym. Sci.* 267 (**1989**) 193.

Okubo, M., Ahmad, H. *J. Polymer Sci. A* 34 (**1995**) 3147.

Okubo, M., Izumi, J. *Colloid Surf., A* 153 (**1999**) 297.

Ottewill, R.H., Shaw, J.N. *Kolloid Z. Z. Polym.* 215 (**1967a**) 161.

Ottewill, R.H., Shaw, J.N. *Kolloid Z. Z. Polym.* 218 (**1967b**) 34.

Tauer, K. *Colloids and Colloid Assemblies,* Caruso, F. (eds.) Wiley-VCH Verlach GmbH & Co. KGaA, Weinham, **2004**, p.13.

Vanderhoff, J.W. *Pure Appl. Chem.* 52 (**1980**) 1263.

Yates, D.E., Ottewill, R.H., Goodwin, J.W. *J. Colloid Interface Sci.* 62 (**1977**) 356.

Appendix B:

B.1 Kaolin Mineral Properties and Applications

Kaolin is one of the most versatile industrial minerals, it is chemically inert over a relatively wide pH range. Kaolin is soft and non-abrasive, and has a low conductivity of heat and electricity. Some use of kaolin, such as in paper coating, or fillers for paints and plastics require very rigid specifications including particle size, colour and brightness and viscosity whereas other uses require no specifications, i.e. in cement where chemical composition is most important.

Kaolin is a white, plastic clay mainly composed of the fine grained platy mineral kaolinite; a white hydrous aluminium silicate, $Al_2Si_2O_5(OH)_4$ containing on average about 29.5% alumina, 46.5% silica, and 14% formula water and appreciable quantities of iron, alkalies and alkali earths. Two structural units are involved in the atomic lattices of most clay minerals. One unit consists of closely packed oxygens and hydroxyls in which aluminium, iron and magnesium atoms are embedded in an octahedral combination so that they are equidistant from six oxygens or hydroxyls. The second unit is built of silica tetrahedrons. The silica tetrahedrons are arranged to form a hexagonal network that is repeated indefinitely to form a sheet of composition, $Si_4O_6(OH)_4$. Kaolin has a moderate refractive index of 1.56, and occurs as extremely small hexagonal shaped crystals of micron and submicron particle size.

Relatively pure kaolins are refractory and fuse at a temperature of approximately 1850 °C [Murray, 1991]. In most instances, kaolins are plastic and fire to a white or near white colour.

The presence of iron and titanium oxide minerals are disadvantageous as they impair whiteness and reduce brightness. The presence of excess silica in the form of quartz or cristobalite generally introduces abrasive problems in specific applications. The presence of micas and feldspar may influence the rheological, brightness and abrasion characteristics. Kaolin is hydrophilic and with a small amount of chemical dispersant to negate the edge charges due to broken bonds, will disperse readily in water. The particle shape of kaolin is an important factor in its utilisation. Kaolin particles that are in the range of 1 μm and below are thin, pseudo-hexagonal plates that orient on a coated surface because of their two dimensional nature.

Kaolin classification and occurrences

The occurrences of kaolin are common, but commercially useable deposits are relatively few in number. The best known and most utilised deposits are in the Cornwall area of south-western England, in Georgia and South Carolina in the United States, and in the lower Amazon region of Brazil [Murray, 2000]. Kaolins are generally classified as primary or secondary deposits. Primary kaolins are formed by the alterations of crystalline rocks such as granite and are found in the location where they are formed. Secondary kaolin deposits are sedimentary in nature and are formed by the erosion of primary deposits [Murray, 1980]. In primary deposits, kaolin commonly makes up 15 to 30% of the total ore, the remainder of the ore consists of unaltered granite including quartz, muscovite and feldspar. Secondary deposits contain far more kaolinite, with the Georgia deposits in the US containing approximately 85% kaolin. In this case, the contaminants include quartz, muscovite, smectite, anatase, pyrite and graphite. Additional differences exist among the two deposit types, primary clays are usually coarse and contain far less anatase and iron oxide than secondary clays [Prasad, et al. 1991].

294

Kaolin deposits in Cornwall and Devon are the mostly widely exploited and well known primary kaolins in the world. Approximately 2.4 million tonnes per year of kaolin are currently produced from these deposits. The kaolins formed are due to the hydrothermal alteration of granite rocks. Heat generated by radioactive decay within the granites has led to the convective hydrothermal circulation of groundwater which has essentially altered the micas and feldspars in the granite to kaolin [Jepson, 1984; Harvey, et al. 1997]. The kaolin content of the commercial deposits in Cornwall range from 10 to 40%. The major non-clay mineral is quartz along with other minor accessory minerals [Manning, et al. 1996]. The two mostly widely exploited secondary kaolin resources in the world are in Georgia (US), and in the Amazon basin in eastern Brazil. Over 7.8 million tonnes are mined annually in Georgia. The formation of these Georgia kaolins has been due to the weathering of granitic rock on the Piedmont Plateau and these clays have subsequently washed and sorted in the lacustrine and shallow marine environment of the Georgia coastal plain. Subsequent shallow burial, low temperature diagenesis and leaching by oxygenated groundwaters is likely to have improved the purity and crystallinity of these sedimentary kaolins. The deposits are generally 85 to 95% kaolinite, the remainder being mainly quartz with minor amounts of muscovite, smectite, ilmenite, anatase, rutile and traces of zircon, tourmaline and graphite [Kesler, 1956; Bates, 1959; Schroeder, et al. 2003].

The secondary kaolins of the Amazon basin are considered to have the potential to dominate the kaolin markets of the world in the near future. The kaolins are derived from tropical weathering of granites from the Guyana shield to the north of the Amazon basin. They are believed to have settled in a lacustrine environment. The kaolinite content in the deposit is comparable to Georgia deposits, comprising 80 to 90% [Prasad, et al. 1991; Sousa, et al. 2007; Costa, et al. 2009].

Mining processes for kaolin

Most of the kaolin in the world is mined by open-pit methods. Although a few underground mines exist, in most cases the cost of production limit underground mining of clay deposits. Mining for kaolin in the Georgia sedimentary belt uses conventional open-pit methods, in Cornwall, the mining is often done by hydraulic methods.

The economy of the mining method depends on the costs associated with overburden removal and the type of mining equipment used depends on the depth of the overburden. During the open-pit mining process the overburden is often removed from the site, the clay is excavated and fed into blungers where it is suspended in water with the aid of a dispersing agent. The clay slurry is pumped to central degritting stations where coarse sand and mica are removed by gravity settling and hydrocyclones followed by screening. The product of this preliminary beneficiation is stored separately in large tanks until testing determines the blending necessary for feed to the main processing plant.

The Cornwall deposits are usually worked by the hydraulic mining preconcentration technique to avoid handling excessive amounts of waste rock. Mining is carried out using water jets at pressures up to 250 psi (17.2 bars) removing the soft kaolin from the matrix leaving behind the hard un-kaolinised rock. As the rock face is washed, the slurry containing the kaolin in suspension flows to be lowest point in the pit. Initial treatment to remove the coarse particles from the slurry is carried out by a series of mechanical systems followed by the separation of finer sand and mica particles in hydrocyclones. Then excess water is drained off, and the slurry is then allowed to settle and thicken in large tanks and finally fed to centrifuges for fine sizing.

Kaolin resources and reserves

The Cornwall kaolins are considered to have a limited future commercial potential this is due to the resources extend vertically downwards and the majority of the surface resource has been mined [Harvey, et al. 1997]. Mining costs will therefore continue to increase.

The Georgia kaolins have been produced from two environments; the mid-Georgia Cretaceous kaolins which are characterised by a larger particle size are limited in reserves. While the east Georgia Tertiary kaolins are finer in particles size and have a higher iron content are plentiful in supply, the depletion of the mid-Georgia kaolin is expected to lead to a focus of production in the eastern region of Georgia.

The reserves of kaolin in Brazil are known to be extensive and of high quality. The processed kaolins from Brazil are currently selling in the global market and are expected to heavily impact the established markets for both the Cornwall and Georgia kaolins. The high quality kaolin market is still currently dominated by the US with growing contributions from Brazil and Australia.

B.2 Surface Characteristics of Kaolin

Interfacial phenomena at the kaolin-water interface are usually controlled by properties including zeta potential, the structure of the electrical double layer, surface potential, and the isoelectric point. A large quantity of literature concerning kaolin surface properties is available [Vasel, 1923; Grim, 1942; Hunter, et al. 1964; Swartzen-Allen, et al. 1974; Williams, et al. 1978; Bolland, et al. 1980; Brady, et al. 1996; Hu, et al. 2003; Greenwood, et

al. 2007; Dohnalová, et al. 2008; Castellano, et al. 2010] and will not be reviewed extensively within this thesis.

Kaolinite is a well defined naturally occurring alumina-silicate with a 1:1 layer structure consisting of one tetrahedral and one octahedral sheet. It is considered that two distinct double layers of charge are present in aqueous solution: one on the edge (*hk*0) faces and another on the flat (001) faces. The charge in the tetrahedral sheet of kaolinite is produced by the occasional substitution of a silicon by an aluminium atom [Herrington, et al. 1992]. The absence of a constituent metal atom from its place in the clay crystal structure would also result in a negative charge on the lattice [Swartzen-Allen, et al. 1974]. Such imperfections are difficult to measure, however, other types of lattice imperfections which may contribute to the negative charge include dislocations and localised bond breakages.

A number of studies have indicated that the edges of kaolin particles are positively charged at pH <7 to 8 [Hunter, et al. 1963b]. These positive charges are believed to arise from the following reactions:

$$-Al-O-Al- \rightarrow \left(-Al-O^- + -Al^+\right) \xrightarrow{H_2O,H^+} 2-Al-OH_2^+ \qquad \text{[B.1]}$$
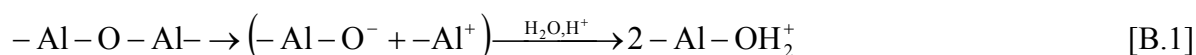
The presence of a positive edge charge has been demonstrated by adsorbing negatively charged gold sol on to the kaolinite edge surface [Thiessen, 1942].

The negative charge on the kaolin particle is compensated by adsorption of cations. In clays which swell in the presence of water the counterions are held on the external surfaces of the aggregates and between the layers, whereas in non-swelling clays the counterions are

adsorbed onto the external surfaces only. In aqueous suspensions, some of these cations may remain in a closely held Stern layer; others diffuse away from the surface and form a diffuse double layer. Provided that they are not fixed by engaging in strong, specific bonding with the kaolin surface or by being trapped between unit layers that have collapsed together irreversibly (lattice collapse), the counterions can undergo ion exchange with other cations present in the system.

Particle associations in kaolin suspensions can occur via face-to-face, edge-to-edge, and edge-to-face interactions. A variety of structures are possible, depending upon the mode of interparticle bonding. Face-to-face associations can produce stacks whose major dimensions are similar to those of unassociated unit layers, the significant difference being in the thickness of the resultant plate structure. If only partial overlap of faces occurs, extended lamellae may be formed whose major dimensions are much different from those of the original particles. If the kaolin plate structures are joined edge-to-face, a card-house type structure is formed, if the pH is raised and the edge faces assume a negative charge, the structure is likely to collapse. Electrostatic repulsion due to high negative surface charge between the particles causes dispersion, and stable suspensions are produced. Peptisation of kaolin due to the breakdown of edge-to-face association has been reported to occur between pH 6.5 and 7.8 [Michaels, et al. 1955; 1964; Street, 1957]. These values indicate the pH for edge-face charge reversal. Indifferent electrolytes, such as NaCl, reduce the effect of edge-to-face attraction [Tombácz, et al. 2006] by compressing the double layer adjacent to both the positively and negatively charged regions and lowering the potential energy for a given separation distance. At high electrolyte concentrations, coagulation ensues due to the predominance of van der Waals attraction as the double layer is further compressed [Olphen, 1964; Tadros, 1980; Johnson, et al. 2000].

Zeta potential of kaolin

Zeta potential is an intrinsic property of a mineral particle in suspension. It determines the strength of the electrical double layer repulsive forces between particles and identifies the stability of a colloidal system. The zeta potential is known as the measurable surface potential of a particle and is also referred to as the potential of the shear plane [Alkan, et al. 2005]. The conventional position of the shear plane is thought to be two to three water molecule diameters (5 Å) from the surface of a particle. However, for particular swelling type clay minerals the shear plane is closer to the Gouy plane [Li, et al. 2003]. Accordingly, the distance between the shear plane and Stern plane may be approximately 200 to 300 Å in the presence of 10^{-4} mol L of 1:1 electrolyte. Most importantly, determination of the charge density on the shear plane, and the surface charge density or the charge density on the Stern plane is possible [Low, 1981]. The charge density on the Shear plane could be calculated from the zeta potential; the surface charge density can be calculated by knowing the values of the total amount of surface charges and the values of specific surface areas. The charges on clay minerals are mainly a permanent charge; thus at any concentration of electrolyte, pH value, and temperature, the total amount of surface charges and surface charge densities should remain constant. In the determination of zeta potential, the Gouy-Chapman theory can be used in the description of the diffuse double layer quantitatively [Westall, et al. 1980].

Potential determining ions

The interface between the solid and the solution may be treated as a semipermeable membrane which allows only the charged species common to both the solid and the solution to pass through. These species are called potential determining ions and are responsible for the establishment of the surface charge of particles [Hunter, 1988]. Their activities in the

liquid play a crucial role in the generation of potential differences across a solid-liquid interface. They are also able to reverse the sign of the zeta potential of a solid. For a cation to be the potential determining ion, it must make the surface more positive upon increasing the cation concentration. Similarly, for an anion to be the potential determining ion it must impart the surface more negative charges with the increasing anion concentration. The potential determining ions for ionic solids such as $CaCO_3$ are the lattice constituent ion, Ca^{2+} and CO_3^{2-}; whereas H^+ and OH^- ions for metal oxides and hydroxides, silicate or clay minerals, some hydrophobic minerals (i.e. coal fines) and some synthetic polymers with sulphate groups [Somasundaran, et al. 1964; Parks, 1965].

Surface potential

The surface potential is theoretically the potential at zero distance from the surface. For oxides and silicates, the surface potential is determined by the activities of potential determining ions. It is important to distinguish between the isoelectric point and the point of zero charge. The point of zero charge denotes the state in which the net surface charge of the solid is zero, the isoelectric point describes the condition at which the potential at the shear plane, i.e. the zeta potential obtained from electrokinetic measurements is zero. The point of zero charge of a mineral usually coincides with the isoelectric point in most cases, except where there is specific ion adsorption at the surface [Das, 2002].

Origins of surface charge

A mineral particle in suspension carries electrokinetic charges depending on the properties of the liquid phase such as pH and ionic strength. The surface charge of clay minerals can

originate due to a number of mechanisms including; dissociation of surface groups, adsorption of ions from solution, and isomorphic substitutions [Wypych, et al. 2004].

In most solid minerals dissociable functional surface groups such as carboxyl (-COOH) and hydroxyl (-OH) are present. These groups may be ionisable depending on the solution pH; a surface is charged either negatively at high pHs or positively at low pHs. For metal oxides and hydroxide:

$$MOH_2^+ \xrightleftharpoons{H^+} \qquad \qquad (positive~surface)$$

$$MOH \xrightleftharpoons{OH^-} \qquad \qquad (neutral~surface)$$

$$MO^- + H_2O \qquad \qquad (negative~surface) \qquad \qquad [B.2]$$
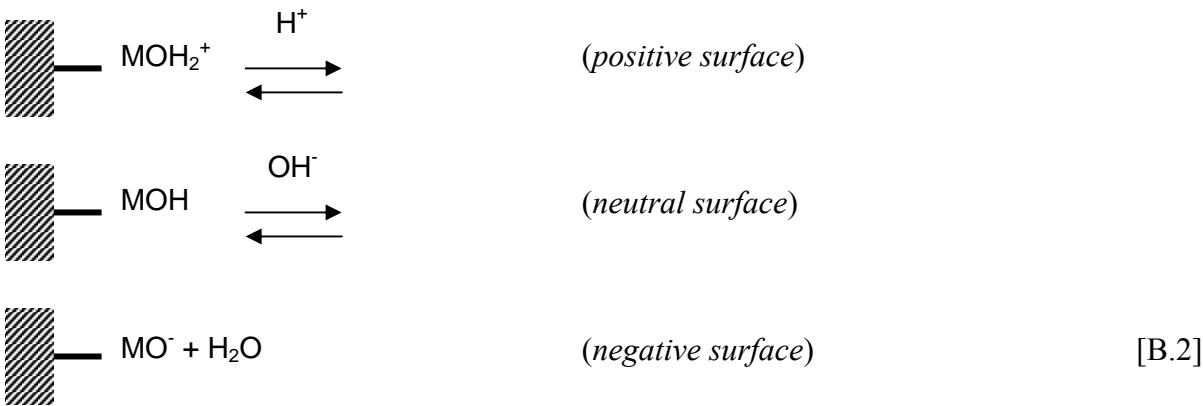
where *M* represents a metal cation at the surface. Consequently, for simple metal oxides and hydroxides, e.g. SiO_2, Al_2O_3, Fe_2O_3, and $AlOOH$, complex metal oxides including clay minerals and some hydrophobic minerals, e.g. coal, H^+ and OH^- ions are considered as the potential determining ions.

Preferential adsorption of ions from solution is observed most commonly and results from the differences in the affinity of two phases for some ions. Some specific ions such as potential determining ions can adsorb strongly on a solid surface and charge the particle or vice versa, a charged particle can become non-charged through such adsorption, for example, adsorption of H^+ and OH^- on oxide minerals as shown in Equations B.3 and B.4. For H^+ and

OH⁻ ions, it is difficult to distinguish whether the charging of a particle is generated from the adsorption or dissociation of these ions [Lyklema, 1982].

$$\text{Si-OH} \quad + \quad \text{H}^+ \quad \rightleftarrows \quad \text{Si-OH}_2^+ \qquad \text{[B.3]}$$

$$\text{Si-OH} \quad + \quad \text{OH}^- \quad \rightleftarrows \quad \text{Si-(OH)}_2^- \qquad \text{[B.4]}$$
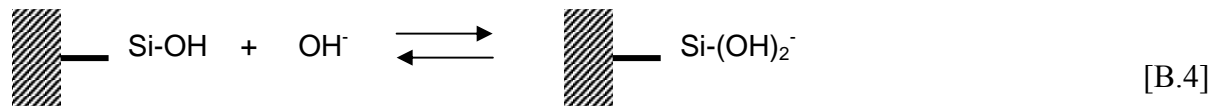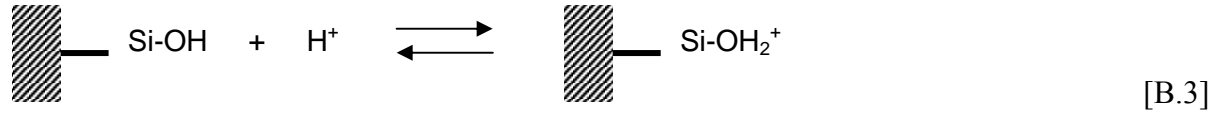
In clay minerals the anionic centres are presented by the polar silanol groups (Si-OH) or relatively non-polar siloxane groups (Si-O-Si). A number of reactions between the hydroxyl groups at the edges and metal ions in aqueous solution including surface binding [Equation B.5], ligand exchange [Equation B.6], and their combination [Equation B.7] are listed [Stumm, 1993; 1997]:

$$S - OH + M^{z+} \Leftrightarrow S - OM^{(z-1)} + H \qquad \text{[B.5]}$$

$$S - OH + L^- \Leftrightarrow S - L + OH^- \qquad \text{[B.6]}$$

$$S - OH + M^{z+} + L^- \Leftrightarrow S - L - M^{z+} + OH^- \qquad \text{[B.7]}$$

The proportion of the edge surfaces and respective hydroxyl groups for kaolinite is reported between 12 and 14% [Ferris, et al. 1975; James, et al. 1982] and for smectite minerals less than 1% [Sondi, et al. 1997].

Most clay and zeolite minerals are generally characterised by alumina silicates and exhibit negative charges in water which results from the substitutions within the crystal lattice of Al^{3+} for Si^{4+} or Mg^{2+} for Al^{3+}. Consequently, negative charges are developed in the lattice to compensate the so called exchangeable cations i.e. Na^+, K^+, and Ca^{2+} entering the crystal structure. When such minerals come in contact with water, some of these cations can easily dissociate leading to negatively charged surfaces. When a mineral particle is immersed in suspension, charged species are transferred across the solid/liquid interface. In equilibrium this condition is characterised by a surface potential and a surface charge density. For example, a negatively charged solid particle in an electrolyte solution; while the oppositely charged counterions will congregate in the vicinity of the particle, coions which have the same charge sign with that of the particle will be repelled from the surface due to electrostatic interactions. Therefore, a charged surface layer and an ionic layer will constitute the electrical double layer with a thickness usually ranging from a few nanometres to a few hundred nanometres.

Electrokinetics of kaolin minerals

The most important types of clay minerals are: kaolinites, smectites, illites and chlorites. Kaolinites and illites exhibit plate-like particles without expanding the lattice due to strong interlayer bonding and strong hydrogen bonding, respectively. The composition of clay mineral and the structural arrangement of octahedral and tetrahedral sheets and minerals account for the differences in the electrokinetic properties. Structural arrangements of tetrahedral and octahedral layers and their combinations constitute the layer charge in clay minerals [Murray, 2000].

Kaolin exhibits very little substitution in the structural lattice resulting in a minimal layer charge and low base exchange capacity. Linkage of a tetrahedral siloxane layer to one dioctahedral or trioctahedral layer forms the structure of 1:1 layer silicate. While in trioctahedral clay minerals all the three sites are occupied by magnesium ions to achieve charge balance, in dioctahedral layer two out of the three positions are occupied by trivalent aluminum ions leading to practically uncharged layers which are held together through van der Waals' forces and partly by hydrogen bonding; kaolinite is a dioctahedral non-expandable clay mineral [Sondi, et al. 2002].

Published literature on the electrokinetic properties of kaolin minerals has become more evident [Hauser, 1945; Nicole, et al. 1970; Ferris, et al. 1975; Williams, et al. 1978; Zhu, et al. 2001; Kosmulski, et al. 2003; Greenwood, et al. 2003; 2007; Dohnalová, et al. 2008]. The isoelectric point of kaolinite has been reported by several researchers [Cases, et al. 1971; Bolland, 1980; Smith, et al. 1993; Yuan, et al. 1998; Hu, 2003; Mpofu, et al. 2003; Alkan, 2005; Cunha, et al. 2006; Chassagne, et al. 2009]. Electrophoresis and streaming potential techniques have been used to measure the zeta potential of kaolin, an isoelectric point at pH 2.2 has been reported [Smith, et al. 1993] and at pH 3 [Cases, et al. 1971]. The surface charge of kaolin at pH 3 agreed with the zeta potential versus pH profile due to the electronegative character of the (001) faces characterised by OH^- or O^2 ions; this induced the particles to move under an applied field even at zero surface charge. Commercial kaolin grades from Georgia (US) yielded isoelectric values in the pH range of 1.5 to 3.5. The variation of clay samples was ascribed to the differences in ionic composition of the clay samples particularly those of exchangeable or soluble calcium ions [Yuan, et al. 1998]. Similarly, the isoelectric range of 2.5 to 3.8 for kaolin samples has been reported, the

mineral-solution interface was significant in determining the surface zeta potentials of the kaolins and in the variance in the isoelectric range [Hu, et al. 2003].

When an alumina silicate layer is disrupted, the valances of the exposed crystal atoms are not completely compensated as they are in the interior of the crystal. These surfaces are called broken-bond surfaces or edge surfaces. The exposed functional groups are active and may act as electron pair donors or acceptors. The free charges may be balanced by the uptake of cations or anions through either chemisorption or electrostatic attraction.

The zeta potential of clay particles inferred from the electrophoretic mobility using the Schmoluchowski equation has been criticised because of the heterogeneous nature of the particle charge. Calculation of the zeta potential and surface charge densities for non-spherical kaolinite assuming an equivalent sphere may result in misleading results. The zeta potential calculated from such mobilities does not reflect the potential at the shear plane because of the screening effect of positive charges on the edges relative to those of negative charges at the face resulting in a lower negative mobility [Luckham, et al. 1999].

B.3 Particle Size Distribution by Sedimentation

This relies on the principle that the terminal velocity of the particle settling under gravity in a suspension depends upon its size and the density difference between the particles and the suspension medium. This follows Stoke's Law:

$$V_0 = \frac{d^2(\delta - \rho)g}{18\eta}$$

[B.8.]

where V_0, is the limiting sedimentation velocity, d, is the particle diameter, $(\delta\text{-}\rho)$ represents the difference between clay and medium, g, acceleration due to gravity, and η the viscosity of the medium. This rearranges to:

$$d = \sqrt{\frac{18\eta h}{(\delta - \rho)gt}} \qquad\qquad [B.9]$$

Appendix B: References

Alkan, M., Demirbas, Ö., Duğan, M. *Microporous Mesoporous Mater.* 83 (**2005**) 51.

Bates, T.F. *Am. Mineral.* 44 (**1959**) 78.

Bolland, M.D.A., Posner, A.M., Quirk, J.P. *Clays Clay Miner.* 28 (**1980**) 412.

Brady, P.V., Cygan, R.T., Nagy, K.L. *J. Colloid Interface Sci.* 18 (**1996**) 356.

Cases, J.M., Touret-Poinsignon, C., Vestier, D. *C.R. Acad. Sci., Paris, Ser. C* 272 (**1971**) 728.

Castellano, M., Turturro, A., Riani, P., Montanari, T., Finocchio, E., Ramis, G., Busca, G. *Appl. Clay Sci.* 48 (**2010**) 446.

Chassagne, C., Mietta, F., Winterwerp, J.C. *J. Colloid Interface Sci.* 336 (**2009**) 352.

Costa**,** M.L., Sousa, D.J.L., Angélica, R.S. *J. South Amer. Earth Sci.* 27 (**2009**) 219.

Cunha, F.O., Torem, M.C., D'Abreu, J.C. *Miner. Eng.* 19 (**2006**) 1464.

Das, K.K. *Interfacial Electrokinetcs and Electrophoresis*, Surfactant Science Series, vol. 106, Delgado, A.V., (eds.), Dekker, New York, **2002**.

Dohnalová, Ž., Svoboda, L., Šulcová, P. *J. Min. Metall. Sect. B* 44 (**2008**) 63.

Ferris, A.P., Jepson, W.B., *J. Colloid Interface Sci.* 51 (**1975**) 245.

Greenwood, R. *Adv. Colloid Interface Sci.* 106 (**2003**) 55.

Greenwood, R. *Private communications*, University of Birmingham, May (**2005**).

Greenwood, R., Lapčíková, B., Surýnek, M., Waters, K., Lapčík, Jr., L. *Chem. Pap.* 61 (**2007**) 83.

Grim, R.E. *J. Geol.* 50 (**1942**) 225.

Harvey, C.C., Murray, H.H. *Appl. Clay Sci.* 11 (**1997**) 285.

Hauser, E.A. *Chem. Rev.* 37 (**1945**) 287.

Hearn, J., Wilkinson, M.C., Goodall, A.R. *Adv. Colloid Interface Sci.* 14 (**1981**) 173.

Herrington, T.M., Clarke, A.Q., Watts, J.C. *Colloids Surf.* 68 (**1992**) 161.

Hu, Y., Liu, X. *Miner. Eng.* 16 (**2003**) 1279.

Hunter, R.J. *Zeta Potential in Colloid Science: Principles and Applications*, Academic Press, London, **1988**.

Hunter, R.J. *Colloids Surf. A* 141 (**1998**) 37.

Hunter, R.J., Alexander, A.E. *J. Colloid Sci.* 18 (**1963**) 820.

Hunter, R.J., Alexander, A.E. *J. Colloid Sci.* 18 (**1963b**) 833.

James, A.E., Williams, D.J.A. *Adv. Colloid Interface Sci.* 17 (**1982**) 219.

Jepson, W.B., *Philos. Trans. R. Soc. Lon. A* 311 (**1984**) 411.

Johnson, S.B., Franks, G.V., Scales, P.J., Boger, D.V., Healy, T.W. *Int. J. Miner. Process.* 58 (**2000**) 267.

Kesler, T.L. *Econ. Geol.* 51 (**1956**) 541.

Kosmulski, M., Dunkhin, A.S., Priester, T., Rosenholm, J.B. *J. Colloid Interface Sci.* 263 (**2003**) 152.

Li, H., Wei, S., Qing, C., Yang, J. *J. Colloid Interface Sci.* 258 (**2003**) 40.

Luckham, P.F., Rossi, S. *Adv. Colloid Interface Sci.* 82 (**1999**) 43.

Lyklema, J. *Colloidal Dispersion,* Goodwin, J.W., (eds.), Dorset Press, Amsterdam, **1982**.

Manning, D.A.C., Hill, P.I., Howe, J.H. *J. Geol. Soc. London* 153 (**1996**) 827.

Michaels, A.S., Bolger, J.C. *Ind. Eng. Chem.* 3 (**1964**) 14.

Michaels**,** A.S., Morelos, O. *Ind. Eng. Chem.* 47 (**1955**) 1801.

Mpofu, P., Addai-Mensah, J., Ralston, J. *J. Colloid Interface Sci.* 261 (**2003**) 349.

Murray, H.H. *Inter. J. Mineral Process.* 7 (**1980**) 263.

Murray, H.H. *Appl. Clay Sci.* 5 (**1991**) 379.

Murray**,** H.H. *Appl. Clay Sci.* 17 (**2000**) 207.

Nicole, S.K., Hunter, R.J. *Aust. J. Chem.* 23 (**1970**) 2177.

Olph**e**n, van, H. *J. Colloid Sci.* 19 (**1964**) 313.

Prasad**,** M.S., Reid, K.J., Murray, H.H. *Appl. Clay Sci.* 6 (**1991**) 87.

Schroeder, P.A., Melear, N.D., Pruett, R.J. *Appl. Clay Sci.* 23 (**2003**) 299.

Smith, R.W., Narimatsu, Y. *Miner. Eng.* 6 (**1993**) 753.

Somasundaran, P., Healy, T.W., Fuerstenau, D.W. *J. Phys. Chem.* 68 (**1964**) 3562.

Sondi, I.J., Milat, O., Pravdic, V. *J. Colloid Interface Sci.* 189 (**1997**) 66.

Sondi, I.J., Pravdic, V. *Interfacial Electrokinetics and Electrophoresis*, Surfactant Science Series, vol. 106, Delgado, A.V., (eds.), Dekker, New York, **2002**.

Sousa**,** D.J.L., Varajão, A.F.D.C., Yvon, J., Scheller, T., Moura, C.A.V. *J. South Amer. Earth Sci.* 24 (**2007**) 25.

Street, N. *J. Colloid Sci.* 12 (**1957**) 1.

Stumm, W. *Colloids Surf. A* 73 (**1993**) 1.

Stumm, W. *Colloids Surf. A* 120 (**1997**) 143.

Swartzen-Allen, S.L., Matijevic, E. *Chem. Rev.* 74 (**1974**) 385.

Tadros, T.F. *Adv. Colloid Interface Sci.* 21 (**1980**) 141.

Thiessen, P.A. *Z. Elektrochem. Angew. Phys. Chem.* 48 (**1942**) 675.

Tombácz, E., Szekeres, M. *Appl. Clay Sci.* 34 (**2006**) 105.

Vasel, A. *Colloid Polym. Sci.* 33 (**1923**) 178.

Westall, J., Hohl, H. *J. Colloid Interface Sci. 12* (**1980**) 265.

Williams, D.J.A., Williams, K.P. *J. Colloid Interface Sci.* 65 (**1978**) 79.

Wypych, F., Satyanarayana, K.G. *Clay Surfaces: Fundamentals and Applications.* Interface Science and Technology, vol. 1, Elsevier Academic Press, London, **2004**.

Yan, C.L., Xue, D.F. *J. Alloys Compd.* 431 (**2007**) 241.

Yuan, J., Pruet, R.J. *Miner. Metall. Process.* 15 (**1998**) 50.

Zhu, X., Jiang, D., Tan, S., Zhang, Z. *J. Eur. Ceram. Soc.* 21 (**2001**) 2879.

Appendix C:

C.1 Classification of Adsorption Isotherms

To understand the significance of the adsorption curve, considering first the Langmuir (*S*, *L*) isotherms, the tangent of the angle, relative to the *y*-axis, of any portion of these curves represents the increment of concentration in the external phase, necessary to maintain a constant increment of concentration, at equilibrium, in the substrate. The slope of the isotherm at any point may be regarded as a measure of the ease with which solute molecules can find vacant sites at the surface.

In the *L*-curve, the slope steadily falls with rise in concentration because vacant sites become more difficult to find with the progressive covering of the surface. In the *S*-curve, the slope at first increases with concentration, because of cooperative adsorption, sites capable of retaining a solute molecule increase. Eventually, in all cases, the slope falls due to saturation of the surface, when no vacant sites remain.

The *H*-curve arises in special cases where the adsorbate-substrate affinity is especially high, in other words, the solute has such high affinity that in dilute solutions it is completely adsorbed, or at least there is no measurable amount remaining in solution. The initial part of the isotherm is therefore vertical and in the most extreme form, the curve is a horizontal line running into the vertical axis.

In the *C*-curve, the feature most common of these system is a substrate which is microporous and a solute which on general chemical considerations is expected to have higher affinity for

the substrate than the solvent [Giles, et al. 1960]. A linear isotherm is therefore consistent with conditions in which the number of sites remains constant throughout the range of solute concentrations up to saturation of the substrate. This means that the surface available for adsorption expands proportionally with the amount of solute adsorbed. Of course the expansion of a structure cannot continue indefinitely and a situation can be envisaged where a substrate can be opened up and an internal area becomes available.

A second slope in the curve may indicate a change in internal structure caused by pressure of the adsorbed solute. A horizontal plateau indicates saturation of all the external and internal area of the substrate. It is possible that isotherms are produced that do not fit readily into the predetermined classification system as outlined, unusual curves may be encountered for short-term, non-equilibrium conditions [Giles, et al. 1964]. Also, the partial breakdown of the substrate structure, variation in energy over the substrate surface or traces of highly surface-active impurities resulting in solvated micelles can determine isotherm curves that may be difficult to interpret.

C.2 Adsorption Isotherm Experiments: General Data

Gel permeation chromatography (GPC) experiments were conducted to determine the molecular weight and molecular weight distribution of the polyelectrolyte poly(diallyldimethylammonium chloride), (polyDADMAC; $C_8H_{16}ClN$). It was apparent that all samples submitted were similar; all polyelectrolyte samples had a broad distribution polymer component and a narrow molecular weight component as described in Figure C.1. The M_W reported by the supplier was between 70,000 to 100,000 g mol. The average computed M_W by GPC was 59,300 g mol., with a polydispersity value of 4.9.
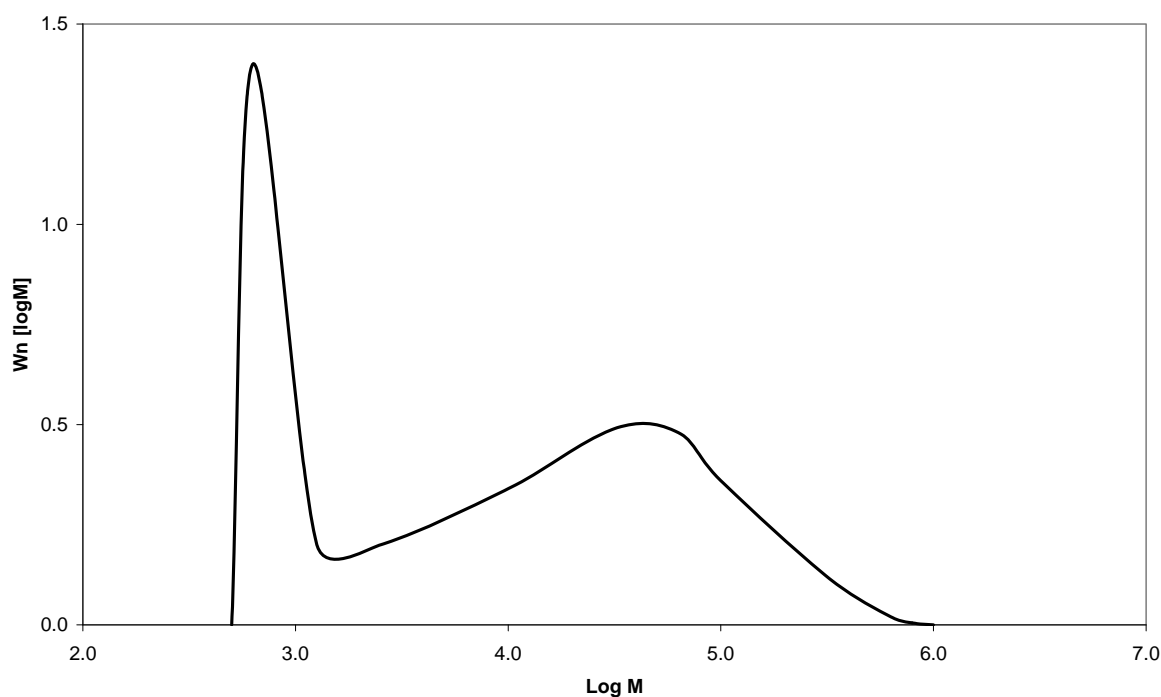
Figure C.1 *Molecular weight (Mw) distribution of polyelectrolyte polyDADMAC by Gel Permeation Chromatography. Experimental data supplied by Rapra Technology Ltd. (Shropshire, UK).*
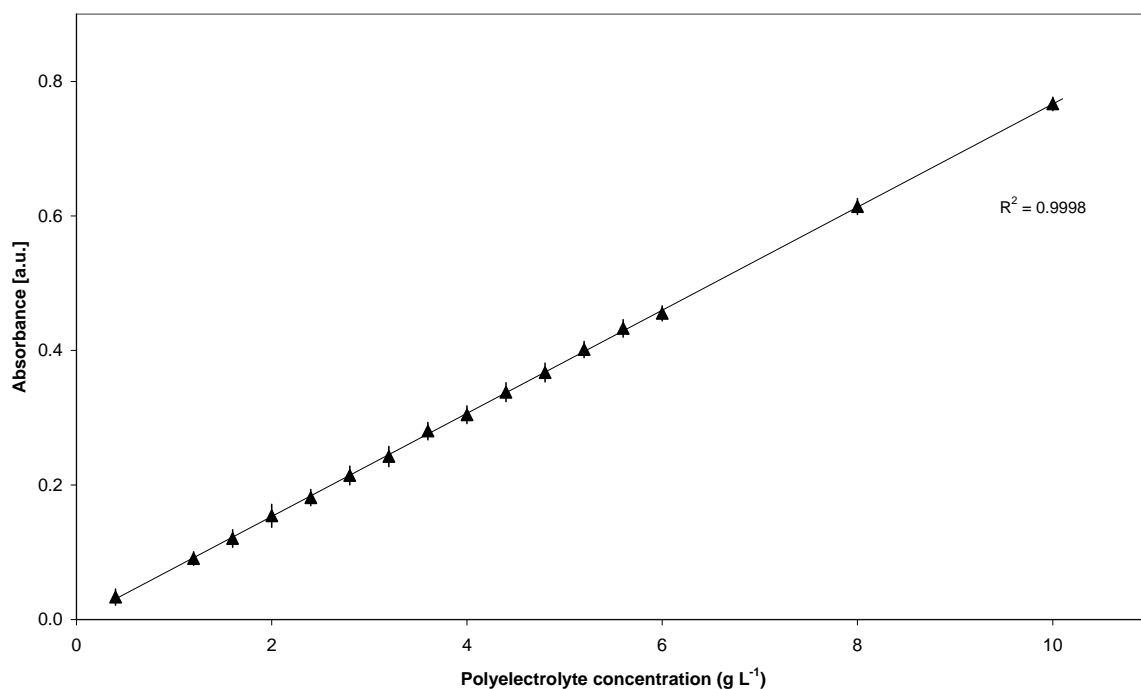
Figure C.2 *Concentration profile for the polyelectrolyte polyDADMAC.*

Known concentrations of polyelectrolyte polyDADMAC were dissolved in ultra pure water without further adjustment of pH. Concentrations of polyelectrolyte were measured by using UV-Vis spectroscopy. A concentration profile for the polyelectrolyte samples are shown in Figure C.2. Comparable experimental intensities were brought about by diluting individual samples to yield an identical absorbance at the wavelength of 240 nm.
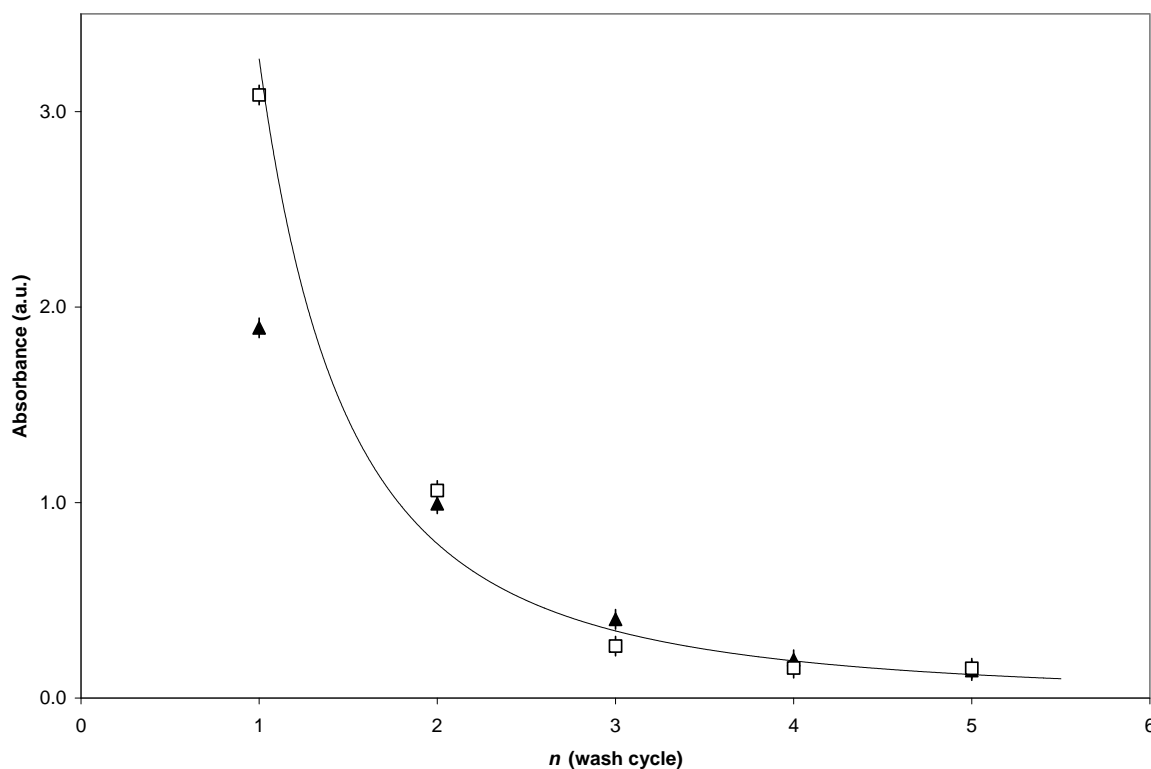
Figure C.3 *UV-vis absorbance values for supernatant from hollow PS (□) and solid PS (▲) samples after 24 hr conditioning.*

Figure C.3 indicates the reduction in absorbance due to cleaning of hollow and solid polystyrene samples. After the fourth and fifth wash cycle, the majority of absorbing material has been removed. The absorbing material was related to the release of alkane groups (C_nH_{2n+n}) from the polystyrene surface and ether compounds (C-O-C) attributed to the polymerisation process of polystyrene.

Even after dialysis of the PS samples, the PS microspheres required further wash cycles to remove unreacted monomer. During the conditioning prior to polyelectrolyte adsorption an increase in the absorbance was measured, this was attributed to the release of weak-bonded chemical groups from the PS surface. An increase in absorbance is shown in Figure C.4.

315
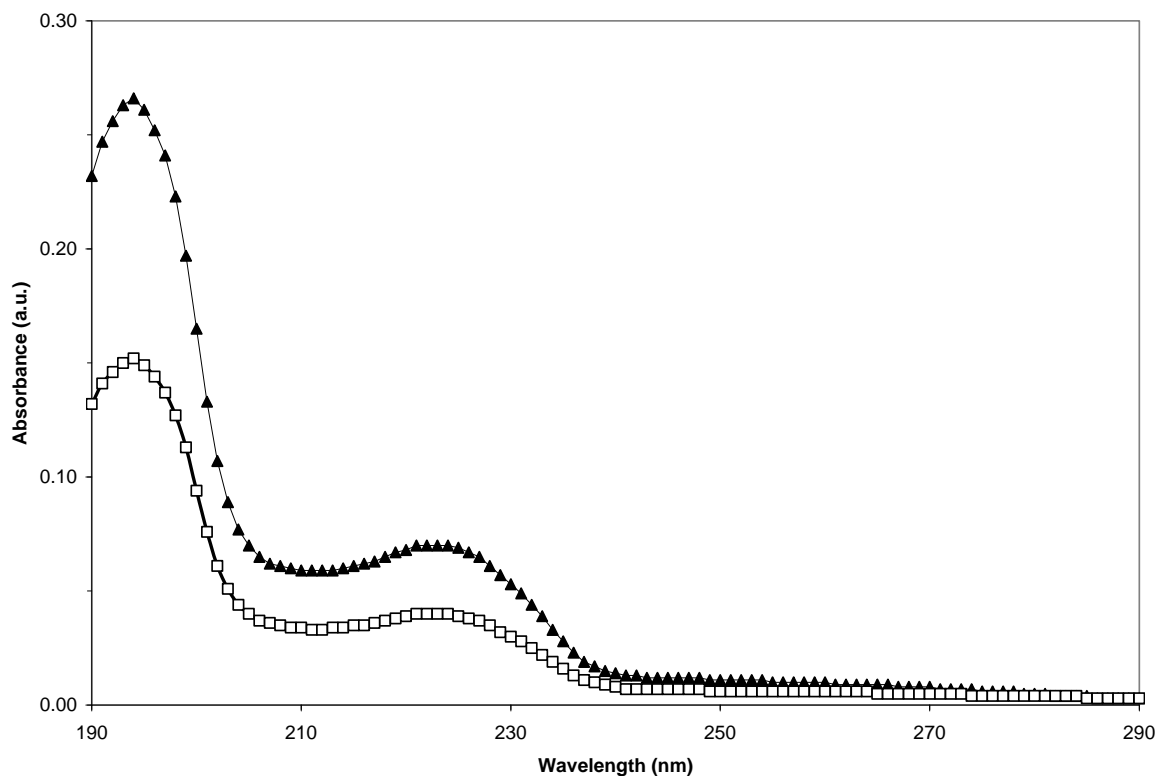
Figure C.4 *Increase in UV-Vis absorbance due to conditioning of hollow PS. Initial absorbance value after cleaning (□); and absorbance after 24 hr conditioning (▲).*

Figure C.4 represents an increase in absorbance due to the further release of chemical groups from the PS surface in solution. The absorbance peaks at wavelengths 194 and 223 nm are related to the release of alkane groups from the PS surface and ether compounds, a result of the polymerisation process.

Appendix C: References

Giles, C.H., MacEwan, T.H., Nakhwa, S.N. *J. Chem. Soc.* 786 (**1960**) 3973.

Giles, C.H., Tolia, A.H. *J. Appl. Chem.* 14 (**1964**) 186.

Appendix D:

D.1 Spray Drying: A Model Review

Several models capable of describing evolving particle morphology exist in the literature, varying in complexity [Erriguible, et al. 2005; Kohout, et al. 2006; Porras, et al. 2007]. A large variety of morphologies are observed when drying droplets to solid particles, identical droplets can dry to small dense, solid particles or large inflated shells depending on their drying history. Two particles subjected to identical drying conditions but with different initial compositions might form particles with markedly different morphologies. Capturing the diversity of possibilities is a challenge when constructing models for droplet drying. The most common way to handle particle formation is by a receding-interface, or shrinking core type approach [Kadja, et al. 2003; Mezhericher, et al. 2008a; 2008b]. Such models assume ideal shrinkage initially until a pre-specified critical moisture content is attained. Thereupon, evaporation is occurring at a clearly defined receding front, separating a wet central core from a dry outer shell with constant properties [Handscomb, et al. 2009].

This appendix chapter has been written to describe various simplified analytical models that can be used to link material properties and process parameters to particle and the resultant product attributes. An engineering approach is used, relying on dimensionless numbers, and approximate expressions are present where the exact equations are cumbersome. However, for this research thesis a model approach to determine the morphology of a spray dried particle is unfeasible, requiring the determination of multiple unknown physical parameters.

Components in a spray dried particle

The key to successful particle engineering is to understand and control the mechanisms that determine the radial distribution of components during the drying process. Several driving forces that may be responsible for separation of components have been suggested. Surface activity may lead to preferential adsorption of components on the droplet surface, causing a diffusional flux towards the surface. On the other hand, as the evaporating droplet shrinks its receding droplet surface leads to increasing solute concentrations at the surface. This causes a diffusional flux away from the surface [Kim, et al. 2009]. The evaporation of a solution droplet in a spray dryer is a coupled heat and mass transport problem. The process is driven by the difference between the vapour pressure of the solvents and their partial pressure in the gas phase. The rate of evaporation is determined by the balance of energy required to vaporise the solvent and energy transported to the surface of the droplet. Various numerical models have been reviewed that described the evaporation of mulitcomponent droplets [Miller, et al 1998; Vehring, 2007].

In the absence of internal convection the distribution of the chemical components in an evaporating droplet can be described by the non-linear diffusion equation. For constant diffusion coefficients and negligible interactions between the solutes the diffusion equations becomes Fick's second law of diffusion. This equation in a one-dimensional form has an analytical solution, if the droplet evaporates at a constant rate, the evaporation rate, κ, is defined as (for a definition of the parameters refer to the Nomenclature at the end of this appendix):

$$d^2(t) = d_0^2 - \kappa t \qquad [D.1]$$

The droplet surface area decreases linearly with time. This equation can also be used to approximate the droplet drying time, which should be smaller than the residence time of the droplet in the spray dryer to allow complete drying.

$$\tau_D = \frac{d_0^2}{\kappa} \qquad\qquad \text{[D.2]}$$

The solution of the diffusion equation can be rearranged so that it yields the surface enrichment, E_i, which is the surface concentration of component i in relation to its average concentration in the droplet [Vehring, et al. 2007].

$$E_i = \frac{c_{s,i}}{c_{m,i}} = \frac{\exp(0.5 Pe_i)}{3\beta_i} \qquad\qquad \text{[D.3]}$$

Here a dimensionless Peclet number, *Pe*, has been used to simplify the equation:

$$Pe_i = \frac{\kappa}{8 D_i} \qquad\qquad \text{[D.4]}$$

β is a function that must be integrated numerically for each *Pe* number to obtain an exact solution [Vehring, et al. 2007]. Alternatively, an approximate expression for Equation D.3 can be used instead [Vehring, 2008]:

$$E_i = \frac{c_{s,i}}{c_{m,i}} = 1 + \frac{Pe_i}{5} + \frac{Pe_i^2}{100} + \frac{Pe_i^3}{4000} \qquad\qquad \text{[D.5]}$$

The average concentration follows from a mass balance.

$$c_{m,i} = c_{0,i} \left(1 - \frac{t}{\tau_D} \right)^{-\frac{3}{2}}$$

[D.6]

With these equations, the surface concentrations of the components can be predicted at any time in the evaporation process as a function of their Peclet number. The parameter, $\tau_{sat,i}$, the time for a component to reach saturation at the surface, can be derived:

$$\tau_{sa,i} = \tau_D \left(1 - \left(S_{0,i} E_i \right)^{\frac{2}{3}} \right)$$

[D.7a]

$$S_{0,i} = \frac{c_{0,i}}{c_{sol,i}}$$

[D.7b]

where the initial saturation of the components, $S_{0,i}$, is the second dimensionless parameter that influences the particle formation process. Further characteristic times are associated with nucleation, growth, and transitions. For components that do not readily crystallise these characteristic times are frequently longer than the precipitation stage defined by:

$$\tau_{p,i} = \tau_D - \tau_{sat,i} = \frac{d_0^2}{\kappa} \left(S_{0,i} E_i \right)^{\frac{2}{3}}$$

[D.8]

In the case a fully or partially amorphous solid is formed. Another parameter becomes useful: $\tau_{t,i}$, the time it would take a component to reach a concentration at the surface that is equal to its true density in the dry state. While this is hypothetical, in a multi-component droplet, this

characteristic time can be used for a rough estimate of the time at which a shell at the surface is formed.

$$\tau_{t,i} = \tau_D \left(1 - \left(P_{0,i} \cdot E_i \right)^{\frac{2}{3}} \right)$$

[D.9a]

$$P_{0,i} = \frac{c_{0,i}}{\rho_{t,i}}$$

[D.9b]

The characteristic times given above are useful for particle design, because they allow an estimate of the sequence of precipitation events at the surface and the time that is available for crystallisation of components.

The equations can be evaluated if a reasonable estimate for the droplet evaporation rate can be found. Calculation of evaporation rates as a function of the processing parameters is not a trivial problem in a realistic spray dryer. A simple approximation is given that uses the following equation for single droplet evaporation [Vehring, 2008]:

$$\kappa = 8 D_g \frac{\rho_g}{\rho_1} \left(Y_s \left(T_e \right) - Y_\infty \right)$$

[D.10]

This expression is a good approximation as long as the partial pressure of the evaporating solvent remains small, i.e. for droplet temperatures that are much lower than the boiling point of the solvent. At high droplet temperatures the effects of Stephan flow [Newbold, et al. 1973] should be included.

To find the mass fraction at the surface of the droplet, Y_s, the equilibrium temperature, T_e, of the evaporating droplet must be determined. This can be done by solving the equation in combination with a Clausius-Clapeyron relationship:

$$\frac{\Delta \widehat{H}v}{\widehat{c}} = -\frac{Le \cdot \left(T_\infty - T_e\right)}{Y_s\left(T_e\right) - Y_\infty} \qquad \text{[D.11]}$$

The Lewis number, *Le*, is the ratio of the thermal diffusivity and the mass diffusivity in the gas phase.

Several corrections for droplet-droplet interactions or for the convective flow around the drying droplets are required to be introduced to describe the actual situation in a spray dryer. Adequate models describing the droplet evaporation have been developed [Elperin, et al. 1995; Handscomb, et al. 2009; Handscomb, et al. 2010]. Modelling of flow fields in spray dryers has been accomplished [Makkinejad, 2001]. The usefulness of the simple approach presented here lies in its potential to provide a quick overview of the general trends for a particular particle design problem. It allows an assessment of the relative importance of various process parameters and material properties. This model cannot describe the processes that occur during the solidification of the particles, such as precipitation or rupturing of shells, and it does not account for surface activity. However, it can approximate the distribution of components prior to solidification and may be predictive of the structure of the dry particle.

Formation mechanisms and the Peclet number

For Peclet numbers smaller than 1, the diffusional motion of the suspended solids or solutes is fast compared to the velocity of the receding droplet surface. In the absence of other driving forces, the solids or solutes remain fairly evenly distributed in the droplet during the evaporation. The surface enrichment is small. If the solutes are freely soluble in the solvent, the initial saturation is also small and the characteristic time for the solute to reach saturation at the surface is close to the droplet lifetime. In this case, solid particles with a particle density close to the true density of the dry components are likely to form. The Peclet number is influenced by a combination of material properties of the suspended solids, solute, and the solvent and processing parameters that determine the evaporation rate.

In the case of Peclet number larger than 1, the surface moves faster than the suspended or dissolved components. Depending on the nature of the component, different mechanisms are triggered once a critical concentration at the surface is reached. Solutes may not have sufficient time to crystallise during the precipitation stage. Instead, a shell may be formed due to the increase in viscosity as the solution transitions to a wet glass at the surface. Molecules with high initial saturation and fast crystallisation kinetics may separate into a crystalline phase. Suspended particles may form a composite shell. Regardless of the nature of the shell formation mechanism, the process is initiated at the surface. The resulting particles can have a range of different morphologies, depending on their size and the properties of their shells in the final stages of the drying process. Solid hollow microspheres can be formed, if the shell becomes rigid quickly and does not buckle or fold. Otherwise, dimpled or wrinkled particles are formed [Tsapis, et al. 2002]. With increasing Peclet numbers the time to reach the critical concentration for the shell formation occurs earlier in the evaporation process on a larger droplet. Hence, the density of the particle decreases.

Slurry droplet evaporation

The drying of a spherical wet particle, which consists of water and suspended solids, is reviewed. Consequently, the overall drying process can be divided in two stages. The first stage includes evaporation from the droplet surface. The second drying stage begins at the point when droplet moisture content falls down to its critical value and a dry porous solid shell is formed. In this stage water evaporation already takes place inside the wet particle at the receding interface between the shell and wet core.

First stage drying

At the beginning of the spray drying process, a typical droplet consists of large amount of liquid and insoluble or dissolved solids. The excessive liquid forms an envelope over the droplet surface, so the drying in the first stage is similar to evaporation of pure liquid droplet [Mezhericher, et al. 2008a]. During the first drying stage a uniform droplet temperature profile is generally accepted. Such assumption is based on small droplet diameters and typical spray drying conditions. Therefore, the appropriate equation of energy conservation is:

$$h_{fg}m_v + c_{p,d}m_d \frac{dT_d}{dt} = h(T_g - T_d)4\pi R_d^2 \qquad \text{[D.12]}$$

where h_{fg}, is the specific heat of evaporation, m_v, the vapour mass transfer rate, m_d, $c_{p,d}$, T_d, and R_d corresponding to mass, specific heat, temperature and radius of the dried droplet and h is the heat transfer coefficient.

If an elementary droplet mass decreasing is proportional to elementary droplet diameter shrinkage, then the droplet radius time-change can be tracked by the following expression [Levi-Hevroni, et al. 1995]:

$$dm_d = -dm_v = \rho_{d,w} 4\pi (R_d)^2 dR_d \qquad\qquad \text{[D.13]}$$

$$\frac{dR_d}{dt} = -\frac{1}{\rho_{d,w} 4\pi (R_d)^2} \dot{m}_v \qquad\qquad \text{[D.14]}$$

where m_v, is the vapour mass and $\rho_{d,w}$, is the density of the liquid fraction of the droplet. The mass transfer rate from the droplet surface is determined according to mass convection law:

$$\dot{m}_v = h_D (\rho_{v,s} - \rho_{v,\infty}) 4\pi (R_d)^2 \qquad\qquad \text{[D.15]}$$

where h_D, is the mass transfer coefficient and $\rho_{v,s}$, and $\rho_{v,\infty}$, are the partial vapour densities over the droplet surface and in the ambient.

The heat and mass transfer coefficients are found from:

$$h = \frac{Nu_d k_g}{2R_d} \qquad\qquad \text{[D.16]}$$

$$h_D = \frac{Sh_d D_v}{2R_d} \qquad\qquad \text{[D.17]}$$

where Nu_d and Sh_d are the corresponding Nusselt and Sherwood numbers, k_g, the drying conductivity and D_v, is the vapour diffusion coefficient. The Nusselt and Sherwood numbers are determined with the help of modified Rabz-Marshall correlations for evaporating spherical droplets [Levi-Hevroni, et al. 1995; Mezhericher, et al. 2008a].

The droplet mass during the first stage of the drying process can be found by integrating Equation D.13:

$$m_d = m_{d,0} - \frac{8}{6}\pi\rho_{d,w}\left[\left(R_{d,0}\right)^3 - \left(R_d\right)^3\right] \qquad \text{[D.18]}$$

where $m_{d,0}$, and $R_{d,0}$, are the initial mass and initial radius of the droplet. The droplet moisture content X_d, which is defined as mass ratio of liquid and solid fractions within the droplet can be derived by the following equation [Mezhericher, et al. 2008b]:

$$X_d = \frac{m_{d,w}}{m_{d,s}} = \frac{m_d}{m_{d,0}}\left(1 + X_{d,0}\right) - 1 \qquad \text{[D.19]}$$

Second stage drying

In the second drying stage, the wet particle is considered as a sphere with isotropic physical properties and temperature-independent shell thermal conductivity. The shell region is treated as one pierced by a large number of identical straight cylindrical capillaries, and the wet core region is assumed to be a sphere with liquid and solids.

The equations of energy conservation for wet core and shell regions of wet particles in the second drying stage are as following:

$$\rho_{wc} c_{p,wc} \frac{\partial T_{wc}}{\partial t} = \frac{1}{r^2} \frac{\partial}{\partial r} \left(k_{wc} r^2 \frac{\partial T_{wc}}{\partial r} \right), \qquad 0 \leq r \leq R_i(t) \qquad \text{[D.20]}$$

$$\frac{\partial T_{cr}}{\partial t} = \frac{\alpha_{cr}}{r^2} \frac{\partial}{\partial r} \left(r^2 \frac{\partial T_{cr}}{\partial r} \right), \qquad R_i(t) \leq r \leq R_p \qquad \text{[D.21]}$$

where T_{wc}, and T_{cr}, are the temperatures of the wet core and shell region of the wet particle, ρ_{wc}, $c_{p,wc}$ and k_{wc}, the density, specific heat and thermal conductivity of the wet core, α_{cr}, the shell thermal diffusivity and R_i and R_p are the radii of the shell-wet core interface and particle outer surface correspondingly. Boundary conditions for the above set of equations are reported elsewhere [Mezhericher, et al. 2008].

The shell-wet core interface receding rate is measured by the following relationship [Levi-Hevroni, et al. 1995]:

$$\frac{d(R_i)}{dt} = -\frac{1}{\varepsilon \rho_{wc,w} 4 \pi R_i^2} \dot{m}_v \qquad \text{[D.22]}$$

where ε is the porosity of the particle shell region and $\rho_{wc,w}$ is the density of the liquid component in the particle wet core.

Assuming that the diameter of the shell pore d_c is much greater than vapour molecular mean free path λ_v, and then the mass transfer rate can be calculated as:

$$\dot{m}_v = -\frac{8\pi\varepsilon^\beta D_{v,cr} M_w p_g}{R_{gc}\left(T_{cr,s} + T_{wc,s}\right)} \frac{R_p R_i}{R_p - R_i} \times \ln\left[\frac{p_g - p_{v,i}}{p_g - \left(\frac{R_{gc}}{4\pi M_w h_D R_p^2}\dot{m}_v + \frac{p_{v,\infty}}{T_g}\right)T_{p,s}}\right] \qquad [\text{D.23}]$$

where $D_{v,cr}$ is the coefficient of vapour diffusion in the shell pores, M_w the molecular weight of the liquid, p_g the pressure of the drying agent, $p_{v,i}$ and $p_{v,\infty}$ the partial vapour pressures at the shell-wet core interface and in the ambient, $T_{wc,s}$ and $T_{cr,s}$ the temperature of the shell-wet core interface and shell outer surface, R_{gc} the universal gas constant and β is the power coefficient.

The particle mass is calculated according to the equation below:

$$m_p = \frac{m_{d,0}}{1 + X_{d,0}}\left(1 - \frac{\rho_{wc,w}}{\rho_{wc,s}}\right) + \frac{4}{3}\pi\rho_{wc,w}\left[\varepsilon R_i^3 + (1-\varepsilon)R_p^3\right] \qquad [\text{D.24}]$$

where m_p is the mass of dried particle and $\rho_{wc,s}$ is the density of solid component in the wet particle wet core. The particle moisture content is controlled by the following expression:

$$X_p = \frac{m_w}{m_s} = \frac{m_p}{m_{d,0}}\left(1 + X_{d,0}\right) - 1 \qquad [\text{D.25}]$$

where X_p is the wet particle moisture content and m_w and m_s are the corresponding to the masses of liquid and solid fractions of the particle.

Particle cracking and rupture

The wet particle dehumidification at elevated temperatures of drying air can result in a possible bubble formation and a boiling inside the particle wet core [Nešić, et al. 1991]. This process is considered responsible for total pressure rising under the porous shell. Consequently, when the pressure difference under the shell and at the ambient is higher than the shell tensile strength, it leads to cracking or rupture of the particle.

When the difference between the partial vapour pressure at shell-wet core interface and the ambient pressure is greater than zero $(p_{v,i} - p_g > 0)$, it can be concluded that the total pressure over shell-wet core interface equals to the partial vapour pressure, which in turn depends on the wet core temperature. Then, the total mass transfer rate through the shell pores is the sum of corresponding diffusion and forced flow rates:

$$\dot{m}_v = \dot{m}_{v,diff} + \dot{m}_{v,flow} = h_D \left(\rho_{v,s} - \rho_{v,\infty} \right) A_p \qquad \text{[D.26]}$$

where $\dot{m}_{v,diff}$ and $\dot{m}_{v,flow}$ are the vapour diffusion and forced mass flow rates, $\rho_{v,s}$ and $\rho_{v,\infty}$ the vapour densities at the particle surface and in the ambient and A_p is the particle outer surface area. Equation D.23 needs to be modified in such a way, that it will take into account the time and radius dependences of the total pressure in the pores of the shell region. The vapour diffusion mass transfer rate is the sum of diffusion mass transfer rate, which arises from vapour pressure gradient, and diffusion mass transfer rate [Kadja, et al. 2003; Mezhericher, et al. 2008a]:

$$\frac{\dot{m}_{v,diff}}{A_{pores}} = -\frac{2 D_{v,cr} M_w}{R_{gc} \left(T_{cr,s} + T_{wc,s} \right)} \frac{\partial p_v}{\partial r} + \frac{2 D_{v,cr} M_w}{R_{gc} \left(T_{cr,s} + T_{wc,s} \right)} \frac{p_v}{p_a} \frac{\partial p_a}{\partial_r} \qquad \text{[D.27]}$$

where p_v is the partial vapour pressure, p_a the partial air pressure and A_{pores} is the mean area of shell cross section, occupied by pores.

The sum of partial pressures gives mixture pressure p_m:

$$p_m = p_v + p_a \qquad \text{[D.28]}$$

By differentiating Equation D.28:

$$\frac{\partial p_m}{\partial r} = \frac{\partial p_v}{\partial r} + \frac{\partial p_a}{\partial r} \qquad \text{[D.29]}$$

The mean area of shell cross section, occupied by pores, is evaluated as:

$$A_{pores} = \varepsilon^{\beta} A_{total} = 4\pi\varepsilon^{\beta} R_p R_i \qquad \text{[D.30]}$$

where A_{total} is total mean area of shell cross section.

Substituting Equations D.28, D.29 and D.30 into Equation D.27:

$$\dot{m}_{v,diff} = \frac{8\pi\varepsilon^{\beta} D_{v,cr} M_w R_p R_i}{R_{gc}\left(T_{cr,s} + T_{wc,s}\right)\left(p_m - p_v\right)}\left(p_v \frac{\partial p_m}{\partial r} - p_m \frac{\partial p_v}{\partial r}\right) \qquad \text{[D.31]}$$

To determine the total forced mass flow rate through the porous shell:

$$\frac{\dot{m}_{flow}}{A_{total}} = -\frac{B_k}{\mu_m} \frac{2M_m p_m}{R_{gc}\left(T_{cr,s} + T_{wc,s}\right)} \frac{\partial p_m}{\partial r}$$

[D.32]

where B_k is the permeability, μ_m and M_m are the dynamic viscosity and molecular weight of the air-vapour mixture.

The model examples given in this appendix indicate the level of sophistication that has been applied to a seemingly simple process as spray drying. If properly understood, these models that describe the basic particle formation and morphology can be used to design particles that have a multifunctional internal structure. A thorough review of the large number of models that predict particle morphology and the spray drying process is beyond the scope of this thesis. It will be interesting to follow whether the added functionality of the particles fabricated with such processes will justify their increased complexity in a commercial setting.

D.2 Spray Drying: General Data

Table D.1 *Flowability of calcined kaolin microspheres based on the Carr's Index value.*

Run	Ratio (*K:PS*)	Calcination Temperature (°C)	Bulk Density (g/cm³)	Effective Bulk Density (ρ_{eff}) (g/cm³)	CI
2 a	1:1	850	0.09 ± 0.01	0.11 ± 0.01	18
2 b	1:1	1000	0.12 ± 0.01	0.15 ± 0.01	20
2 c	1:1	1200	0.18 ± 0.01	0.23 ± 0.02	22
2 d	1:1	1400	0.35 ± 0.01	0.44 ± 0.02	20
3 a	1.5:1	850	0.11 ± 0.01	0.14 ± 0.01	21
3 b	1.5:1	1000	0.13 ± 0.01	0.16 ± 0.01	19
3 c	1.5:1	1200	0.20 ± 0.01	0.25 ± 0.02	20
3 d	1.5:1	1400	0.38 ± 0.01	0.48 ± 0.02	21
4 a	2:1	850	0.14 ± 0.01	0.18 ± 0.01	22
4 b	2 :1	1000	0.17 ± 0.01	0.22 ± 0.02	23
4 c	2 :1	1200	0.24 ± 0.01	0.30 ± 0.02	20
4 d	2 :1	1400	0.41 ± 0.02	0.52 ± 0.03	21
5 a	3:1	850	0.15 ± 0.01	0.19 ± 0.01	21
5 b	3 :1	1000	0.18 ± 0.01	0.23 ± 0.02	22
5 c	3 :1	1200	0.25 ± 0.01	0.32 ± 0.02	22
5 d	3 :1	1400	0.63 ± 0.01	0.80 ± 0.02	21
6 a	4:1	850	0.15 ± 0.01	0.19 ± 0.01	21
6 b	4 :1	1000	0.17 ± 0.01	0.22 ± 0.02	23
6 c	4 :1	1200	0.25 ± 0.01	0.32 ± 0.02	22
6 d	4 :1	1400	0.63 ± 0.01	0.80 ± 0.02	21

Table D.2 *Important sizes of calcined kaolin microspheres prepared at different processing parameters.*

| Run	Ratio (*K:PS*)	Calcination Temp. (°C)	Particle Size d_{10} (μm)	Particle Size d_{50} (μm)	Particle Size d_{90} (μm)	Mean Size (μm)
2 a	1:1	850	6.2 ± 0.9	15.9 ± 0.9	22.8 ± 0.8	15.4 ± 0.8
2 b	1:1	1000	3.7 ± 0.8	13.3 ± 0.8	19.8 ± 0.8	14.4 ± 0.8
2 c	1:1	1200	3.3 ± 0.8	11.6 ± 0.6	17.7 ± 0.6	13.9 ± 0.6
3 a	1.5:1	850	5.0 ± 0.6	12.2 ± 0.4	20.6 ± 0.4	14.4 ± 0.6
3 b	1.5:1	1000	4.9 ± 0.7	11.2 ± 0.4	16.2 ± 0.6	13.4 ± 0.4
3 c	1.5:1	1200	4.3 ± 0.7	10.4 ± 0.6	15.3 ± 0.6	13.2 ± 0.4
4 a	2:1	850	5.8 ± 0.6	13.1 ± 0.6	20.1 ± 0.6	14.5 ± 0.6
4 b	2 :1	1000	4.3 ± 0.7	10.7 ± 0.4	16.8 ± 0.6	13.7 ± 0.6
4 c	2 :1	1200	4.1 ± 0.7	10.1 ± 0.9	14.8 ± 0.6	13.1 ± 0.6
5 a	3:1	850	4.8 ± 0.8	13.8 ± 0.6	21.7 ± 0.6	14.8 ± 0.6
5 b	3 :1	1000	5.3 ± 0.8	11.7 ± 0.6	17.6 ± 0.4	13.9 ± 0.6
5 c	3 :1	1200	5.1 ± 0.9	11.4 ± 0.8	17.0 ± 0.8	13.9 ± 0.8
6 a	4:1	850	4.6 ± 0.8	12.7 ± 0.8	19.2 ± 0.6	14.3 ± 0.4
6 b	4 :1	1000	5.3 ± 0.6	11.3 ± 0.6	16.8 ± 0.6	13.7 ± 0.6
6 c	4 :1	1200	5.2 ± 0.8	10.7 ± 0.6	15.9 ± 0.6	13.6 ± 0.8
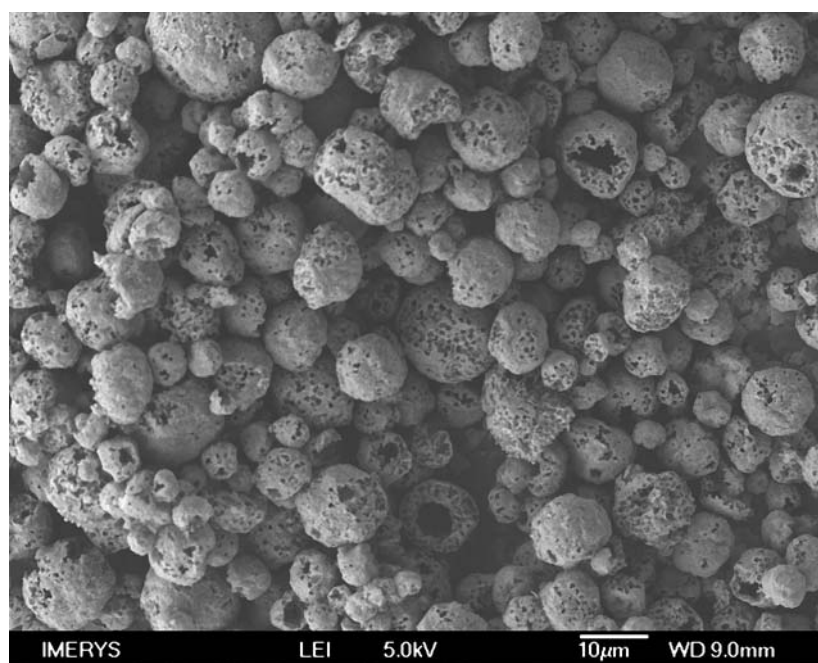
Figure D.1 *Ratio 1.5:1 Spray dried kaolin microspheres calcined at 850 ºC*
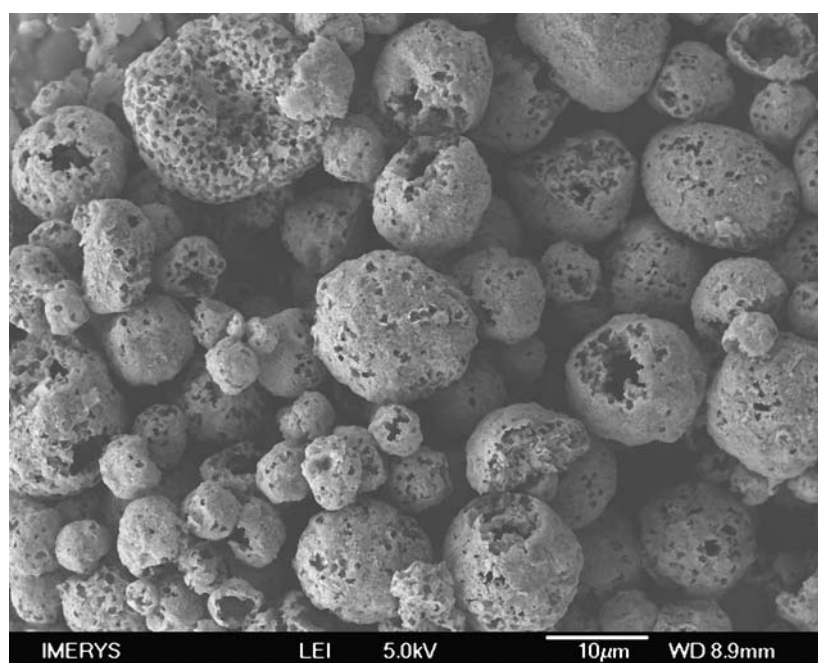

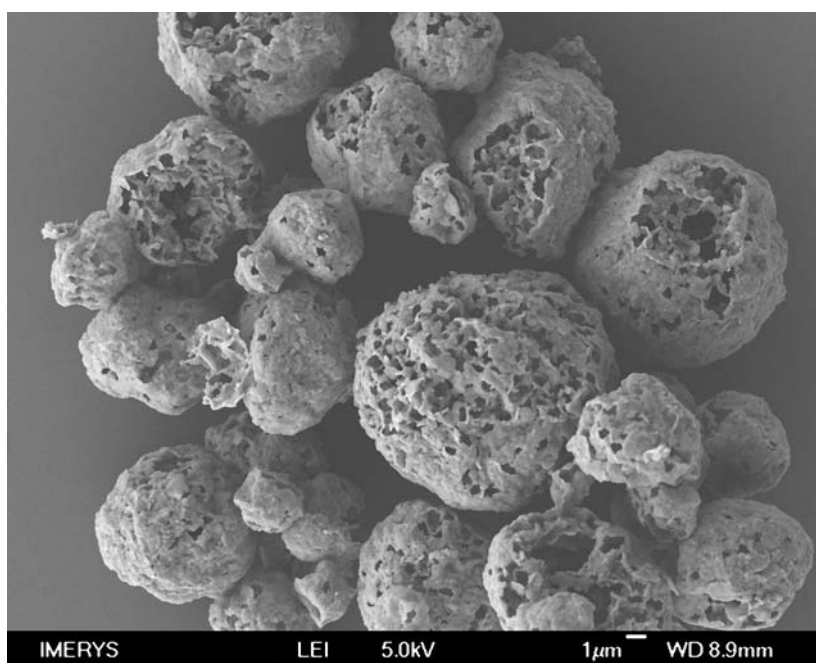**Figure D.2** *Ratio 1.5:1 Spray dried kaolin microspheres calcined at 1000 ºC*

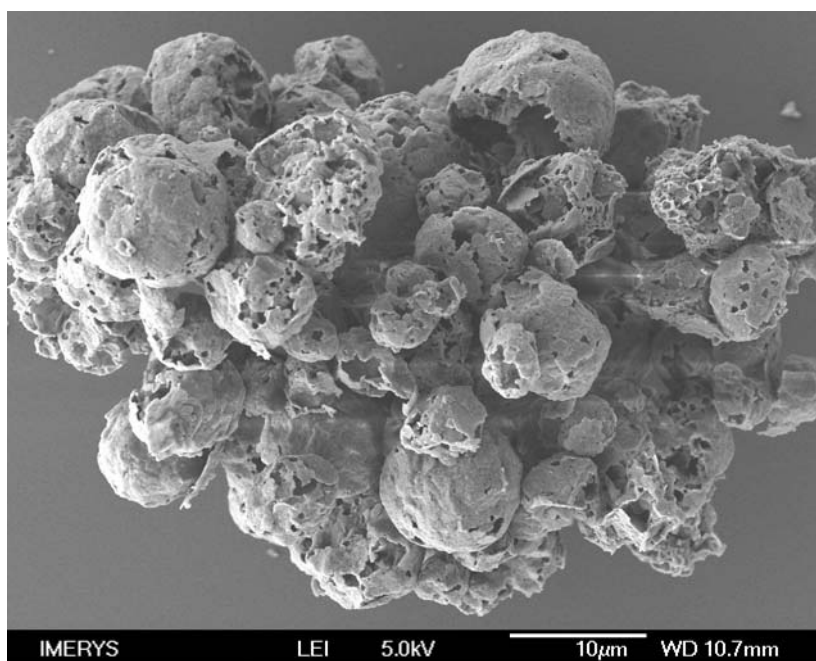**Figure D.3** *Ratio 1.5:1 Spray dried kaolin microspheres calcined at 1200 ℃*

Figure D.4 *Ratio 1.5:1 Spray dried kaolin microspheres calcined at 1400 ℃*
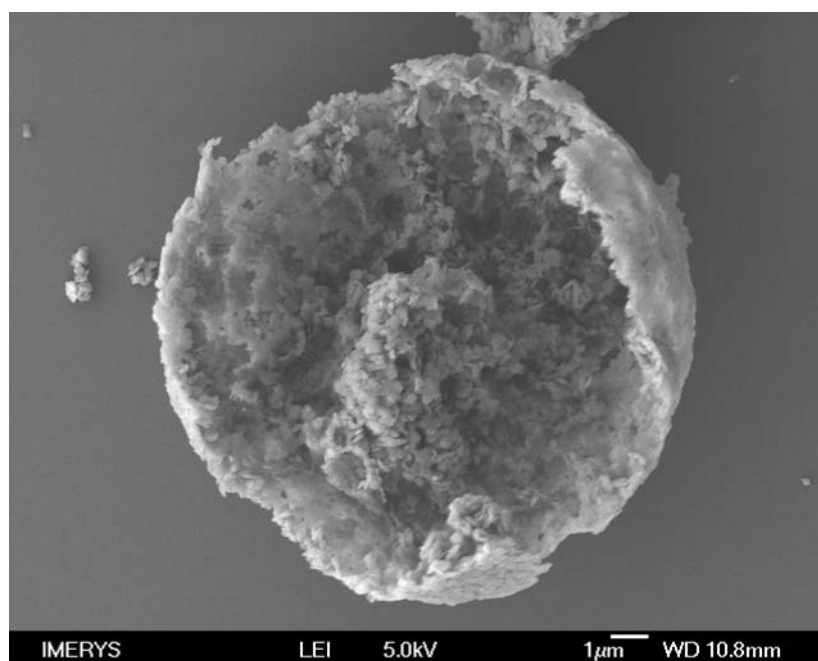
Figure D.5 *Shell structure of a calcined microsphere. Kaolin ratio 1:1; calcination temperature 850 ºC*
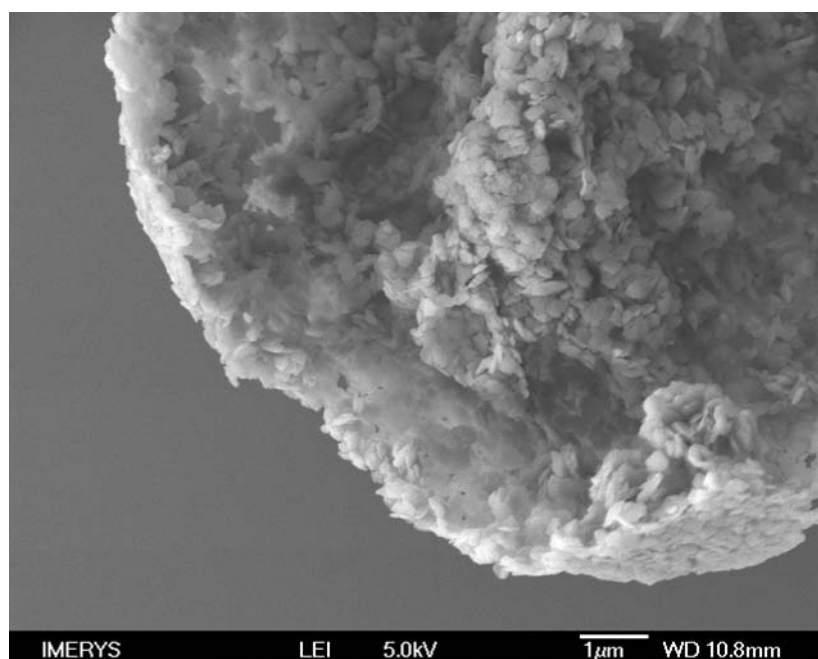

Figure D.6 *Shell structure of a calcined microsphere. Kaolin ratio 1:1; calcination temperature 850 ºC*
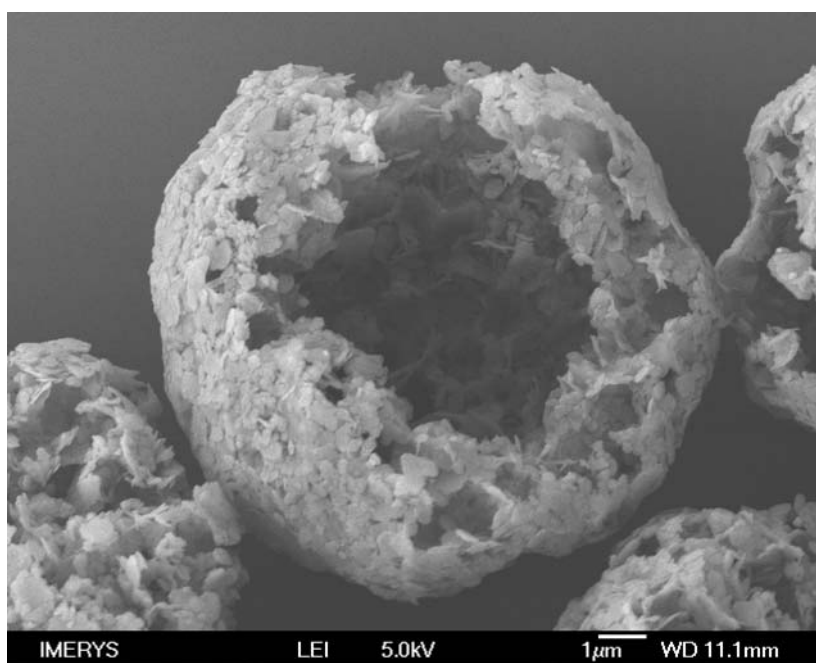
Figure D.7 *Shell structure of a calcined microsphere. Kaolin ratio 1.5:1; calcination temperature 850 ºC*
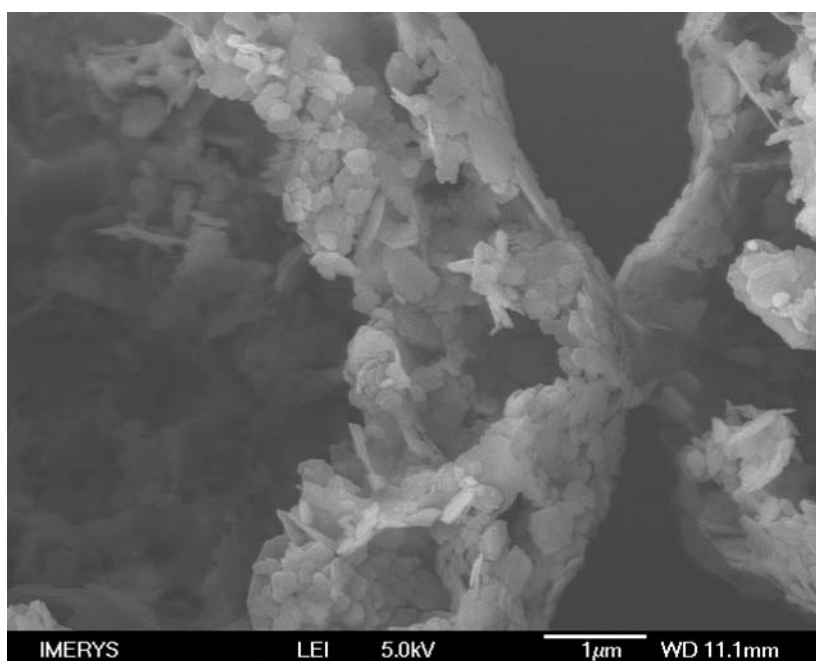

Figure D.8 *Higher magnification of a shell structure of a calcined microsphere. Kaolin ratio 1.5:1; calcination temperature 850 ºC*
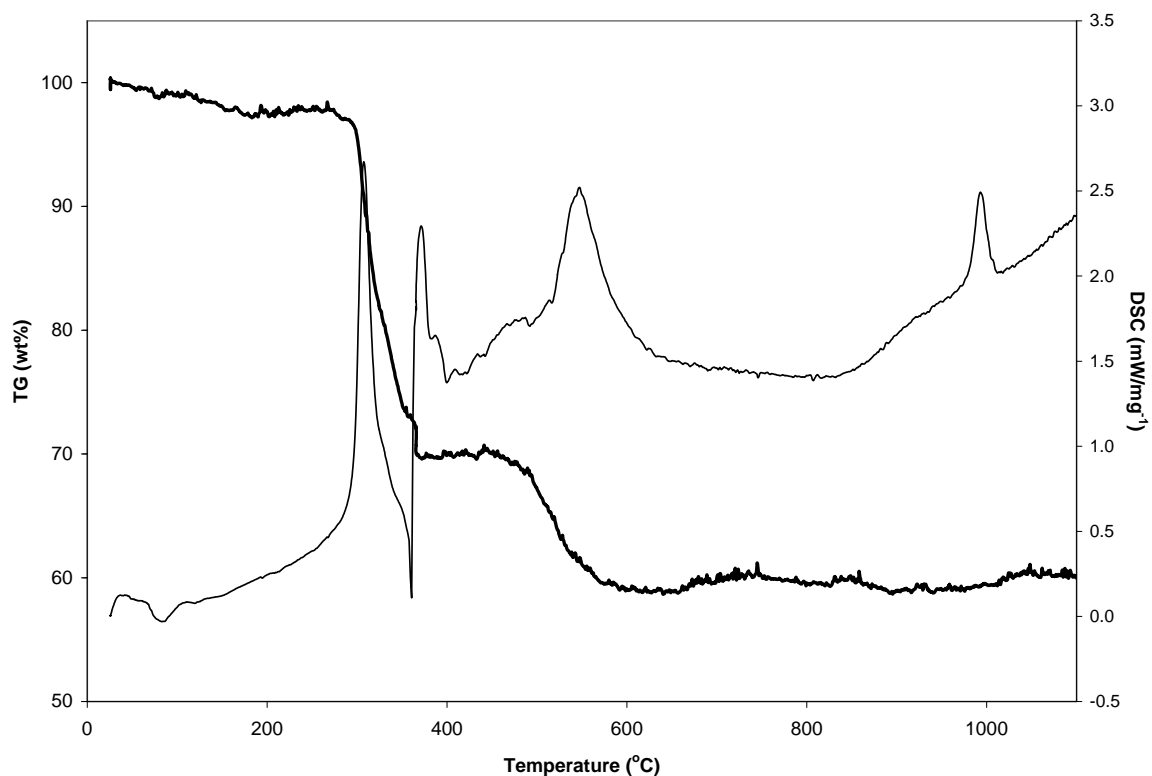
Figure D.9 *Thermal decomposition of spray dried microspheres by TG-DSC. Kaolin ratio experiment 2:1.*
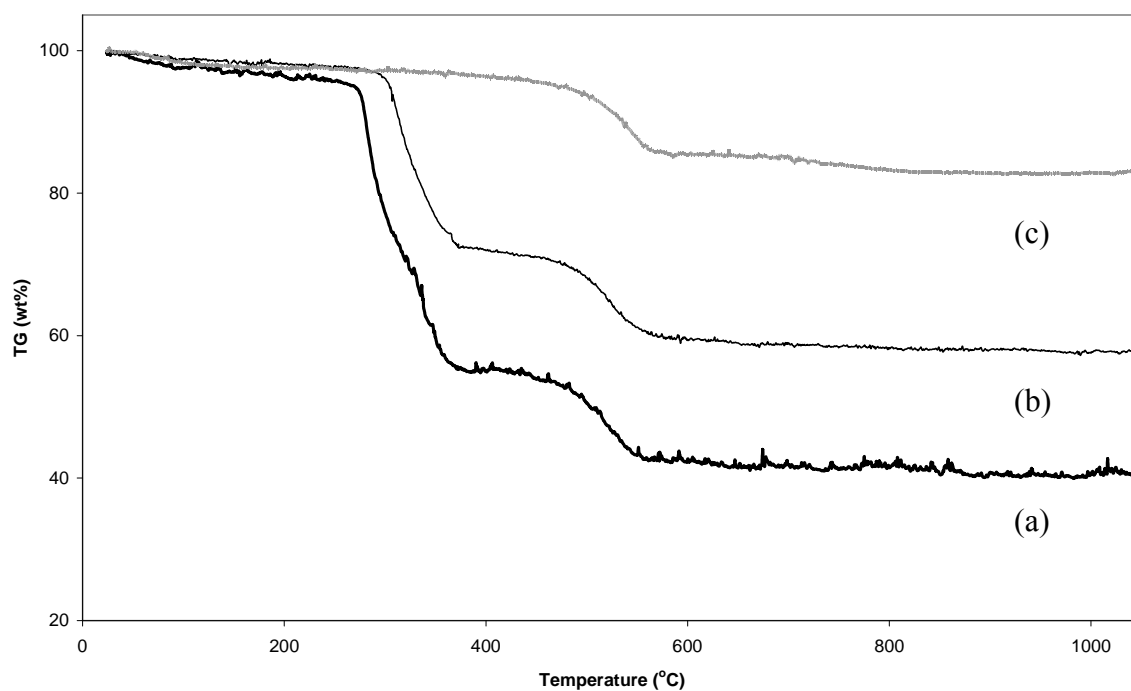

Figure D.10 *Thermal decomposition of spray dried microspheres. TG curves for kaolin ratio experiments 1.5:1 (a) and 3:1 (b). Reference TG curve for kaolin mineral is shown (c).*
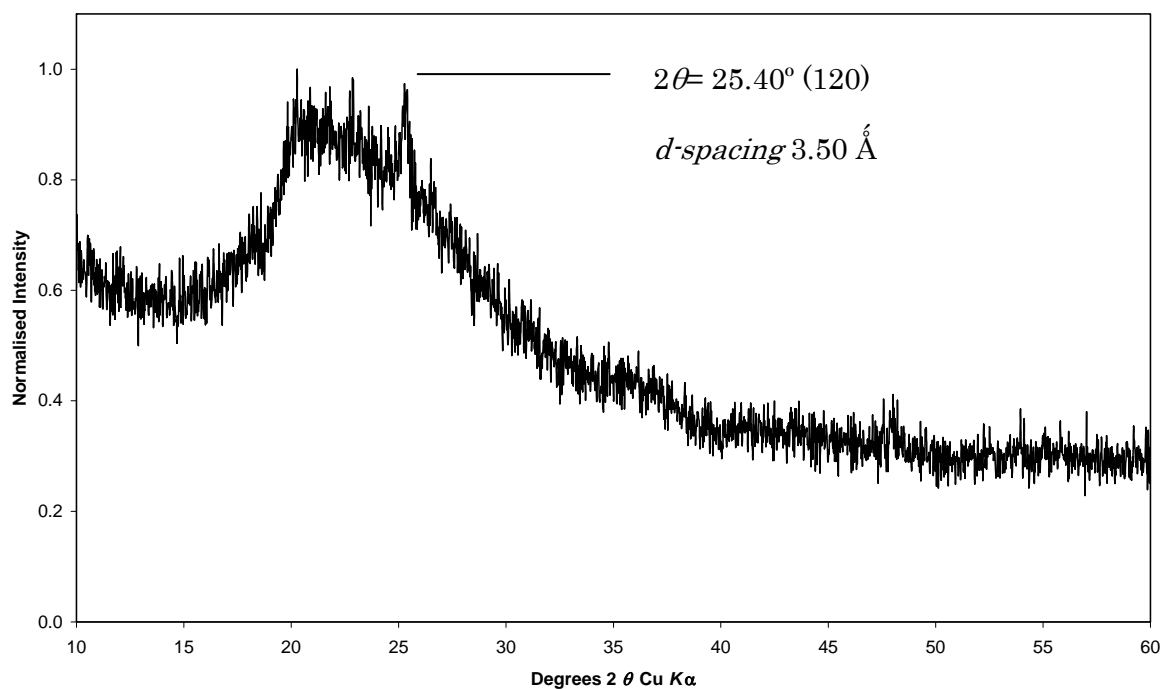
Figure D.12 *XRD pattern of calcined microspheres at 650 °C. Kaolin ratio experiment 1.5:1.*
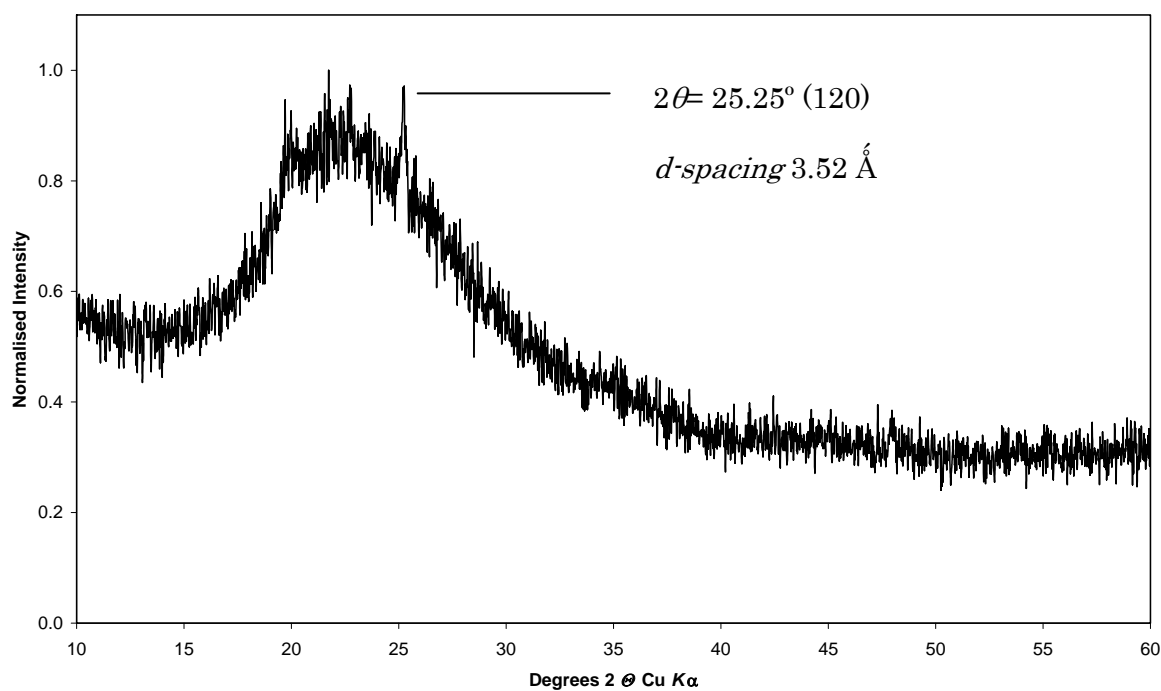

Figure D.13 *XRD pattern of calcined microspheres at 850 °C. Kaolin ratio experiment 1.5:1.*
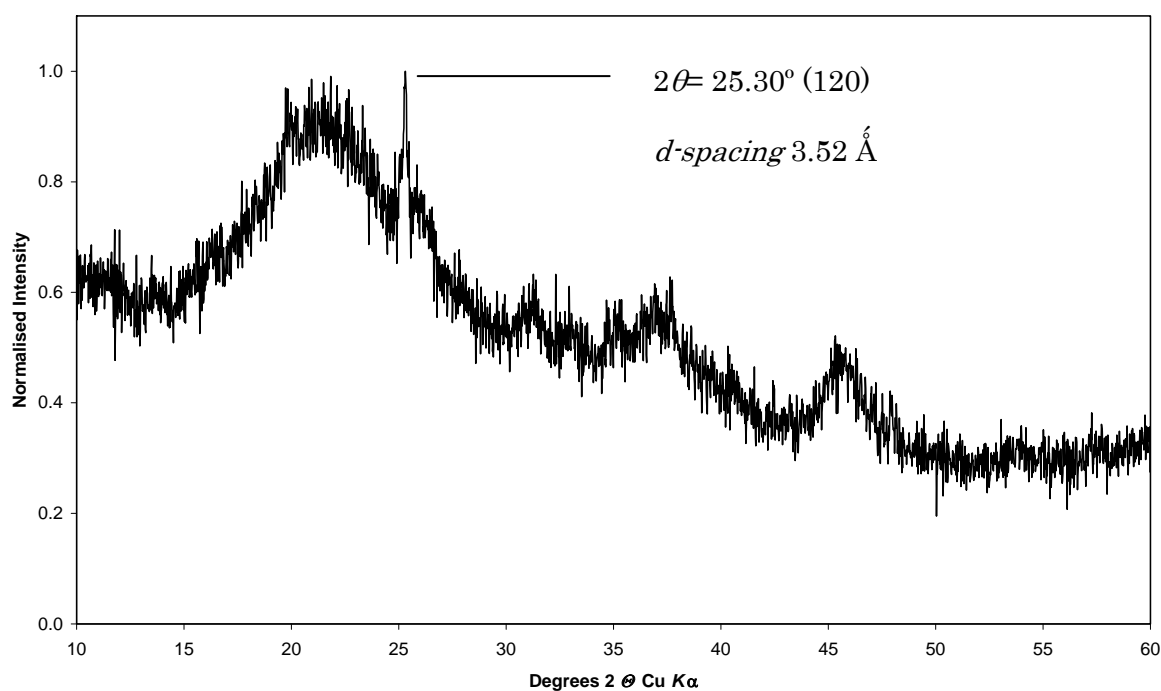
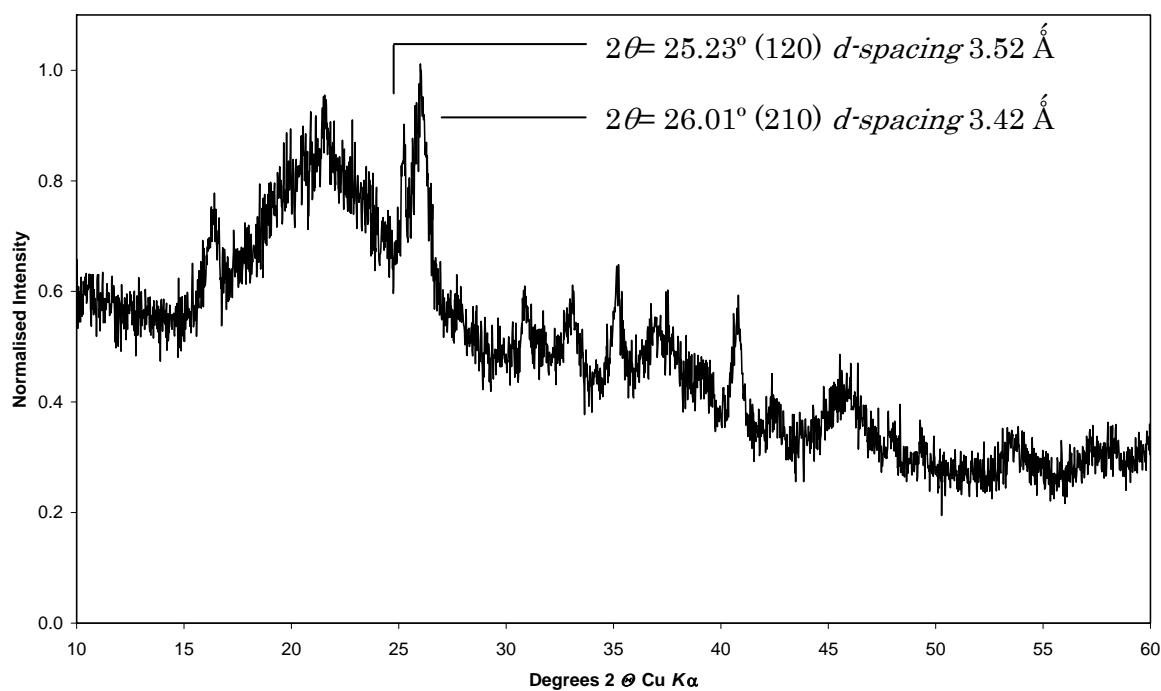**Figure D.14** *XRD pattern of calcined microspheres at 1000 °C. Kaolin ratio experiment 1.5:1.*

Figure D.15 *XRD pattern of calcined microspheres at 1200 °C. Kaolin ratio experiment 1.5:1.*

Table D.3 *Approximate costing for the production of low density kaolin microspheres.*

	Cost (£/tonne)	Account for loss in classifier	Account for loss in calciner	Account for loss in spray dryer	Total Cost (£/tonne)
Overheads	15	-	-	-	15.00
Classifier	6	-	-	-	6.00
Calciner	115	1.25	-	-	143.75
Spray dryer	70	1.25	1.35	-	118.13
Feed	150	1.25	1.35	1.1	278.44
Logistics	10	-	-	-	10.00
Bagging	18.5	-	-	-	18.50
					589.81

Cost analysis was based on the following:

- Fine kaolin feed used.

- Spray drying at 20 wt% solids to give approximate d_{50} of 11 µm.

- Herreschoff calcination process used.

- Air classification process used to degrit.

The following assumptions were made:

- Approximate costings are based on full utilisation of the relevant equipment.

- Assumes that all relevant equipment was available.

- Costs are a combination of fixed and variable costs bases on existing equipment.

- Loss in classifier assumed to be 25%.

- Loss in calciner assumed to be 35%.

- Loss in spray dryer assumed to be 10%.

Appendix D: References

Elperin, T., Krasovitov, B. *Int. J. Heat Mass Transfer.* 38 (**1995**) 2259.

Erriguible, A., Bernada, P., Couture, F., Roques, M.A. *Dry. Technol.* 23 (**2005**) 455.

Handscomb, C.S., Kraft, M., Bayly, A.E. *Chem. Eng. Sci.* 64 (**2009**) 228.

Handscomb, C.S., Kraft, M. *Chem. Eng. Sci.* 65 (**2010)** 713.

Kadja, M., Bergeles, G. *Appl. Therm. Eng.* 23 (**2003**) 829.

Kim, M., Laine, R.M. *J. Am. Chem. Soc.* 131 (**2009**) 9220.

Kohout, M., Grof, Z., Stêpánek, F. *J. Colloid. Interface Sci.* 299 (**2006**) 342.

Levi-Hevroni, D., Levy, A., Borde, I. *Dry. Technol.* 13 (**1995**) 1187.

Makkinejad, N. *Int. J. Heat Mass Trans.* 44 (**2001**) 429.

Mezhericher, M., Levy, A., Borde, I. *Chem. Eng. Process.* 47 (**2008a**) 1404.

Mezhericher, M., Levy, A., Borde, I. *Chem. Eng. Sci.* 63 (**2008b**) 12.

Miller, R.S., Harstad, K., Bellan, J. *Int. J. Multiph. Flow* 24 (**1998**) 1025.

Nešić, S., Vodnik, J. *Chem. Eng. Sci.* 46 (**1991**) 527.

Newbold, F.R., Amundson, N.R. *A.I.Ch.E Journal* 19 (**1973)** 22.

Porras, G.O., Couture, F., Roques, M. *Dry. Technol.* 25 (**2007**) 1215.

Tsapis, N., Bennett, D., Jackson, B., Weitz, D.A., Edwards, D.A. *Proc. Natl. Acad. Sci. USA* 99 (**2002**) 12001.

Vehring, R., Foss, W.R., Lechuga-Ballesteros, D. *Aerosol Sci.* 38 (**2007**) 728.

Vehring, R. *Pharm. Res.* 25 (**2008**) 999.

Appendix D. Nomenclature

Variable	Definition	Variable	Definition
A	Surface area	Y_s	Mass fraction of solvent at surface
A_{total}	Total mean area of shell cross section	Y_∞	Mass fraction of solvent, away from surface
B_k	Shell permeability		
C	Empirical coefficient	*Greek letters*	
$c_{0,i}$	Initial concentration, component i	A	Thermal diffusivity
$c_{s,i}$	Surface concentration, component i	B	Empirical power coefficient
$c_{sol,i}$	Solubility, component i	E	Shell porosity
$c_{m,i}$	Average concentration, component i	K	Evaporation rate
c_p	Specific heat	Λ	Molecular mean free path
D	Diameter	M	Dynamic viscosity
d_0	Initial diameter	P	Density
D	Diffusion coefficient, liquid phase	ρ_g	Drying gas density
D_g	Diffusion coefficient, gas phase	ρ_t	True density
D_v	Vapour diffusion coefficient	ρ_l	Droplet density
E_i	Surface enrichment, component i	τ_D	Characteristic droplet drying time
H	Heat transfer coefficient	τ_{sat}	Characteristic time to saturation
h_D	Mass transfer coefficient	τ_p	Characteristic time for precipitation
h_{fg}	Specific heat of evaporation	τ_t	Characteristic time to true density
ΔH_v	Standard enthalpy change of vaporisation		
K	Thermal conductivity	*Subscripts*	
Kn	Knudsen number	A	Air
Le	Lewis number	C	Shell capillary
M	Mass	Cr	Particle shell
m_v	Vapour mass transfer rate	D	Droplet
M	Molecular weight	$Diff$	Diffusion
Nu	Nusselt number	F	Final point of drying process
P	Pressure	$Flow$	Forced flow
P_0	Initial density ratio	G	Drying agent
Pe	Peclet number	I	Shell-wet core interface
R	Radial space coordinate	M	Air-vapour mixture
R	Radius	P	Particle
R_{gc}	Universal gas constant	*pores*	Shell pores
Re	Reynolds number	R	Radial direction
Sh	Sherwood number	S	Solid fraction or surface
S_0	Initial saturation	Sat	Saturated
T	Time	V	Vapour
T	Temperature	W	Liquid faction, water
T_e	Equilibrium temperature, droplet	Wc	Particle wet core
T_∞	Gas temperature, away from droplet	0	Initial point of drying process
X	Moisture content	∞	Bulk of drying agent

343